Numerical modelling of morphological impacts of Offshore Wind Farms

Thesis submitted in accordance with the requirements
of the University of Liverpool for the
degree of Doctor of Philosophy by

Elizabeth Katherine Christie

January 2014

Contents

List of Figures

List of Tables

List of Symbols

Δ	Mesh size taken as the surface of an element in 2D and the volume in 3D
η	Free surface elevation
κ	Von Karman constant (≈ 0.4)
λ	Wavelength
λ_p	Bed porosity
ν_T	Tracer diffusion coefficient
ν_t	Eddy viscosity
ω_i	Intrinsic angular frequency
$\overline{u}$, $\overline{v}$, $\overline{w}$	Depth averaged velocity components in x, y and z
Φ_b	Dimensionless bed load transport parameter
ρ	Fluid density
ρ_0	Reference density
ρ_s	Sediment density
σ	Sigma co-ordinate
τ_0	Bed shear stress
τ_f	Form drag component of the bed shear stress
τ_s	Skin friction component of the bed shear stress
τ_t	Component of the bed shear stress relating to sediment transport

τ_w Bed shear stress under waves

τ_{cr} Threshold bed shear stress for the movement of sediment

τ_{wf} Form drag component of the wave bed shear stress

τ_{ws} Skin friction component of the wave bed shear stress

Θ Direction of wave propagation

θ Shields parameter

θ_{cr} Critical Shields parameter

θ_{ip} Rank of the plane under consideration

ε_s Sediment diffusivity

$\vec{\ }$ Denotes a vector

$|\langle u_{eff}\rangle|$, $|\langle v_{eff}\rangle|$ Magnitude of the effective approach velocity in the x and y direction, respectively

A Cross sectional area of a structure perpendicular to the water particle velocity

a Total cross sectional area divided by effective cross sectional area

A_b, A_s Coefficients for the bed load and suspended load

a_m Amplitude of the tidal constituents

A_{Eff} Effective wet cross-sectional area

A_{sur} Surface area

A_{Total} Total cross-sectional area

B Coefficient for wave evolution

b Dimensionless coefficient

C Concentration of sediment

c Wave speed

C_D Quadratic drag coefficient

c_g Group velocity

C_m Inertia coefficient

C_s Dimensionless coefficient, $C_s = 0.1$ in this study

D Pile diameter

d Sediment grain size

d_* Dimensionless grain size

D_f Sediment deposition flux

d_{50} Median grain diameter

d_{90} Grain diameter for which 90% of the grains by mass are finer

E Wave energy

E_f Net erosion flux

e_{ij} Strain rate tensor

F Wave variance density spectrum

f Frequency

F_D Drag force

F_e Energy flux

F_I Inertial force

f_r Relative frequency

F_s Force exerted on a structure

F_u, F_v Drag force in the x and y direction, respectively

f_w Frequency of any given wave height

F_x, F_y Wave forcing in the x and y direction

g Acceleration due to gravity

h Water depth

H_0 Representative significant wave height

H_s Significant wave height

k Wave number

k_r Ripple roughness

k_s Nikuradse equivalent sand grain roughness

L Length scale

l Length of the vertical section of a pile

L_m Mixing length

m_1, m_2 Dimensionless coefficients

$MOFAC$ Morphological acceleration factor

N Wave action

n Number of structures

p Pressure

p_{atm} Atmospheric pressure

Q_b Mass bed-load transport rate per unit width

q_b Volumetric bed-load transport rate per unit width

Q_s Mass suspended load transport rate per unit width

q_s Volumetric suspended load transport rate per unit width

Q_t Total mass sediment transport rate per unit width

q_t Total volumetric sediment transport rate per unit width

R Rouse number

r Rotor blade diameter

S Scour depth

s Relative sediment density $s = \rho_s/\rho$

S_c Sediment source or sink term

S_f Source or sink of the fluid

S_h Sink term in momentum equation

S_T Source or sink of the tracer

S_w Wave source or sink term

S_x, S_y, S_z Source terms for the x, y, and z directions

S_{xx}, S_{xy}, S_{yy} Radiation stress tensors

T Wave period

t Time

T_p Peak period

T_r Passive or active tracer

T_{Hydro} Hydrodynamic period

T_{Morpho} Morphological period

U Mean flow velocity

u, v, w Three dimensional velocity components

u_* Shear velocity or friction velocity

u_1 Velocity in the x direction in the first horizontal plane

U_m Wave orbital velocity

u_∞ Free surface velocity

u_{conv}, v_{conv} Convective velocity in x and y

u_{cr} Critical entrainment velocity

u_{eff}, v_{eff} Effective approach velocity in the x and y direction, respectively

v_1 Velocity in the y direction in the first horizontal plane

W_s Settling velocity of sediment grains

x Horizontal coordinate

y Horizontal coordinate orthogonal to x

z Height above the sea bed

z_0 Bed roughness length

z_1 Vertical distance from the bed to the first horizontal plane

z_a Reference height marking the top of the boundary layer

z_f Bottom elevation

z_s Free surface elevation

z_{ref} Depth of the interface between bed-load and suspended load layers

ν Kinematic viscosity

K_C Keulegan-Carpenter number

Re Reynolds number

Vol Volume

Acknowledgements

I would like to express my gratitude to my primary supervisor Dr Ming Li for his guidance, focus, advice and continuous support throughout this research. I would also like to thank my secondary supervisor Professor Richard Burrows for his advice. I am indebted to Dr John Harris, at HR Wallingford, for his discussions and new ideas throughout the research. I am also grateful to Dr Charles Moulinec, at STFC, for advising me on TELEMAC HPC and being a general font of computing knowledge. I would like to thank Cliff Addison and Dave Love for their computing support.

This work has been aided by the use of HPC computing grants including HECToR class 1b access funding, and N8 HPC access provided and funded by the N8 consortium and EPSRC. I would also like to acknowledge the use of data throughout this study made available by, the Environment Agency, CEFAS, National Oceanography Centre, BODC, and COWRIE.

I would like to thank my friends and colleagues for their support and for all the great times we have had over the last few years. And last but by no means least, I would like to thank my family for putting up with me when I have been stressed, and being amazingly supportive, loving and caring. Thank you so much.

Abstract

Demand for renewable energy resources to reduce greenhouse gases for EU targets, has led to a recent rapid development of Offshore Wind Farms (OWF). As OWFs become larger and multiple sites are developed, it becomes increasingly important to determine the wind farms impact on the coastal environment for design and planning. It is well established that the wind turbine monopiles at OWFs modify the flow in the localised area of the structure, to create a complex 3D flow structure, which ultimately results in scour hole formation.

This present research aims to determine the impact of an OWF at both the localised and coastal scale through large scale modelling with the structures represented as islands in the mesh. This method is thought to be an improvement on the typical method of representing the structures as a resistance term in the grid, as it is able to capture some of the complex flow at the structure. The TELEMAC modelling package is used, with the hydrodynamics determined by the TELEMAC-3D module, the waves by the TOMAWAC module, and sediment transport by the SISYPHE module. Validation of the model at the structure showed good agreement with empirical data in the near field of the structure. Tidal flows are well predicted across the water depth, whilst scour formation is well predicted in front of the pile, there are areas of accretion in the wake which are unexpected.

The large scale impact of the wind farm on coastal processes was assessed and compared over two wind farm sites, representing different coastal environments. The Burbo Bank wind farm is situated in a coastal bay, whereas Scroby Sands OWF is an open coast site. In both cases the wind farm was seen to block the flow and influence the large scale coastal sediment pathways. At Burbo Bank the wind farm enabled stirring of sediment into suspension, and influenced the sediment transport over the south east corner of Liverpool Bay. The Scroby Sands wind farm was found to reduce the sediment flux magnitude in the vicinity of the array.

The long term morphological impact is also determined for the Burbo Bank OWF over a year period, with a morphological acceleration factor. Two methods are compared for generation of a set of representative waves, based on frequency of occurrence and wave energy. Both methods indicate that over a year period the wind farm has a large influence on sediment transport pathways, and increases sediment flux across the Great Burbo Flats. Maximum scour depth predictions at the structures showed good agreement with empirical formula. The pattern of scour for the representative waves based on frequency of occurrence, fits well with measured scour at the wind farm array.

Chapter 1

Introduction

1.1 General background

The need to reduce greenhouse gas emissions as set out by the Kyoto Protocol on climate change for the United Nations, has led to the European Union (EU) setting legally binding targets for renewable energy production. In 2007, the EU set a target that by 2020 20% of the EU energy consumption would be from renewable energy sources. The UK's part of this target equates to 15% of the UK's energy usage (Department of Energy and Climate Change, 2012). This energy is expected to come from a range of sources including biomass, offshore wind, onshore wind, marine energy, solar and heat pumps. The development of offshore wind farms is planned to make up a significant part of the renewable target, with an expected offshore wind capacity of $18GW$ in 2020.

There has been rapid development within the offshore wind sector in recent years to reach these targets. Currently the UK's offshore wind farms have a capacity of $3.6GW$; this is made up of 22 sites with a total of 1075 wind turbines currently operational (Renewable UK, 2012). There are a further $3.4GW$ either in construction or with planning consent, $8.6GW$ in planning stages, and up to $30GW$ in pre-planning stages (Department of Energy and Climate Change, 2012). Development has occurred in three Rounds, where Round 1 wind farms are operational, Round 2 are currently either operational, in construction or planned, and Round 3 are in the planning and pre-planning stages. As the offshore wind

sector has progressed, the wind farm sites have increased in size and scale, and are increasingly located in deep waters. At a Round 3 site the most likely number of turbines will be in the $100's$, and the typical area will exceed $1000km^2$.

With such a rapid development, it has become increasingly important to determine any influence that offshore wind farms may have on the natural environment. In particular, with the significant increase in scale, the impacts from the offshore wind farms on coastal processes and morphodynamics has become more important. Knowledge of this area would aid in future planning and wind farm placement. In practice, all of the existing wind farm sites have been fully examined in Environmental Impact Assessments (EIA) during the planning phases (ABPmer, 2002, 2012; Navitus Bay Development Limited, 2014; Royal Haskoning, 2010), with numerical modelling taking place where appropriate. However, due to the limitation of current understanding and modelling techniques, the models have to rely on considerable simplifications and hence have significant uncertainties in their results.

Firstly, OWF foundations are usually modelled as a resistance term in the computational mesh, due to limitations of affordable resolution in the model and computing resources (Lambkin et al., 2009). It is well established that these structures influence the localised environment by creating complex 3D hydrodynamic flow (Sumer and Fredsøe, 2002; Whitehouse, 1998). For large numbers of OWF turbine foundations, group effects may have considerable impacts away from the site, and hence have an impact on the overall morphological processes at a much bigger scale. The present coastal numerical models with an unstructured mesh provide the possibility to represent flows around the individual structures, as well as flows at a regional scale. The current research examines whether a numerical mesh with resolution of the individual turbine structure can improve the modelling capability both near the structure (near field) and far from the OWF site (far field).

Secondly, in most existing studies, only shorter term (less than a year) mor-

phodynamic impacts from these OWF are examined. However, the design life span of the OWF generally covers more than 20 years, which means their long term influence on coastal processes is not clear.

Thirdly, these studies are often site specific, and there is no generic understanding of the OWF impacts to both estuarine and open coastal situations. With several OWFs at Round 1 & 2 in operation, it is possible to look at the impacts for the OWF in different geo-morphological scenarios. The Scroby Sands and Burbo Bank wind farms are both Round 1 sites and are currently operational, they are both small sites and are in relatively shallow water depths. The two sites represent different coastal conditions with Scroby Sands in an open coast site, and Burbo Bank in a dynamic bay with an estuary. The small scale and varying coastal processes make them ideal test sites for numerical modelling.

1.2 Objectives

The Objectives of this research are:

- To investigate the impact of OWF on waves and currents interactions at a coastal scale.
- To study sediment transport at OWF to determine both localised and coastal scale impacts.
- To compare the wind farm impacts at sites with different geo-morphological settings.
- To determine the morphological impacts of offshore wind farm over long time scales.

1.3 Structure of the thesis

- Chapter 2 reviews the existing literature in two parts. Initially physical processes are reviewed, including the physics of sediment transport, coastal

dynamics, the impact of structures on hydrodynamics and sediment transport including scour hole formation. Finally the literature review discusses types of sediment transport models, large scale coastal morphological models, and examples of structures within morphological models.

- Chapter 3 introduces the numerical models used in this study, including TELEMAC-2D/3D, TOMAWAC and SISYPHE.

- Chapter 4 validates the TELEMAC, TOMAWAC and SISYPHE modules for use in near field modelling of structure interactions. This is achieved through comparison with experimental data, and by comparison to other numerical models.

- Chapter 5 focuses on the calibration of the model for hydrodynamics, waves and sediment transport at the two test sites, East Anglia and Liverpool Bay.

- Chapter 6 presents the short term impacts of the offshore wind farm at the two test sites. Discussing the impact of the wind farm on the tide, waves and sediment transport, in both the near and far field.

- Chapter 7 presents the long term impacts of the Burbo Bank wind farm, through the use of a representative tide and waves and a morphological factor.

- Chapter 8 concludes the work by discussing the results with respect to the objectives and includes proposals for future work within this area.

Chapter 2

Literature Review

2.1 Coastal processes

To understand the overall movement of sediment within the coastal zone, it is necessary to understand the underlying forcing by the complex hydrodynamics within the region.

2.1.1 Wave dynamics

Short period surface waves in the coastal region are largely generated by the wind. Their properties are dependant on the wind conditions and the fetch length for the area. As waves travel into shallow water they become influenced by the seabed which modifies their character and causes them to become more non-linear.
In shallow water, where the wave length is much greater than the water depth, the speed of waves depends only on the water depth as;

$$c = \sqrt{gh} \tag{2.1}$$

where c is the wave speed, g is the acceleration due to gravity, and h is the water depth.

This leads to wavelengths becoming shorter and wave energy per unit area becoming more concentrated in shallow water. When waves travel into progressively shallow water their periods remains constant, whilst the wave height increases and wave length decreases. This shoaling process causes increasingly non-sinusoidal

wave shapes to evolve, as they become asymmetric on the vertical and horizontal axes. Elgar et al. (1988) studied wave shoaling on a beach slope and found that with decreasing depth, velocity became asymmetric as the waves shoaled, modifying the shape of waves to form a short peaked crest and a long shallow trough.

In cases where waves travel at an oblique angle to the coastline, their height and length are further altered by seabed. As depth decreases the wave speed decreases, if the wave travels at an angle to the coast the part of the wave crest which first enters the shallow water slows, whilst the wave in the deeper water travels at a constant speed, causing the wave crest to bend. This process is known as refraction and can also occur in areas with varying bathymetry such as at sandbanks, leading to local modifications of the wave. Diffraction can also occur when the waves encounter objects in the water and results in wave energy being scattered and spread into the shadow area of an object (Dean and Dalrymple, 1991). In natural conditions wave diffraction and refraction effects may occur at offshore structures and large seabed features.

In very shallow waters waves continue to transform, within the surf zone the wave acceleration also becomes asymmetric, giving the wave a pitch forward shape. Wave height increases in further shoaling water, eventually reaching a limit when it will break, the height limit is dependant on the type of wave. The particle velocities at the crest of the wave become greater than the velocity of the rest of the wave, this causes the wave crest to overturn.

2.1.2 Currents

Currents in the ocean can be generated by various sources including the tides, waves, river outflows and pressure gradients. The tides are generated due to gravitational pull on the oceans by celestial bodies. They can be described as a sum of a series of harmonics with varying phases, caused by the gravitational forces from different celestial bodies and their interaction. The speed of tides can also be defined by the shallow water equation (Eq. (2.1)), as the wavelength is much greater than the water depth.

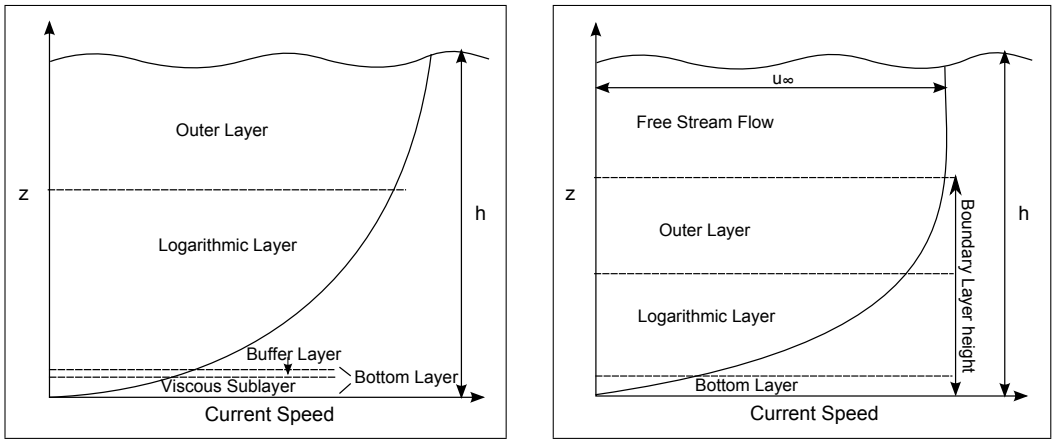

(a) (b)

Figure 2.1: Schematic of the sub-division of the boundary layer for a smooth bed. Showing a) the shallow water case in which the boundary layer occupies the water depth, and b) the deep water case in which the water is deeper than the boundary layer thickness. Where z is the height above the seabed, h is the water depth, and u_∞ is the free surface velocity

The dynamics in the near bed section of the water column are very important for sediment transport, as it is here that the water movement is imposed on the sediments. Directly at the seabed, friction forces cause the velocity to be zero. The friction is then transferred higher up the water column by the shear stresses caused by internal viscosity (Dean and Dalrymple, 1991). Far from the bed the flow is no longer affected by the seabed friction, this section of the water column is the free stream flow (Figure 2.1). The part of the water column where the shear stresses act and the velocity varies with height is defined as the bottom boundary layer. The bottom boundary layer thickness is time varying under tidal flows, in shallow water it can extend to the sea surface (Figure 2.1a), whereas in deep water it only takes up the near bed region with an overlying free stream flow section (Figure 2.1b). Within the bottom boundary layer the velocity varies with height to give a logarithmic profile, this variation of the velocity with height is given by

$$U(z) = \frac{u_*}{\kappa} ln \frac{z}{z_0} \tag{2.2}$$

where z is the height above the bed, u_* is the shear velocity, κ is the von Karman

constant, where $\kappa = 0.40$, and z_0 is the bed roughness length.

The friction exerted on the sea bed by the current is known as the bed shear stress; it is not easily measured, and is usually determined by empirical formulae based on other flow parameters. The bed shear stress can be defined in terms of the shear velocity, u_*, as

$$\tau_0 = \rho u_*^2 \tag{2.3}$$

where ρ is the water density.

The bed shear stress can be divided into the following components

$$\tau_0 = \tau_s + \tau_f + \tau_t \tag{2.4}$$

where τ_s is the skin friction component of the bed shear stress, τ_f is the form drag component of bed shear stress, and τ_t is the component relating to sediment transport caused by momentum transfer to move the grains (Soulsby, 1997).

The skin friction acts on the individual grains, whereas the form drag acts on the seabed features, such as bedforms. The form drag is due to uneven distribution of pressure at the bed surface and above the bedforms. The sediment transport component becomes important at very fast flows, caused by the loss of momentum in the flow due to moving sediment grains. The bed shear stress is dependant on the flow and also on the sea bed roughness.

Under tidal conditions the bottom boundary layer is typically turbulent, this turbulence is generated by the flow velocity components fluctuating about their phase averaged values. The level of turbulence within the flow can be described by the Reynolds number which is the ratio between inertial and viscous forces, as;

$$Re = \frac{UL}{\nu} \tag{2.5}$$

where L is the length scale, taken here as the height above the bed, and ν is the kinematic viscosity. Typically flow begins to become turbulent when $Re > 2300$.

Wave current interaction

Waves can make a significant contribution to sediment transport within the coastal zone. In the absence of tides, waves produce an oscillatory bottom boundary layer, the thickness of which is much smaller than that of a tidal current. However, as the boundary layer thickness is smaller there is a greater change in velocity with height, which leads to greater bed shear stresses (Nielsen, 1992). The bed shear stress for waves can similarly be described in terms of skin friction and form drag components

$$\tau_w = \tau_{ws} + \tau_{wf} \tag{2.6}$$

where τ_{ws} is the skin friction component of the wave bed shear stress, and τ_{wf} is the form drag component of wave bed shear stress.

In the coastal zone it is common for waves and currents to occur together, waves have little influence on tides in deep water, but in shallow coastal waters they can influence tidal dynamics. When waves and currents occur together, the bottom boundary layers for the waves and current interact non-linearly. This non-linear interaction results in greater bed shear stresses than the sum of the wave and tide components, commonly the bed shear stresses are $30 - 40\%$ higher (Soulsby, 1997). However, in most existing morphological models, the transport of sediment due to wave action alone is often ignored. In general, it is assumed that the waves act to stir up the sediment, allowing the tides to transport it.

2.1.3 Sediment transport

A grain of sediment will move if the motion forces are greater than the stabilising forces. A sediment grain will experience a drag force, a lift force due to streamlines bending over the roughness elements causing changes in pressure, and the force of the immersed weight of the sand grain (Van Rijn et al., 1993).

The balance of these forces can be expressed in a dimensionless form in terms of the Shields parameter;

$$\theta = \frac{\tau_s}{(\rho_s - \rho)gd} \tag{2.7}$$

where τ_s is the skin friction component of bed shear stress, g is the acceleration due to gravity, ρ_s is the density of the sediment grains, d is the diameter of the sediment grains.

Sediment movement occurs when the bed shear stress reaches a critical value, τ_{cr}. This can also be expressed in terms of the Shields parameter, as θ_{cr}, denoting the threshold of motion (Soulsby, 1997). When the threshold of motion is reached, sand grains on the bed begin to move as bed load transport. At the critical bed shear stress, grains begin to move with incipient motion where one or two sand grains roll along the bed. With increasing bed shear stress saltation occurs where the grains begin to hop over the surface, then many layers of grains start to move. Bed-load transport is defined as the part of the total load where the grains are supported by intergranular collisions, rather than the fluid drag (Bagnold, 1956). At greater shear stresses sand grains are entrained into the water column higher above the bed, and suspended sediment transport occurs. The sand grains will only remain in suspension if the upward component of the turbulent velocity is greater than the grains settling velocity, W_s. The settling velocity can be determined by various empirical and semi-empirical formulae, relating the grain diameter and density of the sediment and water. The settling velocity is commonly defined in terms of the dimensionless grain size, d_*, as;

$$d_* = \left[\frac{g\,(s-1)}{\nu^2}\right]^{1/3} d_{50} \tag{2.8}$$

where s is the ratio of the densities of the sediment and water ($s = \frac{\rho_s}{\rho}$), ν is the kinematic viscosity, and d_{50} is the median grain diameter. Van Rijn's settling velocity formula is suitable for non-cohesive sediments, it defines W_s as;

$$W_s = \frac{(s-1)g{d_{50}}^2}{18\nu} \text{ if } d_{50} \leq 10^{-4} \tag{2.9}$$

$$W_s = \frac{10\nu}{d_{50}}\left(\sqrt{1 + 0.01\frac{(s-1)g{d_{50}}^3}{18\nu^2}} - 1\right) \text{ if } 10^{-4} \leq d_{50} \leq 10^{-3} \tag{2.10}$$

$$W_s = 1.1\sqrt{(s-1)gd_{50}} \text{ if } 10^{-3} \leq d_{50} \tag{2.11}$$

The total transport rate is calculated as the sum of the bed load and suspended

load as;

$$Q_t = Q_b + Q_s \tag{2.12}$$

where Q_t is the total sediment transport rate, Q_b is the bed load transport rate, and Q_s is the suspended load transport rate.

2.1.4 Coastal morphology

The sediment transport influences the coastal zone by modifying the bed level, leading to changes in coastal morphology. Increasing sediment transport leads to bed erosion in the localised area, whereas decreasing sediment transport causes deposition of sediment as it drops out of suspension. Generally, it is the commonly occurring and fairly large waves with tidal currents which make the largest contribution to long term sediment transport (Soulsby, 1997). Extreme conditions, such as seen at storms, make a limited contribution to long term sediment dynamics. In most cases the coastal morphology will tend to an equilibrium, unless a disturbance is applied to the system.

2.2 Offshore wind farm structure impact

The design process for coastal structures takes into account the physical impacts on the structure such as wave, and tides, as well as the stability of the structure and it's impact on the coastal environment. There are various wind turbine foundations designs, which are best suited to different types of location. The types of foundations can be classified as gravity based, monopile, tripod structure and floating structures (Arshad and O'Kelly, 2013). Within the UK the current wind farms are located in relatively shallow areas and mainly use the monopile foundation (Renewable UK and The Crown Estate, 2013).

2.2.1 Foundation design

In the present study only monopile foundations are considered, the monopile foundation represents the most commonly used solution for installations at water depths of up to $25m$. Jacket structures have been used within the UK at

the Beatrice demonstration site and the Ormonde wind farm, it is thought they will become more common in the future for large turbines of $6MW$, and when wind farms are built in deeper waters over $35m$ (Renewable UK and The Crown Estate, 2013). Due to the simplicity of the monopile structure no special fabrication method is required. A pile can be driven into the seabed with use of a piling hammer, a hole can be drilled and the monopile grouted in, or a combination of driving and drilling can be used (de Vries et al., 2011). The way that the monopile is going to be placed in the sea bed depends on the soil characteristics and water depth. The monopile structure does not require any sea bed preparation but if the site is sensitive to scour, then scour protection is needed.

In addition to the structure, the offshore wind turbine generator also needs to connect to the shore so that the power generated can be linked with the electricity grid. This is usually through electrical cables buried under the surface of the sea floor. In the present study the buried cables are not taken into account in order to simplify the model simulation. The cables buried under the seabed surface can also lead to disturbance of local sediment transport and scour (Carroll et al., 2010).

2.2.2 Flow-structure interactions

Coastal structures are subjected to tidal currents and wave loading. The force of a wave and current on a cylinder can be calculated by the Morison equation. The Morison equation divides the force exerted on a structure into a drag and inertia component (Morison et al., 1950) as;

$$F_s = F_D + F_I \tag{2.13}$$

where F_D is the drag force and F_I the inertial force which are expressed as

$$F_D = 0.5 C_D \rho A U |U| \tag{2.14}$$

$$F_I = \rho C_m Vol \frac{\partial U}{\partial t} \tag{2.15}$$

where C_D is the drag coefficient, A is the cross-sectional area of the object perpendicular to the velocity, U is the water particle velocity, C_m is the inertia

coefficient, Vol is the volume of the object, and t is time. The Drag force is dependant on the shape of the cylinder, roughness, Reynolds number and turbulence; whilst the inertia force is dependant on flow acceleration.

The Morison equation holds true when the cylinder is relatively slender, when $D/\lambda < 0.2$, where D is the pile diameter, and λ is the wavelength. The slender structures do not influence the wave propagation pattern, whereas for $D/\lambda > 0.2$ diffraction will occur scattering the wave energy (Sarpkaya, 1987). The scattered wave may lead to localized patterns from multiple structure interactions, although this is likely to only be the case for larger wind farm foundations such as gravity base foundations (Cooper and Beiboer, 2002).

2.2.3 Scour

Coastal structures are vulnerable to erosion, which can effect the structural stability and result in structural failure. In areas where there is need for scour protection, the cost of the wind turbine foundation can make up more than 30% of the total cost (Sumer et al., 2007). The depth of erosion must therefore be quantified to aid with wind farm and monopile foundation design.

In the near field, the presence of a pile will influence the localised hydrodynamics (Figure 2.2). The flow will produce a horseshoe vortex in front of the pile, followed by lee wake vortices behind the pile, finally streamlines at the side of the pile will contract (Sumer and Fredsøe, 2002). This process leads to an increase in bed shear stress, therefore also an increase in sediment transport which cause scour at the pile. Scour can be classified as clear-water or live-bed scour depending on background conditions. Clear-water scour occurs when the bed shear stress, τ_0, in the vicinity of the pile is greater than the critical bed shear stress for sediment transport, τ_{cr}, but, the ambient bed shear stress is less than τ_{cr}. Live-bed scour occurs when everywhere on the bed $\tau_0 > \tau_{cr}$ (Whitehouse, 1998).

For fine sediment types liquefaction may occur at the pile, which can result

in structural failure. Liquefaction is the state when the effective stresses between sediment grains disappear, and the sediment and water together act as a fluid (Sumer, 2014). Liquefaction occurs due to wave action at the pile, either through a gradual build up of pore pressure, or momentarily due to a vertical pressure gradient as the wave passes over.

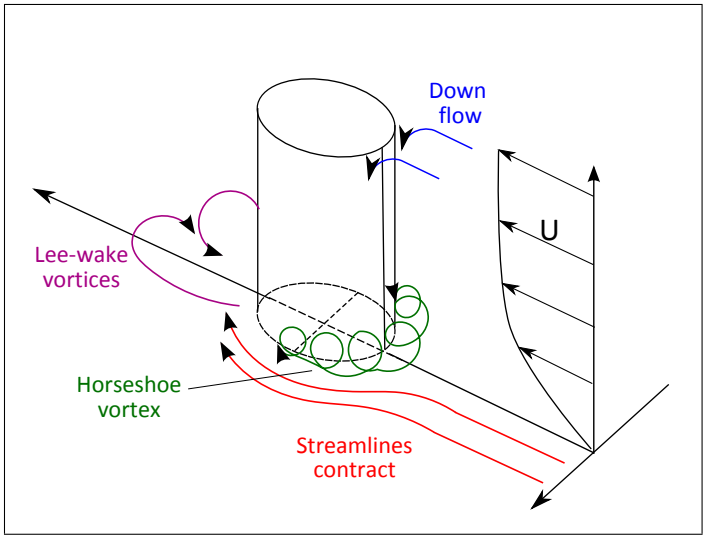

Figure 2.2: Hydrodynamics around a cylinder in a tidal flow

The scour hole depth and extent are dependant on the local hydrodynamics, and are generally time varying (Harris et al., 2010). At the Scarweather Sands meteorological mast, the time variation of scour was assessed with use of a multi-beam echo sounder. Scour depth was found to vary between low and high water, with average values of $0.59D$ and $0.27D$. In tidal flow the sediment eroded on the flood tide can be deposited on the ebb, this backfilling decreases the scour hole depth compared to a unidirectional flow. Scour holes will eventually reach an equilibrium where the scour hole depth will no longer increase, this happens quicker in faster currents (Den Boon et al., 2004).

Under waves, the scour hole generation is determined by the Keulegan-Carpenter number (Sumer et al., 1992), K_C, which is defined as

$$K_C = \frac{U_m T}{D} \tag{2.16}$$

where U_m is the wave orbital velocity at the bed, and T is the wave period.

For $K_C < 6$ no scour will occur, for $6 < K_C < 200$ scour hole extent and depth increases with K_C, and for $K_C > 200$ the scour hole acts as for a tidal current (Den Boon et al., 2004). Sumer et al. (1992) found through physical testing that for conditions where $K_C > 6$, no horseshoe vortex or lee wake vortices will occur, hence the lack of scour at these conditions. Harris et al. (2010) found that under waves and currents, with similar velocity magnitudes, the scour hole generation is suppressed by the waves, the greatest scour is seen in tests of tidal currents only.

The maximum depth of a scour hole is an important parameter for monopile foundation design and is commonly calculated by an empirical formula. Most formulae are based on an understanding of the most important processes contributing to scour and laboratory test data (Lambkin et al., 2009).

The most commonly used empirical formula used is from a standard for offshore wind farm foundations set out by Det Norske Veritas (Det Norske Veritas, 2004). The maximum scour depth occurs when $S/D = 1.3$, where S is the scour hole depth. Sumer and Fredsøe (2002) extended the work of Breusers et al. (1977), to produce a maximum scour depth formula based on live bed scour experimental tests for sandy grains as;

$$\frac{S}{D} = 1.3 \pm 0.7 \tag{2.17}$$

Similarly the Opti-Pile Design tool (Den Boon et al., 2004), based on a series of monopile tests under sandy grain sizes, uses a ratio of $S/D = 1.75$ for current only cases.

Under waves, as stated earlier, the scour is dependant on the Keulegan-Carpenter number. Sumer et al. (1992) expressed the scour depth under waves with live bed scour as;

$$\frac{S}{D} = 1.3\{1 - exp(-b(K_C - 6))\} \tag{2.18}$$

where b was found empirically as 0.03.

Carreiras et al. (2000) found that scour under non-linear waves can also can be calculated by Eq. 2.18, as long as the near pile wave properties are applied. It is also important to look at the impact of marine growth on the monopiles. At sites in the North Sea the monopiles have seen marine growth of up to $100mm$ (Det Norske Veritas, 2004), increasing the pile diameter and potentially varying turbulence patterns.

Measured data at wind farm sites around the UK suggest the maximum scour depth can be found within this range of predictions from the empirical formulae. The greatest scour depths seen at UK wind farm sites have been found at Scroby Sands with a maximum scour hole depth of $1.38D$, and at Robin Rigg where the monopile average scour depth was measured at $1.77D$ (Carroll et al., 2010). Both sites show higher ratios than expected from the Det Norske Veritas (2004) equation, but are within the standard deviation for the Sumer et al. (1992) equation.

Both Robin Rigg and Scroby Sands are located on sandy sediment types in areas with multiple sandbanks. The sediment type at a wind farm location has a large influence on the development of scour holes in terms of depth and extent. Typically for clay seabed sediments the scour is very slow and shallow or not present at all (Lambkin et al., 2009). At the Kentish flat site, which is situated in an area of clay seabed with a small layer of fine sediment on top, the scour depth 18 months after installation had maximum values of $0.34D$. Barrow wind farm site also shows this variation of scour holes with sediment type. In areas of the site with a sandy seabed, scour hole maximum depth reached $1.21D$, whereas in the parts of the site with glacial till sediment overlain with a small layer of sand, scour hole depth reached $0.5D$. Large seabed grain sizes also show low scour depths, the North Hoyle site situated in gravel and sandy gravel found no scour at most monopile foundations, with maximum scour of $0.125D$.

Within wind farm sites, interaction between pile scour holes does not occur for monopile arrays as turbine spacing is typically in the order of $5 - 9r$, where r is the rotor blade diameter (Cooper and Beiboer, 2002). Piles with multiple

supports e.g. tripod and jacket piles will have more complex hydrodynamics as flow and turbulence between the supports will interact. The individual scour holes at each support will be encompassed by a group scour hole, this process is known as global scour and results in a general lowering of the bed. Sumer et al. (2005) found through laboratory testing that global scour depth increased with increasing number of piles, but the local scour holes at each individual piles remained constant, this is likely due to increased turbulence with more monopiles.

2.2.4 Structure impacts

Measurements of the in-situ impact of offshore wind farms on hydrodynamics in the area around the pile are limited. However, there is a data derived from physical modelling at cylinders and pile foundations under various conditions. Hjorth (1975) studied the influence of a cylinder on steady turbulent smooth bed flow, by carrying out a series of physical modelling experiments. The horseshoe vortex generated by the cylinder was found to influence the boundary layer flow within a distance of $4D$ from the cylinder. To the sides of the cylinder the velocity was enhanced within a distance of $1D$. In the lee wake of the cylinder the sediment entrainment into the water column occurred up to a distance of $8D$ from the cylinder. Hjorth (1975) also looked at the bed shear stress pattern surrounding a pile, and found that beneath the horseshoe vortex the bed shear stress could be amplified by a factor of 5 from background values, at the sides of the pile the amplification can be up to 8 times background values (when Re = $6\text{x}10^4$). Sumer et al. (1997) studied bed shear stress amplification at a pile under waves and oscillatory flow. Figure 2.3 presents Sumer et al. (1997) comparison of the bed shear stress amplification in the lee wake of cylindrical and square piles for different K_C values. It was shown that the bed shear stress increases with increasing K_C number. The area influenced by the pile also increases with increasing K_C, with a maximum bed shear stress at $X/D = 1$. Sumer et al. (1997) also showed that the greatest bed shear stress are seen with a steady current, due to the influence of the horseshoe vortex for the steady flow. Whereas for the waves, the bed shear stress amplification is mainly caused by streamlines contracting.

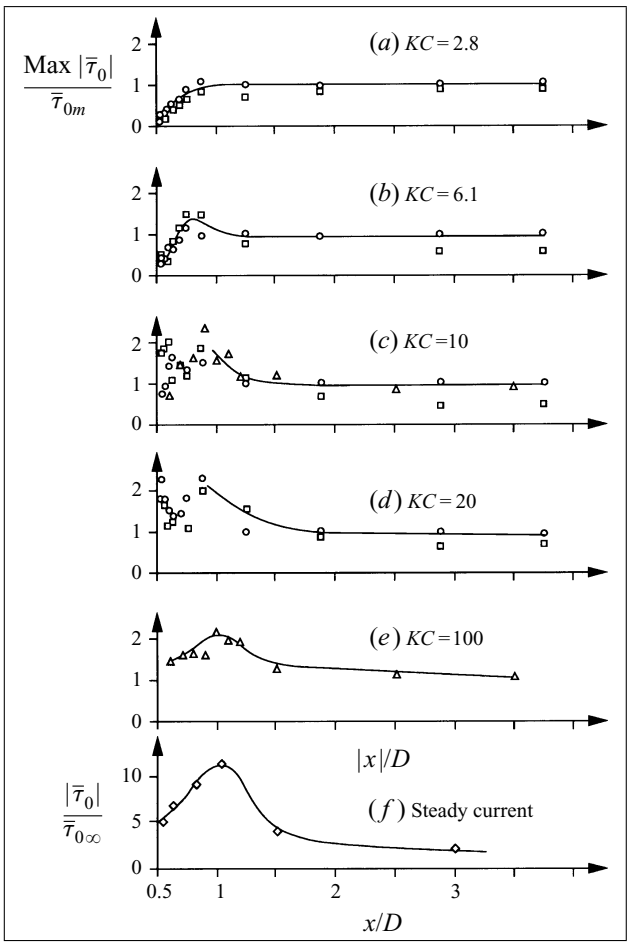

Figure 2.3: Amplification of the bed shear stress along the x-axis at the lee-side of a pile. Circles show the circular pile experiments, squares show the square pile experiments and triangles show the oscillatory tunnel experiments. From Sumer et al. (1997)

At wind farm sites studies have looked at scour hole development around the monopiles, but there is little evidence of the impacts from the whole array on the coastal and estuarine morphology. The recent survey at Scroby Sands offshore wind farm has shown some unusual large scale wake effects adjacent to the foundations forming a long tail of scour (Figure 2.4). At the Scroby Sands site, the tail scours are transitionary and have been recorded up to a distance of $95D$ (ABPmer et al., 2008). This suggests that with particular conditions, the offshore wind farm can potentially cause influences to the surrounding environment at a much larger scale than expected (Whitehouse et al., 2011).

Influence of the wind farm on the wind fields also been studied with the use of satellite remote sensing.Christiansen and Hasager (2005) has revealed the potential changes of wind field behind the farm can extend as far as $20km$, which will be significant in terms of wave dynamics as well as tidal flows at the site. This suggests, the need for further examination on the far field impacts of the wind farm to the large scale coastal processes.

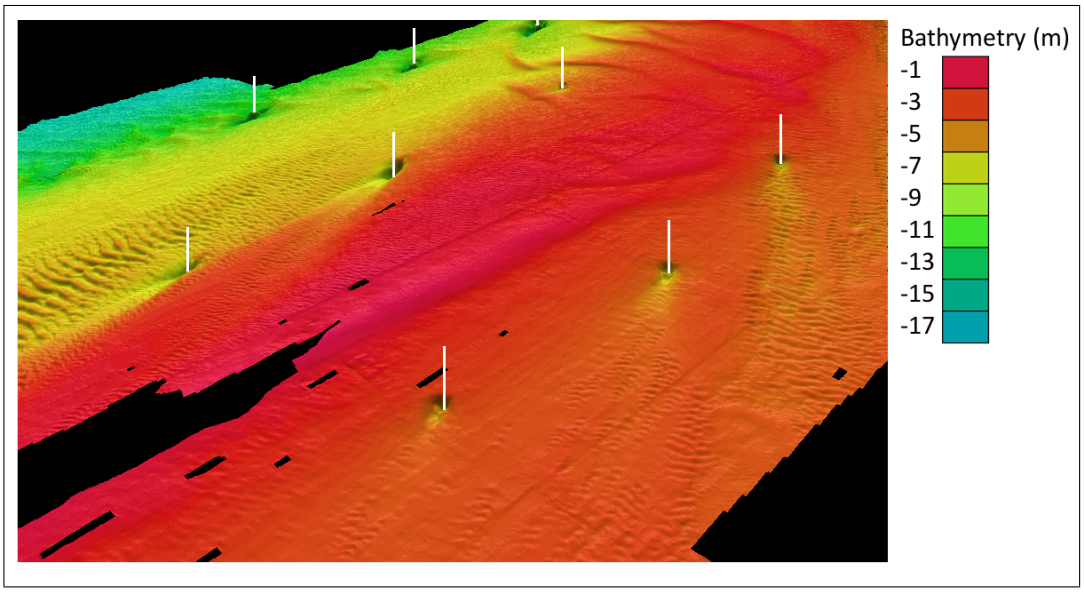

Figure 2.4: Scroby Sands offshore wind farm bathymetry image, highlighting Scour around wind turbine monopiles and tail scour. After Rees et al. (2006) and the Collaborative Offshore Wind Research into the Environment (COWRIE)

2.3 Modelling

The use of empirical models to determine scour hole properties is an important first step for structural design, however, it ignores the complex dynamics associated with the structure interaction. The understanding of these dynamics has been furthered through the use of numerical models. These models are very detailed and allow resolution of the complex hydrodynamics, but are computationally expensive.

2.3.1 Near field CFD modelling

Computational fluid dynamics (CFD) methods have been applied to scour modelling, both in 2D to quickly assess the scour process, and in 3D to allow the complex flow to be reproduced. Various CFD techniques have been studied including modelling based on the Reynolds Average Navier Stokes (RANS) equation. Roulund et al. (2005) used a RANS model to study scour at bridge piers and Liu (2008) used a similar process to model tidal flows, both models were able to replicate the vortex pattern produced in the lee wake of the structure. With greater computational power available other modelling methods have been used, such as large eddy simulation (LES) (Kirkil et al., 2008; Tseng et al., 2000), which are shown to be able to replicate vortex shedding and resolve horseshoe vortices. Rodi (1997) compared the resolution of vortex shedding for a RANS and an LES model past a square and circular cylinder, finding that the RANS model under predicted the amplitude of the turbulence fluctuations, but the frequency was well predicted for both models.

Coastal modelling

To determine the impact of a wind farm array rather than just one foundation, requires the use of much larger scale coastal models. These coastal scale models are site specific to allow the study of the impact of the wind farm on hydrodynamics, sediment transport and bed morphology.

Large scale coastal models usually have a similar set up, with separate modules

which can be coupled to calculate tidal currents, waves and sediment transport. Tidal currents are calculated either in 2D with the use of the depth averaged Navier-Stokes Equations, or with the 3D Navier-Stokes Equations. Waves are calculated through use of phase averaged models, such as WAM, TOMAWAC and SWAN; or phase resolving models, such as Boussinesq models. Phase averaged models describe the conservation of wave energy and computes the statistics of the sea surface, whereas phase resolving models describe the sea surface. If waves are run coupled with the tidal flow it is usually possible to include wave-current interactions. The current and waves are used to calculate the sediment transport. Sediment transport variations allow sea bed evolution to be calculated which can then be read back into the tide and wave calculations so that new bed levels are included.

Sediment transport can be calculated in terms of bed load and suspended load transport. Bed load transport is calculated by an empirical formula, most transport modules are based on the Shields parameter, θ. The Einstein dimensionless bed load transport parameter, Φ_b, is defined as;

$$\Phi_b = \frac{q_b}{\sqrt{g\,(s-1)\,d}} \tag{2.19}$$

where q_b is the volumetric bed load transport rate per unit width, and s is the relative sediment density $s = \rho_s/\rho$.
The bed load transport formula can be written in terms of the Φ_b as;

$$\Phi_b = m_1\,(\theta - \theta_{cr})^{m_2} \tag{2.20}$$

where θ is the Shields parameter, θ_{cr} is the critical Shields parameter, m_1 and m_2 are constants which are empirically derived. The constants are found to vary with flow conditions, leading to specific formulae for steady flow (Meyer-Peter and Müller, 1948), oscillatory flow (Ribberink, 1998), and under waves and currents (Soulsby, 1997).

Suspended sediment is resolved by coastal models, it is usually expressed in terms of an advection-diffusion equation (Amoudry et al., 2009) as;

$$\frac{DC}{Dt} = \frac{\partial W_s C}{\partial z} + \nabla.\,(\varepsilon_s \nabla C) + S_c \tag{2.21}$$

where C is the sediment concentration, ε_s is the sediment diffusivity, and S_c is a sediment source or sink term.

The suspended load transport per unit width, q_s, can then be calculated with the flow velocity as;

$$q_s = \int_{z_a}^{h} U(z)C(z)dz \tag{2.22}$$

where h is the water depth, and z_a is a reference height near the bed which marks the top of the bed load layer.

The total load transport, q_t, is defined as;

$$q_t = q_b + q_s \tag{2.23}$$

The total load transport is used to calculate the bed evolution over a time step, using the Exner equation

$$(1 - \lambda_p)\frac{\partial z_f}{\partial t} = -\frac{\partial q_t}{\partial x} \tag{2.24}$$

where λ_p is the bed porosity, and z_f is the bottom elevation.
This modified bathymetry can then be included in the hydrodynamic module.

2.3.2 Long term coastal morphology modelling

The life span of an offshore wind farm is typically in the order of 20 years, therefore the impact studies should not be restricted to only short periods, but should also consider the long term impacts. The selection of suitable long term morphological models is vital for coastal management strategies (Amoudry and Souza, 2011).

Morphological evolution occurs over long time periods, but is driven by short term variations in the coastal hydrodynamics which causes sediment transport. It is not feasible, due to computational time and expense, for all hydrodynamic forcing over a period of years or decades to be included in a morphological model. The coastal model must therefore be simplified to enable longer running periods. This can be done by simplifying the coastal domain and focusing on the area of

interest, such as using beach profile models for studying long term behaviour of seabed features, and coastline models to study long term variations in the coastline location (Roelvink et al., 2012). Alternatively, a full 2D or 3D coastal model can be used with the input simplified.

Input schematisation reasons that the morphological evolution over long time scales can be predicted from a small subset of hydrodynamic forcing. The input schematisation involves choosing representative tides and waves which produce the same residual sediment transport patterns as the full set of waves and tides over a given period, such as a spring-neap cycle (Lesser et al., 2004). This method gives a reliable approximate average morphological change over time, but it lacks precision as input schematisation cannot take account of individual events (Cowell et al., 2003).

In order to reduce the input boundary forcing for a model it is first important to determine which coastal processes play a role in sediment transport within the region of study in space and time. Some processes may have little influence in small time periods but come to dominate over large time scales (De Vriend et al., 1993). The output of these models are tested for accuracy of prediction using statistical methods such as the Briar Skill Score to determine differences between measured and predicted results (Sutherland et al., 2004).

Tidal variation over a long time period is predictable as the sum of the tidal harmonics. The tidal constituents act over different cycles with a range of periods, it is therefore computational expensive to compute a full representation. Tidal input can be reduced to a single or multiple representative tides that can replicate the residual hydrodynamic and morphological patterns over the period of interest. Single representative tides are commonly referred to as a morphological tide, which is calculated to represent the residual sediment transport and direction of the sediment transport over a spring-neap cycle (Latteux, 1995). This calculation results in a single representative morphological tide which retains the shape of the tidal curve and has an amplitude $7 - 20\%$ higher than a mean tide

(De Vriend et al., 1993). For cases where the bathymetry is simple it is usually appropriate to use a single representative wave. In areas of complex bathymetry, or where the shape of the tidal curve varies across the site, multiple representative tides should be used (Latteux, 1995).

Waves are treated separately from tides, the wave climate is defined statistically over a historical period and divided into representative wave conditions. This can be done by the *Single representative wave* or *Multiple representative wave* method (De Vriend et al., 1993). The *Multiple representative wave* used by Steijn (1992) simplifies the wave input by reducing the waves sorted by wave height and direction into a small number of combinations weighted by their influence on sediment transport. Alternatively the *Single representative wave* as used by Chesher and Miles (1992) groups the wave directions and calculates a representative wave height for each group, these are run with a weighting factor applied.

The chronology of the representative waves can also be important. Dissanayake (2011) studied wave chronology for three representative waves at the Ameland inlet over 50 years, finding that wave chronology had a significant impact on predicted changes. Brown (2008) also included wave chronology for long term morphological modelling of the Dyfi Estuary, by dividing the wave properties by season and selecting representative waves for each, keeping the annual wave chronology. However, Dong and Chen (2001), found that wave chronology made only a relatively weak influence on long term shoreline erosion. The wave chronology effect was found to be much smaller than the impact due to wave climate variations. The impact on wave chronology is dependant on the physical processes occurring, as the conclusions from studies of reversible processes cannot be applied to irreversible processes, such as spit erosion (Dong and Chen, 2001).

For long term morphological prediction, various bed updating methods are used. One of the simplest approaches is to linearly extrapolate the morphological change from a spring neap cycle, although this method is likely to over predict

the bed evolution, as coastal systems usually tend to an dynamic equilibrium (Davies and Villaret, 2003). A commonly used long term bed evolution prediction is made with a Morphological Acceleration Factor (MOFAC) (Lesser et al., 2004; Roelvink et al., 2012), which accelerates the bed updating, therefore extending the morphological development period by MOFAC multiplied by the hydrodynamic period.

$$MOFAC = \frac{T_{Morpho}}{T_{Hydro}} \tag{2.25}$$

where T_{Morpho} is the morphological period, T_{Hydro} is the hydrodynamic period the model will be run for. Variable morphological factors can be used to take into account different wave conditions, in these cases the value of MOFAC is weighted by the occurrence of the specific wave condition.

The morphological factor method of long term morphological conditions is based on the assumption that bed level and sediment transport patterns changes are approximately linear over the run period (Lesser, 2009). To ensure the validity of the linear development the MOFAC number should not be too high, the MOFAC value should be limited so that bed level change in one tidal cycle is not greater than 10% of the water depth (Dissanayake, 2011).

2.3.3 Structures within coastal morphological models

Environmental Impact Assessments (EIA) are carried out at commercial wind farm locations (ABPmer, 2002; Rees et al., 2006) to mitigate against wind farm impacts as part of the design. They require understanding of the impacts on coastal morphology, sediment pathways, coastal protection, contaminants and coastal protection (Lambkin et al., 2009), on both a local and far field scale.

Most existing modelling of the far field impacts of offshore wind farms relies on the commonly used coastal morphological model system. To represent wind farm foundation structures in the model poses considerable challenges, as these models are designed for shallow water with simplified flow conditions. Modelling the large scale impact of the structure usually involves parameterisation of their localised effects, due to the high computational expense of resolving the structure

explicitly in the mesh. A typical method used in commercial wind farm modelling involves including a resistance term to the wave and current equations to represent effects of the structure in the far field (Lambkin et al., 2009).

The wave friction factor and current related bed shear stress are increased until the force is equal to the Morison equation output at point locations. The forces exerted on vertical structures by the flow can be given by

$$F_u = \frac{\rho C_D D}{2} u_{\text{Eff}} |\langle u_{\text{Eff}} \rangle| \Delta l \tag{2.26}$$

$$F_v = \frac{\rho C_D D}{2} v_{\text{Eff}} |\langle v_{\text{Eff}} \rangle| \Delta l \tag{2.27}$$

where F_u & F_v are the drag force on the pile in the x and y direction, u_{Eff} & v_{Eff} are the effective approach velocities, $|\langle u_{\text{Eff}} \rangle|$ & $|\langle v_{\text{Eff}} \rangle|$ are the magnitude of the effective approach velocity, D is the pile diameter, and l is the length of the vertical section of the pile.
The effective approach velocity is given as;

$$u_{\text{Eff}} = \langle u \rangle \{ \frac{A_{\text{Total}}}{A_{\text{Eff}}} \} = \langle u \rangle a \tag{2.28}$$

where A_{Total} is the total cross-sectional area (i.e. the cross-sectional area of the water column), A_{Eff} is the effective wet cross-sectional area (i.e. the cross-sectional area of the water column that is not blocked by the piles), and a is the ratio of the total cross-sectional area to the effective wet cross-sectional area, a = $\{ \frac{A_{\text{Total}}}{A_{\text{Eff}}} \}$

The forces can be expressed as a sink term in the momentum equations, given as;

$$S_{h_x}^{\ t} = \frac{n}{A_{sur}} \frac{D}{2} C_D U^2 \tag{2.29}$$

where n is the number of structures, A_{sur} is the surface area and U is the mean flow velocity. This can be applied in the model by increasing the roughness at the structure location. This representation of the structure allows the change in velocity, water depth to be represented, but will ignore vortex shedding.

The use of a resistance term in the mesh characterises the net interaction between the wind farm monopile and the flow, but ignores the complex near field

hydrodynamics at a pile (Figure 2.2), which occur at a mesh resolution lower than that of the computational mesh. The lateral forces of the vortex shedding are ignored, these forces are much smaller than in line forces, and are equal and opposite so will cancel out as a time mean value. It also ignores the horseshoe vortices, flow acceleration and increase in wake turbulence. However, whilst ignoring these near field impacts, the impact on hydrodynamics in the far field are represented well by the parameterisation (Lambkin et al., 2009). Using this method it is possible to study the large scale impact on sediment transport patterns by the wind farm. However, due to the lack of representation of the near field scour causing processes such as the horseshoe vortex, downflow and wake vortex the scour at a monopile cannot be quantified with this method. Instead the scour is usually studied by use of one of the empirical formula. The impact of the scour holes on the far field sediment transport is not included in the EIA models, this impact could be important especially at Scroby Sands where long tail scour has been measured in the wake of a pile.

Various wind farm Environmental impact assessments (EIA) have modelled the wind farm impact on the hydrodynamics and sediment transport, through the above parameterisation of the wind farm foundations. Table 2.1 presents a comparison of impacts at 3 wind farm sites and one hypothetical site in terms of magnitude and extent. In all cases the numerical modelling occurs early in the planning process, as such, the worst case scenario of all the design plans is modelled. In some cases the choice of type of wind farm foundation and spacing of wind farm layout was not decided at the point of modelling and therefore the worst case was chosen, which may differ from the final design choice.

In all the wind farm cases studied, the impact of the wind farm on the water depth is negligible in the far-field, and in most cases is similar to the level of accuracy that the numerical model can predict. The impact on the velocity is greater, showing maximum average reduction in velocity over the wind farm area in the range of $1 - 8\%$. Reductions in velocity are seen in the wake of the structures, which at some phases of the tide extend further than the wind turbine

spacing, leading to wake interaction. The Hypothetical wind farm and Burbo Bank study, both examine the far field impact of the wind farm on the velocity, showing small reductions at a distance of $6km$ away, and in the wake of the wind farm, respectively.

The impact of the wind farm on the wave climate is also assessed by the studies in Table 2.1. Close to the structure, for the Hypothetical and Burbo Bank wind farms, amplification if the wave height of $1.84 - 3\%$ is seen close to the structure. There are wakes behind the foundations with a reduction in wave height, the wake lengths extend beyond the spacing of the wind farm, indicating the occurrence of wake interaction. Within the array the Rampion and Galloper wind farms show a reduction in wave height of $7.5 - 9\%$ for the worst case waves tested. In the far field, both the Burbo Bank and Rampion wind farms have a reduction in wave height of $5 - 6\%$ in the wake of the array. The Hypothetical wind farm sees changes in wave height $6km$ from the array of -1.5%, and at Galloper, $10km$ from the array reductions are seem of -2%. Within the wind farm array changes to wave direction are no greater than 3%. It is clear from these cases that in the worst case conditions, the wind farm can influence the waves within a large area around the site.

The wind farm studies suggest that the influence of the wind farm on the sediment flux, is in general, only within the wind farm array, or the near vicinity. It is only the Rampion wind farm which shows a change in the coastal dynamics in the far field, with a reduction of longshore transport with the wind farm, by 5%.

Site	Foundation	Tidal Hydrodynamics	Wave Hydrodynamics	Sediment Transport Flux
Hypothetical wind farm Cooper and Beiboer (2002)	Monopile 5m diameter 30 turbines 300m spacing	*Water Depth* Far Field: $6km$ from the array $\pm 0.017\%$ *Velocity* Within Array: average reduction 8%, wake interactions at some phases of tide $> 60D$ wake extent Far Field: $6km$ from the array -0.72%	*Wave Height* Structures: maximum amplification 1.84%, at some phases of the tide wake interactions occur of length $> 60D$ Far field: $6km$ from the array max -1.58% *Wave Direction* Within Array: maximum and minimum modifications $+1.7°$ & $-1.0°$	Far Field: Peak concentration change 3% next to the array
Burbo Bank ABPmer (2002)	Monopile $4m$ diameter 30 turbines $400m$ spacing	*Water Depth* Far Field: At the edge of the array $\pm 0.001m$ *Velocity* Within Array: Wakes detectable up to $100D$ Far Field: Edge of the array maximum reduction $-0.046ms^{-1}$, and $1.5°$ flow direction change	*Wave Height* At Structure: maximum modification $\pm 3\%$ for 1:1 wave Within Array: Wake interactions between foundations $> 100D$ Far Field: In the wake of the array maximum changes $< 0.6\%$ for 1:1 wave and 6% for 1:50 wave	Far Field: No overall impact on sediment flux
Galloper wind farm ABPmer (2011)	Gravity Base $45m$ diameter 106 turbines	*Water Depth* Within Array: Maximum changes $\pm 0.03m$ *Velocity* At Structure: maximum reduction 11% Within Array: maximum decrease over array $4 - 5\%$	*Wave Height* Within Array: Maximum reduction for a 1:10 wave -9% Far Field: Within $1km$ of array, maximum reduction -5%, $10km$ from array maximum reduction -2% *Wave Direction* Within Array: maximum modifications $\pm 3°$	Within Array: Changes in bed shear stress are within wind farm area and up to $0.5km$ away
Rampion wind farm ABPmer (2012)	Gravity Base and monopile $33.5m$ and $6m$ diameter respectively	*Water Depth* Far Field: maximum modification $< 0.01m$ *Velocity* Within Array: Maximum average changes -1%, flow direction modifications $\pm 5°$	*Wave Height* Within Array: maximum reduction $< 7.5\%$ Far Field: In the wake of the array reduction of $< 5\%$, with no changes $6km$ away *Wave Direction* Within Array: wave direction modifications $< 1\%$	Within Array: Bed shear stress changes minor significance Far field: A Decrease in the rate of longshore transport $< 5°$

Table 2.1: Maximum impacts of various wind farm sites to hydrodynamics and sediment transport as part of the worst case scenario numerical modelling

Neill et al. (2009) used a similar approach to model the impact of tidal energy converters on the large scale sediment dynamics of the Bristol Channel. An energy extraction term was included in the momentum equation at turbine locations, this is equivalent to an additional bottom friction term. The modified hydrodynamics were then used to calculate sediment transport where changes in morphodynamics were seen up to 50km away from the tidal turbine site. The magnitude of the impact was found to depend on the tidal asymmetry at the point of extraction, and the greatest morphodynamic impacts of the wind farm were seen at areas of bed load parting and convergence within the estuary and were of the order 20% of the bed load change with no tidal farm. In this study feedback from the change in bathymetry on the hydrodynamics are not incorporated in the model, but the morphodynamic change in 1D transects is calculated.

The resistance term approach has the advantages of being simple to use in the coastal model system, however, it does not represent the structure directly. The consequence of such simple representation is that the complex flow-structure interactions are missing. These to some extent affect the accuracy of the models.

Structures in coastal wave models

Most research in this area has focused on modelling wave and structure interaction. The foundation structures are commonly represented using a transmission coefficient, as a sub-grid feature, or as a dry point in the mesh. Depending on the size of the structure and the in-coming waves, the effects can be significant to the overall wave height distribution and wave direction at the site.

Ponce de León et al. (2011) studied the impact on waves at an OWF using both a WAM and a SWAN model. For single monopile tests, the monopile was represented as a sub grid feature in the mesh, consisting of a polygon with modified transmission and reflection coefficients. The influence of including diffraction in the model was determined as part of the single monopile tests. With diffraction included the directional spreading of the monopile wake was found to be

increased, and further down the wake the diffraction acts to smooth the variation in significant wave height. At the whole wind farm scale the structures are represented as dry points in the mesh. The wind farm site was found to reduce spectral wave energy, which led to a shift in the wave direction. This wave energy blocking effect was found to decrease when fewer monopile foundations were modelled.

Alari and Raudsepp (2012) also used a SWAN model to look at the regional effects of an OWF on waves, with the turbine structure represented as a dry point in the mesh. At the regional scale, the significant wave height at the wind farm site was found to be reduced by 0.25 - 1 %. Gandara and Harris (2012), again used a SWAN model to study wave impact at a hypothetical wind farm in the Gulf of Mexico. In this study the wind variation across the site was also calculated using the WaSP model to study the wind wake. The wind model determined that the maximum reduction in wind velocity at the individual monopile locations was $10 - 11\%$. It was found that wave blockage effects were greater when wind wake effects were included by $6.73 - 8.52\%$.

2.4 Conclusion

Impacts of the wind farm on coastal processes indicate that the the tidal flow can be modified by the wind farm, showing overall reduction at the wind farm and in some cases in the far field. The wind farm impacts on the wave regime is more commonly studied, and also shows impacts on the conditions within the wind farm site and in some cases further afield. Whilst small scale CFD models prediction of sediment transport at an individual pile is well established, there is little evidence from numerical modelling, that the sediment pathway in the large scale is influenced by the wind farm. However, these large scale models do not include the scour modelling at the individual turbine foundations, as this is not parameterised in the model.

This project aims to bridge the gap of modelling wind farm impacts between the detailed, but computationally expensive near pile models that can resolve the complex 3D flow and calculate scour, and the large scale coastal models with the structure represented as friction term. The vortices and associated turbulence have a large influence on the sediment transport and it is these factors which are being ignored by the large scale coastal models currently used.

Chapter 3

Numerical Model

In Chapter 2, coastal modelling is introduced and various methods of modelling coastal structures, including offshore wind farms, are discussed. The current chapter focuses on the model set up and configuration used for the present research.

TELEMAC modelling system is a numerical model developed by EDF, it is written in Fortran90. It can be run on both PC, Linux and UNIX platforms, in either parallel or serial mode (Hervouet, 2007). The model consists of multiple modules which are used to represent various physical processes. In this research the TELEMAC-3D module is used to determine 2D/3D hydrodynamics, the TOMAWAC module is used to model waves within the domain, and SISYPHE is used to compute sediment transport.

The TELEMAC modelling system has been used widely for a variety of applications within the coastal domain and for riverine flow (Brière et al., 2007; Brown and Davies, 2009; Park and Vincent, 2007; Robins and Davies, 2010). The modelling system was chosen for this research due to its good performance in parallel (Moulinec et al., 2011) and for the ability to spatially discretize with a finite element grid, allowing small features on shorelines and uneven bathymetry to be fully resolved. In addition TELEMAC is open source, allowing the user to modify the code, and has a strong user and help community.

3.1 Navier-Stokes equations

The overall governing equation for fluid motion is described by the Navier-Stokes equations which assumes constant density and a Newtonian fluid. In the Cartesian form the Navier-Stokes equation is expressed as;

Conservation of mass:

$$\frac{\partial u}{\partial x} + \frac{\partial v}{\partial y} + \frac{\partial w}{\partial z} = 0 \tag{3.1}$$

where u, v and w are the velocity components in the x, y and z directions.

The conservation of momentum is given as;

$$\frac{\partial u}{\partial t} + u\frac{\partial u}{\partial x} + v\frac{\partial u}{\partial y} + w\frac{\partial u}{\partial z} = -\frac{1}{\rho}\frac{\partial p}{\partial x} + \nu_t \nabla^2 (u) + S_x \tag{3.2}$$

$$\frac{\partial v}{\partial t} + u\frac{\partial v}{\partial x} + v\frac{\partial v}{\partial y} + w\frac{\partial v}{\partial z} = -\frac{1}{\rho}\frac{\partial p}{\partial y} + \nu_t \nabla^2 (v) + S_y \tag{3.3}$$

$$\frac{\partial w}{\partial t} + u\frac{\partial w}{\partial x} + v\frac{\partial w}{\partial y} + w\frac{\partial w}{\partial z} = -\frac{1}{\rho}\frac{\partial p}{\partial z} - g + \nu_t \nabla^2 (w) + S_z \tag{3.4}$$

where t is time, ρ is density, p is pressure, g is the acceleration due to gravity, ν_t is the viscosity coefficient, ∇^2 is the Laplacian operator, and S_x, S_y & S_z are source terms.

3.2 TELEMAC-2D/3D

Within TELEMAC-3D the equations are derived from the full Navier-Stokes equations with the following assumptions;

- A time-varying free surface
- An incompressible fluid, i.e the density of a fluid element doesn't change with motion.

- Boussinesq approximation, where the density differences are neglected except when the density variation results in buoyancy forces, i.e. when multiplied by gravity.

- In the current research a hydrostatic pressure assumption is used, the pressure at a point is dependant only on the surface atmospheric pressure and the weight of the water column above the point. A non-hydrostatic version of TELEMAC-3D is also included in the TELEMAC modelling package.

The 3D computational domain is divided into many horizontal planes to achieve the required resolution in the vertical direction. In particular, this study uses a sigma transform to specify 13 depth layers for all computations. The layers are arranged between the free surface and seabed, the distance between two adjacent layers varies spatially taking up a specified fraction of the water column at each node location.

The equations solved by TELEMAC-3D are expressed below, including the momentum equation for a passive or active tracer.

$$\frac{\partial u}{\partial x} + \frac{\partial v}{\partial y} + \frac{\partial w}{\partial z} = 0 \tag{3.5}$$

$$\frac{\partial u}{\partial t} + u\frac{\partial u}{\partial x} + v\frac{\partial u}{\partial y} + w\frac{\partial u}{\partial z} = -g\frac{\partial z_s}{\partial x} + \nu_t \nabla^2(u) + S_x \tag{3.6}$$

$$\frac{\partial v}{\partial t} + u\frac{\partial v}{\partial x} + v\frac{\partial v}{\partial y} + w\frac{\partial v}{\partial z} = -g\frac{\partial z_s}{\partial y} + \nu_t \nabla^2(v) + S_y \tag{3.7}$$

$$p = p_{atm} + \rho_0 g(z_s - z) + \rho_0 g \int_z^{z_s} \frac{\Delta\rho}{\rho_0} \partial z \tag{3.8}$$

$$\frac{\partial T_r}{\partial t} + u\frac{\partial T_r}{\partial x} + v\frac{\partial T_r}{\partial y} + w\frac{\partial T_r}{\partial z} = \nu_T \nabla^2(T_r) + S_T \tag{3.9}$$

where p_{atm} is the atmospheric pressure, z_s is the free surface elevation, ρ_0 is the reference density, $\Delta\rho$ is the variation in density, T_r is a passive or active tracer, ν_T is the tracer diffusion coefficient, and S_T is the tracer source or sink.

The pressure terms within the continuity and momentum equation are vertically integrated to calculate the water depth, through the 2D equations;

$$\frac{\partial h}{\partial t} + \frac{\partial(\overline{u}h)}{\partial x} + \frac{\partial(\overline{v}h)}{\partial y} = 0 \tag{3.10}$$

$$\frac{\partial \overline{u}}{\partial t} = -g\frac{\partial z_s}{\partial x} \tag{3.11}$$

$$\frac{\partial \overline{v}}{\partial t} = -g\frac{\partial z_s}{\partial y} \tag{3.12}$$

where $\overline{u}$ and $\overline{v}$ are the 2D depth-averaged flow velocity components in the x and y direction.

Unlike the 3D solution, the TELEMAC-2D solves the Shallow water or Saint Venant equations, which are derived by depth integrating the 3D Navier-Stokes equations at each node within the domain. Assuming an incompressible fluid, hydrostatic pressure and the Boussinesq approximation for momentum. The 2D model is therefore valid in areas where the horizontal length scale is much greater than the vertical length scale, and for flows with negligible vertical acceleration. The continuity equation for conservation of mass, momentum equations in x and y and a conservation equation for a tracer are given as follows;

$$\frac{\partial h}{\partial t} + \overline{u} \cdot \vec{\nabla}(h) + h\mathrm{div}(\vec{\overline{u}}) = S_f \tag{3.13}$$

$$\frac{\partial \overline{u}}{\partial t} + \vec{\overline{u}} \cdot \vec{\nabla}(\overline{u}) = -g\frac{\partial z_s}{\partial x} + S_x + \frac{1}{h}\mathrm{div}(h\nu_t\vec{\nabla}\overline{u}) \tag{3.14}$$

$$\frac{\partial \overline{v}}{\partial t} + \vec{\overline{u}} \cdot \vec{\nabla}(\overline{v}) = -g\frac{\partial z_s}{\partial y} + S_y + \frac{1}{h}\mathrm{div}(h\nu_t\vec{\nabla}\overline{v}) \tag{3.15}$$

$$\frac{\partial T_r}{\partial t} + \vec{\overline{u}} \cdot \vec{\nabla}(T_r) = S_T + \frac{1}{h}\mathrm{div}(h\nu_T\vec{\nabla}T_r) \tag{3.16}$$

where $\vec{}$ denotes a vector, $\vec{\nabla}$ is an operator for the gradient, S_f is the source/sink of fluid, and S_T is the source/sink of the tracer.

3.2.1 Sources and sinks

The source and sink terms that can be taken into account in both TELEMAC 2D & 3D include; wind, Coriolis force, bottom friction, and source and sinks of momentum.

In 2D the friction acts on each finite element within the domain due to it's depth-integrated nature, the friction velocity is based on the depth averaged flow. In 3D the vertical structure of the flow is taken into account, as the friction acts only on the elements immediately above the sea bed.

In 2D the bed shear stress is calculated from the depth averaged mean flow velocity using the quadratic friction coefficient, C_D

$$\tau_0 = \frac{1}{2}\rho C_D \overline{U}^2 \tag{3.17}$$

where t_0 is the bed shear stress and $\overline{U}$ is the depth averaged mean flow velocity.

The quadratic friction coefficient, C_D is calculated in this research using the Nikuradse bottom friction formula where;

$$C_D = 2\left[\frac{\kappa}{\log\left(\frac{11.036h}{k_s}\right)}\right]^2 \tag{3.18}$$

where h is the water depth, κ is the Von Karman constant ($\kappa = 0.41$), and k_s is the Nikuradse bed roughness height. Adjustments to the bed roughness height k_s is used to calibrate the model in sections 5.1.2 & 5.2.2.

In 3D, using the Nikuradse law, the bottom friction is determined from the velocity in the near-bed horizontal plane, and assumes a logarithmic profile. The bottom friction is calculated in terms of the friction velocity, u_* defined as

$$u_* = \sqrt{\frac{\tau_0}{\rho}} = \sqrt{\nu_t\left(\frac{\partial U}{\partial z}\right)} \tag{3.19}$$

where U is the mean flow velocity.

The friction velocity, u_* is deduced by assuming a log profile in the first plane above the bed as;

$$u_* = \left[\frac{\kappa}{\log\left(ln\frac{z_1}{z_0}\right)}\right]^2 {u_1}^2 {v_1}^2 \tag{3.20}$$

where z_1 is the vertical distance from the bed to the first horizontal plane, u_1 and v_1 are the velocity in the first plane, z_0 is a the bed roughness length, which relates to the Nikuradse bottom roughness, $z_0 = \frac{k_s}{30}$.

3.3 Turbulence models

In TELEMAC-3D the turbulence calculation is based on a horizontal and vertical turbulence closure, due to the difference in eddy scale in the two directions. In TELEMAC-2D only the horizontal turbulence model is used. In both cases, the turbulence can be modelled with a mixing length equation, large eddy simulation (LES) or the k-epsilon turbulence closure model. The k-epsilon model is best capable to model the turbulence with temporal and spatial varying generation and dissipation. However, due to computational time and model stability issues, LES and mixing length equations are used within this study. This is considered reasonable as the main focus of the current study is the impacts of the OWF to the far field processes at the coastal regional scale. The strong variations in turbulence around individual structures are unlikely to exert influences beyond the near field scale.

The horizontal turbulence is modelled with the Smagorinsky scheme, a Large Eddy Simulation (LES) model. The horizontal velocity field is explicitly solved for large scale eddies and implicitly solved for small eddies using a sub-grid scale model, the mixing length is proportional to the size of the grid. This model does not take into account dispersion terms for the 2D case. The Smagorinsky equation is expressed as;

$$\nu_t = {C_s}^2 \Delta^2 \sqrt{2 e_{ij} e_{ij}} \tag{3.21}$$

where C_s is a dimensionless coefficient taken as 0.1 in this study; Δ is the mesh size taken as the surface of the element in 2D and the volume in 3D, e_{ij} is the strain rate tensor defined as;

$$e_{ij} = \frac{1}{2}\left(\frac{\partial \overline{u_i}}{\partial x_j} + \frac{\partial \overline{u_j}}{\partial x_i}\right) \tag{3.22}$$

where the subscript $_{i,j}$ indicates the direction x and y.

For the vertical turbulence model a mixing length model developed by Nezu and Nakagawa (1993) is used. This model takes into account that with no wind, the turbulent viscosity tends to zero at the free surface. The mixing length expresses the viscosity coefficient in terms of Prandtls theory.

$$\nu_t = {L_m}^2 \sqrt{2 e_{ij} e_{ij}} \tag{3.23}$$

where L_m is the mixing length parameter. The mixing length parameter is calculate using the Nezu and Nakagawa model as;

$$L_m = \kappa z \sqrt{1 - \frac{z}{h}} \tag{3.24}$$

3.4 TOMAWAC

TOMAWAC is a phase averaged third generation spectral wave model. The waves propagate and evolve through solving of the wave action conservation equation at each node (Benoit et al., 1996). Wave action, N, is a wave quantity which is always conserved even in the presence of tidal currents, it is defined as;

$$N = \frac{F}{\omega_i} \tag{3.25}$$

where F is wave variance directional spectrum or wave energy density, and ω_i is the intrinsic angular frequency.

The wave evolution equation can be expressed in the Cartesian form as;

$$\frac{\partial(BF)}{\partial t} + \dot{x}\frac{\partial(BF)}{\partial x} + \dot{y}\frac{\partial(BF)}{\partial y} + \dot{\Theta}\frac{\partial(BF)}{\partial \Theta} + \dot{f}_r\frac{\partial(BF)}{\partial f_r} = BS_w(x, y, \Theta, f_r, t) \tag{3.26}$$

where the operator $\dot{}$ denotes the time transfer ratios of each variable given by the linear wave theory, Θ is propagation direction, S_w is a source/sink term, B is expressed as;

$$B = \frac{c_g}{(2\pi)^2 k f_r} \tag{3.27}$$

c_g is the intrinsic group velocity of the waves, defined as $c_g = \frac{\partial \omega_i}{\partial k}$ where k is the wave number. The intrinsic wave frequency, f_r, is defined as $f_r = \frac{\omega_i}{2\pi}$.

TOMAWAC is capable of modelling random multi-directional waves based on the super-position of sinusoidal waves. The source/sink term, S_w, in equation (3.26) takes account of the contribution from physical processes not resolved in the wave evolution equation. The physical processes included in the TOMAWAC model are; wind-driven wave generation, white capping energy dissipation, non-linear quadruplet interactions, bottom friction induced energy dissipation, bathymetric breaking induced energy dissipation, and non-linear triad interactions.

The wave induced currents are accounted for when coupled with the tidal hydrodynamics with the two dimensional wave forcing, F_x and F_y defined as;

$$F_x = -\frac{\partial S_{xx}}{\partial x} + \frac{\partial S_{xy}}{\partial y} \qquad\qquad F_y = -\frac{\partial S_{xy}}{\partial y} + \frac{\partial S_{yy}}{\partial y} \tag{3.28}$$

where S_{xx}, S_{xy} & S_{yy} are the radiation stress tensors.

The wave forcing, F_x & F_y, are read into TELEMAC, the current can then be calculated in the x and y directions. In 3D the F_x and F_y are assumed to be constant across the depth, therefore the resultant wave-driven current will be uniformly distributed in the vertical direction.

3.5 SISYPHE

The sand transport for non-cohesive and mixed sediments is calculated by the SISYPHE module. The total transport rate at each computational node is split into bed-load and suspended-load transport. The bed-load is calculated through one of 10 available semi-empirical bed load transport formulae. In the present study the Soulsby-Van Rijn formula is used as it is suitable for use in cases with combined currents and waves;

$$q_{b,s} = A_{b,s}\overline{u}\left[\left(\overline{u}^2 + \frac{0.018}{C_D}{U_m}^2\right)^{0.5} - \overline{u}_{cr}\right]^{2.4} \tag{3.29}$$

where U_m is the orbital velocity of waves, C_D is the quadratic drag coefficient due to the current, A_b & A_s are the bed load and suspended load coefficients, respectively, calculated as;

$$A_b = \frac{0.005h\left(d_{50}/h\right)^{1.2}}{\left[(s-1)gd_{50}\right]^{1.2}} \qquad A_s = \frac{0.012d_{50}{d_*}^{-0.6}}{\left[(s-1)gd_{50}\right]^{1.2}} \tag{3.30}$$

where d_{50} is the median grain size, d_* is the dimensionless grain size defined as;

$$d_* = \left[\frac{g(s-1)}{\nu^2}\right]^{1/3} d_{50} \tag{3.31}$$

The critical entrainment velocity, $\overline{u}_{cr}$ is defined as;

$$\overline{u}_{cr} = 0.19{d_{50}}^{0.1}\log_{10}\left(\frac{4h}{d_{90}}\right) \text{ if } 0.1mm \leqslant d_{50} \leqslant 0.5mm \tag{3.32}$$

$$\overline{u}_{cr} = 8.5{d_{50}}^{0.6}\log_{10}\left(\frac{4h}{d_{90}}\right) \text{ if } 0.5mm \leq d_{50} \leq 2mm \tag{3.33}$$

where d_{90} is grain diameter for which 90% of the grains by mass are finer.

The suspended load is computed through integration of the sediment flux, i.e. the product of the flow velocity vector and sediment concentration across the water depth at each computational node. The flow velocity vector is provided by TELEMAC 2D and TELEMAC 3D. The sediment concentration is calculated through the following depth-integrated transport equation when TELEMAC 2D is used;

$$\frac{\partial C}{\partial t} + u_{conv}\frac{\partial C}{\partial x} + v_{conv}\frac{\partial C}{\partial y} = \frac{1}{h}\left[\frac{\partial}{\partial x}\left(h\varepsilon_s\frac{\partial C}{\partial x}\right) + \frac{\partial}{\partial y}\left(h\varepsilon_s\frac{\partial C}{\partial y}\right)\right] + \frac{(E_f - D_f)_{z=z_{ref}}}{h} \tag{3.34}$$

where C is the suspended sediment concentration, ε_s is the sediment diffusivity coefficient ($\varepsilon_s = 10^{-2}m^2s^{-1}$), E_f is the net erosion flux, D_f is the sediment deposition flux, z_{ref} is the depth of the interface between the bed-load and suspended layers, and u_{conv} & v_{conv} are the depth averaged convective velocities defined as;

$$u_{conv} = \frac{\int_{z_{ref}}^{h} u(z)C(z)dz}{\int_{z_{ref}}^{h} C(z)dz} \tag{3.35}$$

$$v_{conv} = \frac{\int_{z_{ref}}^{h} v(z)C(z)dz}{\int_{z_{ref}}^{h} C(z)dz} \tag{3.36}$$

The three dimensional suspended sediment concentration is calculated within TELEMAC 3D as;

$$\frac{\partial C}{\partial t} + \mathrm{div}((\vec{U} + \vec{W}_s)C) = \mathrm{div}(\varepsilon_s \cdot \vec{\nabla} C) \tag{3.37}$$

where $\vec{U}$ is the mean flow velocity vector, ε_s is the sediment diffusivity coefficient ($\varepsilon_s = 10^{-2} m^2 s^{-1}$), $\vec{W}_s$ is the settling velocity, defined using the van Rijn equation, suitable for non-cohesive sediments, as;

$$\vec{W}_s = \frac{(s-1)g{d_{50}}^2}{18\nu} \text{ if } d_{50} \leq 10^{-4} \tag{3.38}$$

$$\vec{W}_s = \frac{10\nu}{d_{50}} \left(\sqrt{1 + 0.01 \frac{(s-1)g{d_{50}}^3}{18\nu^2}} - 1 \right) \text{ if } 10^{-4} \leq d_{50} \leq 10^{-3} \tag{3.39}$$

$$\vec{W}_s = 1.1\sqrt{(s-1)gd_{50}} \text{ if } 10^{-3} \leq d_{50} \tag{3.40}$$

where ν is the kinematic viscosity.

In 3D a Rouse profile is assumed for the vertical distribution of sediment concentration, the profile is defined as;

$$C(z) = C_{z_{ref}} \times \left[\frac{z-h}{z} \frac{z_{ref}}{z_{ref} - h} \right]^R \tag{3.41}$$

where R is the Rouse number, defined as;

$$R = \frac{\vec{W}_s}{\kappa u_*} \tag{3.42}$$

where u_* is the friction velocity for the total bed shear stress.

It should be noted that in the 3D simulation, the bed shear stress is based on the velocity vectors immediately above the bed and the bed-load transport

is assumed to be in the same direction. Whereas in the 2D simulation, the bed shear stress is computed from the depth-averaged flow velocity vector and the direction follows that of the depth averaged flows. In the cases where strong variation of flow direction exist across the depth, such as the complex flows near the structures, the 2D simulation can lead to a higher level of uncertainty due to the simplifications.

After the total load transport rate is computed, the bottom evolution can then be evaluated with the Exner equation. The bed morphology is updated at each specified morphological time step;

$$(1 - \lambda_p)\frac{\partial z_f}{\partial t} + \text{div}\,(\vec{q_t}) = 0 \tag{3.43}$$

where λ_p is the bed porosity ($\lambda_p = 0.4$), z_f is the bottom elevation, div is an operator for the divergence, and q_t is the total-load volumetric transport rate ($q_t = q_b + q_s$).

In all model runs in this research, the bed is specified as rough and the reference level concentration is calculated by Bijker $z_{ref} = k_r$, where k_r is the ripple roughness.

3.6 Representation of wind farm monopile in the mesh

The monopile foundations are represented as islands in the mesh, the edge of which consists of 40 nodes to approximate a circular shape. The mesh is then created with concentric rings of decreasing density away from the monopile (Figure 3.1). The smallest mesh sizes next to the monopiles are $0.4m$, increasing to $3.5m$, $20m$ away from the pile.

It should be noted that the equations solved in the model mean that the model is not capable of representing the complex flow structure around the monopile. The vertical flow structures will not be fully resolved, therefore at the pile the

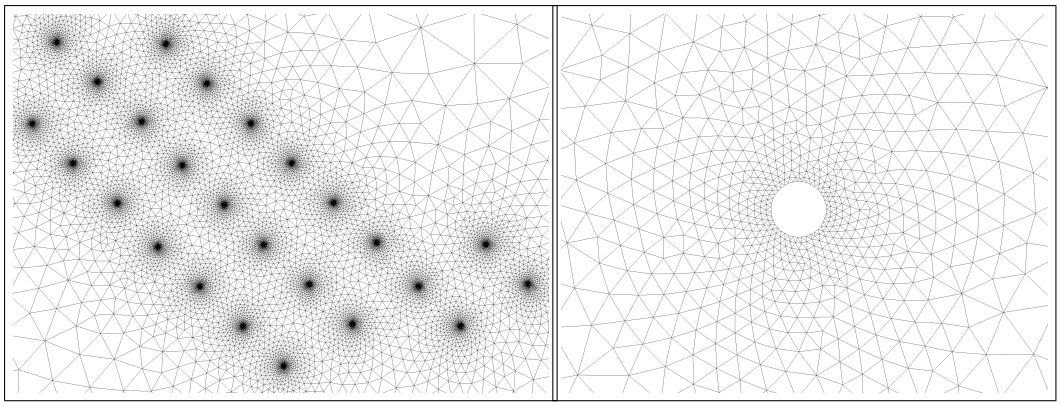

(a) (b)

Figure 3.1: Offshore wind farm monopile represented in the mesh showing a) the Burbo Bank wind farm mesh and b) mesh surrounding one monopile foundation.

results must be treated with some caution. However, further from the pile the results are thought to be valid, this is discussed further in the validation chapter.

3.7 Numerical methods

The TELEMAC modelling system uses the finite element method to solve the continuous model equations on a discrete domain. The domain is divided into triangular areas known as elements, for which there are 3 nodes at 3 vertices. It is at the nodes that discrete values of the calculation variables are calculated from partial differential equations, which are approximated using numerical methods. The individual elements tesselate to make up the entire domain, the Blue Kenue software was used to create the mesh. The finite element method allows the use of varying domain resolution, where coastlines, bathymetry change and areas of interest can be resolved with use of a fine mesh over these regions.

In 3D, the 2D mesh is repeated over a specified number of vertical planes, the spatial discretization uses prisms with 6 nodes. The vertical grid is created by converting the z co-ordinates into sigma co-ordinates, which varies the height of each plane with water depth. The sigma co-ordinates are used in this research with the proportions of the water depth specified (Figure 3.2), this approach al-

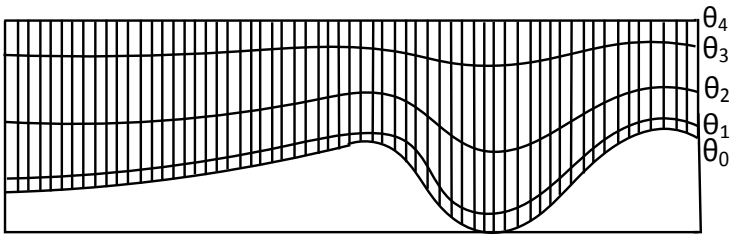

Figure 3.2: 3D mesh vertical structure built with sigma co-ordinates

lows vertical mesh refinement in areas of interest. The conversion of z-coordinates into sigma co-ordinates is calculated as;

$$\sigma = \frac{z}{(h+\eta)} \tag{3.44}$$

where η is the free surface elevation.

Using sigma co-ordinates the thickness of the layers varies over the domain, but the normalized thickness remains constant. The sigma transform used is;

$$z(x, y, ip) = z_f(x, y) + \theta_{ip}\,(z_s(x, y) - z_f(x, y)) \tag{3.45}$$

where ip is the rank of the plane under consideration, and θ_{ip} varies between $0 \leq \theta_{ip} \leq 1$ representing the fraction of the water column. In this research 13 planes are used of $\theta_1 = 0$, $\theta_2 = 0.02$, $\theta_3 = 0.1$, $\theta_4 = 0.2$, $\theta_5 = 0.3$, $\theta_6 = 0.4$, $\theta_7 = 0.5$, $\theta_8 = 0.6$, $\theta_9 = 0.7$, $\theta_{10} = 0.8$, $\theta_{11} = 0.9$, $\theta_{12} = 0.99$, $\theta_{13} = 1.0$.

3.8 Boundary conditions

The shoreline and islands in the mesh, including the wind farm monopiles, have a closed wall boundary condition with slip/friction. The open ocean boundaries in the mesh are set with a prescribed water depth, and free velocity and tracers. The incoming tide is driven by 7 tidal constituents (M_2, S_2, N_2, K_2, P_1, O_1, K_2), generated by the Tidal Model Driver (Egbert and Erofeeva, 2002), at each point of the offshore boundary. The boundary free surface is calculated in the BORD subroutine from the given amplitude, phase and period.

Tidal Constituent	Period (hour)	Amplitude (m)	Phase (°)
M_2	12.42	3.151	323.6
S_2	12.00	1.020	8.79
N_2	12.66	0.598	302.1
K_2	11.97	0.290	6.72
K_1	12.93	0.128	192.2
O_1	25.82	0.125	43.09
P_1	24.07	0.060	166.09

Table 3.1: Typical components of 7 tidal constituents at Princes Pier

$$\eta_j = \sum_{i=1}^{7} a_{mi,j} cos(f_{i,j} t) \tag{3.46}$$

where a_m is the amplitude of the 7 tidal constituents, j is the notation of the element along the open boundary, f is the frequency, and η is the free surface elevation. The typical components for the 7 tidal constituents at Princes Pier in the Mersey Estuary (Figure 5.5) are given in Table 3.1.

The elevations at the boundary points are used to calculate the flow velocities at the boundary through the Thompson boundary condition, which uses the characteristics method. In TELEMAC 3D the flow velocity is prescribed at each boundary point with constant values through the water column, i.e. a uniform flow profile.

3.8.1 Errors in the modelling method

There are many factors which contribute to the errors in the solution. The errors that could exist from the method of solving the equations include;

- Discretization errors. This is the difference between the equations solved in the discrete domain and time step compared with the full numerical solution of the equations. This can be minimised through creation of a good quality mesh and time step tuning.

- Truncation error. This is the difference between the partial differential equations solved and the finite equations, and is dependant on mesh quality.

- Convergence errors. The equations are solved by iteration to a prescribed level of accuracy, this allows a decrease in computational time. Within TELEMAC the accuracy level for the equation solution can be specified.

3.8.2 TELEMAC scaling

To run the model over the complex bathymetry with a wind farm represented in the mesh requires a large number of elements in the mesh. This is due to several factors contributing to the consideration of the mesh resolutions and run time;

- The OWF is resolved in detail in the present study, which means a very fine mesh has to be used around the wind turbine foundations. With a large number of turbines within the OWF, the total number of mesh points will be considerably increased.

- The coastal process involves complex interaction between the waves, tide and the resultant sediment transport. In order to get the model to simulate the complex interaction properly, a fine mesh is very often required near the headlands, islands and the sites where dramatic bathymetry changes occur.

- As the present study aims to examine long term morphology changes around the wind farm site. The simulation will have to run over a large number of time steps in order to predict the evolution over long time periods.

Therefore the required computing time is very high for the present study, which means that TELEMAC needs to be run in the parallel mode on a high performance computing cluster. The modelling system is capable of running in parallel on separate computing nodes, based on domain decomposition. The model was originally designed for a small number of subdomains (2-32). Moulinec et al. (2011) developed the partitioning method to enable meshes of up to 25 million elements to be employed. The present research follows the same method for the computation on a Solaris HPC system.

In order to test the scaling of TELEMAC a large mesh of 3.1 million elements was run in 2D over one tidal cycle. The TELEMAC modelling system shows good performance with scaling as seen in Figure 3.3 , showing an exponential decrease in run time with increased number of computing nodes.

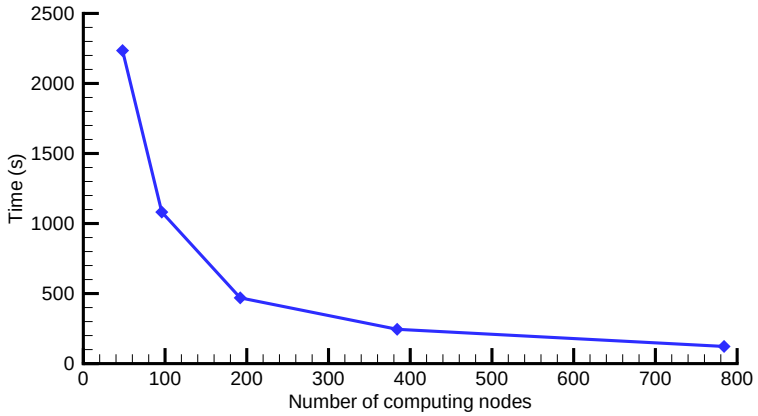

Figure 3.3: TELEMAC model scaling plot for a 3.1 million element mesh run over one tidal cycle

3.9 Model setup

Each module can be run separately or coupled, either internally or through the chaining method. During internal coupling the hydrodynamic files call the wave and sediment modules, and data is shared. The coupling period can be specified in all cases, although as calculation of suspended sediment requires solving of a transport equation, the coupling period must be set to 1 for TELEMAC coupled with SISYPHE. The hydrodynamic and wave data is transferred to SISYPHE to calculate sediment transport and to update the bed, which is read into hydrodynamics for the next time step. Internal coupling is computationally intensive, but CPU time is reduced by running the modules in parallel. Details of the coupling between different modules is shown in Figure 3.4.

The calculations are run from a steering file, in which the model files and parameters are specified. The Geometry files contains the mesh nodes and bathymetry, and is created in Blue Kenue in a selafin format. The boundary

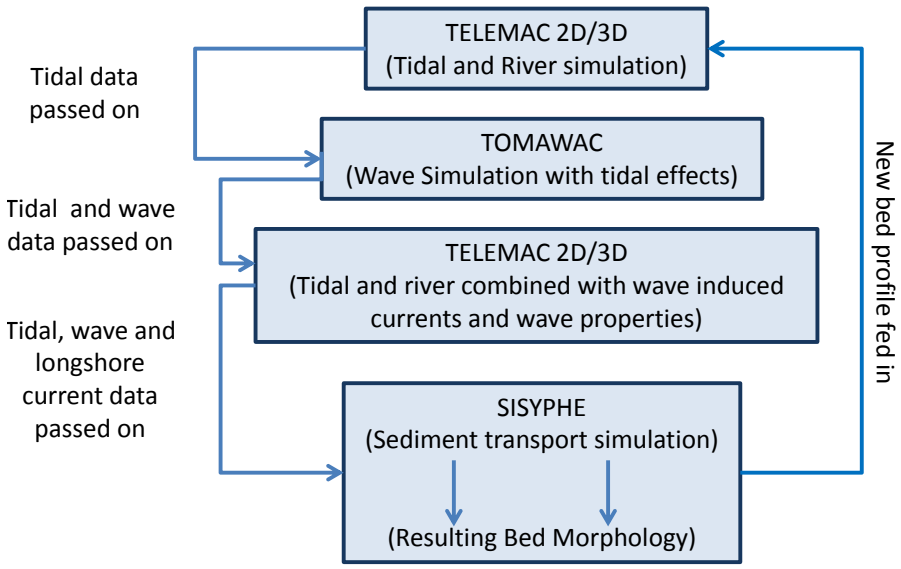

Figure 3.4: Simulation procedure for morphodynamic modelling with the TELEMAC modelling system

condition file is also generated in Blue Kenue and specifies the boundary type and location. The TELEMAC modules can be modified by the user by calling modified FORTRAN files from the steering file.

Chapter 4

TELEMAC Model Validation

4.1 Single monopile test

To verify the TELEMAC 3D models capability for prediction of complex flows around a single cylinder, the model was tested against the available experimental data of Roulund et al. (2005). The steady flow is directed past a circular pile at a speed of $0.326ms^{-1}$ with a water depth of 0.54m. The experimental set up has a bed roughness height of $0.14cm$, and an overall Reynolds number based on the depth averaged flow velocity of 1.7x10^5.

The numerical mesh follows the experimental set up with a channel width of $4.0m$ and a length of $8m$. A cylinder of diameter $0.536m$, is placed at the centre of the channel as shown in Figure 4.1. The numerical mesh has a varying element size of $0.1m$ at the boundary and is gradually refined to $0.01m$ adjacent to the cylinder. The total number of triangle elements is 18,352.

In total 15 layers are used in the vertical direction in the model. The time step is set as $0.01s$ and after more than 1,000 steps the solution converged to a quasi-steady state. The computed results were then compared with the experimental measurements.

The computed flow velocity along the central plane in the streamline direction is compared with the measured values at various levels above the bed as

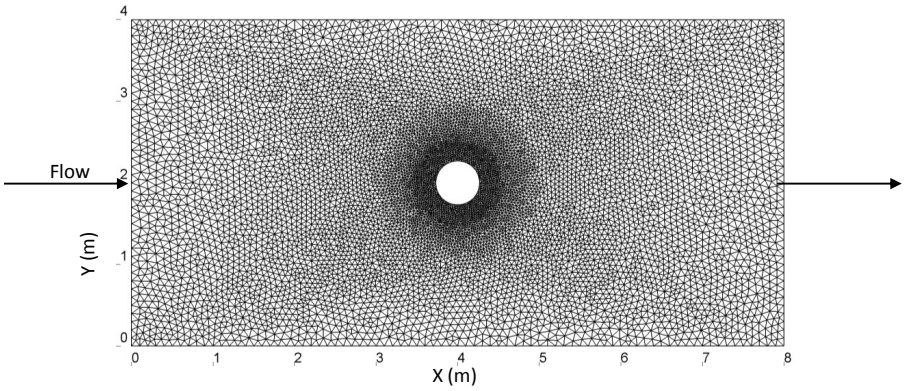

Figure 4.1: Numerical mesh for a single cylinder in a channel, experimental set up by Roulund et al. (2005)

shown in Figure 4.2. The model results follow the measured data very well even close to the bed, given that the model is based on simplifications and the flows are complex and 3D. The model tends to under predict the flow speed at the downstream locations close to the pile at lower levels above the bed, i.e. $1.3cm$ to $9.3cm$, although the model results show similar trends to the measurements. Immediately upstream of the pile, the model results over predicts the flow velocity compared with the measured data, which could lead to enhanced sediment scouring. Further away from the bed, the model results tend to be lower than the measured velocity at the immediate upstream of the pile, however, downstream the predicted velocities are generally greater than the experimental values. The overall agreement at both upstream and downstream are acceptable.

The computed flow velocity vector is compared with the measured data across the depth adjacent to the pile as shown in Figure 4.3. Upstream of the monopile the model, the predictions show a good agreement with the experimental results. There is a decrease in velocity as the flow approaches the pile, with a downflow seen at the pile and flow reversal near the bed at a height of $\frac{z}{\delta} = 0.25$. Downstream of the monopile flow reversal close to the pile is seen in both the model predictions and experimental results, with turbulence near the bed. The stagnation point, where the flow reverses direction, occurs further behind the pile for the model prediction (3-3.5D) than is seen in the experiment (1.5-2D).

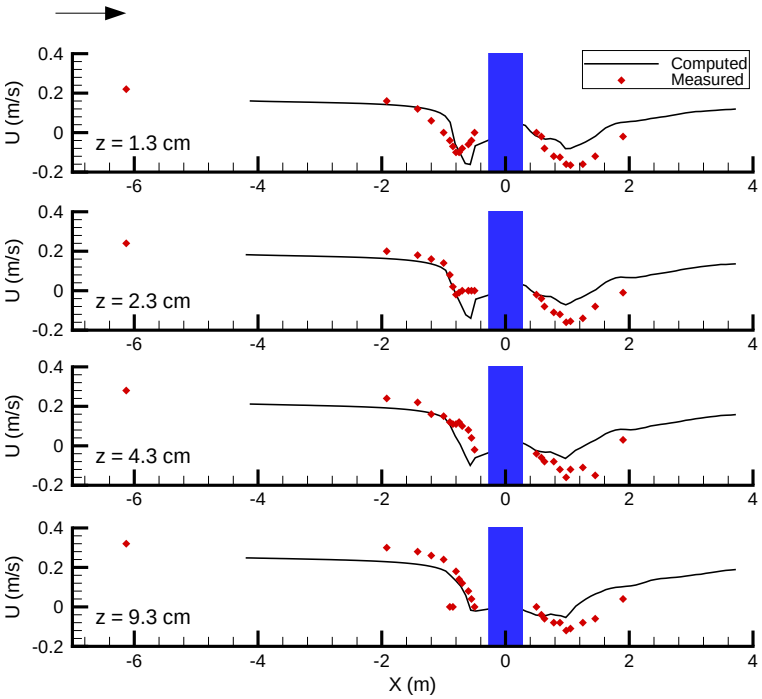

(a)

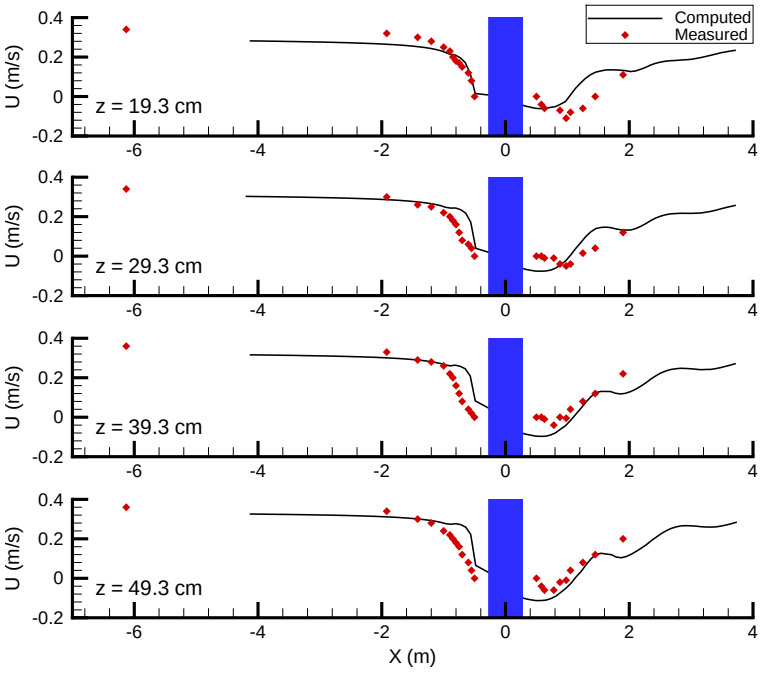

(b)

Figure 4.2: Comparison of computed and measured flow velocity past a single cylinder along the central plane at various heights above the bed. The solid lines are computed results and the symbols are the laboratory measured data

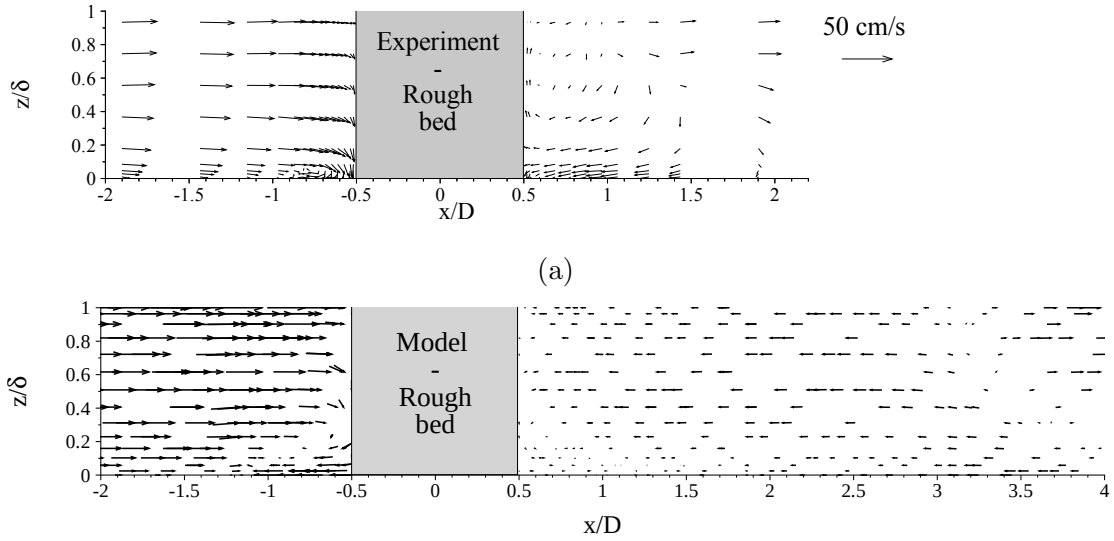

Figure 4.3: Flow velocity vector across the water depth close to a pile for a) computed data, and b) measured data

Figure 4.4 shows the comparison of computed and measured bed shear force enhancement factor around the pile under the steady flow condition. The overall pattern is similar between the measured and computed shear force distribution. The maximum enhancement factor in the predicted values follows the experimental data, with a value of approximately 7 at the pile, reducing to a value of 1.0 at distance of 1D from the pile. However, it is clear that the model over-predicts the shear forces between 0.5D and 1D distance from the pile. The enhancement factor reaches 2.0 and occupies a large part of the area adjacent to the pile, whereas, the measured shear force amplification reduces to 1.0 fairly closely to the pile. The maximum shear force is located slightly further downstream in the model results compared with the measured data. Given the simplification of the model concepts, the overall agreement is considered to be good.

The scour formation computed by the model is compared with the measured data for Test 3 of Roulund et al. (2005). In these test conditions the pile in the channel has a diameter of $0.1m$, with a water depth of $0.4m$ and a flow speed of $0.46ms^{-1}$. The bed is mobile with a uniform sand of $0.26mm$ diameter. Fig-

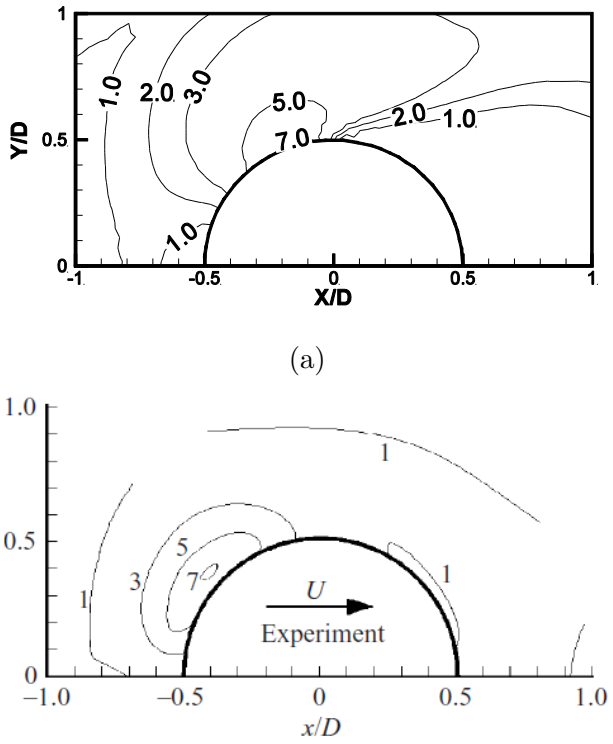

Figure 4.4: Bed shear force enhancement factor around a single pile, for a) the computed data and b) the measured data

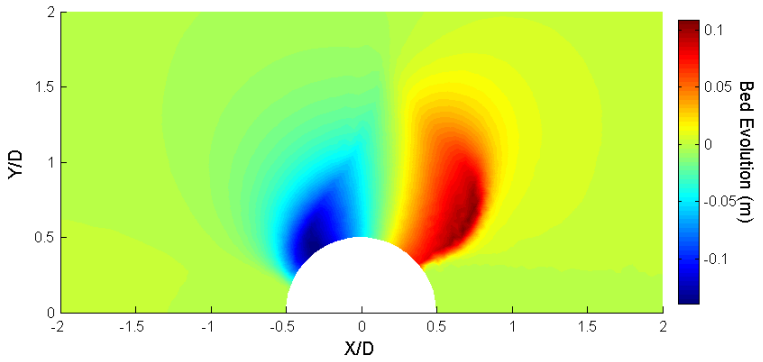

Figure 4.5: Computed scour pattern at a pile in a channel, using the Test 3 experimental conditions of Roulund et al. (2005)

ure 4.5 presents the computed bed evolution after 3 hours, when the bed has approached an equilibrium. The bed evolution shows a general pattern of scour at the side-front of the pile and accretion behind. The experimental bed shear force (Figure 4.4), suggests that the scour at the side-front of the pile lies further towards the front than is seen in the computed results.

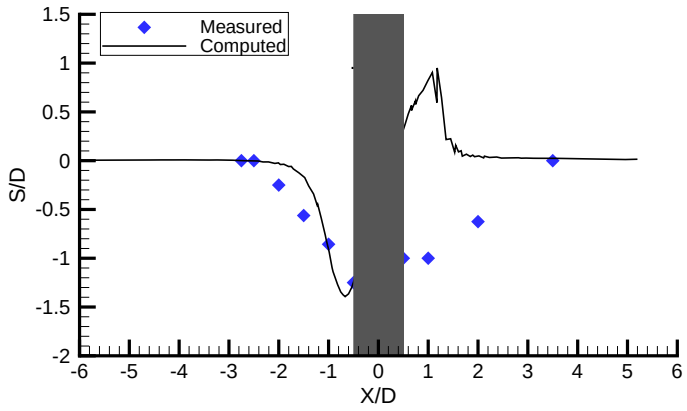

Figure 4.6: Comparison of computed and measured scour depth along the central axis, using the experimental conditions of Roulund et al. (2005)

The computed and measured scour cross-section at the pile are shown in Figure 4.6. There is good agreement for the maximum scour in front of the pile. However, behind the pile the accretion of the sediment in the model diverges from the scour pattern seen in the measured values.

A similar result has been found by other studies using large scale coastal models to study scour. Weilbeer and Jankowski (2000) modelled scour at a cylinder using TELEMAC, applying an eddy viscosity turbulence model in the horizontal and a mixing length turbulence model in the vertical direction. The 3D flow was modelled using the hydrostatic version TELEMAC and the horseshoe vortex in front of the pile was generated, whereas for the non-hydrostatic version the horseshoe vortex disappeared. The sediment transport at the pile was studied, and a scour pattern was formed in front of the pile, due to the horseshoe vortex, with little scour in the wake. Simoons (2012) studied scour at a cylinder using the Delft-Flow model, and assessed the scour pattern formation for various sediment transport formulae. For all sediment transport formulae, an area of deposition

was found in the wake of the pile in-line with the flow, which was not seen in bed level measurements. It was hypothesised that this was due to the velocities in the modelled wake not being high enough to generate the scour, this may be due to location of the separation point on the cylinder, or the under-prediction of vertical velocities.

The difference in scour pattern for this validation, is likely to be a result of the model not fully resolving the vertical flow, due to limitations of using the shallow water equations. Therefore, the eroded sand from the front of the pile is transported with the flow to the back of the pile and then deposited there to form the accretion, rather than scour as shown in the laboratory.

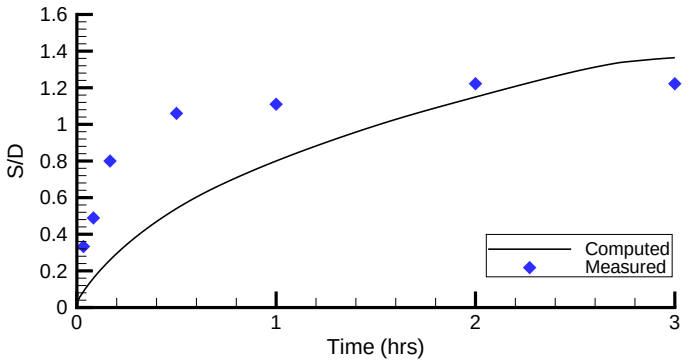

Figure 4.7: Comparison of computed and measured scour development in front of the pile, using Test 3 experimental conditions of Roulund et al. (2005)

Figure 4.7 presents a comparison of computed and measured bed evolution in front of the pile over time. It is clear that the model is able to follow the maximum scour depth after it reaches the equilibrium. Initially the model under predicts the erosion compared with the measured data. This is largely due to the lack of vertical flows in the model as discussed previously. However, at the later stage the scour development is controlled by the horizontal advections and the model is able to match the experimental data reasonably well.

From the above comparison we can see that the model based on shallow water equations is able to resolve certain detailed flow structures in the horizontal directions. However, the vertical flows are missing from the model results which

clearly influence the sediment transport and scour around the pile. The resultant bed evolution is in reasonable agreement with the measured value in front of the pile. Behind the pile, the model predicts accretion due to the slowing down of the flow speed and lack of the vertical flows. In the Burbo Bank and Scroby Sands sites, the flow is largely dominated by the tidal flows, with constant changing flow directions, unlike the steady flow case we see here. It is therefore reasonable to use the model for scour prediction.

4.2 Wave dynamics around a single monopile

The wave module, TOMAWAC has also been tested for its performance adjacent to a structure. Available experimental measurements of waves close to a monopile are very limited and there is no detailed data that can be used for the model comparison. Therefore, a series of model simulations were carried out based on a Boussinesq wave model in the MIKE system. The Boussinesq model includes all main physical processes involved in wave propagation in shallow water and interaction with the structure. This includes wave diffraction, refraction, breaking and bed friction, and is considered to be suitable for the wave field prediction close to structures.

In the current study, the Boussinesq model is set-up for a flat bed with $10m$ water depth, which is a typical bathymetry for an offshore wind farm site in the UK. The monopile is located in the middle of the domain as a vertical structure. Three different offshore waves of $2m$ wave height and periods of 4, 6 and 8 seconds, are specified at the bottom boundary. These waves represent commonly seen conditions at the Burbo Bank wind farm site (ABPmer, 2002), the most common wave period at the site is $4s$. The model was used to investigate the wave field with the structure, initially the three waves were specified as regular waves. Figure 4.8 presents the wave height distribution adjacent to the pile computed by the MIKE model. It is clear that the presence of the pile only causes minor changes in the wave height distribution for the $4s$ period waves (Figure 4.8a). The scattering and reflection in front of the pile becomes apparent for

the 6s period waves (Figure 4.8b) and the most significant for $8s$ period (Figure 4.8c). This increase in scattering and reflection occurs as the wave length becomes closer to the diameter of the pile, in this case the $8s$ wave has the closest wavelength to the pile diameter, $4m$, similar findings can also be found in Cooper and Beiboer (2002). To further evaluate the $8s$ wave condition, a random wave case was simulated in which the significant wave height is set at $1.0m$ and peak period is $8s$ as shown in Figure 4.8d. The wave reflection and scattering is still visible in the random wave case, but less significant than the regular wave case due to the spreading of the individual incident waves.

TOMAWAC was then applied to the $4s$ and $6s$ wave conditions, and the computed wave height distribution is presented in Figure 4.9. Due to the formulation of the model, TOMAWAC treats each case with an equivalent random wave condition. From the TOMAWAC results it is clear that the wave reflection and scattering is not seen in these figures. However, the reduction of wave height behind the pile is similar to that in the Boussinesq model. These differences could lead to differences in the sediment transport and scour development in front of the pile. However, the overall pattern of sediment transport is expected to be similar, particularly in the area behind the pile.

4.3 Discussion

As discussed in Chapter 3, the TELEMAC model system is based on the shallow water equations, which in turn are based on the assumption that the water depth compared with the horizontal length scale is small. With the presence of the OWF monopile, the typical length scale is the wake behind the structure where the most dramatic changes take place. At a pile, the length scale of the wake can range up to $100D$ based on most literature (ABPmer, 2002; Cooper and Beiboer, 2002). For a $5m$ diameter structure, the wake could be up to $500m$ long. Therefore, as the OWF's are located in shallow waters of water depth $5 - 30m$, the shallow water assumption is valid. However, in the area close to the structure where the horizontal length scale is less than the water depth, the model

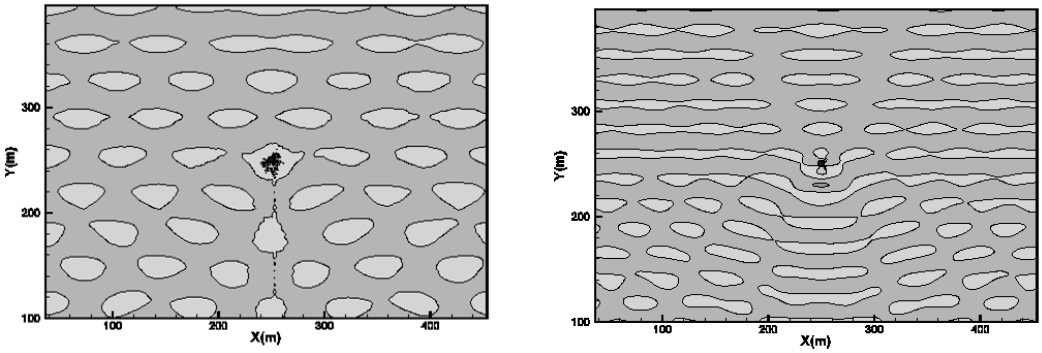

(a) (b)

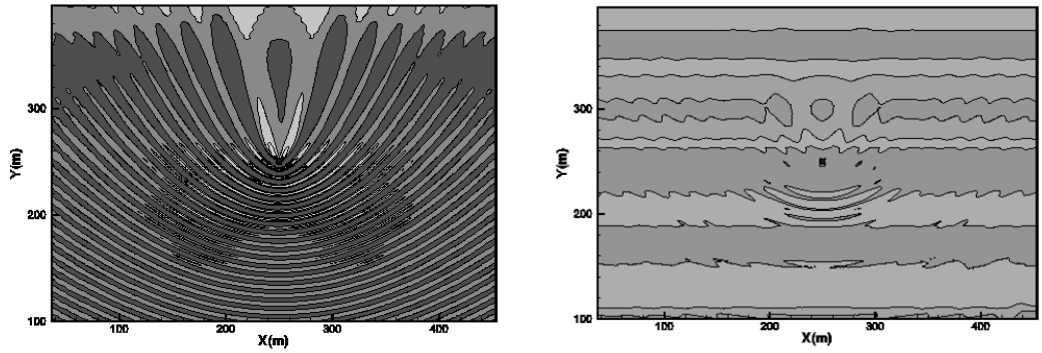

(c) (d)

Figure 4.8: Computed wave height distribution adjacent to a pile calculated by the MIKE Boussinesq model, for a) wave 1, b) wave 2 c) wave 3, and d) equivalent random wave for wave 3

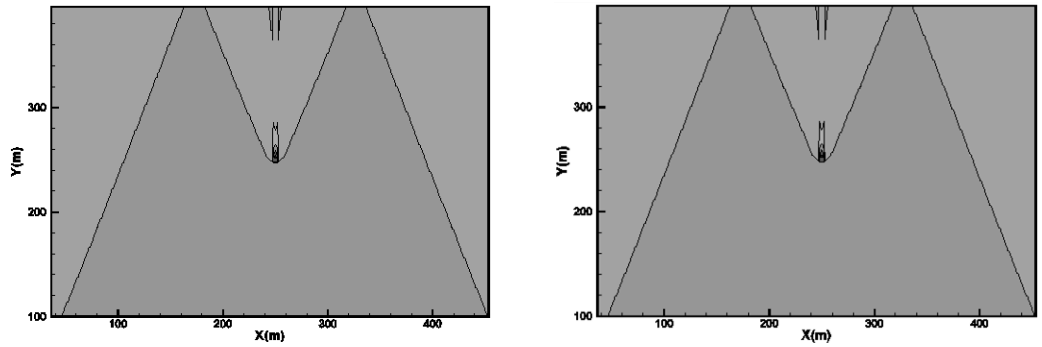

(a) (b)

Figure 4.9: Computed wave height distribution adjacent to a pile calculated by TOMAWAC, for a) wave 2, and b) wave 3

assumption will not be applicable and hence the results are strictly speaking not valid.

The model also assumes that the pressure distribution across the water depth is linear, this assumption is clearly not valid for the region very close to the monopile. Further from the pile, the flow field gradually recovers to the background flow values, and the pressure becomes linearly distributed. Therefore, it is considered reasonable to use the model results at distances greater than the water depth away from the pile. Interestingly, comparisons between model predictions and measured data indicate that the accuracy of the models results are acceptable even very close to the monopile, in both hydrodynamics and sediment transport as shown in Figures 4.2, 4.3 and Figure 4.6. The level of accuracy of the model's prediction of the complex flows close to the monopile could be determined by modelling more refined laboratory data.

The overall aim of the present study is to investigate the impacts from the OWF structures to the marine environment at a regional scale. Whilst the results close to the monopile are shown to indicate the changes due to the presence of structures, they should be treated with caution.

Chapter 5

Model Calibration

The current chapter focuses on the model calibration at two test sites. These test sites represent different types of coastal systems; Liverpool Bay located in the Eastern Irish Sea represents a closed bay with an estuary, whereas East Anglia is an open coast case.

5.1 Liverpool Bay

Liverpool Bay is a relatively shallow area of the Irish Sea, with depths of up to $50m$. Within Liverpool Bay are three offshore wind farms located close to the coast; Burbo Bank, North Hoyle and Rhyl Flats, consisting of 25, 30 and 25 monopile turbines respectively, with a monopile foundation diameter of $4 - 5m$. Burbo Bank is chosen here as the wind farm test site, due to the sites complex hydrodynamics, large tidal flow and freshwater inflow into the vicinity.

Burbo Bank is located in the South-East corner of Liverpool Bay (Figure 5.1), between the estuaries of the Mersey and Dee. The wind farm is situated on the Great Burbo Flats, which is edged by the Little Burbo sandbank to the North, the larger Great Burbo to the East and Newcome Knoll to the West (ABPmer, 2002). There is a dredged channel for navigation to the Mersey Estuary, which surrounds the site to the North and East, and is controlled by training banks. The sediments in the bay are largely fine to medium grain size, with some gravel and a small amount of muddy substrate, mostly found within the estuaries.

The OWF is a Round One wind farm, built and run by Dong Energy Ltd, it has been in operation since January 2007 with a generating capacity of $90MW$ over the 25 turbines. The wind farm site covers an area of $10km^2$, approximately $6.4km$ from the Wirral and Liverpool coastline. The wind turbine monopile foundations are $5m$ in diameter and spaced a minimum of $560m$ apart, there are also three export cables running from the site. In order to prevent scour at the monopile foundations, a filter layer of 25-30m diameter slate cobbles was installed before construction began. Additionally rock armouring was placed post-construction, the combination of filter layer and rock armour means that around the foundations the bed level is raised by $1.5m$ (Carroll et al., 2010).

The tide flows into Liverpool Bay from the Georges channel and the North Channel, the two flows meet and travel east into the bay. It is a tidal dominated area with a peak tidal range of $10m$ and tidal currents can exceed $2ms^{-1}$ at headlands (Simpson et al., 2002). There is a strong flood tide and a weaker ebb, which acts over a longer time period (Pingree and Griffiths, 1979). Polton et al. (2011) found that over a 2 year period the ratio of depth-averaged flood to ebb flow speeds was 1.2. At the wind farm site the flood tide is even more dominant over the ebb, as the dredged channel forces the flow over the Great Burbo Flats and through the channel at the ebb tide (Thomas et al., 2002). The sediment type within Liverpool Bay is fine to medium sands, Figure 5.2 presents the median grain size, d_{50}, distribution for the region.

The Clwyd, Dee, Mersey and Ribble Estuary create a large freshwater inflow into the bay, this flow is highly variable with daily mean fluxes for all four estuaries totalling 61 to $1404m^3s^{-1}$ (Polton et al., 2011). The freshwater flow generates horizontal stratification, vertical stratification at ebb tides which becomes mixed during flood tides, and density currents (Polton et al., 2011). The density differences lead to a residual current as shown by Polton et al. (2013) in Figure 5.3, the residual currents from tide-averaged ADCP data are shown at two locations in Liverpool Bay. The near bed residual current travels towards the coast in an

Figure 5.1: Sea bed features map of Liverpool Bay with the wind farm site highlighted as a red rectangle, (EDINA Digimap)

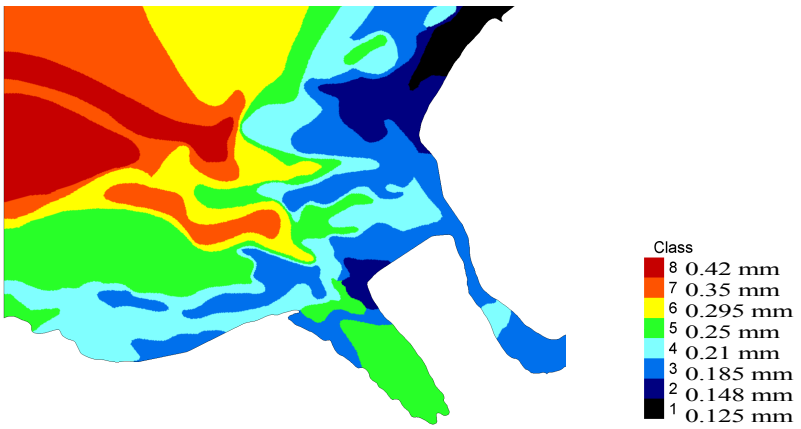

Figure 5.2: Median grain size (d_{50}) distribution map of Liverpool Bay, after HR Wallingford (1991*a*)

Easterly or South-Easterly direction, whereas at the surface the current flows in a time-averaged Northerly direction (Heaps, 1972; Howlett et al., 2011). The flood dominance creates a net sediment transport into the bay, with the Mersey Estuary acting as a sediment sink.

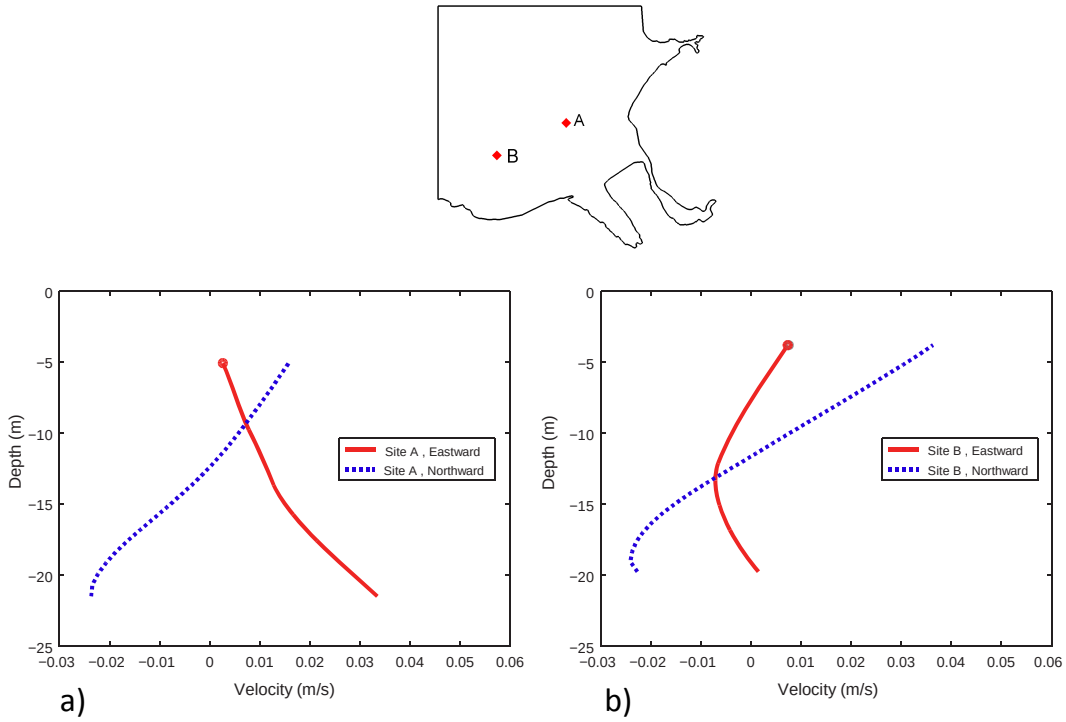

Figure 5.3: Residual current from tide-averaged ADCP data at two locations in Liverpool Bay. From Polton et al. (2013)

Waves within Liverpool Bay are predominantly from the North and West, these are the largest waves as this direction has the longest fetch. Storm surges also occur from the North-West, caused by wind stress on the surface elevation due to the shallow bay (Brown and Wolf, 2009). The maximum storm surges seen are $2.5m$, which has caused flooding in some low coastal regions.

5.1.1 Model set up

To calibrate the model in Liverpool Bay, the finite element mesh consists of 9885 elements (Figure 5.4) for the 2D case. The smallest element size is $300m$ to allow

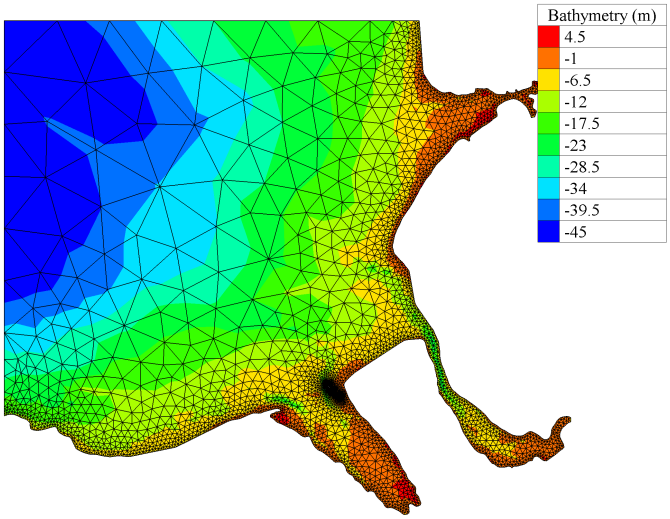

Figure 5.4: Liverpool Bay finite element mesh with bottom bathymetry shown

good resolution of the coastline and Hilbre Island, the largest element size is $7km$. For the 3D case the water column is divided into 13 depth layers, creating a mesh of 128,505 elements for the required vertical resolution. Thirteen vertical depth layer heights are specified so that the vertical mesh can be refined near the sea bed for sediment transport, and near the surface for comparisons with sea surface current measurements. The layer heights are specified as 0, 0.02, 0.1, 0.2, 0.3, 0.4, 0.5, 0.6, 0.7, 0.8, 0.9, 0.99 and 1.0 fractions of the water depth at the node location.

The bathymetry of Liverpool Bay is derived from a number of sources as in Carroll (2012).

- Hydrographic survey of the inner Mersey Estuary by the Mersey Dock and Harbour Company from 1977.
- Environment Agency LiDAR and sonar survey of the Mersey Estuary from 2002.
- Environment Agency LiDAR survey of the Dee Estuary and Liverpool Bay from 2003.
- Environment Agency LiDAR survey of the Ribble estuary from 2004

- Offshore bathymetry is taken from POLCOMS, Irish sea model (Holt and James, 2001), which is compiled from surveys used for admiralty charts.

The shoreline and islands have a closed wall boundary, the rest of the domain is an open flow boundary (Figure 5.5). The sea boundary was set with a prescribed water depth, free velocity and free tracers.

Riverine discharge is also included as a model input, with annual mean flow rate specified at open boundaries with fixed velocity of the Dee, Mersey, Douglas and Ribble estuaries as $33.70m^3s^{-1}$, $37.22m^3s^{-1}$, $4.16m^3s^{-1}$, and $33.04m^3s^{-1}$ respectively. The flow rates are yearly average data from the National River Flow Archive at the Centre of Ecology and Hydrology. At the Ribble and Dee rivers the bathymetry indicates tidal flats at the mesh boundary. In these locations the boundary bathymetry is artificially lowered to $-2m$ to allow the flow discharge to occur at a wet boundary point, which, is a common practice method.

The initial mean sea level is set at a constant elevation of 2m, and the Coriolis effect is taken into account. The sea bed is defined as rough, with the bottom friction calculated by the Nikuradse bottom friction law. This was chosen as in TELEMAC-3D the bed shear stress is related to the near bed velocity assuming a log law with the Nikuradse formula, whereas it is calculated as a depth average for all other formula options. The Nikuradse bottom friction coefficient is varied to calibrate the model in Section 5.1.2. The Smagorinsky turbulence model is used for horizontal turbulent modelling with the mixing length model used for vertical turbulence.

5.1.2 Tidal water level

The model tidal output is calibrated against free surface elevation data from the UK National Tide Gauge Network, various locations around Liverpool Bay (Figure 5.6);

- Gladstone Dock, 53.4497°N, 3.0181°W
- Llandudno, 53.3317°N, 3.8252°W

- Alfred Dock, 53.4054°N, 3.0150°W
- Hilbre Island, 53.3847°N, 3.2289°W

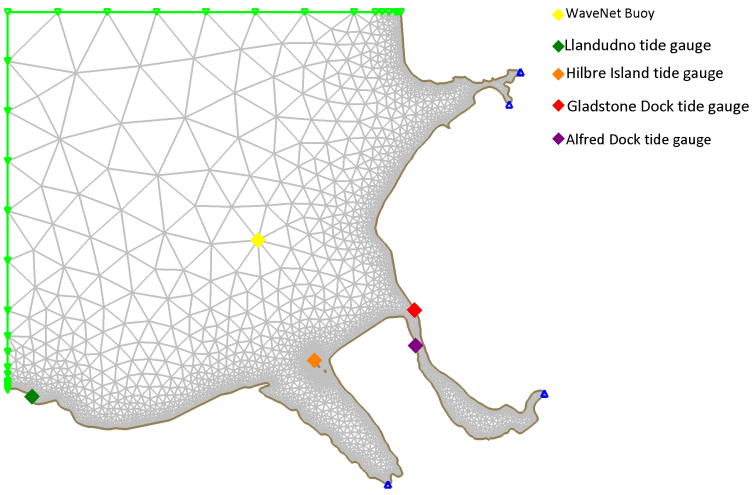

Figure 5.5: Liverpool Bay mesh boundary conditions, with tide gauge and wave buoy locations shown. The green line represents a model boundary with defined water depth, the blue line represents a boundary with the velocity defined

The model is run over a spring neap cycle, the comparison covers the period 30/08/2007 at 22.45pm, to 9/9/2007 at 6.15am, this time period was chosen as there is a large amount of coincident tide and wave data. Initially sensitivity testing is carried out with a scaling factor applied to the initial tidal constituents calculated by the tidal model driver, to calibrate against the tide gauge free surface height.

Figure 5.6 presents the model prediction compared with the free surface elevations at the four tide gauge locations. It should be noted that the tidal forcing used along the open boundary is based on long term equilibrium tidal constituents. When applied to the specific site, uncertainties associated with local bathymetry and meteorological conditions can lead to errors in the model prediction. To minimise these errors, various scaling factors are tested on the forcing boundary conditions.

The overall model predictions are in good agreement with the tide gauge data in all four locations. In particular, the tide gauges by the Mersey Estuary (Gladstone Dock and Alfred Lock) show the best agreement, with the only differences being a slight over prediction of the peak spring flood. The Llandudno and Hilbre Island locations both show a slight over prediction at the spring tides. This difference is partly due to the locations, the Llandudno site is very close to the boundary and the Hilbre Island site is behind the shadow area of the island with very shallow water, which affects model accuracy.

The root mean squared errors (RMSE) were calculated over 10 tidal cycles at each tidal gauge location, the errors were summed for each Scaling Factor to determine the best fit to the tide gauge data. Figure 5.7 presents the RMSE for the different tidal inputs, the smallest RMSE is seen at a scaling factor of 1, therefore from this testing it was not deemed necessary to use a scaling factor.

A sensitivity test was also carried out for different values of the Nikuradse bed friction factor to further calibrate the model predictions. Overall, the variations are small but an improvement in calibration was achieved. Figure 5.8 presents the root mean squared error for different bottom friction values. The smallest RMSE corresponds to a Nikuradse bottom friction value of 0.012, which is similar to values used in previous studies (Carroll, 2012).

Sea Surface Velocity

The sea surface currents for the 3D model run are calibrated against high frequency radar data covering Liverpool Bay (Howarth et al., 2007). The radar data was obtained from a phased average $13MHz$ High frequency radar, with two radar sites at Formby Point, located north of Liverpool, and at Abergele, situated along the North Wales Coast. These locations and radar frequency allow surface currents to be assessed up to $100km$, with data available in a grid like structure to cover the area. The model sea surface currents were calibrated against 4 sites near to the Burbo Bank wind farm location (Figure 5.9). The sea

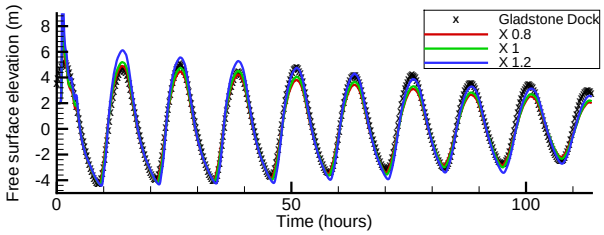

(a)

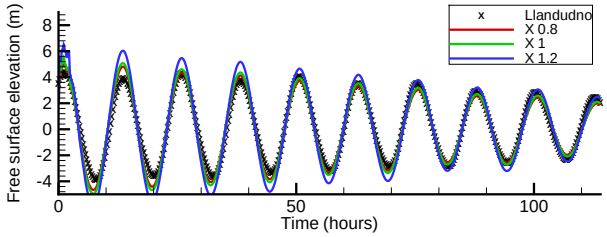

(b)

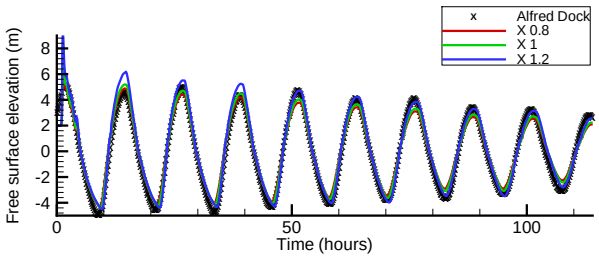

(c)

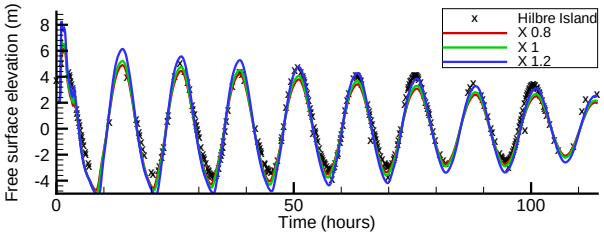

(d)

Figure 5.6: Tidal calibration comparing predicted free surface elevations with tide gauge data at 4 sites in Liverpool Bay, at a) Gladstone Dock tide gauge, b) Llandudno tide gauge, c) Alfred Dock tide gauge, d) Hilbre Island tide gauge. The tide gauge locations are presented in Figure 5.5. Data provided by the UK National Tide Gauge Network

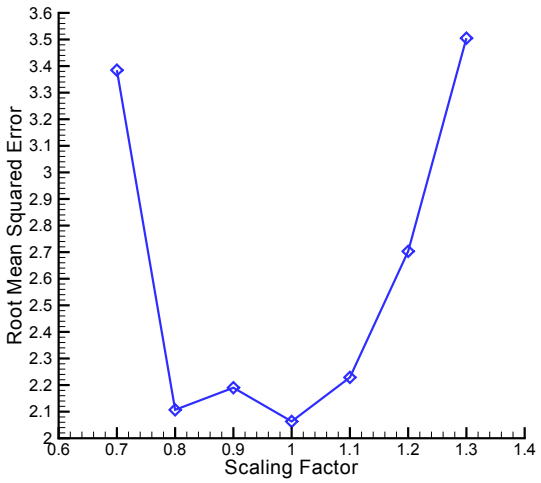

Figure 5.7: Root mean squared error for different scaling factors applied to the tidal input

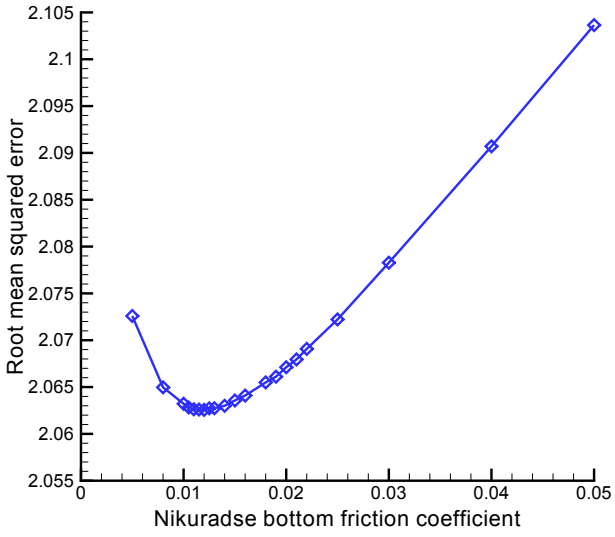

Figure 5.8: Root mean squared error for different Nikuradse bottom friction coefficients

surface from the model prediction is taken as the point at 0.99 water depth.

Figure 5.9 presents the measured and predicted sea surface velocity comparisons, for all sites the phase of velocity predicted by the model is in good agreement with the radar data. For Site 91 (Figure 5.9b) located near the edge of the mesh, the model slightly over-predicts the magnitude of the sea surface velocity at spring tides, with a better agreement during the neap tides. Conversely site 178 (Figure 5.9c) under predicts the sea surface velocity during the neap tides, but shows good agreement at the springs. Site 236 (Figure 5.9d) located closest to the wind farm site has very good agreement with the radar data across the spring-neap cycle. Site 294 (Figure 5.9e) is also located close to the wind farm site, here the model under-predicts the bursts in sea surface velocity seen in this region. Site 294 is located close to the dredged channel for the Mersey estuary, as the riverine discharge is taken as a yearly average for this model, variations in flow are not seen. Unfortunately, the river flow gauge was not in operation during this period so impact of the river flow on the sea surface velocity at Site 294 cannot be discussed.

It should be noted that all the surface velocity observations are subject to the wind at the site. However, in the model simulation, the wind effects are not included, which may influence the model prediction. Figure 5.10 presents the wind speed and direction at Hilbre Island for the calibration period. The wind direction is relatively constant during the period, whilst the wind speed shows an initial high wind speed decreasing over the time period, with some bursts of increased speed. The bursts in the wind speed correspond with some of the higher sea surface velocities seen at Site 294, which were under-predicted by the model (Figure 5.9e). Peaks of both wind speed and sea surface velocity at Site 294 are seen at the 8-9, 19, 44-45, and 57 hours, which helps explain the under predictions here. The uncertainties in the local bathymetry can also affect the model predictions in 3D current profiles as shown in previous studies (Carroll, 2012).

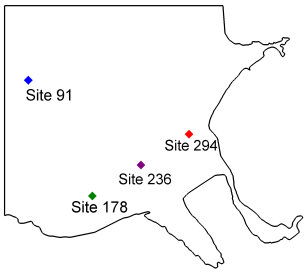

(a)

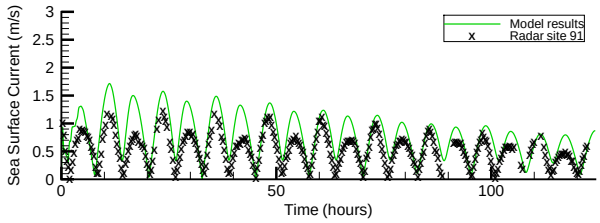

(b)

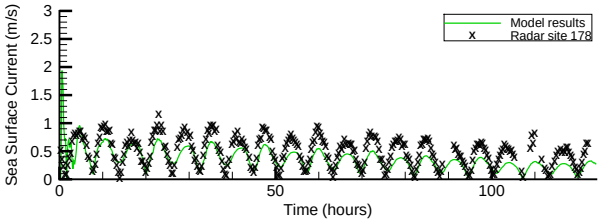

(c)

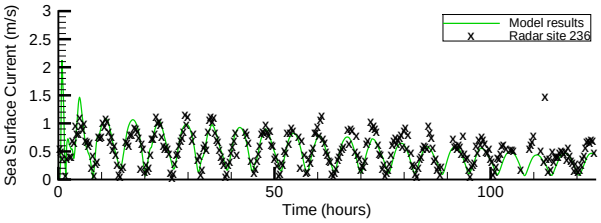

(d)

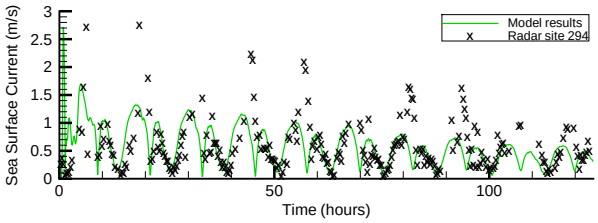

(e)

Figure 5.9: Comparison between high frequency radar sea surface velocity and predicted sea surface current at 4 locations in Liverpool Bay. The site locations are b) site 91, c) site 178, d) site 236 and e) site 294. Data provided by the National Oceanography Centre's Coastal Observatory (COBS)

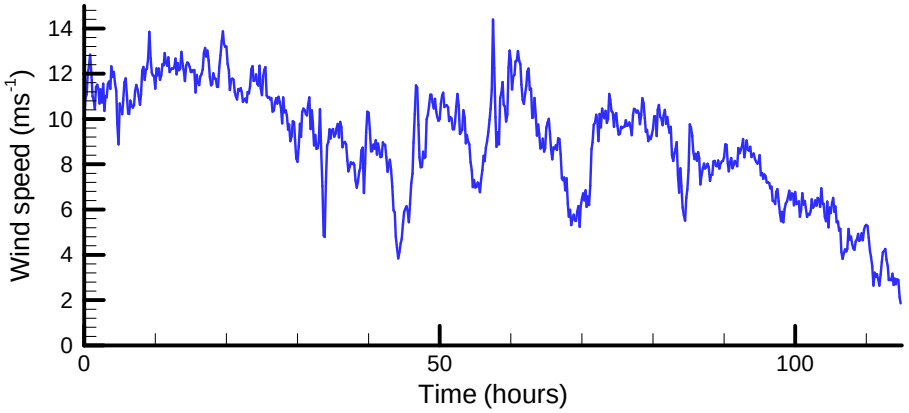

(a)

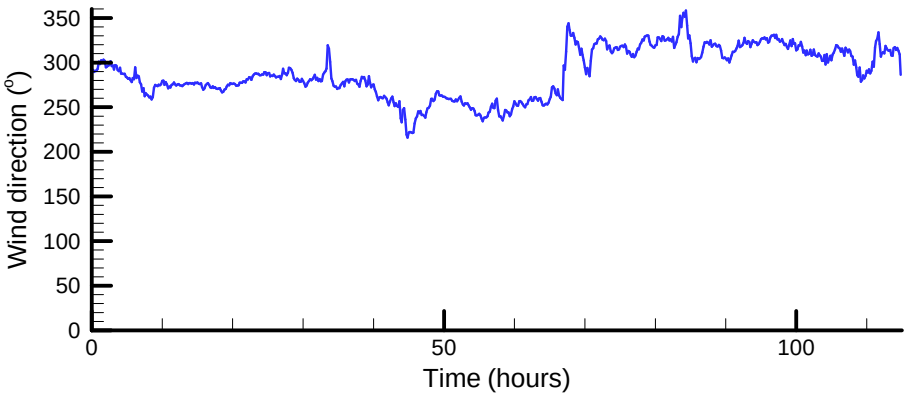

(b)

Figure 5.10: Wind conditions at Hilbre Island for the period 30/08/2007 - 04/09/2007. Presenting a) wind speed, and b) wind direction. Data provided by the National Oceanography Centre's Coastal Observatory (COBS)

5.1.3 Vertical velocity profile

To validate the models performance for 3D sediment suspension and transport predictions, it is necessary to calibrate the 3D velocity structure predicted by the model. The flow velocity profile is compared with available measurements completed by HR Wallingford during the Mersey Barrage Study (HR Wallingford, 1991*b*, 1992). A mean spring tide with a tidal range of 8.4*m* is used in this test. The computed flow velocity magnitude at the three locations (Figure 5.11) are compared with the observed data in Figure 5.12, 5.13 and 5.14, in which the solid lines are computed results and the symbols are measured data.

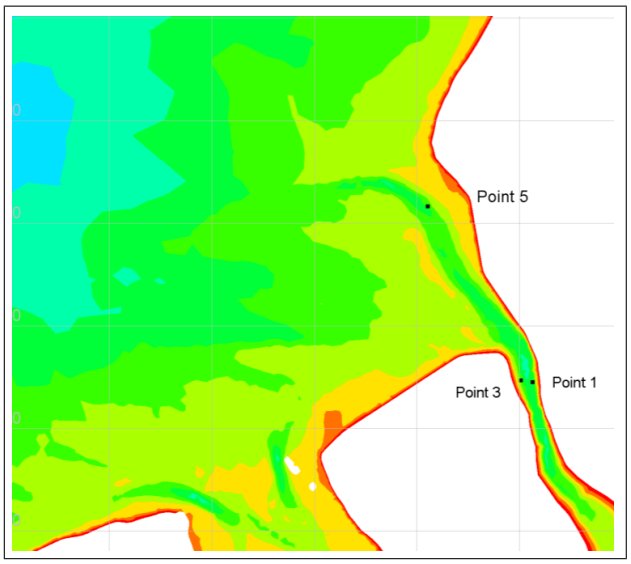

Figure 5.11: Observed measurement location for the flow velocity comparison in the Mersey Estuary and Liverpool Bay. After HR Wallingford (1991*b*, 1992)

It is clear that the predicted flow velocity across the depth at Position 1 and Position 3 in the narrows follow the measured data very well. The maximum peak flow speed at flood and ebb in both figures have been predicted fairly closely to the measured data. The model result also correctly simulated the asymmetry in the flood and ebb in both positions, i.e. the sharp increase in flow speed in the flood period and the prolonged increase and decreases of the speed in the ebb phase. In Figure 5.14 at Position 5, the model noticeably under-predicts the maximum ebb flow speed. In addition, the fairly quick drop of flow speed during

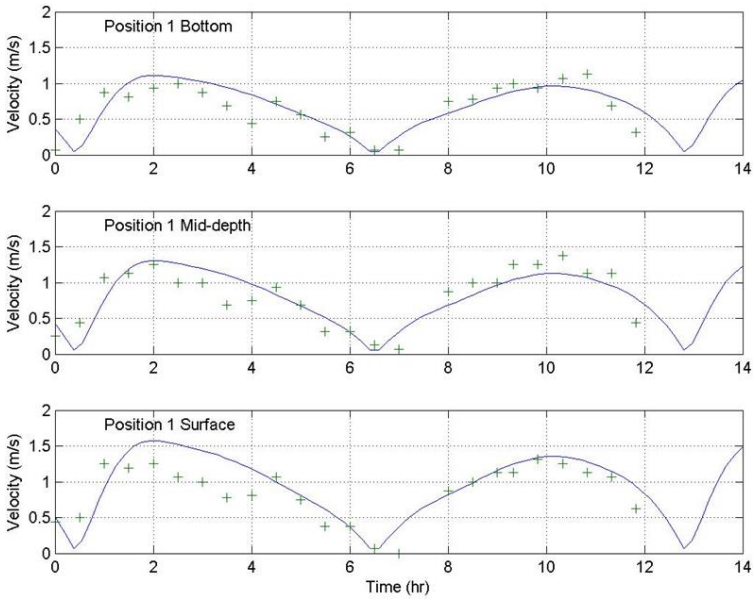

Figure 5.12: Comparison of computed and measured flow velocity at three levels above the bed at position 1 in the Mersey Estuary. After HR Wallingford (1991*b*, 1992)

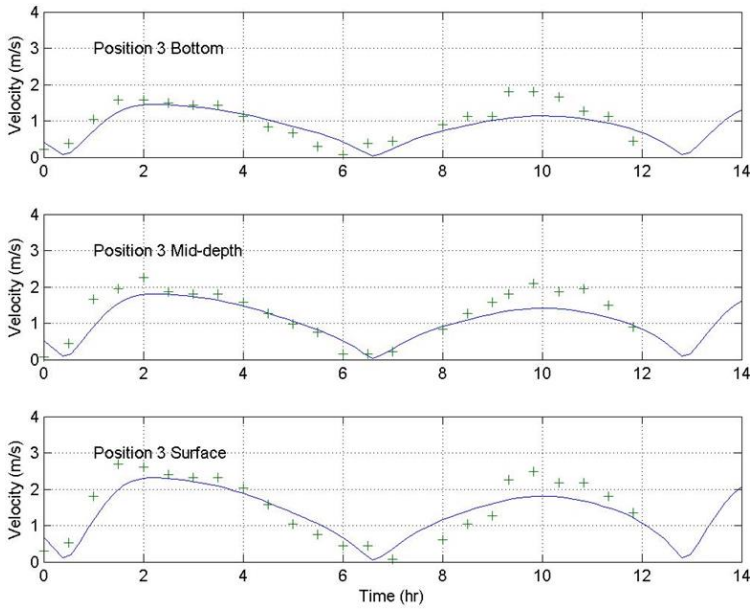

Figure 5.13: Comparison of computed and measured flow velocity at three levels above the bed at position 3 in the Mersey Estuary. After HR Wallingford (1991*b*, 1992)

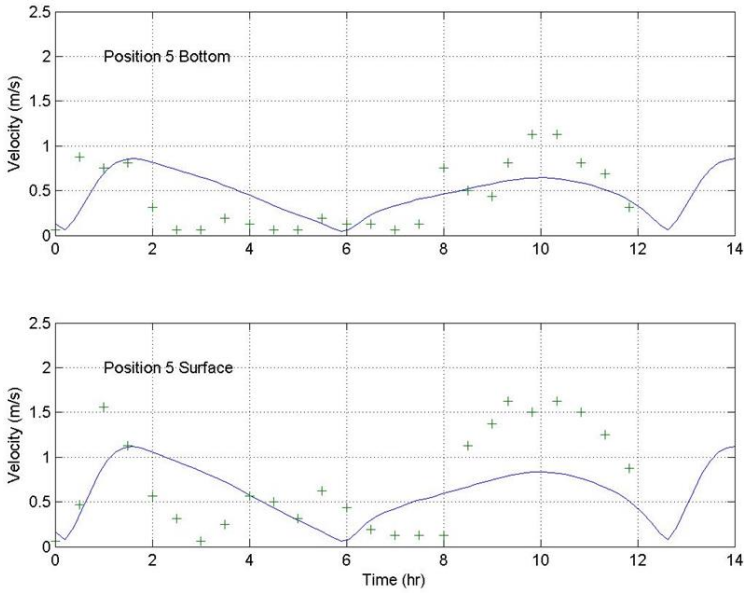

Figure 5.14: Comparison of computed and measured flow velocity at two levels above the bed at Position 5 in Liverpool Bay. After HR Wallingford (1991*b*, 1992)

the flood (i.e. $2hrs$ to $6hrs$) is also not seen in the model prediction. These differences can be contributed to the discrepancies in the bathymetry used in the model and the actual values. The bathymetry in the Mersey estuary has been surveyed fairly regularly and the model uses the more recent survey data. While in the Liverpool Bay, the bathymetry is still largely relying on the marine map that has been generated in the early 1970's. The surface wind effects could also influence the data, which is not included in the present simulation.

5.1.4 Waves and wind

The waves were calibrated by a model run with TELEMAC-3D coupled with TOMAWAC taking wave and current interaction into account. Dynamic waves were generated by applying time varying wave height, period and direction. The wave boundary used scaled data from a WaveNet buoy located in the centre of Liverpool Bay, at 53.6347N, 3.556W in $24m$ of water. A time varying wave condition is specified at each open boundary mesh point to represent the offshore storm propagating towards the shallow water. A constant wind is also applied to all the node points within the mesh. This wind is calculated by taking an

average wind velocity and direction over the calibration time frame, the wind velocity component along x is $2.85ms^{-1}$ and along y is $-6.75ms^{-1}$. The wind input and generation is modelled with Janssen's equation, a quasi-linear theory, which only takes into account exponential growth. White-capping is taken into account using the Komen et al. formula, and depth induced dissipation is included in the model with Battjes and Janssen's model.

Figure 5.15 presents the wave height, direction and wave period model predictions for different scaling factors of the wave height compared against the WaveNet buoy data (CEFAS). Similar to the tidal level comparison, various scaling factors have been applied to the offshore wave forcing, so that variations of the meteorological conditions during the test period can be taken into account. The wave height is scaled to generate the best fit to data at the WaveNet buoy site, as the wave properties evolve over the domain from the mesh edge. The model predicted values generally agree well with the data, the changes in height, direction and period are capable of being predicted by the model, particularly for the large storms at 10-20 hours, 60 hours and 80-90 hours. However, the reduction in wave height at 90 hours is delayed in the model prediction compared with observations. Similarly the rapid variation in the wave angle between 70-80 hours and 110-120 hours are not captured well by the model. This is possibly due to the quickly changing wind during the storms at the site, which is not included in the model simulation, similar to the findings in Wolf (2005).

The root mean squared error between model predictions for different scaled wave height input files and the wave buoy data are shown in Figure 5.16. The RMSE values show that the model predicts the wave height and period well. The wave direction RMSE values shows a lesser agreement between measured and predicted values. This is due to the time shift in the model prediction results, as the model is slow to pick up the rapid changes in wave direction. The wave height, direction and period all show a lower RMSE at scaling factors of 1.1 to 1.5, a scaling factor for the wave height of 1.3 is therefore chosen for future use.

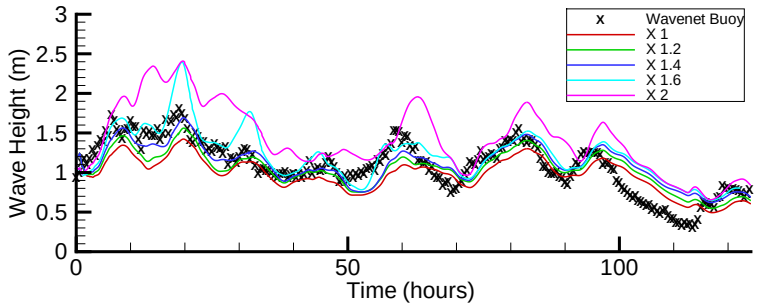

(a)

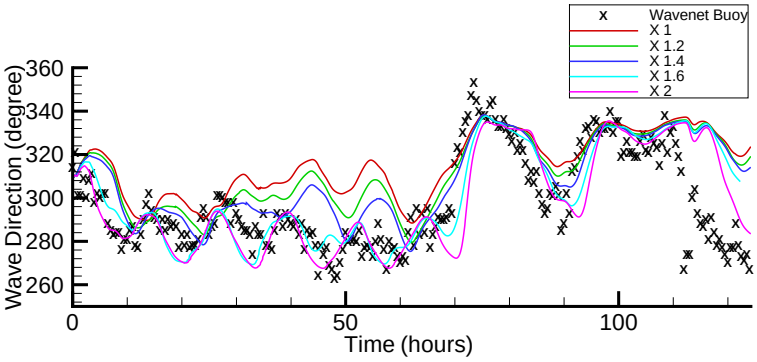

(b)

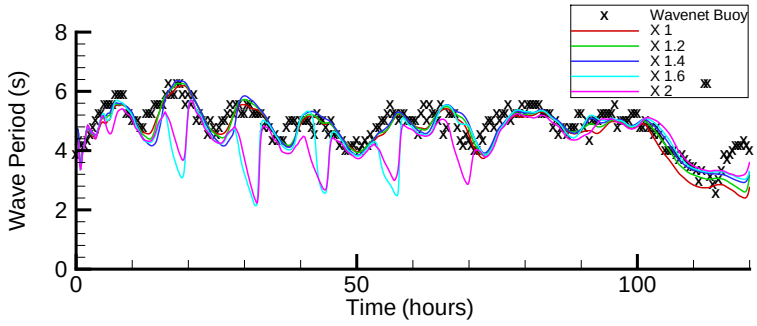

(c)

Figure 5.15: Comparison of model prediction with different scaling factors, with measurements from the WaveNet buoy in Liverpool Bay for a) significant wave height b) wave direction and c) wave peak period. Data provided by CEFAS

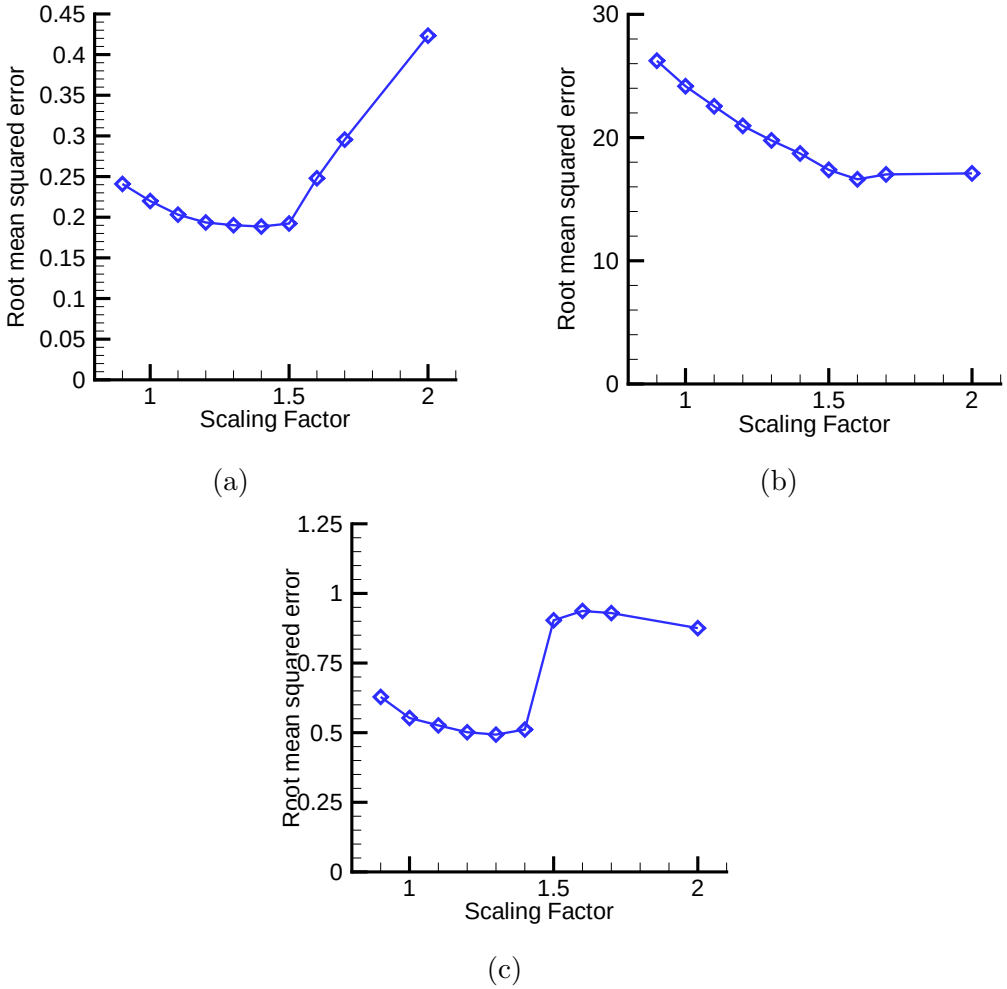

Figure 5.16: Root mean squared error for different scaling of the wave height input for a) significant wave height, b) wave direction, and c) wave peak period. Data provided by CEFAS

5.1.5 Sediment transport

Sediment transport rate

The sediment transport rate prediction is examined through comparison with sediment flux data from the Mersey Estuary, at the Narrows near the estuary mouth. The data was obtained from HR Wallingford (1991*a*), and consists of hydrodynamic and sediment data. The sediment flux was determined over both a neap and spring tidal cycle in calm conditions by use of a sediment sampler, current metre and bed sampling frame to determine the bed datum, measurements are every 30 minutes. The model was run for a tide only case, as the sediment data was collected at calm conditions and the Mersey Estuary is influenced more by tides than waves. The Soulsby-van Rijn formula was used to calculate the sediment transport.

Calibration of sediment grain size was completed using the sediment flux measurements in the Mersey estuary for the neap tide. Figure 5.17 presents the model predicted sediment flux for model runs with sediment grain sizes of $d_{50} = 0.2mm$, $0.22mm$, $0.25mm$, $0.3mm$ and $0.4mm$. The peak fluxes of sediment are well predicted by the model at 0-1 hours and 12 hours. However, the peak sediment flux at 6 - 9 hours occurs earlier in the tidal cycle in the model predictions than the measured sediment flux. The predicted sediment flux magnitude, shows greatest agreement with the measured data for the model run with a mean grain size of $0.22mm$. The whole domain was therefore given a constant grain size of $d_{50} = 0.22mm$ for the future model runs.

Figure 5.18 presents the sediment flux over the spring and neap cycle. The spring cycle case shows a good agreement with the observations in both magnitude and phases of the sediment flux peaks. The agreement for the neap condition shows a good agreement with the magnitude of the sediment flux over the tidal cycle (Figure 5.18b). However, a time shift is seen in the predicted sediment flux during the ebb phase to low water at 10 hours. The model predicts an increase in sediment earlier in the tidal cycle than the measured data. This time difference of the sediment transport peak is likely to be due to the sensitivity of the

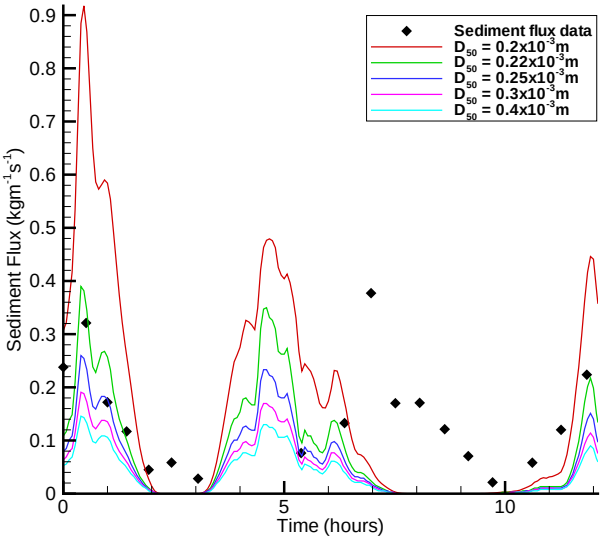

Figure 5.17: Comparison of measured sediment flux within the Mersey Narrows at a neap tide, and model predicted sediment flux for different d_{50} grain size diameters. Measured data from HR Wallingford (1991a)

predicted flow to the river bathymetry. The water level is low at this time of the tidal cycle, in shallow water the flow velocity is influenced by water depth, as the volume of water must travel through a smaller area. A slight difference in depth between the bathymetry at the measured time period and the model bathymetry can change when the peak velocity occurs, and therefore when sediment transport occurs. It should be noted that the magnitude of the fluxes during the neap tide is two orders of magnitude smaller than at the spring tide. The overall agreement is therefore considered to be satisfactory as the broad trend and magnitudes are reproduced by the model.

Vertical sediment profile

The model computed sediment concentrations at various phases of the tide are compared with the measurements from a Mersey tidal barrage feasibility study completed by HR Wallingford (1991a). Suspended sediment concentration were collected at Point A (Figure 5.19) within the Mersey estuary under a mean spring tide at several heights above the bed. The model was set-up according to the experimental conditions, with a mean spring tide range of $8.4m$. The sediment

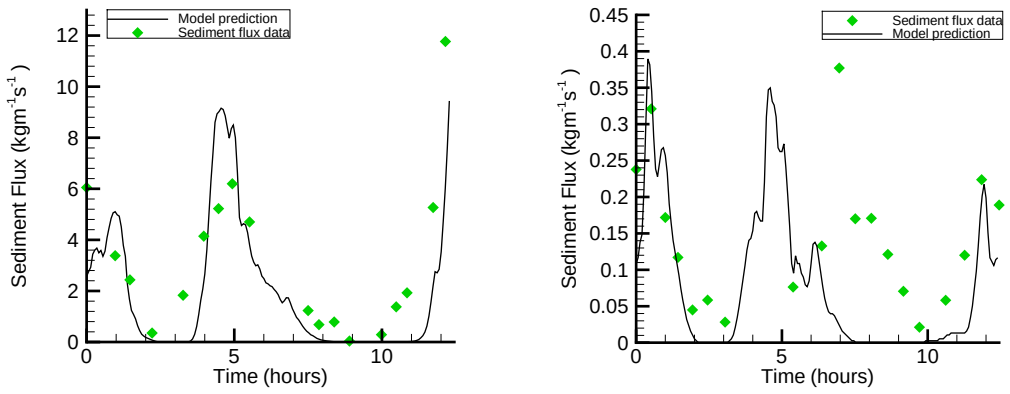

(a) (b)

Figure 5.18: Sediment flux within the Mersey Narrows for a) spring tide and b) neap tide. Data obtained from HR Wallingford (1991*a*)

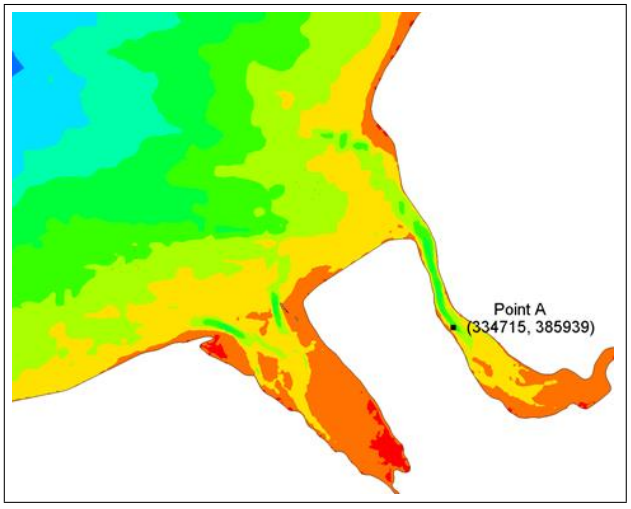

Figure 5.19: Position of the suspended sediment concentration sampling point A in the Mersey Estuary. From HR Wallingford (1991*a*)

particle size is assumed to be uniform of $0.22mm$ across the whole area. The model was run with 15 depth layers over two tidal cycles and the results were collected during the 2nd tidal cycle.

Figure 5.20 presents the computed and measured flow velocity and suspended sediment concentrations at Point A, across the water depth over different phases of the tidal cycle. In general the model predicts the flow velocity very well throughout the tidal cycle. The model under-predicts the suspended sediment concentration at the maximum ebb phase of the tide (Figure 5.20b). At the maximum flood (Figure 5.20f) there is good agreement between predicted and measured values. At slack water (Figure 5.20h) there is an over-prediction of suspended sediment concentration near to the bed. The differences seen between the measured and predicted values are partly due to the variations in sediment particle sizes in suspension over the tidal cycle, as the model uses a uniform grain size. Overall the agreement is considered to be good.

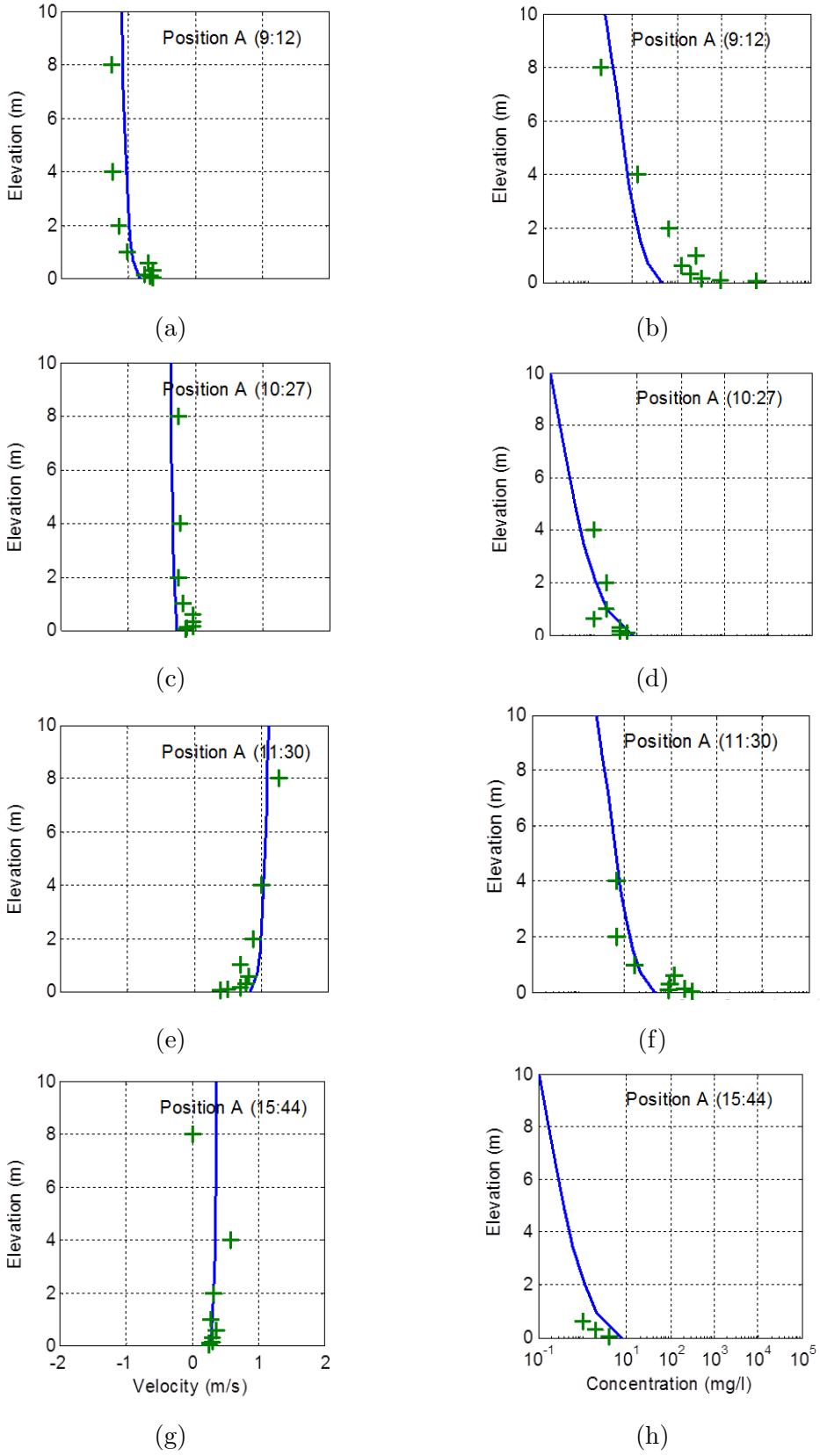

Figure 5.20: Comparison of predicted and measured flow velocity and suspended sediment concentration at different heights above the bed at Point A over various phases of a spring tide. The solid lines denote the computed values and the symbols are for the measured data. Data obtained from HR Wallingford (1991*a*)

5.2 East Anglia

The Scroby Sands wind farm, located in the south eastern area of the North Sea, off the coast of East Anglia, has been chosen as the second test site (Figure 5.21). The area represents an open coast site, and is a dynamic location with complex bed features. It is generally considered to be a worst case scenario location for predicting wind farm impacts. The Scroby Sands wind farm sits on the Middle Scroby sandbank, it consists of 30 wind turbines with $4.2m$ diameter monopile foundations, over an area of $4km^2$ (Rees et al., 2006). The wind farm has a minimum distance to the shore of $2.3km$ and the turbines are spaced a minimum of $320m$ apart. Scroby Sands was developed by E.ON UK, and has been generating since July 2004 with a capacity of $60MW$.

There are two sandbank systems within this area the Norfolk Banks, and to the south the Great Yarmouth Sandbanks. The Scroby Sands sandbank is part of the Great Yarmouth sandbanks and runs in North-South direction, approximately $2km$ from the coast. It is made up of three parts with channels between, these are North, Middle and South Scroby (Thurston, 2011). At Sea Palling, to the north of the wind farm site a series of nine shore-parallel breakwaters have been built to prevent beach erosion.

The tides are primarily in a north - south direction, with the flood tide running almost shore parallel. There is an amphidromic point in the southern North sea between the coasts of East Anglia and The Netherlands, the mean tidal range is $2-2.5m$ depending on location along the coast. Storm surges occur in the area particularly from the north and the coastline is susceptible to flooding (Heaps, 1983). Waves within the area are moderate and mainly from the North East.

Within the south-eastern North Sea the sediment is typically of a medium grain size, and the seabed has a range of bedforms including sand ripples, sand waves and sandbanks. There is a complex recirculation of sediment between inner and outer sandbanks (HR Wallingford et al., 2002), due to residual flows from gyre formations at the sandbanks (Horrillo-Caraballo and Reeve, 2008). Long-

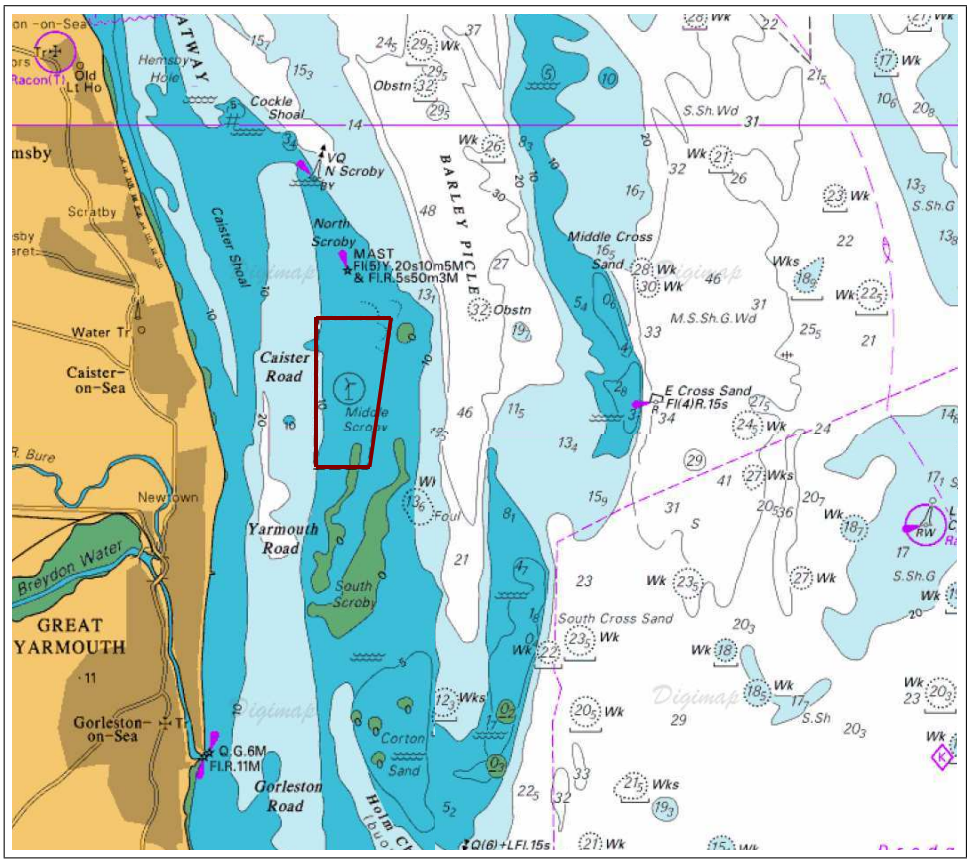

Figure 5.21: Sea bed features map off East Anglia with Scroby Sands wind farm highlighted by the red rectangle, (EDINA Digimap)

shore drift also plays a part in the sediment transport within the area by moving coarse grains towards the south (Reeve et al., 2001). The sandbank system is a dynamic system, the Scroby Sands sandbank is believed to have migrated $1km$ northwards since 1866 (Horrillo-Caraballo and Reeve, 2008). At the wind farm site the wind turbine monopiles have created very large scour formations including scour pans, and wake scour (Rees et al., 2006).

5.2.1 Model set up

The East Anglian mesh is comprised of 6474 elements for the 2D case. The smallest elements of $20m$ are found surrounding the Sea Palling breakwaters, and the largest element are $7km$ at the edge of the mesh (Figure 5.22). As for the Liverpool Bay mesh the depth is divided into 13 depth layers for 3D model runs, which produces a mesh size of 84162 elements.

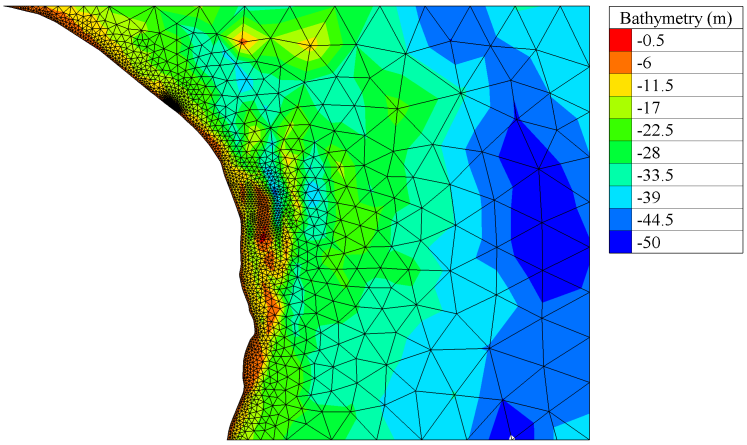

Figure 5.22: East Anglia finite element mesh with bottom bathymetry shown

The mesh bathymetry was compiled with data from the British Geological Survey, and from the LEACOAST 2 survey project for the area around the Sea Palling breakwaters (Wolf et al., 2008). Figure 5.23 presents the boundary condition for the East Anglian Mesh. The three open coast sides of the mesh have an imposed water depth as calculated by the Tidal Model driver, and free velocities and tracers.

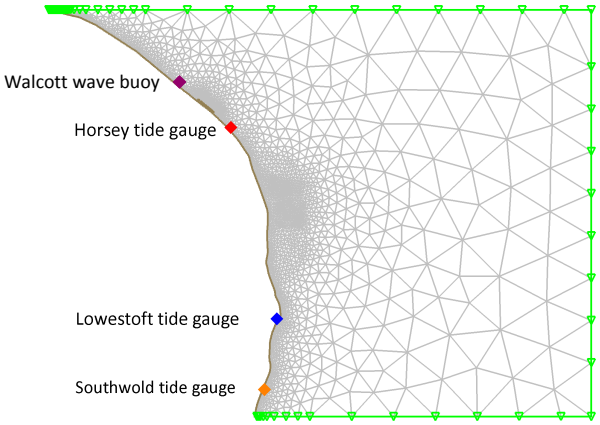

Figure 5.23: East Anglia mesh boundary conditions with tide gauge and wave buoy locations highlighted

5.2.2 Tidal water level

Data from the UK National Tide Gauge Network at the Lowestoft tide gauge, and water depth measurements from wave buoy data at Horsey and Walcott (Figure 5.23) are used to calibrate the model against tidal free surface elevation. The model was run for a period of 10 tidal cycles and calibrated against the data from a start time of 8.00am 8/4/2008. Figure 5.24 presents the comparison of the free surface elevation at these sites, with scaled tidal elevation input data. At the Horsey site, located to the North of Scroby Sands wind farm, the free surface elevation height shows good agreement with the measured data. At this site the model shows a phase shift in the tidal wave, this is likely due to the amphidromic point off the coast of East Anglia, which is difficult to replicate in the model. For both the Lowestoft and Southwold sites the model predicted tidal free surface elevation is in phase with the tide gauge data, and the free surface magnitude is well represented.

Figure 5.25 shows the calculated RMSE error at the Lowestoft and Southwold sites for the model runs with a different scaling factor on the tidal water height input. At these locations the model prediction shows the best fit with the measured data for an input with a scaling factor of 1.2.

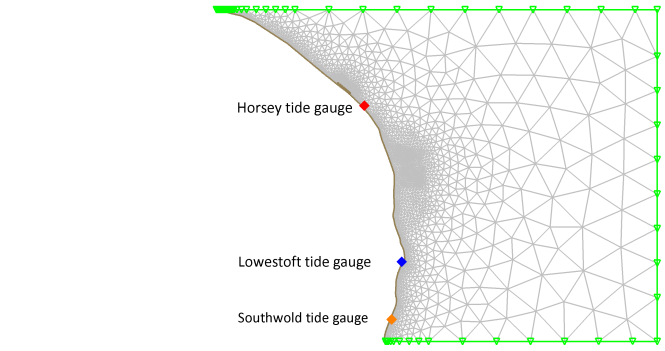

(a)

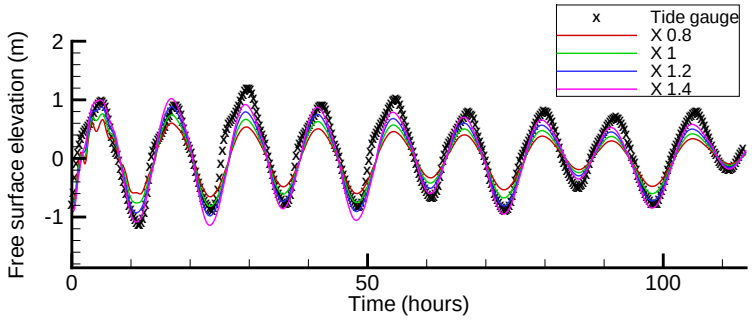

(b)

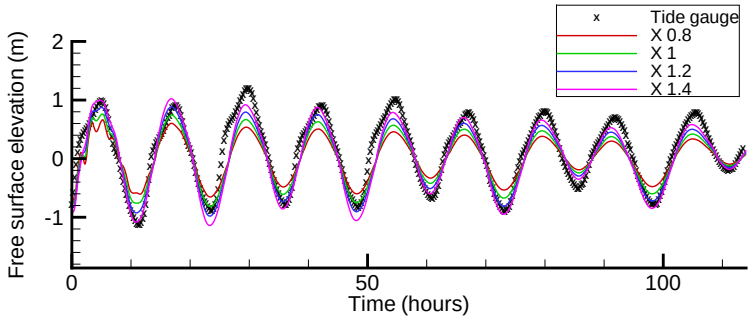

(c)

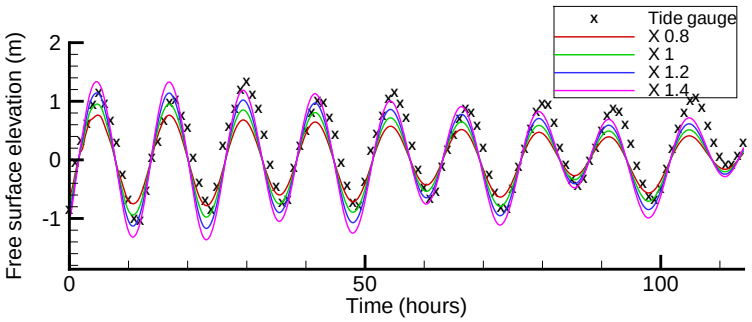

(d)

Figure 5.24: Comparison between predicted free surface elevation and tidal gauge data at 3 sites off East Anglia. At b) Horsey c) Lowestoft, and d) Southwold. Data provided by the UK National Tide Gauge Network

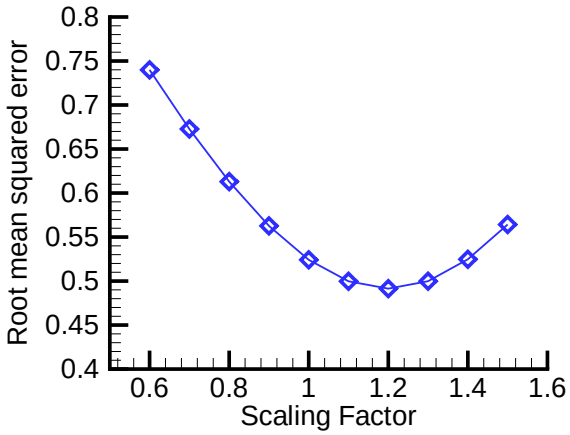

Figure 5.25: Sum of the root mean squared error at the Lowestoft and Southwold sites for different tide input scaling

A sensitivity test was carried out for different values of the Nikuradse bottom friction coefficient. The bottom friction coefficient was found to only make slight changes to the model prediction at the tide gauge and wave buoy sites. Figure 5.26 presents the root mean squared error for model predictions with different bottom friction values. The bottom friction coefficient with the best fit in this case is 0.03, which will be used in all future runs.

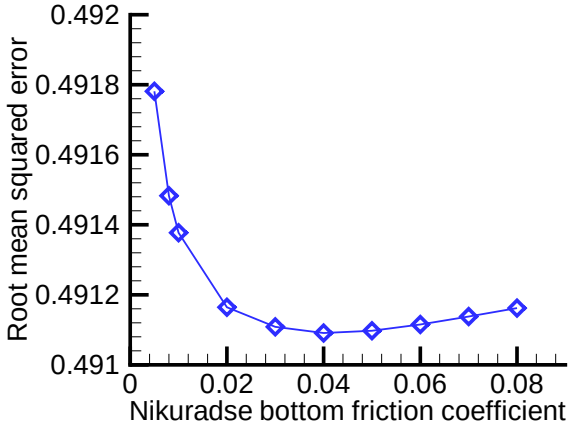

Figure 5.26: Sum of the root mean squared error at the Lowestoft and Southwold sites for different Nikuradse bottom coefficients

5.2.3 Waves and wind

The wave buoys at Horsey and Walcott are used to calibrate the East Anglian TOMAWAC model. As there are no offshore wave buoys in this domain, the data from the Horsey wave buoy is used as the wave input for the model. These values are applied at each edge node and are constant throughout the site. The model input is varied by scaling the wave height in order to obtain the closest model predictions. A constant wind is applied across the domain, calculated as an average over the model run period. The wind velocity values are calculated as wind component along $x = -9.667ms^{-1}$ and along $y = 5.708ms^{-1}$. The wave buoys in this area are in shallow water, which makes both water depth and the calculation of breaking dissipation very important for correct model prediction. For this site the Thornton and Guza depth induced breaking formula (Thornton and Guza, 1983) gave the best agreement with the wave buoy data.

The measured wave height, direction and period at the Horsey and Walcott wave buoys are compared with the model prediction from different scaled inputs in Figures 5.27 and 5.28. For both the Horsey and Walcott buoys the wave height magnitude is generally well predicted, although there is a time difference between measured and predicted values at the peak wave heights. The wave directions, which are taken as an area average, and the wave period agree less well. The wave direction model prediction shows less variation over the tidal cycles than is seen in the model results. The wave period model prediction doesn't include some of the sudden changes in period after 50 hours. This is likely to be due to the very shallow location of the wave buoys, where the wave diffraction and reflection are likely to be significant, and also due to the wind variation as a constant wind is applied to the model. The wind conditions over the same time period are presented in Figure 5.29. There is an increase in wind speed after 50 hours which corresponds with the sudden changes in wave direction and wave period seen at both Horsey and Walcott, suggesting that the stronger winds are modifying the wave conditions at the wave buoy locations.

A calculation of the sum of root mean square error for just the wave height

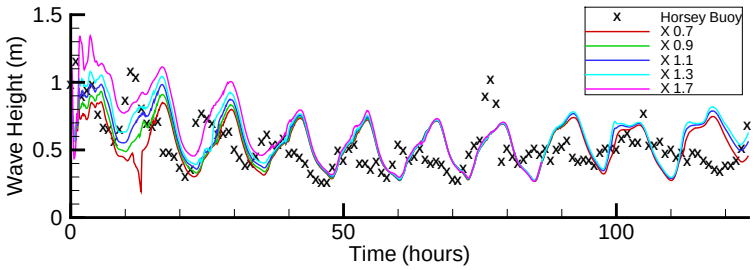

(a)

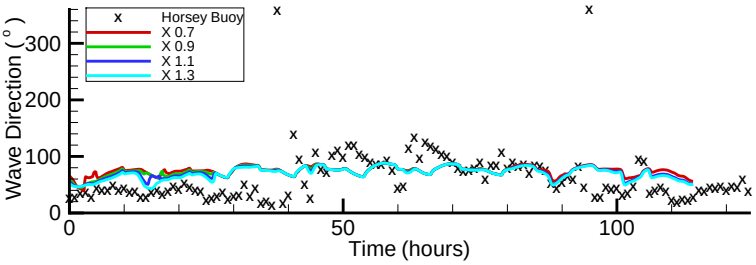

(b)

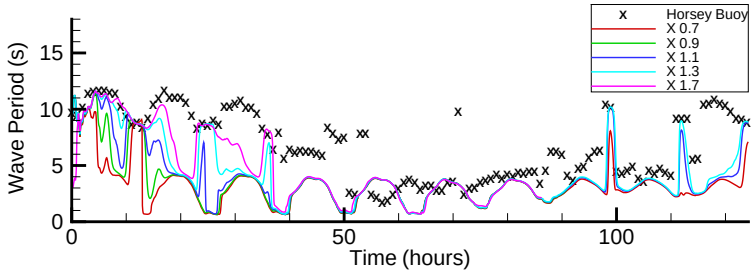

(c)

Figure 5.27: Comparison of model prediction at different scaling factors with the Horsey Wave Buoy, for a) wave height; b) wave direction; and c) wave period. Data provided by the Environment Agency

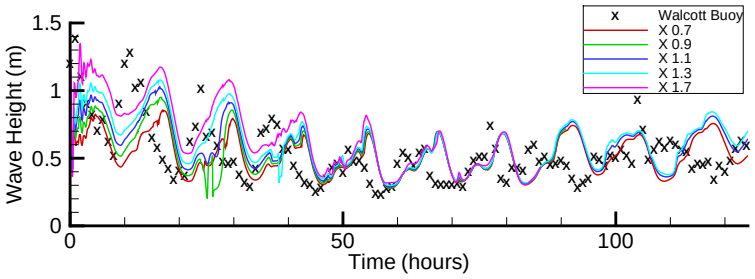

(a)

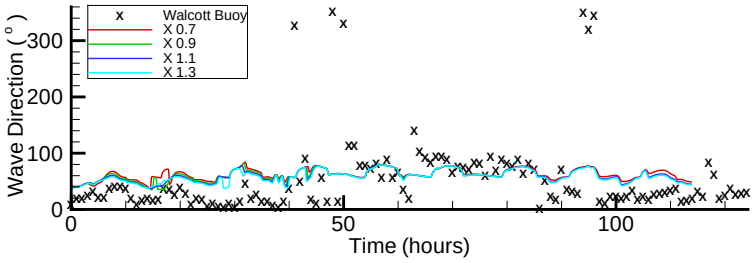

(b)

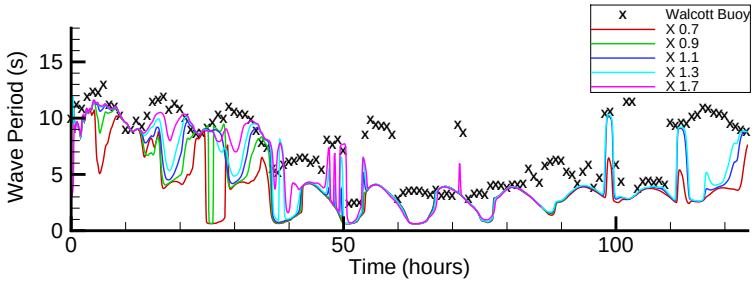

(c)

Figure 5.28: Comparison of model prediction at different scaling factors with the Walcott Wave Buoy, for a) wave height; b) wave direction; and c) wave period. Data provided by the Environment Agency

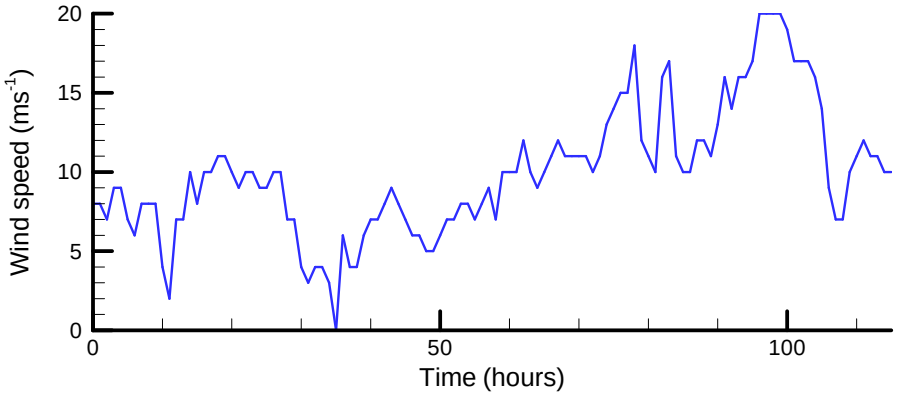

(a)

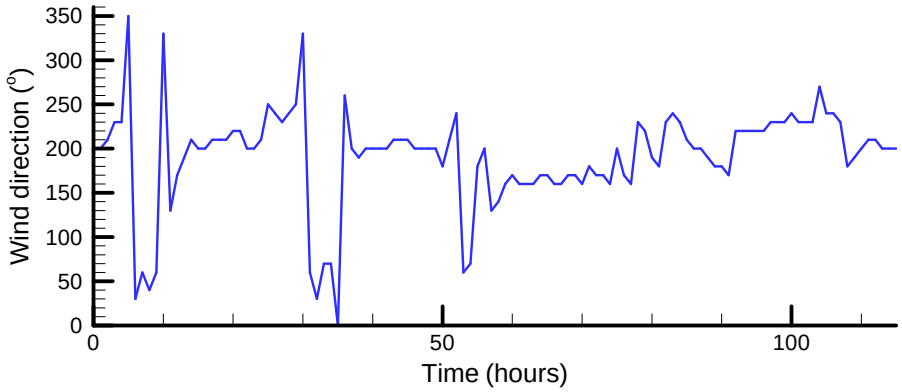

(b)

Figure 5.29: Wind conditions at the Horsey wave buoy for the period 30/08/2007 - 04/09/2007. Presenting a) wind speed, and b) wind direction

at both wave buoys suggests a scaling factor of 1.1 produces the closet values to the wave buoy data, as presented in Figure 5.30.

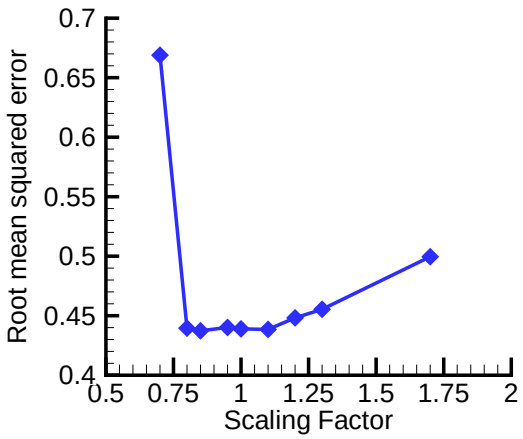

Figure 5.30: Root mean square error for different scaling factors of the wave height boundary input

5.2.4 Sediment Transport

Suspended transport flux

The predicted sediment transport flux at the Sea Palling breakwater is compared with observed suspended particulate matter data that was collected by the LEACOST-2 Project (Bolaños et al., 2012). The data was measured with an acoustic backscatter sensor at various locations around the breakwater structure. The model is compared against a site located on the seaward side of the breakwater system, over two tides from 8.00pm 5/12/2006. The model is run with wave data for the time period included.

The predicted sediment flux data at Sea Palling for different d_{50} mean grain size diameters are presented in Figure 5.31. The Sea Palling site sediment flux is very sensitive to grain size variation, with large flux differences between the grain sizes. For all the model predictions the sediment flux peak occurs slightly later in the tidal cycle than the measured data. This time shift in the sediment flux peaks is consistent with the phase shift seen at the free surface in Figure 5.24. The best agreement between predicted and measured sediment flux data

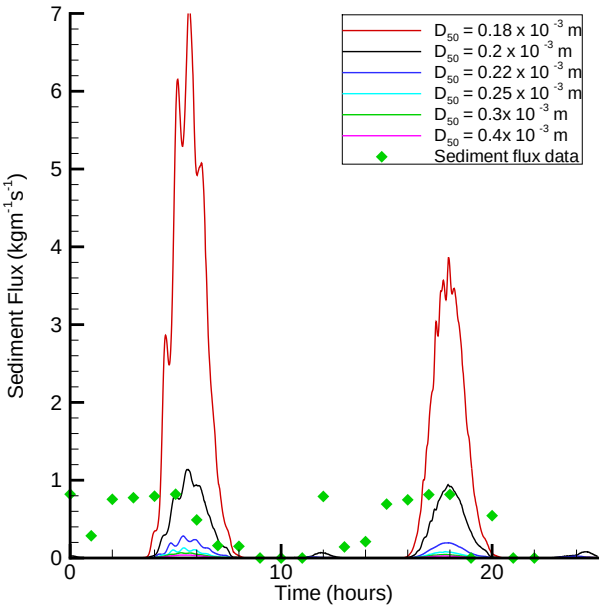

Figure 5.31: Comparison of measured sediment fluxat the Sea Palling breakwater and model predicted sediment flux for different d_{50} grain size diameters. Data obtained from Bolaños et al. (2012)

occurs with a model d_{50} grain size of $0.2mm$, this value is therefore used in all subsequent model runs.

The sediment flux for the model run with $d_{50} = 0.2mm$ is compared with the measured flux in Figure 5.32. There is a good agreement with the sediment flux magnitude over the two tides, but the slight time shift of the peak flux is seen. The time shift in the peak flux is due to a similar time shift in the free surface elevation predictions. The Sea Palling site is a very shallow area where slight differences in the water depth from the real bathymetry and model bathymetry will influence the hydrodynamics and therefore the sediment flux. Given these uncertainties, the sediment flux predictions show good agreement with the measured flux.

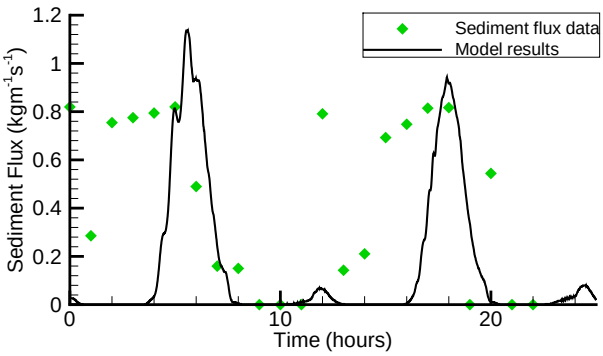

Figure 5.32: Sediment flux data from the Sea Palling breakwater compared against modelled prediction. Data obtained from Bolaños et al. (2012).

Chapter 6

Short term impacts

In order to assess the impact of the offshore wind farm on coastal processes, the model results over one tidal cycle are analysed in detail at both the Burbo Bank and Scroby Sands site. The coupled model of TELEMAC-3D, TOMAWAC and SISYPHE are run for meshes with no wind farm present, and with a wind farm represented in the mesh, to assess the impact of the wind farm to the coastal environment.

With the ability to represent the monopiles in the mesh, the impact in the short term at the individual structure scale on the tidal flow, waves and sediment transport is assessed. The computed results are also analysed at a regional scale, and common features for both sites are identified, including the wind farm acting to block the flow. At both sites the presence of the wind farm is shown to influence the large scale coastal sediment transport pathyways, and therefore coastal morphology.

The results presented here concentrate on the short term period, over one tidal cycle. The potential long term impacts, over a period of a year, are discussed in the following chapter.

6.1 Liverpool Bay

6.1.1 Burbo Bank OWF

The Burbo Bank Offshore Wind Farm consists of 25 wind turbines, each turbine is supported by a monopile with a diameter of $5m$. The site is located on the Great Burbo Flats within Liverpool Bay. The sediment type is fine to medium sand, a mean grain size of $0.22mm$ is applied to the whole domain.

6.1.2 Model settings

The model was applied to the Liverpool Bay site for conditions with and without the wind farm, over a mean neap and mean spring tide. The tidal amplitude is determined from tidal range values from the year 2007, with tidal ranges of $4.12m$ for neap and $8.94m$ for spring tides.

In addition to the tide, the wind-induced surface waves are also important for sediment dynamics. For the short term impact assessment, the aim is to determine the impacts of the offshore wind farm on the coastal processes under extreme conditions. A set of *worst case conditions* have therefore been selected for the model runs. These wave conditions were defined using a year of field records from 01/01/2007 - 31/12/2007 at the Liverpool Bay WaveNet site as presented in Figure 6.1. At this location the dominant wave direction is in the range $255 - 345°$, with the greatest heights also associated with this direction range.

To determine the *worst case* wave conditions, the wave records were initially grouped into wave direction ranges of 30°. The dominant wave directions were then determined as seen in the wave rose (Figure 6.1) as $285°, 315°, 255°$ and $345°$. Within each of these wave range categories the maximum wave height was determined with the associated wave period, the chosen wave conditions for model runs are presented in Table 6.1. All the model test run conditions and names for the model runs with and without a wind farm present are shown in Table 6.2.

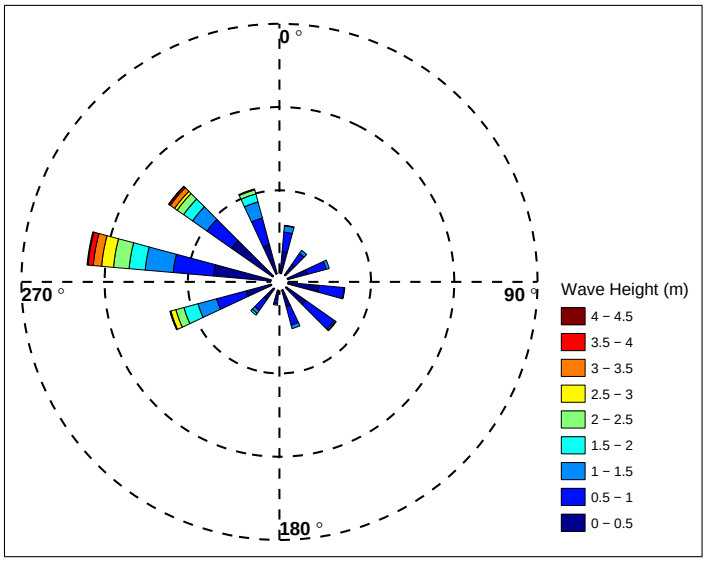

Figure 6.1: Wave rose for Liverpool Bay over the year 2007, recorded at the Liverpool Bay WaveNet Buoy. Data provided by CEFAS

Number	Wave Direction (°)	Wave Height (m)	Wave Period (s)
1	285	4.22	9.09
2	315	4.00	7.69
3	255	3.61	7.69
4	345	2.83	7.14

Table 6.1: Worst case wave conditions chosen for model runs in Liverpool Bay

Name	Conditions
N	Neap tide only
N1	Neap tide coupled with wave 1
N2	Neap tide coupled with wave 2
N3	Neap tide couple with wave 3
N4	Neap tide couple with wave 4
S	Spring tide only
S1	Spring tide coupled with wave 1
S2	Spring tide coupled with wave 2
S3	Spring tide couple with wave 3
S4	Spring tide couple with wave 4

Table 6.2: Model run conditions for Liverpool Bay

6.1.3 Far field impacts

As discussed in Chapter 5, Liverpool Bay is a relatively shallow region with depths of up to $50m$. Figure 6.2 presents the bathymetry over the whole of Liverpool Bay, with the wind farm site highlighted. Within the region the depth gradually decreases towards the Mersey Estuary. The Burbo Bank wind farm site is located in a region of 5 to $15m$ depth. To the North and East of Burbo Bank OWF are sandbanks (Figure 6.3), with a dredged channel beyond the sandbanks. Liverpool Bay's tidal flow is flood dominated with a peak flood tidal direction of 127.4° and a peak ebb tidal direction of 307.4°.

Waves

The wind-induced surface waves within Liverpool Bay play an important role in transporting sediment within the region. With the presence of the wind farm turbine structures, the wave propagation is affected through diffraction and reflection around individual monopiles. The spectral distribution can also be affected as shown in previous studies, Ponce de León et al. (2011), Alari and Raudsepp (2012), and Gandara and Harris (2012). These changes can, to some extent, lead

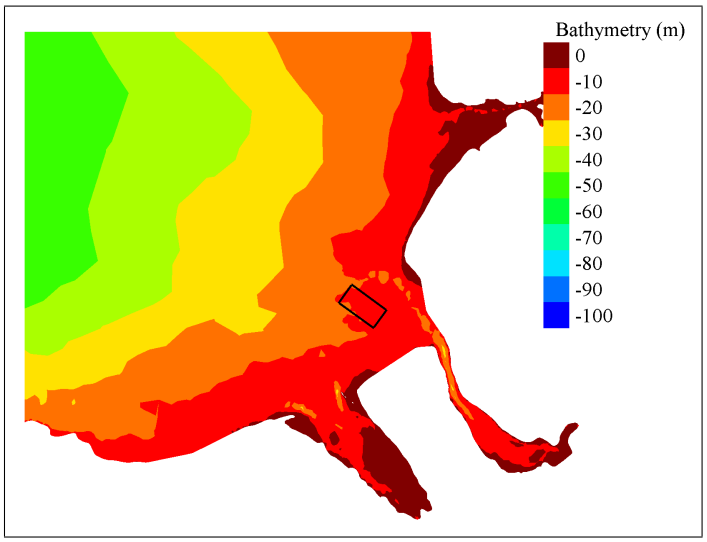

Figure 6.2: Bathymetry of Liverpool Bay with the wind farm location and sampling points highlighted

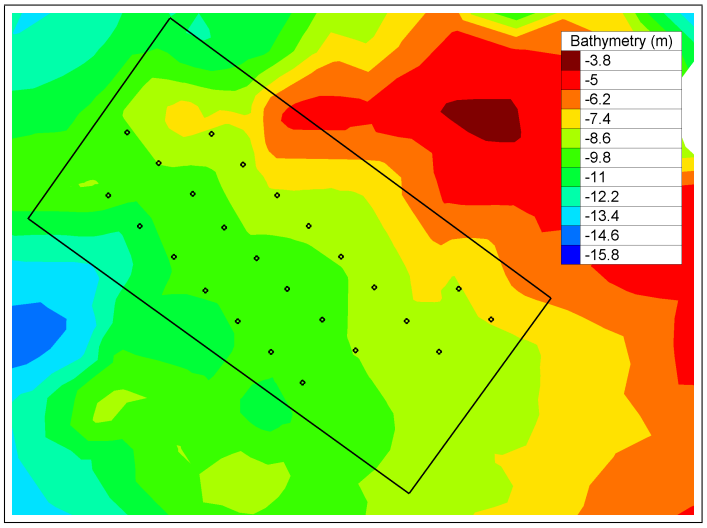

Figure 6.3: Bathymetry at the Burbo Bank wind farm site in Liverpool Bay with the wind turbine monopiles highlighted

to modifications of hydrodynamics and sediment transport at the site. Another important effect of the wind farm is the direct modification of the wind field at the site, which results in a reduction of wave height and modification of wave angles, as shown by Gandara and Harris (2012). However, due to the complex interactions between the wind and turbine operations, the precise changes of the wind field are still not fully understood. Therefore, the interaction of the wind and turbine is not included in the study, although it is an area for future research.

The wave heights and direction vectors for the wave 1 condition at a spring tide, are shown in Figure 6.4 across the Liverpool Bay area at two phases of the tide; peak flood velocity and slackwater. It can be seen that wave height across Liverpool Bay follows a similar pattern over the tidal cycle. The greatest wave heights are seen offshore, the wave directions here are constant. As the water depth decreases the wave amplitudes become smaller, and at very shallow water depths the waves are scattered and the direction is variable. During the slackwater phase of the tide (Figure 6.4b) the wave heights are slightly greater closer to the shore, than during the flood phase. In the regional scale the wave direction is slightly shifted in a clockwise direction at the wind farm site, this shift is seen further at the location of the dredged channel.

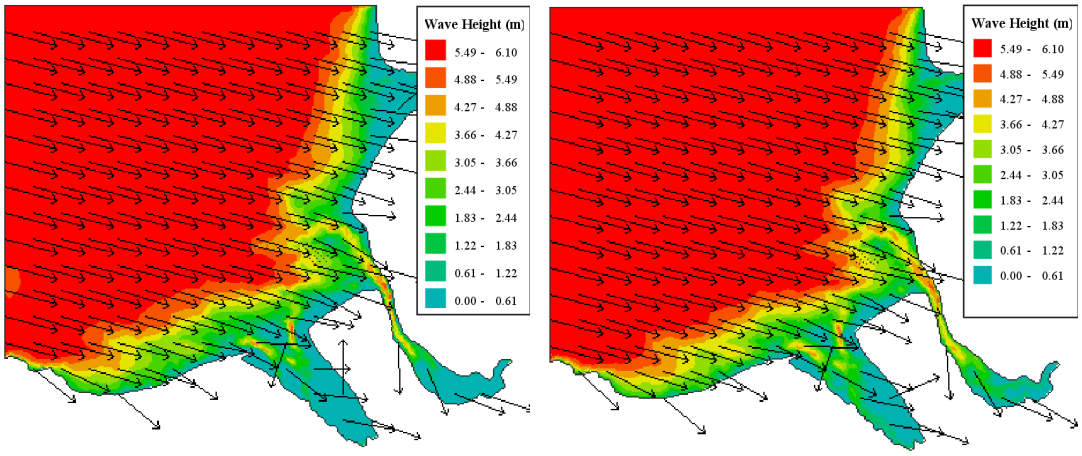

(a) Flood phase (b) Slackwater

Figure 6.4: Wave height and direction for a spring tide coupled with wave 1 over Liverpool Bay compared at two phases of the tidal cycle

Water depth

To analyse the impact of the wind farm on a far field scale, Figure 6.5 presents the free surface elevation and velocity direction for a spring tide coupled with wave 1 at three phases of the tide with and without the wind farm. Over the tidal cycle the tide travels into Liverpool Bay, travelling in a south-easterly direction. At slack water there is a change in direction (Figure 6.5b),and in the ebb phase the tidal flow travels out of the bay to the north west. As the tidal flow reaches the Great Burbo Flats the direction changes, so that the majority of the tide flows around this area. This does not appear to be an impact of the OWF, but rather the bathymetry, as it occurs with and without the wind farm present. There appears to be very little difference in free surface elevation at the regional scale, with and without the wind farm.

Figure 6.6 presents a closer look at the water depth for a spring tide at low water over the south west corner of Liverpool Bay, with no wind farm (Figure 6.6a) and with the wind farm in the mesh (Figure 6.6b). A similar pattern of water depth variation is seen, with water depth decreasing towards the south west corner of the region, and deep water seen in the Mersey Estuary. Even at this smaller scale little impact of the wind farm is seen.

Flow velocity

Figure 6.7 presents the tidal velocity across Liverpool Bay for a spring tide coupled with wave 1. The velocity distribution is shown at a peak flood and peak ebb phase of the tidal cycle, for the case with no wind farm (Figure 6.7a & 6.7c) and with the wind farm (Figure 6.7b & 6.7d). During the flood phase the flow velocity distribution across the domain is largely the same with (Figure 6.7b) and without the wind farm (Figure 6.7a). The tidal flow travels across Liverpool Bay in a south-westerly direction, at the Mersey Estuary the direction changes as the flow enters the estuary. The case with the wind farm shows a smaller area of high velocity at the entrance to the Mersey estuary and in the Mersey Narrows than with no wind farm, which suggests the wind farm has a blocking effect on the

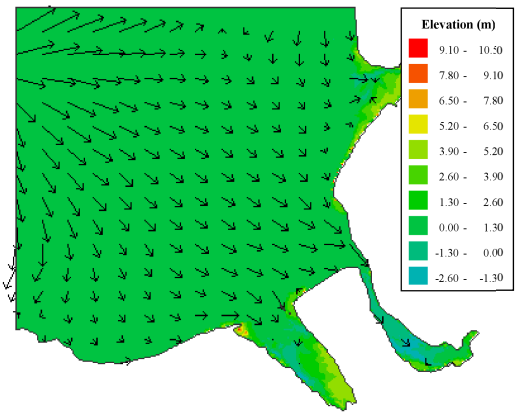

(a) Flood phase, without OWF

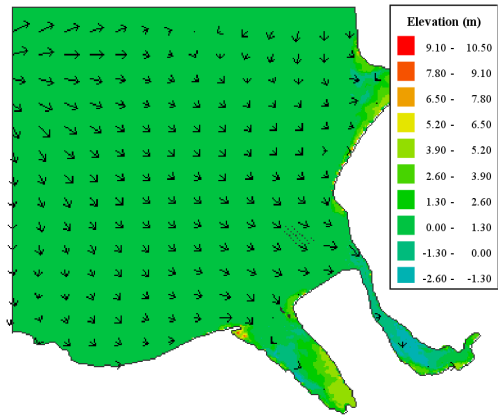

(b) Flood phase, with OWF

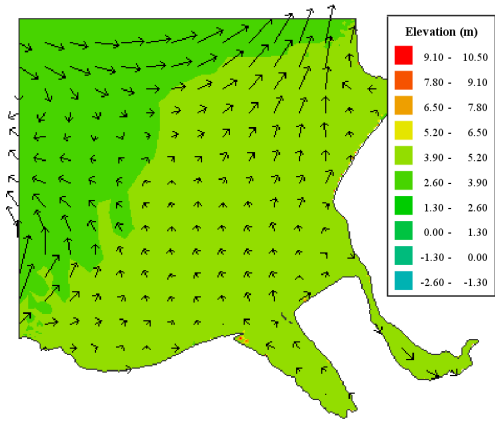

(c) Slackwater, without OWF

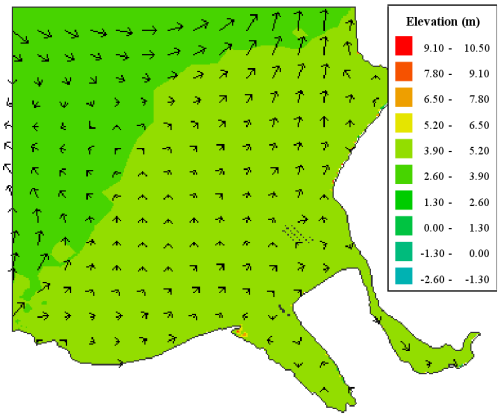

(d) Slackwater, with OWF

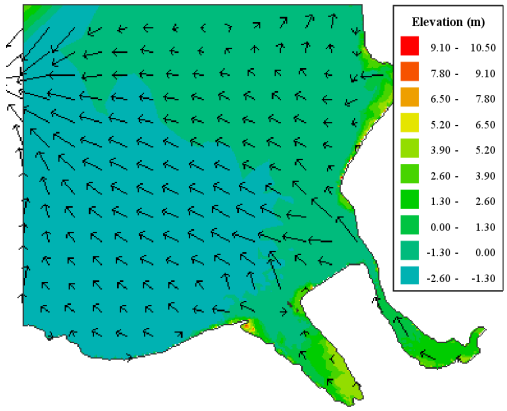

(e) Ebb phase, without OWF

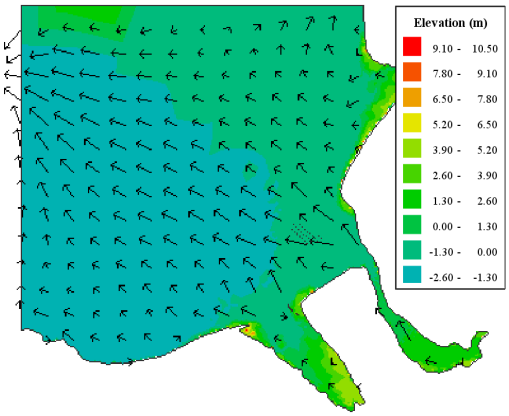

(f) Ebb phase, with OWF

Figure 6.5: Free surface elevation and flow velocity for a spring tide coupled with wave 1 over Liverpool Bay compared at different phases of the tidal cycle, with and without the wind farm

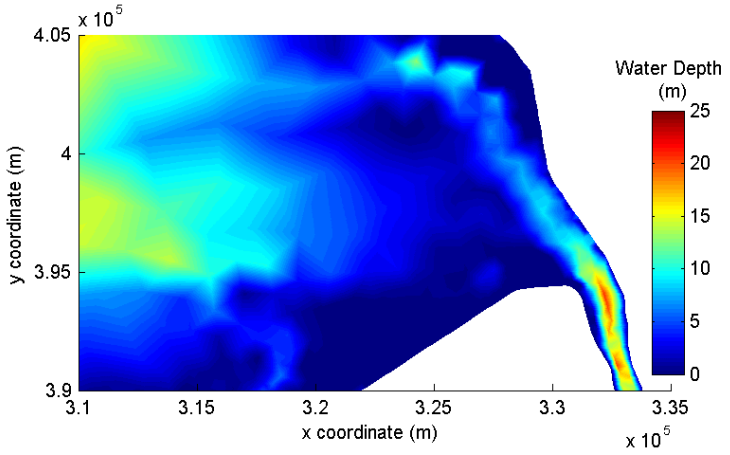

(a)

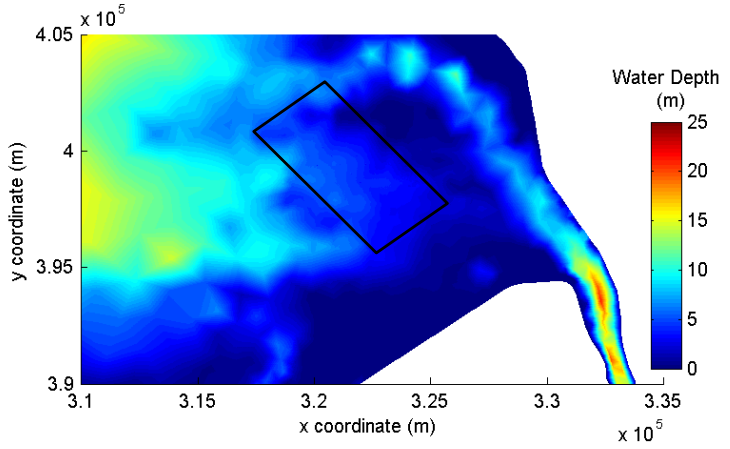

(b)

Figure 6.6: Minimum water depth for a spring tide with a) no wind farm present and b) wind farm present

flow. During the ebb phase of the tidal cycle the velocity is again largely similar across the domain with (Figure 6.7d) and without the wind farm (Figure 6.7c). Over the majority of Liverpool Bay the ebb flow is in a north easterly direction. As noted for Figure 6.5 the ebb flow travels around the area of the Great Burbo Flats, with a large flow travelling through the dredged channel. In the case with the wind farm (Figure 6.7d), the Mersey Narrows has a slightly higher velocity magnitude. At the mouth of the Mersey the higher velocities are spread in a wider area, again suggesting a blocking effect as the flow travels around the wind farm site.

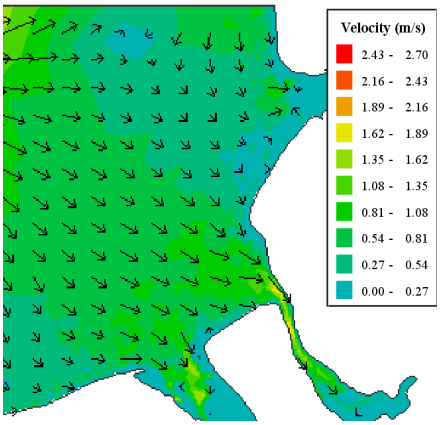

(a) Flood phase, without OWF

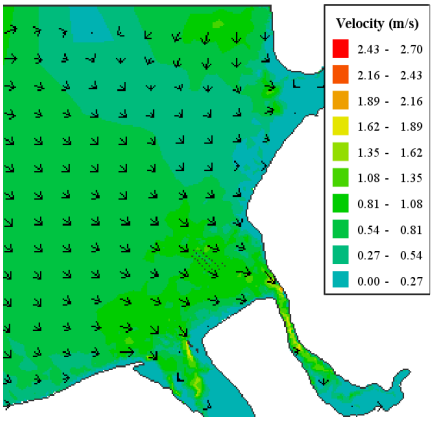

(b) Flood phase, with OWF

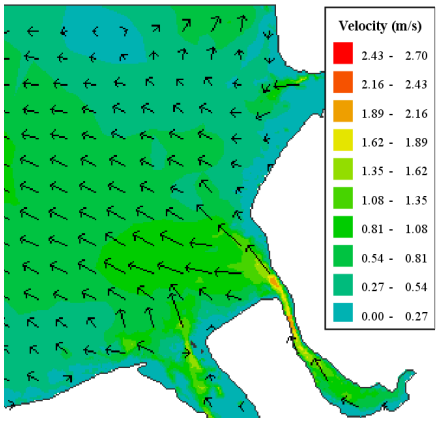

(c) Ebb phase, without OWF

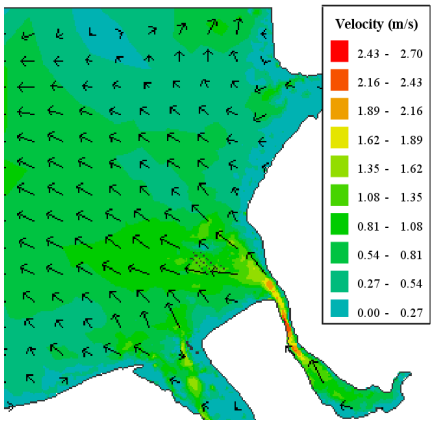

(d) Ebb phase, with OWF

Figure 6.7: Flow velocity for a spring tide coupled with wave 1 over Liverpool Bay compared at the flood and ebb phases of the tidal cycle, with and without the wind farm

Sediment transport and bed evolution

Figure 6.8 shows the computed residual transport flux across Liverpool Bay with and without an OWF for a spring tide only and for a spring tide coupled with wave 1. The majority of Liverpool Bay is shown to have no, or very little residual sediment flux. The main areas with a residual flux are seen in, or near, the estuaries of the Dee and Mersey. The Dee estuary has large areas of tidal flats, which could explain the residual transport here, there is also a large net transport at Hilbre Island. The Mersey estuary displays a divergent point at the Narrows, sediment in the mouth of the estuary above the narrows travels out of the estuary, and below the Narrows the residual sediment flux is into the estuary. There is little difference seen in the residual transport flux patterns between the case with spring tide only and spring tide coupled with wave 1. The wind farm, however, is found to have an influence on the residual sediment transport. With no wind farm, the majority of the transport flux out of the Mersey Estuary travels along the dredged channel around the top of the Burbo Flats (Figure 6.8c). With the wind farm, there is a split in the sediment pathway which causes a large proportion of the sediment to travel to the bottom of the wind farm site.

Sediment transport in and out of the wind farm area is determined by integrating the sediment flux along a box, of size $5.45km$ x $3.75km$, surrounding the wind farm over a tidal cycle. Figure 6.9 presents the area used to calculate the sediment flux, the top, bottom, left and right lines of the box are taken separately and the sediment flux is integrated along the lines. This method allows the sediment transport dynamics within the region to be determined. The results are analysed first for a spring tide only model run, for the test case with no wind farm (Figure 6.11) and with a wind farm present (Figure 6.12). The free surface elevation for the tidal cycle is presented in Figure 6.10, the tide begins with slack water, followed by the flood and the ebb tide.

Figure 6.11 shows the sediment flux over a tidal cycle for the y direction (Figure 6.11a) and x direction (Figure 6.11b). In figure 6.11a the flux in the y direction is taken as the flux across the top and bottom lines and the net differ-

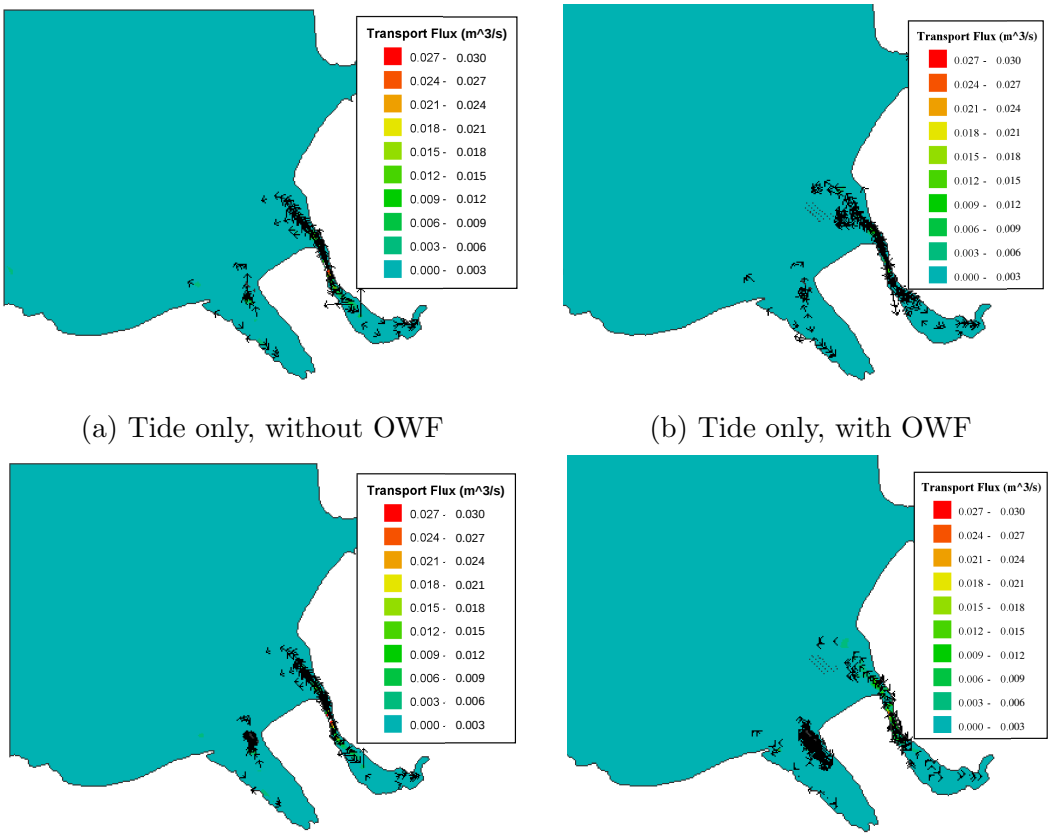

(a) Tide only, without OWF

(b) Tide only, with OWF

(c) Tide Wave 1, without OWF

(d) Tide Wave 1, with OWF

Figure 6.8: Tidal residual sediment flux over Liverpool Bay with and without a wind farm, for a tide only and tide coupled with wave 1

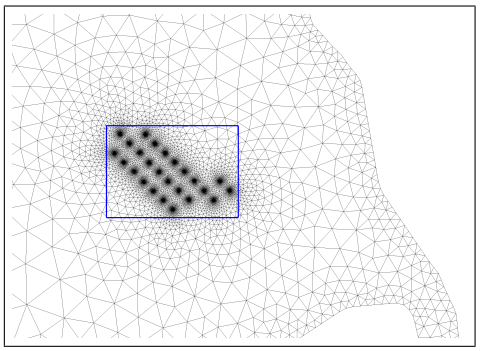

Figure 6.9: Location of integration line to calculate the movement of sediment at the wind farm site

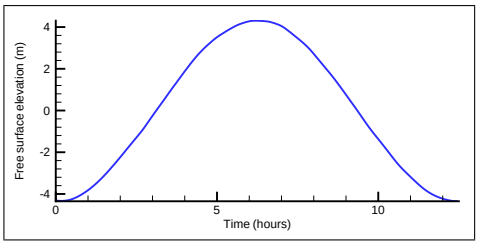

Figure 6.10: Free surface elevation over the spring tidal cycle in Liverpool Bay for sediment flux calculations

ence between the two (i.e. bottom line flux - top line flux). The positive values show the flux entering the wind farm area and the negative values show the sediment flux leaving the region. Figure 6.11b presents the sediment flux in the x direction, calculated as the flux across the left and right lines of the box and the net difference (i.e. right line flux - left line flux).

In Figure 6.11a the sediment flux in the y direction across the top and bottom of the wind farm sites behaves similarly over the tidal cycle but in opposite directions. The difference between the flux on the top and bottom line gives the net sediment movement. In this case the flood part of the tide leads to a decrease in sediment at the wind farm site, whereas the ebb tide shows initially an increase followed by a decrease. This reversal in sediment flux during the ebb tide could be due to the flow travelling along the channel rather than across the wind farm site. Overall there is a decrease of sediment within the area along the y direction over the tidal cycle when no wind farm is present. When compared with the case with a wind farm present, (Figure 6.12a) the magnitudes of sediment flux are similar for both, suggesting that overall the wind farm allows flow to penetrate through the site and there is no large impact on sediment flux. However, there are variations in the flux caused by the wind farm, the no wind farm case has a narrower peak for the flood tide whereas for the wind farm case the sediment flux is spread, suggesting that the wind farm has a dispersion effect on the sediment flux, and may help to stir the sediments allowing movement earlier in the tidal cycle. In the ebb phase of the tidal cycle the sediment flux reversal is not seen to the same extent.

The sediment flux magnitudes are greater in the x direction than in the y direction. In the x direction, the flux for both the wind farm (Figure 6.12b) and no wind farm (Figure 6.11b) case shows a decrease in sediment within the region for the flood phase and an increase in the ebb phase. The magnitude at the ebb phase is greater, leading to sediment entering the region, overall, along the x direction. Again, the peak at the flood phase has a greater spread in the wind farm case than in the no wind farm case. The sediment flux at the ebb phase occurs earlier in the tidal cycle for the wind farm case than for the no wind farm case, suggesting that the wind farm helps to stir up the sediments at lower velocities in the tidal cycle. However, this effect diminishes as the velocity increases, as the maximum ebb sediment flux is much greater for the no wind farm case than for the wind farm case.

The sediment flux at the wind farm site is also plotted for a spring tide coupled with wave 1, for both the no wind farm (Figure 6.13) and the wind farm case (Figure 6.14). Generally for the no wind farm case, the sediment flux is similar with and without the wave, although the net flux in the flood phase for the y direction reverses direction. For the wind farm case the x direction shows a similar pattern as for no wave. The y direction, however, shows a much larger sediment flux in the flood phase, with sediment moving into the wind farm area. The ebb phase also sees enhanced transport than seen with no wave coupling. Wave 1 acts in a similar direction to the mean tidal direction, but its effects are only seen in the y direction, this is likely to be due to the sand bank to the north east of the site limiting the wave impact.

Mersey Estuary sediment flux

The sediment flux into and out of the Mersey estuary was calculated by integrating along a line at the mouth of the estuary over a tidal cycle. The location of the line is shown in Figure 6.15, it is located on the seaward side of the Mersey estuary sediment flux divergence point, where the net sediment flux travels out

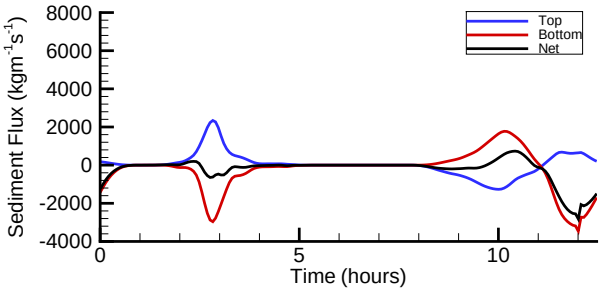

(a)

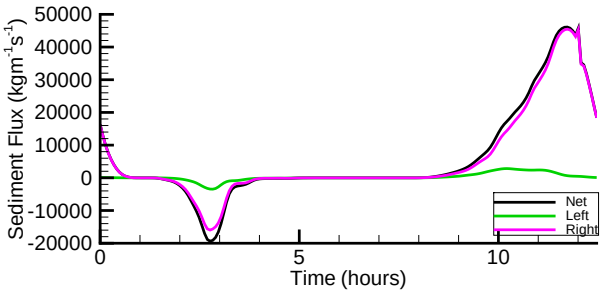

(b)

Figure 6.11: Sediment flux integrated along a box surrounding the wind farm area for a spring tide without the wind farm. The plots show the sediment flux along a) the top and bottom line, and b) the left and right lines. Also indicated are the difference between the two showing the level of sediment gained or lost within the wind farm site over a tidal cycle

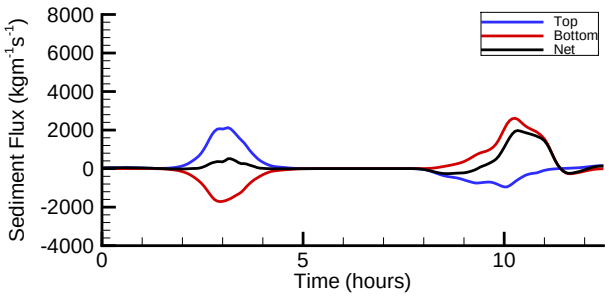

(a)

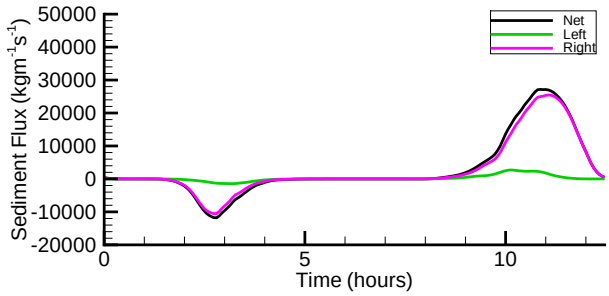

(b)

Figure 6.12: Sediment flux integrated along a box surrounding the wind farm area for a spring tide with a wind farm present. The plots show the sediment flux along a) the top and bottom line, and b) the left and right lines. Also indicated are the difference between the two showing the level of sediment gained or lost within the wind farm site over a tidal cycle

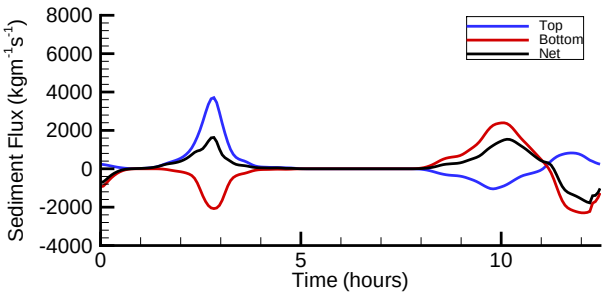

(a)

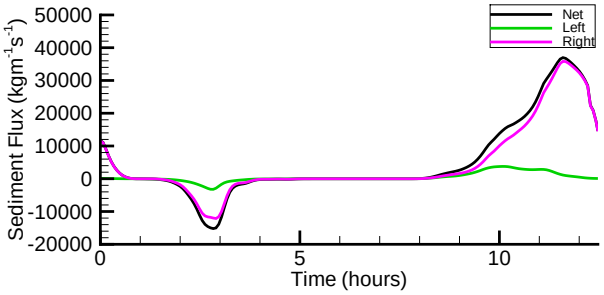

(b)

Figure 6.13: Sediment flux integrated along a box surrounding the wind farm area for a spring tide coupled with wave 1 without the wind farm. The plots show the sediment flux along a) the top and bottom line, and b) the left and right lines. Also indicated are the difference between the two showing the level of sediment gained or lost within the wind farm site over a tidal cycle

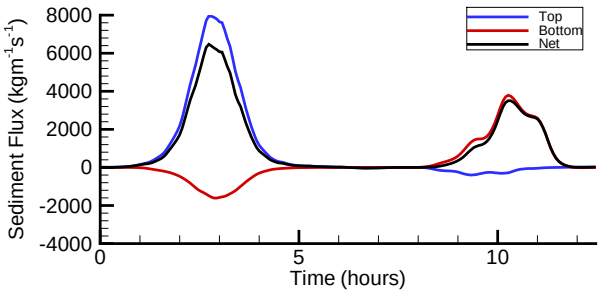

(a)

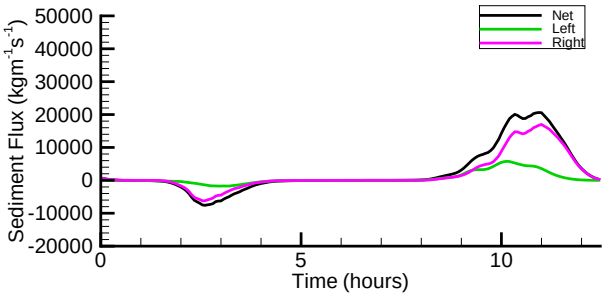

(b)

Figure 6.14: Sediment flux integrated along a box surrounding the wind farm area for a spring tide coupled with wave 1 with a wind farm present. The plots show the sediment flux along a) the top and bottom line, and b) the left and right lines. Also indicated are the difference between the two showing the level of sediment gained or lost within the wind farm site over a tidal cycle

of the estuary (Figure 6.8). The sediment flux along the mouth of the estuary is plotted over a spring tide for a case with no wind farm and with a wind farm, in Figure 6.16. The positive sediment flux represents sediment moving into the estuary and negative flux is out of the estuary and into Liverpool Bay. Initially during the ebb phase of the tidal cycle there is a net sediment flux out of the estuary, followed by a net flux into the estuary during the flood phase. At this location, with and without the wind farm, the sediment flux is greatest for the ebb phase and there is a net sediment flux over the tidal cycle out of the estuary. The ebb phase sediment flux is similar with and without a wind farm present, however, there is a slight time shift in the peak ebb flux with the wind farm to earlier in the tidal cycle. During the flood phase there is a greater sediment flux into the estuary with no wind farm than with the wind farm. This is due to the lower velocity at the mouth of the estuary during the peak flood for the wind farm case (Figure 6.7), which is caused by the blocking effect of the wind farm. Over the tidal cycle, at this location across the estuary, the wind farm decreases the sediment flux into the estuary, therefore, enhancing the residual flux out of the estuary.

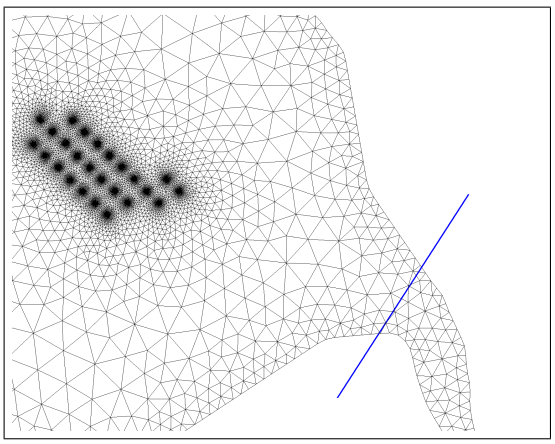

Figure 6.15: Map of Liverpool Bay highlighting the integration line across the Mersey Estuary used to calculate the sediment flux into/out of the estuary

Bed evolution

Figures 6.17 & 6.18 present the bed evolution over the whole wind farm site for the neap tide model runs (Figure 6.17) and the spring tide model runs (Figure

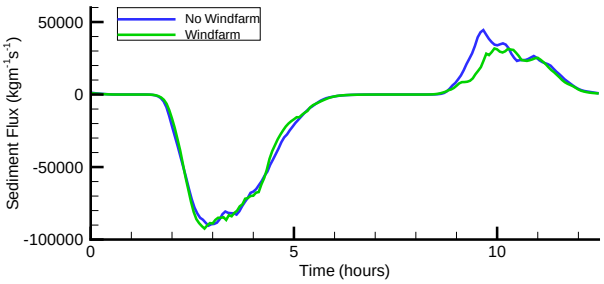

Figure 6.16: Sediment Flux over a tidal cycle into and out of the Mersey Estuary for a spring tide run for a case with and without a wind farm present

6.18). The wind farm site takes up an area of 1.76x10$^7 m^2$. Overall there is a net deposition at the site over a tidal cycle for all cases, with the neap tide test runs showing lower bed evolution than the spring tide test runs. For the neap tide case the volume of deposition and erosion is similar for all cases, except wave 3, which shows a greater volume. The spring tide cases are more influenced by the wave-current interaction, with the greatest volumes of erosion and deposition occurring at the largest wave heights (Waves 1 & 2). The waves appear to have a bigger impact on erosion than on deposition, which fits with the hypothesis that the waves help to stir the sediment at the turbine foundations.

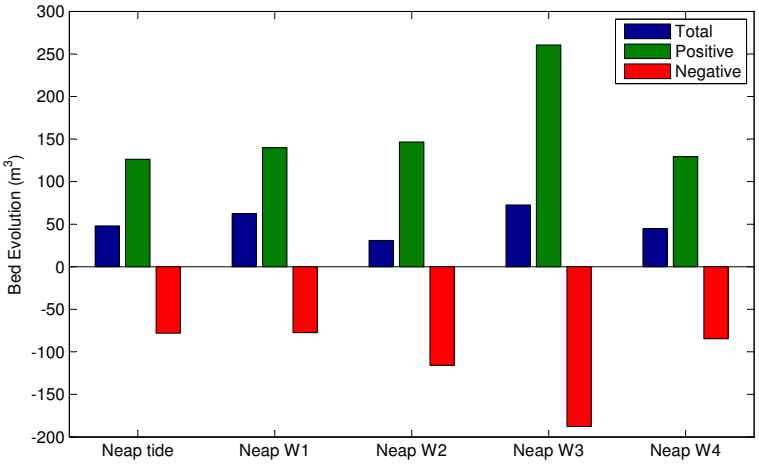

Figure 6.17: Bed evolution bar chart over a wind farm site for the neap tide test runs. The plot shows total evolution change, positive bed change and negative bed change

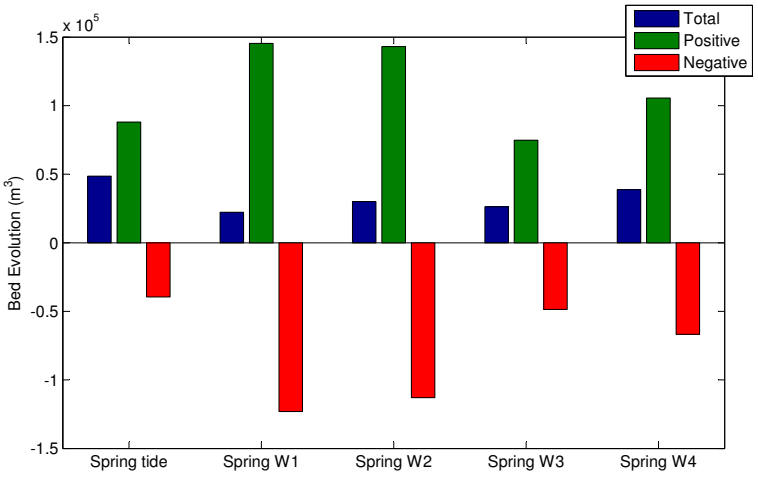

Figure 6.18: Bed evolution bar chart over a wind farm site for the spring tide test runs. The plot shows total evolution change, positive bed change and negative bed change

6.1.4 Near field impacts

Waves

The distribution of wave height over the Burbo Bank wind farm, is compared for wave 1 and wave 3 coupled with both a neap and spring tide in Figure 6.19. The significant wave heights for wave 1 and 3 are $4.22m$ and $3.61m$, respectively. For all the model runs, a common pattern of wave height over the wind farm site is seen. The wave height decreases as the wave travels to the North East of the site, due to a sandbank at the edge of the site creating a sudden change in bathymetry.

For both the wave 1 model runs, the decrease in wave height in the wake of pile is clearly seen at the wind farm scale. The wake spreads further from the pile taking up a large part of the wind farm area, before recovering to the background values. The neap case (Figure 6.19a) shows a smaller decrease in wave height than the spring tide case (Figure 6.19b), although the length scales of the wake are similar for both. No interaction between the structure foundation and the wakes can be seen in the wave 1 case, due to the orientation of the wind turbine monopiles in relation to the dominant wave angle. However, both the wave 3 cases (Figure 6.19c & 6.19d) show an interaction between the wakes behind the indi-

vidual wind turbines, this is evidenced by the wave height contour lines joining between foundations. This wake interaction is likely to make further non-linear interactions occur at the site, and means most of the site is influenced in some way by a modification in wave height. As discussed in Chapter 2, wake lengths greater than the wind farm spacing are detectable in the numerical model results for a hypothetical wind farm (Cooper and Beiboer, 2002), and the Burbo Bank wind farm Environmental Impact Assesment (ABPmer, 2002). In both of these studies wake interactions are seen when waves from the worst case scenario are modelled.

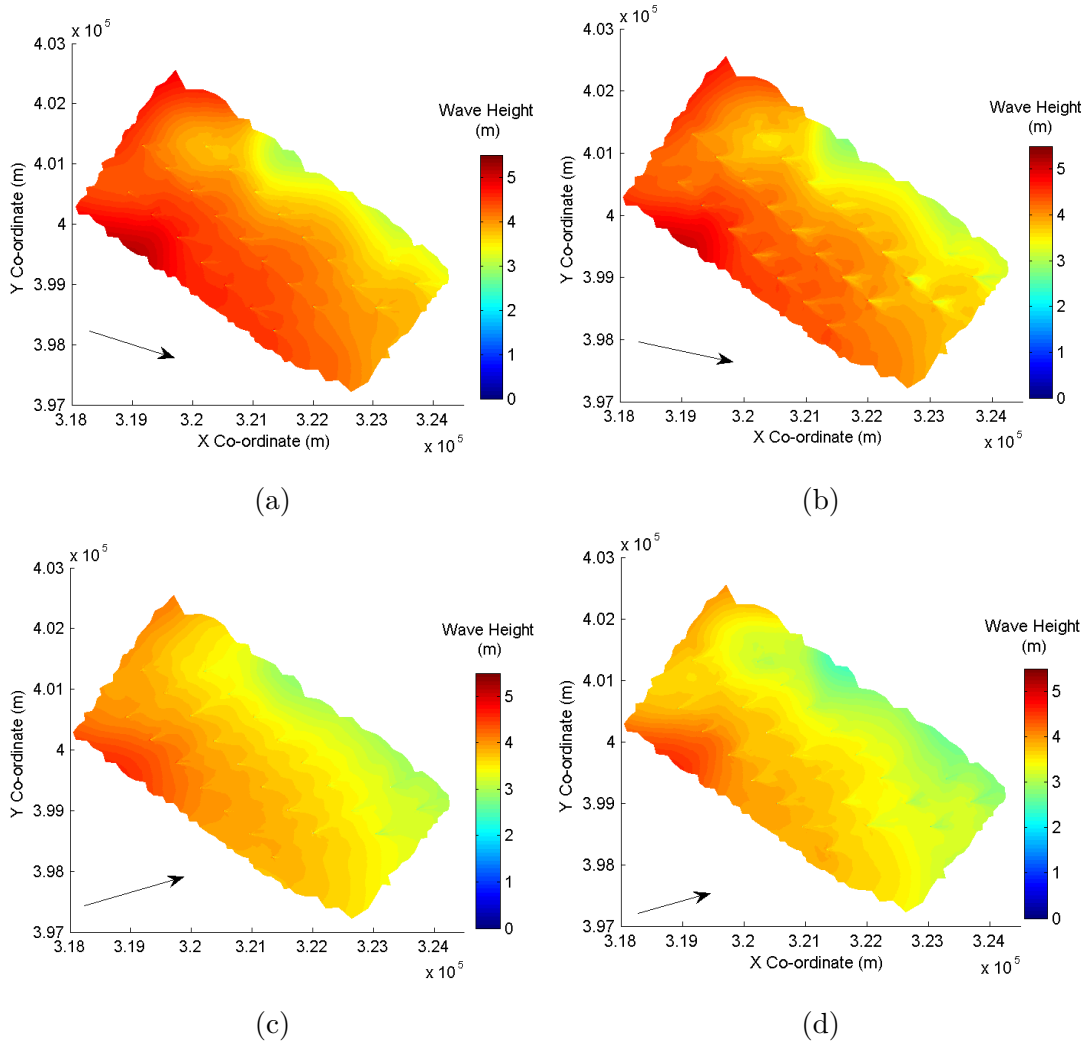

Figure 6.19: Wave height over the wind farm area at the peak water depth for a) neap tide wave 1, b) spring tide wave 1; c) neap tide wave 3 and d)spring tide wave 3. Arrow indicates wave direction

Figure 6.20 presents the wave height variation at an individual pile, the wave

height is taken as a tidal cycle-averaged value to remove water depth influence. The results are analysed for a neap and a spring tide coupled with wave 1, with a wave height of $4.22m$, and wave 4, with a wave height of $2.83m$. In all cases an increase in wave height is seen at the sides of the front of the pile, this is due to the wave being reflected off the structure and scattered. Behind the pile wave height is reduced to zero, gradually increasing to background values. The lee wake in wave height shows a greater spread for the wave 1 cases (Figure 6.20a & 6.20b) than the wave 4 cases (Figure 6.20c & 6.20c), which is likely due to the wave 1 having a greater amplitude. Generally the neap tide cases show a greater wave height over the plotted region than the spring tide cases.

A cross section of the wave height variation across a single turbine foundation, taken along the axis of the model run wave direction for neap and spring tides is presented in Figure 6.21. The cross sections are taken as a mean wave height over one tidal cycle to remove the effect of variation in tidal velocity or water depth. For the neap tide cases (Figure 6.21a) the wave height is in general greater over the domain than for the spring tide cases (Figure 6.21b). The wave heights for the different model runs are more spread for the spring tide case, than for the neap tide case, here only the highest wave shows a greater amplitude value. Therefore, there appears to be less variation between structure impact for the different wave inputs in the neap tide case. In all cases a clear variation in wave height is seen across the monopiles. In front of the monopile a sharp increase in wave height is seen, caused by wave-wave interaction with the waves being reflected off the structue. Behind the pile the wave height is lower, and gradually increases as distance from the pile increases. For both the neap and spring cases, the recovery of the wake does not occur in the distance of $35D$ behind the pile. For the neap wave case at $35D$ behind the pile, the wave height is closer to the background value than for the spring tide case, which still sees a reduction in wave height of up to $0.3m$ from ambient values.

The structure impact on wave period is not apparent at the large scale of the wind farm but there are localised impacts at the individual piles. Wave period

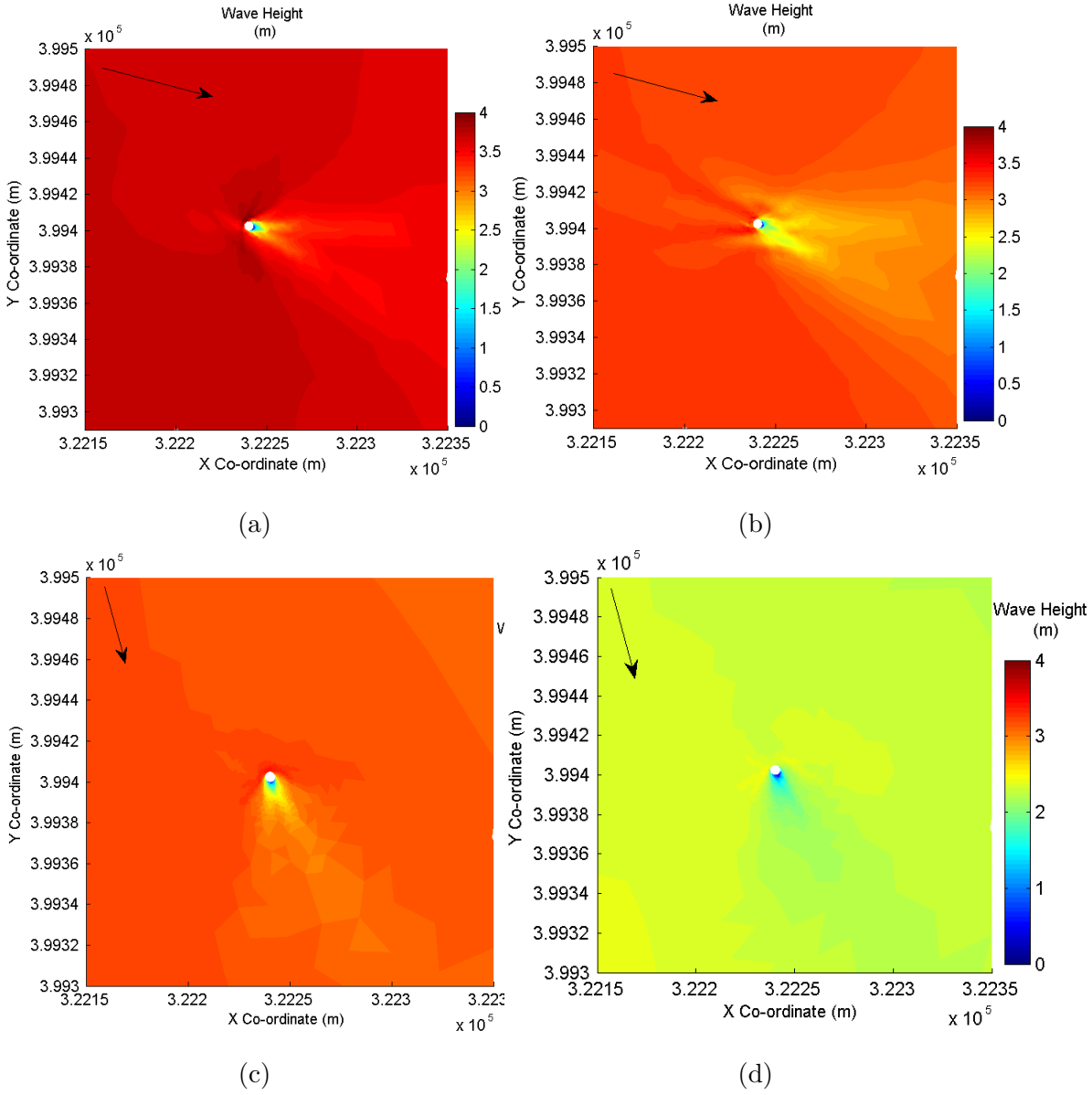

Figure 6.20: Tide mean wave height over one turbine monopile for a) neap tide wave 1, b) spring tide wave 1; c) neap tide wave 4 and d) spring tide wave 4. Arrow indicates wave direction

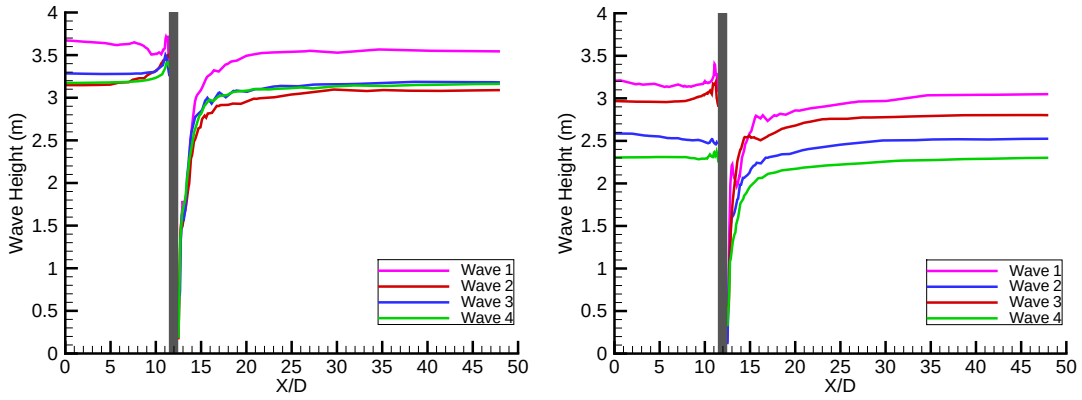

Figure 6.21: Mean wave height over one turbine monopile along the line of wave direction for a) neap tide and b) spring tide

variations at one turbine taken at the maximum water depth for the neap tide coupled with wave 1 and the spring tide coupled with wave 1 are presented in Figure 6.22. The flow modifications around the pile cause variations in the period in the wake. The waves are scattered as they travel around the structure, and wave-wave interactions occur. There is a general decrease in the wave period in the wake due to the wave-wave interactions, the wake has a short extent but a wide spread. The neap tide case (Figure 6.22a) has an overall greater peak period than the spring tide case (Figure 6.22b), which suggests the wave-current interaction varies for the different flow velocities.

Again the impact on wave direction is not seen at the wind farm scale but localised effects are evidenced at the monopile turbine. Figure 6.23 shows the difference between the boundary wave direction and the wave direction at a foundation site for a neap and spring tide coupled with wave 1 and wave 2. Wave 1 has a direction of 285°, wave 3 has a direction of 255°. For all cases a diffraction pattern is seen, with a change in the wave direction in the wake of the pile. In the wake, one side shows a positive change in direction whilst the other side shows a negative change in direction, and immediately behind the pile is the largest directional change. This occurs as the wave is bending around the structure turning clockwise at the top of the pile and anticlockwise at the bottom, exhibiting a diffraction pattern.

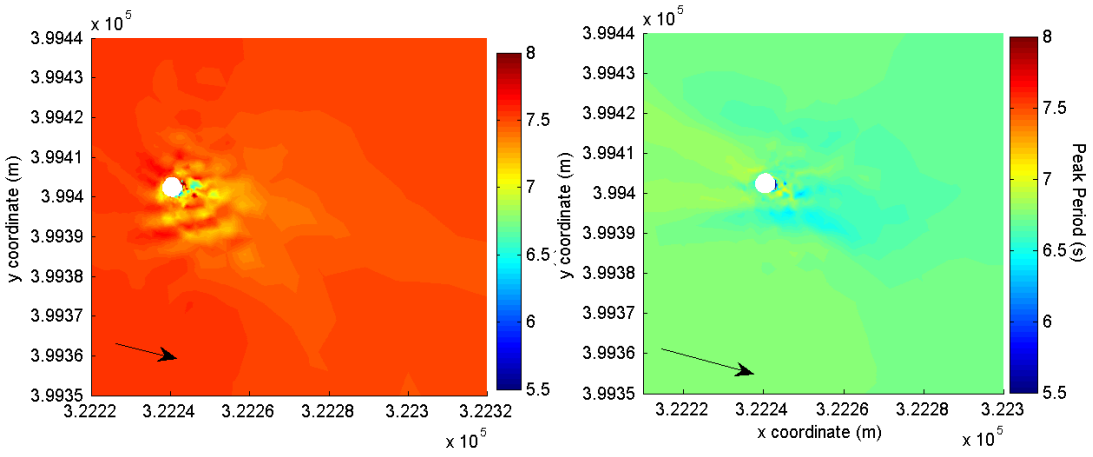

(a) (b)

Figure 6.22: Peak period at the maximum water depth over one turbine monopile for a) neap tide coupled with wave 1, and b) spring tide coupled with wave 1

Water depth

The near field variation in surface elevation across one wind turbine monopile is presented in Figure 6.24, for the turbine at the top of the Burbo Bank site. The computed surface elevation for the three conditions are presented at the ebb for; a spring tide only (Figure 6.24a), a spring tide couple with wave 1 (Figure 6.24b), and a neap tide only (Figure 6.24c). For the two spring tide cases a decrease in water depth is seen in front of the pile, with high water depths at the side and a decrease in water depth in the lee wake of the pile. The wake appears to be of a greater extent and spread for the spring tide coupled with wave 1 case than the spring tide only case. The neap tide has an overall smaller water depth, and exhibits a different pattern around the structure (Figure 6.24c). The water depth around the turbine for the neap tide is only modified from background values in a very small region. An increase in water depth is seen to the sides at the front of the pile followed by a lower water depth just behind. For the neap case there is no evidence of a lee wake from the turbine. The variation in patterns is likely to have an influence on sediment transport.

The water depth taken as a cross section across a single wind turbine founda-

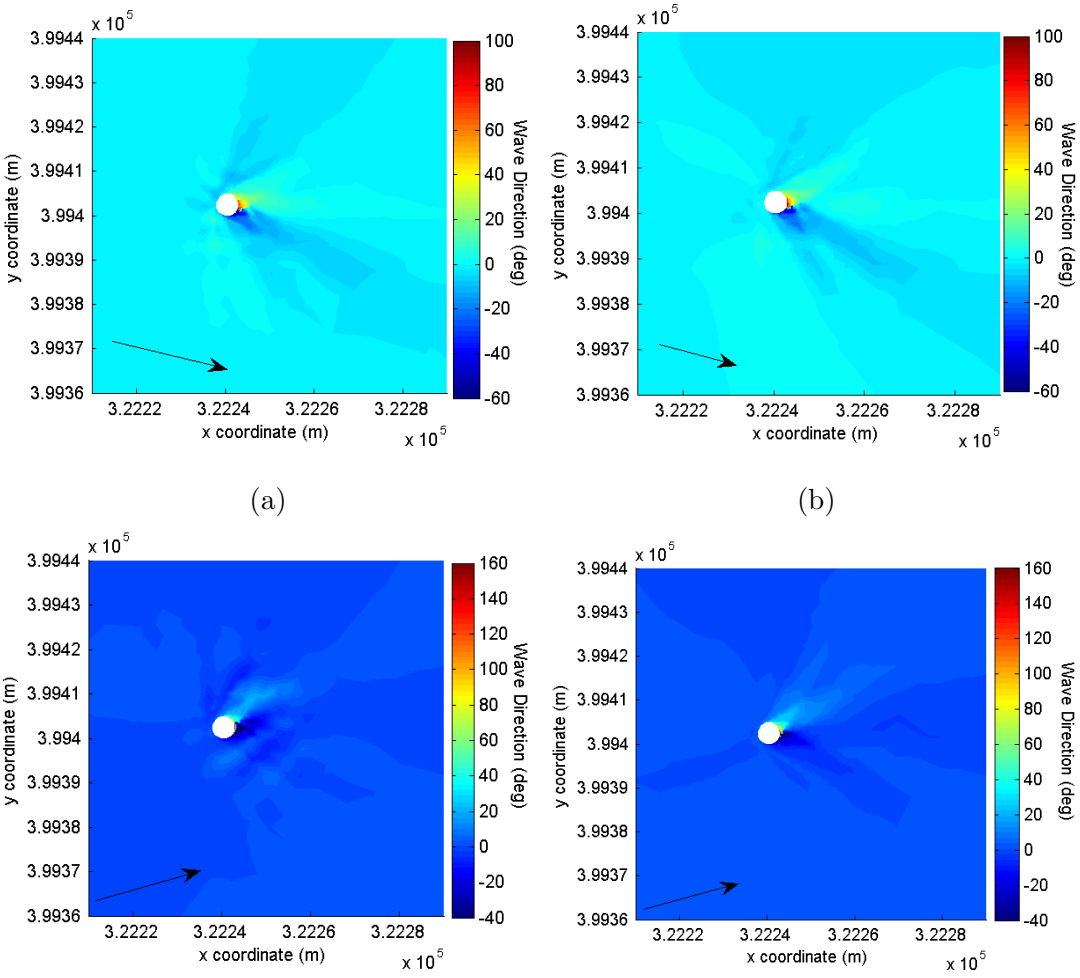

Figure 6.23: Difference in wave direction from the boundary value at peak water depth over one turbine monopile for a) neap tide wave 1, b) spring tide wave 1, c) neap tide wave 3, and d) spring tide wave 3

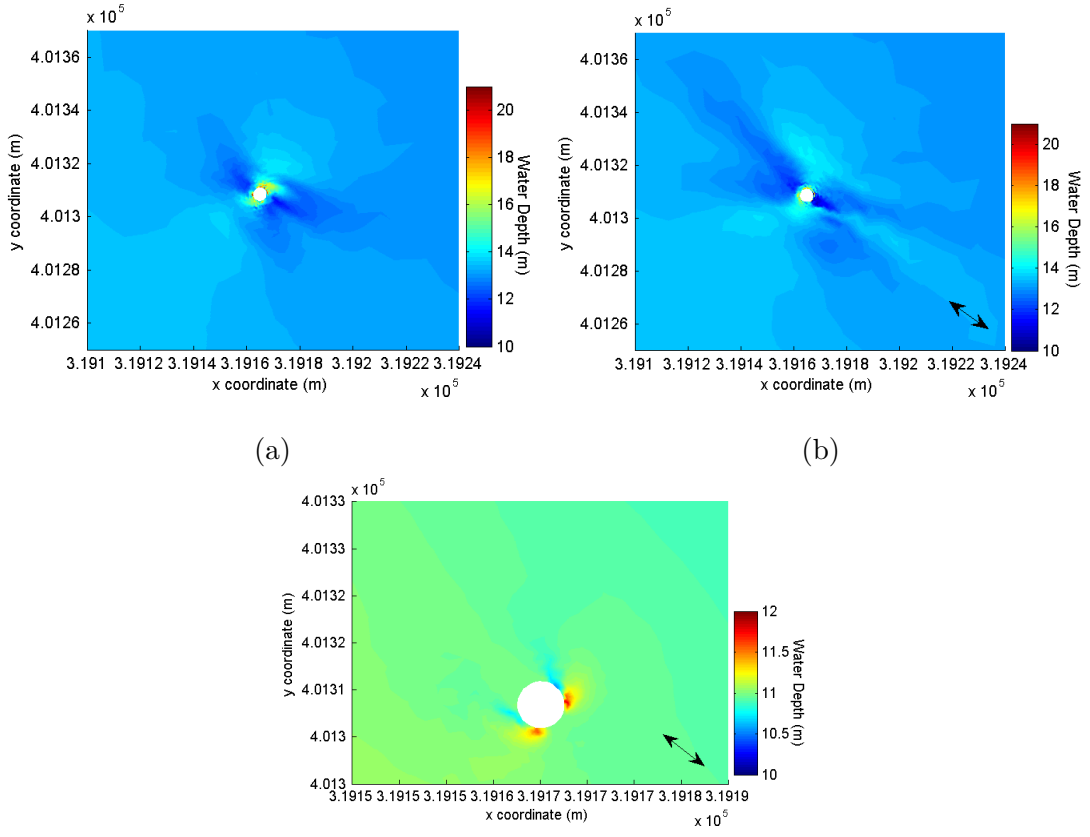

Figure 6.24: Water depth over one wind turbine monopile compared with no wind farm present, at maximum water depth for a) spring tide, b) spring tide coupled with wave 1, and c) neap tide only. The arrow indicates the mean tidal direction taken at a location away from the wind farm site

tion for all model runs is plotted in Figure 6.25. The water depth data is taken at the peak water depth over the line of the mean tidal direction. For the neap tide model runs (Figure 6.25a) there is very little variation in water depth at the monopile location. A small decrease in water depth is seen in front of the pile followed by a similar sized decrease behind the pile, which recovers quickly. All the model runs show similar features, with the neap tide only case showing an overall greater water depth, the smallest water depth is for the largest waves. The spring tide model runs (Figure 6.25b) shows greater variation of water depth. All cases show a decrease in water depth in front of the pile, followed by high water depth at the pile. This increased water depth in front of the pile is due to the tide reflecting off the structure. In the lee wake the water depths are very high at the pile location and then decrease in the following $1D$. The peak in water depth in the lee-wake is not thought to be plausible, and is likely to be caused by the simplification of the 3D flow structure in the TELEMAC model. The water depth recovers fairly rapidly in the lee-wake, for all cases within $5D$ of the pile. The greatest variations in water depth are seen for the wave 1 and 2 runs, this could be because both of these waves have directions similar to the tidal mean direction, therefore the wave interaction is seen along the mean tidal direction cross-section line.

Flow velocity

The depth mean velocity variations across the wind farm site are examined for a neap tide only, a spring tide only and spring tide coupled with wave 1, in Figure 6.26. The depth mean velocity is taken at the peak flood velocity. In Liverpool Bay the flood tide is dominant; therefore, these plots examine the greatest velocities at the Burbo Bank site. For all model cases examined, the velocity variation due to the structure interaction can be seen on the wind farm scale. The decrease of velocity in lee wake extend to distances of $40D$ beyond the turbine. For the neap tide case (Figure 6.26a) the overall velocity is less than for the spring tide cases. The velocity wakes behind the turbines extend on average $18D$, but at some foundation locations up to $40D$. The velocity wakes do not extend far

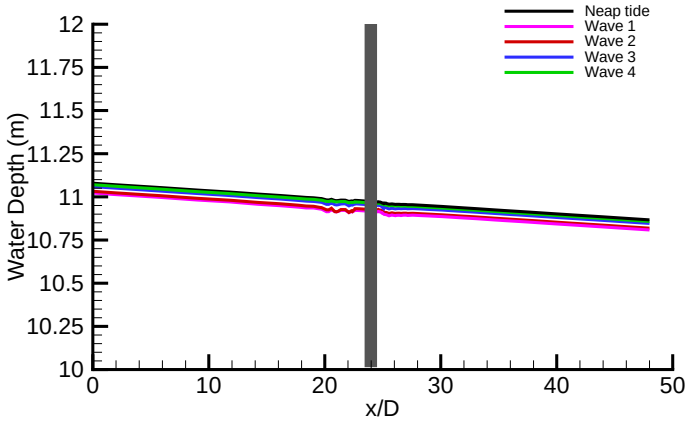

(a)

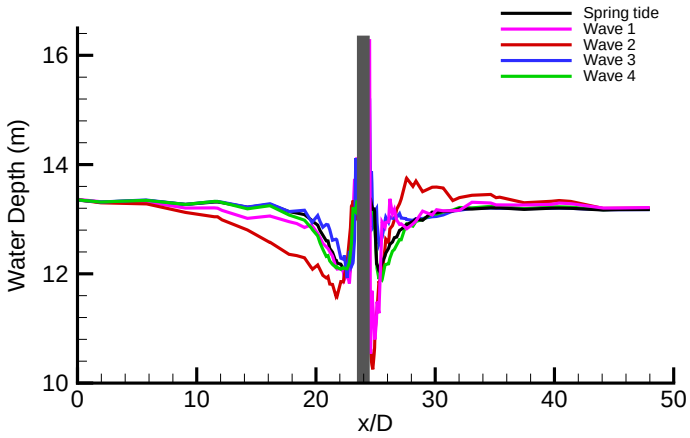

(b)

Figure 6.25: Water depth variation across a single wind turbine foundation for a) neap tide model runs, and b) spring tide model runs

enough to see an interaction between the foundation wakes. For the spring tide only case, no interaction can be seen between the velocity wakes caused by the monopile foundation. The lee wakes extend up to $40D$ behind the foundations, and show a greater wake spread than the neap case, which could be due to the higher velocities. The spring tide coupled with wave 1 case shows interaction between the velocity wakes at the turbine, as the orientation of the wake is shifted so that the wake travels along the line where the structures are closer together. A chain of wakes that end at the proceeding turbine foundation is seen on the southern side of the Burbo Bank OWF. The orientation of the wake has unusually shifted towards the wave direction, suggesting a non-linear interaction between the tide and waves. It is also apparent that for the cases with no waves, the deeper areas of the wind farm site have greater velocities than in the case with waves.

In order to understand the structure impacts on the flow velocity further, the small scale interactions at a single monopile are studied. Figure 6.27 highlights the depth averaged velocity magnitude at a peak ebb velocity for a neap tide only (Figure 6.27a), spring tide only (Figure 6.27b), and spring tide coupled with wave 1 (Figure 6.27c). A similar wake effect is seen in all cases, with a general pattern of a rapid decrease in flow velocity in front of the pile, which decelerates to zero at the pile. The sides of the pile show a flow acceleration consistent with streamlines contracting. Behind the pile there is a wake in flow velocity, which gradually recovers to the background velocity values. For the neap case the flow acceleration at the side of the pile is extended further from the pile than for the spring tide cases, this may have an impact on bed shear stress and sediment stirring. The spring tide only has a narrow wake and quick recovery of the wake, whereas the wave case shows a greater spread of the wake and slower recovery to the background value. This suggests that with the wave present, the peak current direction has wider spread than that of the tide only cases. The wake therefore follows the flow and spreads at various angles around the structure. As discussed in Chapter 2, Hjorth (1975) found from physical experiments of a current at a cylinder, that the velocity was enhanced within $1D$ of the sides of the cylinder.

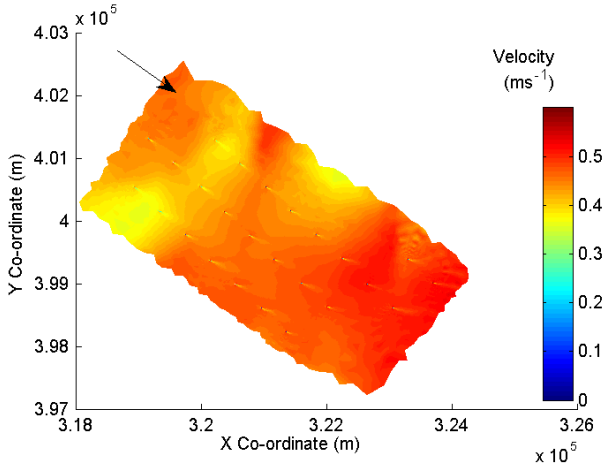

(a)

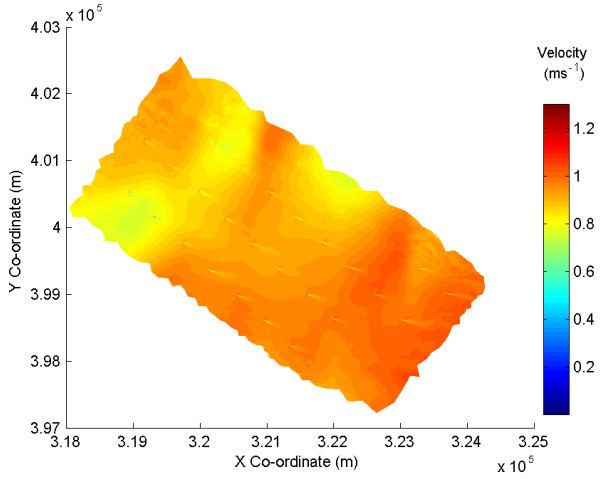

(b)

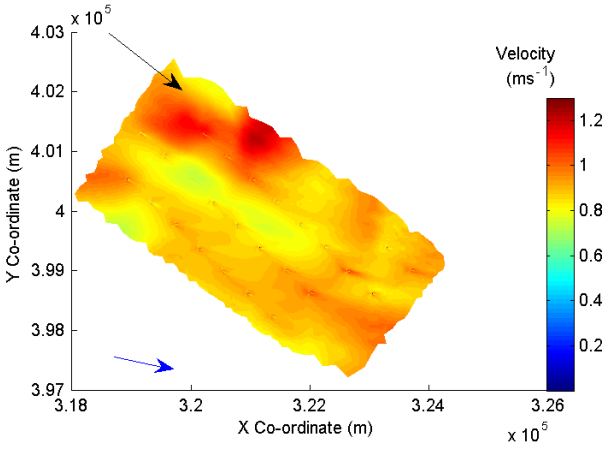

(c)

Figure 6.26: Depth averaged velocity magnitude over the wind farm area at peak flood for a) neap tide only, b) spring tide only, and c) spring tide coupled with wave 1. Black line indicates the wind direction, and the blue arrow gives wave direction

The results from the present study indicates a an amplification area of $0.5D$ for the spring tide only case.

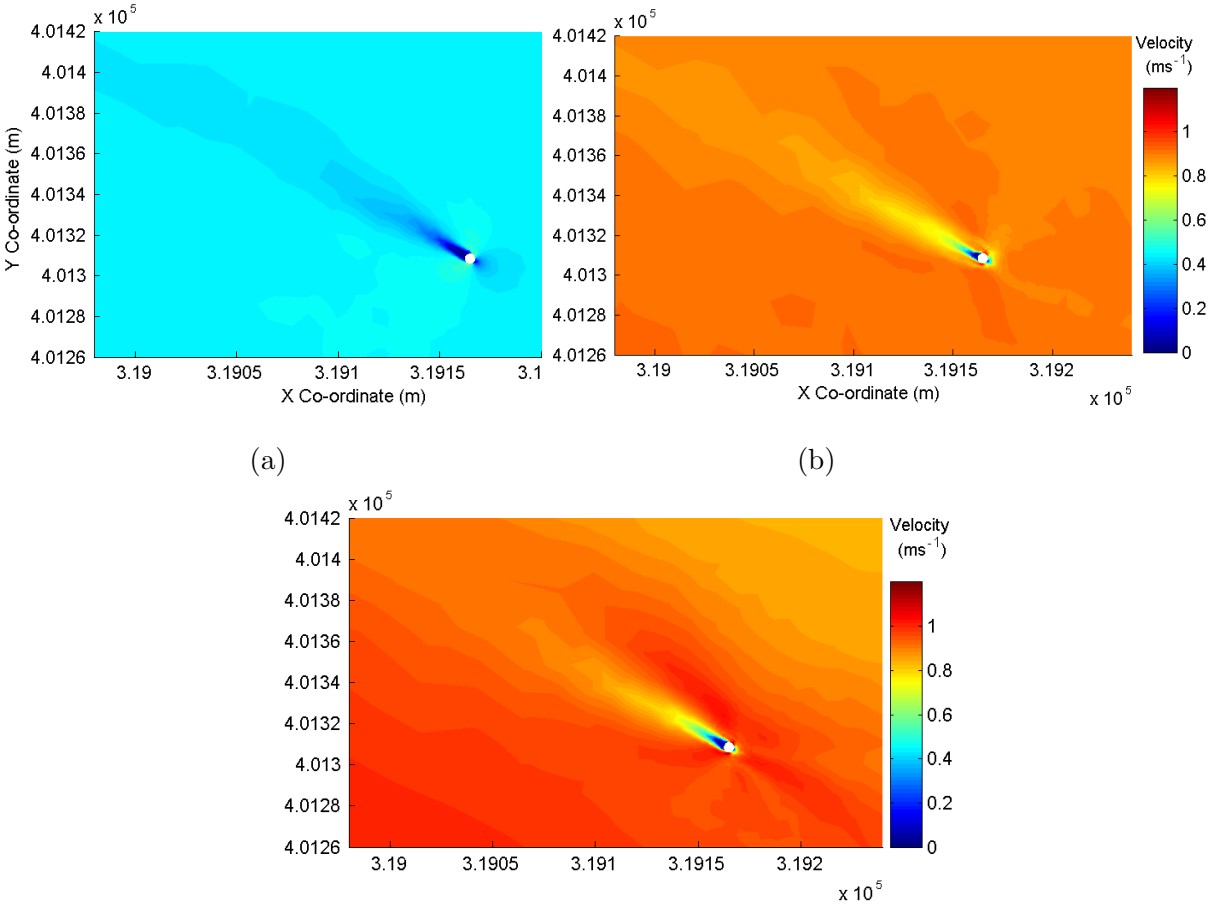

Figure 6.27: Depth averaged velocity magnitude over one turbine at peak ebb velocity for a) neap tide only, b) spring tide only, and c) spring tide coupled with wave 1

In Figure 6.28 the velocity wake due to the structure interaction is investigated further through a vertical cross section, along the line of the mean tidal direction. The cross sections are taken at the peak flood velocities for a neap tide only (Figure 6.28a), spring tide only (Figure 6.28b), and a spring tide coupled with wave 1 (Figure 6.28c). The neap tide shows a clear decrease in velocity in the wake of the pile, with a short recovery to background values within $12D$ from the pile. The velocity in the wake at the bed appears to be greater than in the mid water column. For the spring tide only case the logarithmic vertical velocity

profile is present at a distance of $12D$ in front of the pile. The velocity decreases closer to the pile, with the lowest velocity seen near the bed. At the pile, a sharp increase in velocity is seen, this is due to the streamlines contracting. In the wake of the pile, the velocity is near zero close to the pile gradually increasing with distance. For the case of spring tides coupled with wave 1 (Figure 6.28c), the logarithmic vertical velocity is seen far in front of the pile, in this case the highest velocities take up a greater proportion of the water column than in the spring tide only case. In the wake of the pile the velocities are greater than seen at the spring tide case, this is due to the wave action direction accelerating the flow on a different plane. The recovery behind the pile to a background vertical velocity profile is similar for both the spring tide and spring tide wave 1 cases.

Figure 6.29 presents the vertical velocity profiles in front of the monopile (Figures 6.29a, 6.29b & 6.29c) and in the wake of the structure (Figures 6.29d, 6.29e, 6.29f & 6.29g), for the cases presented in Figure 6.28. A logarithmic velocity profile is clearly seen at a distance of $11.5D$ in front of the pile (Figure 6.29a). Both the spring tide cases show a similar profile, with the neap tide having an overall lower velocity. A similar pattern is seen at a distance of $5.5D$ in front of the pile, it appears the structure does not influence the flow at this location. At $0.5D$ in front of the pile (Figure 6.29c) the impact of the structure is begun to be seen. The velocities across the water depth are greater at this location and the variation of velocity with depth occurs over a larger section of the water column. Immediately in the wake of the pile, at $-0.5D$ (Figure 6.29d), the lower velocities associated with the wake are apparent. Some turbulence appears in the flow here as the velocity is quite variable with height. At a distance $4.5D$ in the wake (Figure 6.29e) the logarithmic profile is again apparent. The velocities have increased with distance from the structure but are not yet at the background values, the variation of velocity with height also occurs over a larger section of the water column. The vertical velocity profiles for the spring tide cases both show they have returned to ambient values at a distance $16.5D$ in the wake of the monopile (Figure 6.29g). The variation across the monopile shows a similar recovery for both the spring tide cases over the distance from the pile. However,

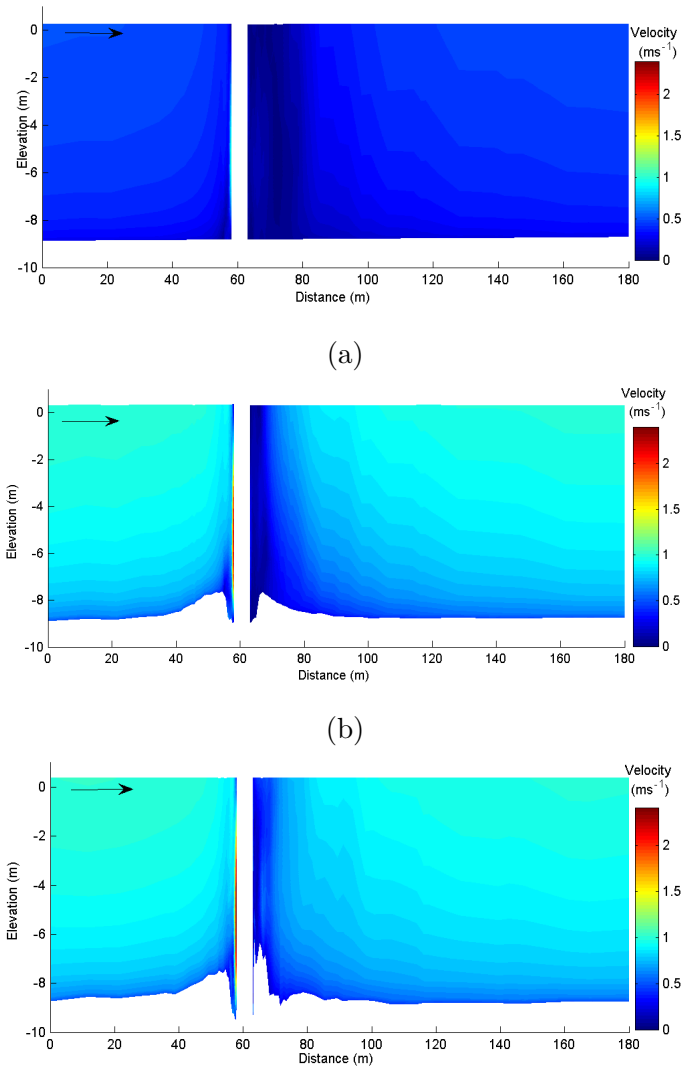

(a)

(b)

(c)

Figure 6.28: Velocity vertical cross section across a wind farm monopile for a) neap tide only, b) spring tide only, and c) spring tide coupled with wave 1. Arrow indicates the tidal flow

in the vicinity of the pile, the profile of the spring tide coupled with wave 1 differs from the spring tide only case, due to the influence of the wave on the flow.

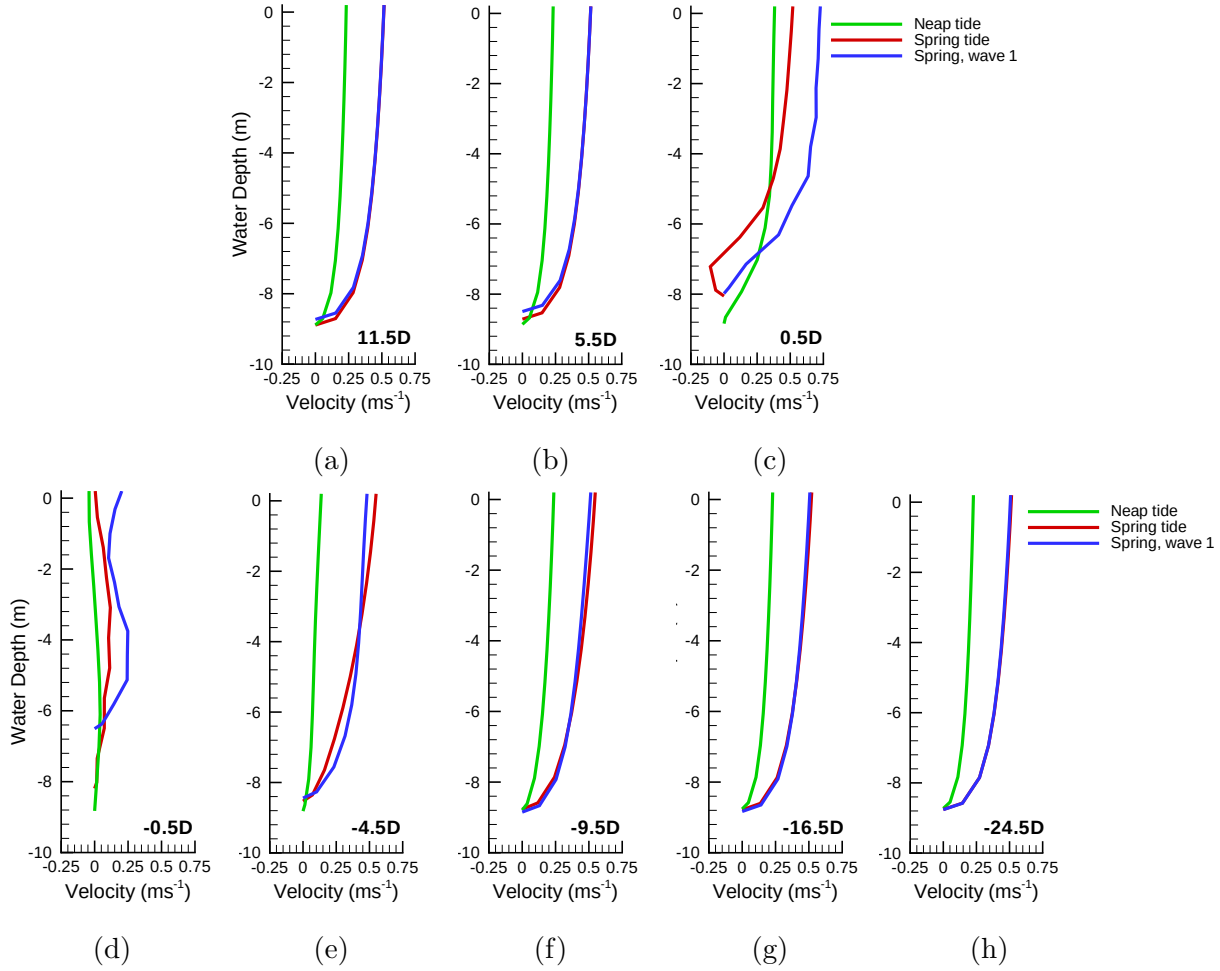

Figure 6.29: Vertical velocity profiles across a wind farm monopile at various distances from the monopile for a Neap tide only, Spring tide only and Spring tide coupled with wave 1

Sediment transport and bed evolution

The tide averaged sediment transport flux is examined for both a neap tide and a spring tide (Figure 6.30). In both cases a flood dominance is seen in the sediment transport with greater fluxes seen for the wake generated by the flood tide. Both cases show a lower sediment flux along the line of mean tidal direction than for background values. The greatest transport for the neap case (Figure 6.30a) is seen at the sides of the pile, due to the contraction of streamlines and associated increase in bed shear stress in this area. The very high fluxes are in a localised

area close to the pile, the transport flux then diminishes and spreads further from the pile.

The pattern for the spring tide (Figure 6.30b) shows a similar high sediment transport flux at the sides of the pile. However, here it is displaced slightly away from the pile and has a much greater spread. The clear flood dominance is seen with the greatest flux occurring behind the pile for the flood case, for the ebb tide the fluxes are much lower.

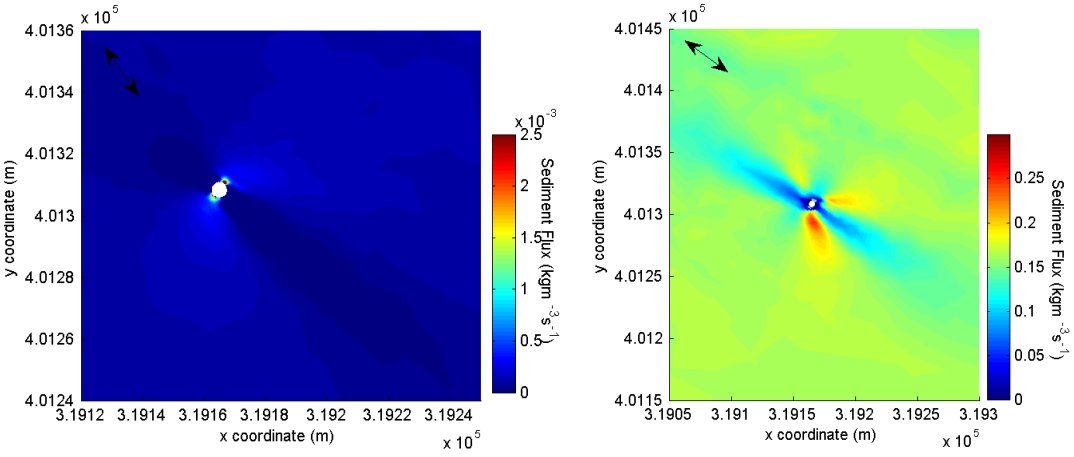

(a) (b)

Figure 6.30: Mean sediment flux at a pile over a tidal cycle for a) a neap tide only and b) a spring tide only

The bed evolution over a tidal cycle has been collated for the spring tides for each wave condition, and presented in Figure 6.31, the black line represents wave direction and the blue arrow represents mean tidal direction. In all cases there is an area of erosion in the immediate area around the wind turbine foundation, there are also small areas of deposition, particularly at the side of the piles. Comparing between the four wave directions, it is apparent that the tidal flow direction has a greater influence on bed flow than the wave direction, as the areas of erosion are all aligned along the line of the mean tidal direction. However, the spread of erosion at the piles is greater for the larger waves, 1 and 2, (Figure 6.31a & 6.31b) than for the slightly smaller wave heights of wave 3 and 4 (Figure 6.31c & 6.31d), indicating that the largest waves enhance sediment

transport away from the pile.

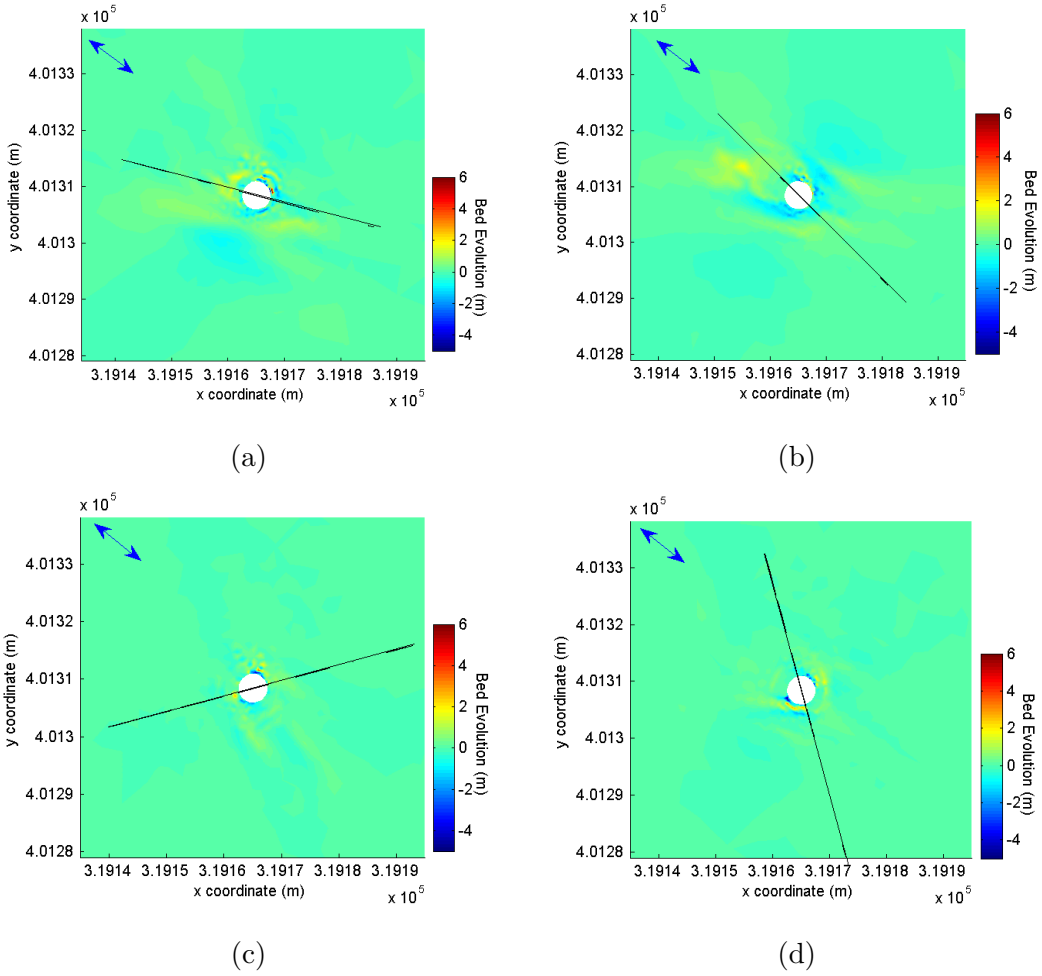

Figure 6.31: Bed evolution over a tidal cycle for a spring tide coupled with a) wave 1, b) wave 2, c) wave 3, and d) wave 4. The black line indicates wave direction and the blue arrow indicates the mean tidal direction

The total bed evolution over one tidal cycle in the region surrounding one foundation for all the spring tide test cases is presented in Figure 6.32. The region studied covers an area of $5985m^2$ surrounding the foundation. The total bed evolution is plotted with the volume of positive bed changes, i.e. deposition, and negative bed changes, i.e. erosion. In all cases the erosion and deposition are large across the site, but the net impact is relatively small. In all the cases, except wave 3, there is a net deposition in the area surrounding the monopile. The largest waves (waves 1 & 2) show the greatest erosion and deposition across the site , whilst waves 3 and 4, have similar volumes to the tide only case. This

suggests that only the very highest waves have a large influence on sediment transport in the localised area of a pile.

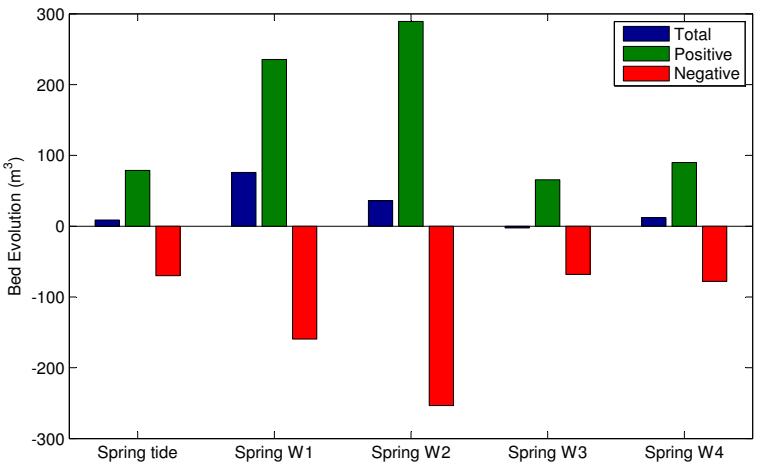

Figure 6.32: Bed evolution bar chart over a monopile turbine site for the different test run conditions. The plot shows total evolution change, positive bed change and negative bed change

6.2 East Anglia

6.2.1 Scroby Sands OWF

The Scroby Sand Offshore Wind Farm consists of 30 wind turbines, each with a monopile with a diameter of $4.2m$. The wind farm is located on the Middle Scroby Sandbank, off the coast of East Anglia. The sediment type within the region is of medium grain size.

6.2.2 Model run settings

A similar process is used to determine the short term impacts of the wind farm at the Scroby Sands OWF. The model is run for a neap tide, with a tidal range of $0.71m$, and a spring tide with a tidal range of $1.54m$. To determine the worst case impacts of the wave-current interaction the spring tide is also run coupled with waves. Due to the very shallow water depth at the Scroby Sands OWF, the wave height is diminished as the water depth shallows at the sand bank in the model (Figure 6.34). Therefore the wave runs are only modelled with the spring tide, as the neap tide showed little variation in output between the different wave conditions.

The *worst case wave conditions* were determined from data at the Horsey wave buoy site for the year 2008. The same process was used as for Liverpool Bay, the wave direction was divided into ranges of 30°, and the dominant wave directions were then determined. Figure 6.33 presents the wave rose for the site, the dominant directions here are $45°, 15°, 75°$, and $105°$. The peak wave height was determined for each of the directions, with the associated wave period. The wave conditions used for the model runs are presented in Table 6.3. All the model test run conditions and name for the model runs for the Scroby Sands OWF are shown in Table 6.4.

As previously discussed, the Scroby Sands OWF is situated on the Middle Scroby sand bank (Figure 6.34), this is a very shallow site with water depths of

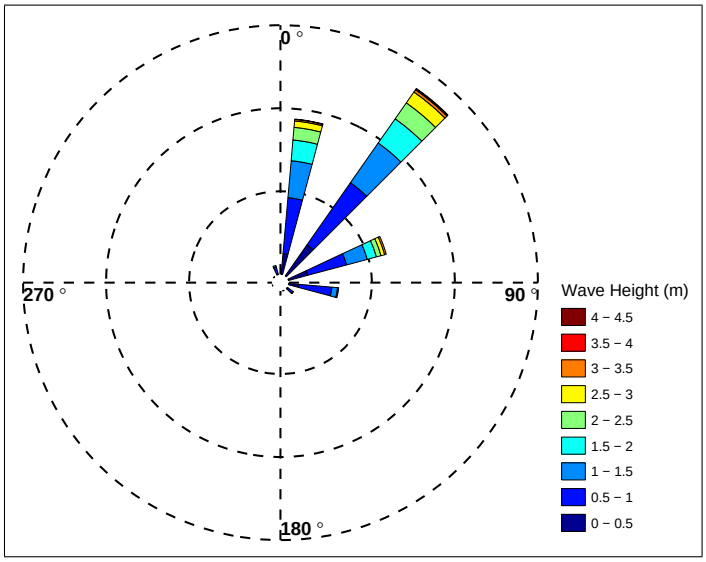

Figure 6.33: Wave rose for the year 2008 from the Horsey wave buoy. Data provided by the Environment Agency

Number	Wave Direction (°)	Wave Height (m)	Wave Period (s)
1	45	4.5	8.48
2	15	3.92	8.10
3	75	3.31	7.12
4	105	1.84	4.58

Table 6.3: Worst case wave conditions chosen for model runs for East Anglia

Name	Conditions
N	Neap tide only
S	Spring tide only
S1	Spring tide coupled with wave 1
S2	Spring tide coupled with wave 2
S3	Spring tide couple with wave 3
S4	Spring tide couple with wave 4

Table 6.4: Model run conditions for East Anglia site

between 1 and $10m$.

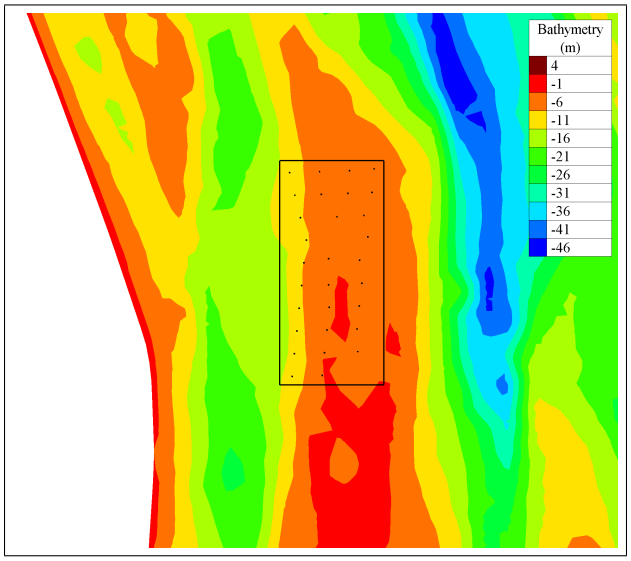

Figure 6.34: Bathymetry at the Scroby Sands wind farm site

6.2.3 Far field impacts

Waves

The wave heights and direction vectors for the wave 1 condition at a spring tide, are shown in Figure 6.35. The wave conditions are presented across the East Anglia mesh at two phases of the tide; ebb and slackwater. It can be seen that the wave height is greatest offshore, and decreases in the shallow water at the coastline and on the sand bank. The smallest wave height is seen on the Middle Scroby sand bank where the wind farm is located, this is due to the low water depth. The wave direction is largely constant throughout the mesh but shows a large shift in direction at the sand bank. There is very little difference in wave height and direction between the different phases of the tide.

Water depth

Figure 6.36 presents the free surface elevation and velocity direction for a spring tide coupled with wave 1 at three phases of the tide with and without the wind

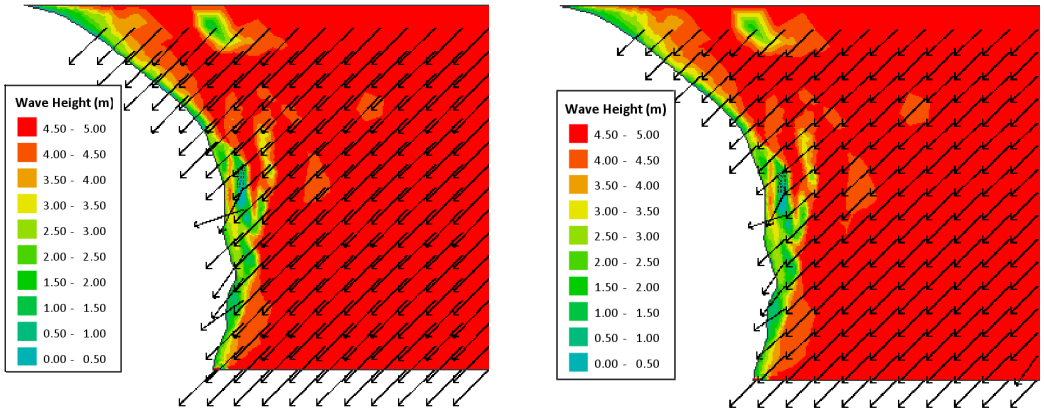

(a) Ebb phase (b) Slackwater

Figure 6.35: Wave height and direction for a spring tide coupled with wave 1 over the East Anglia mesh compared at two phases of the tidal cycle

farm. The tide travels into the region from the north during the flood phase of the tide (Figure 6.36e), reverses at slack water, and leaves the region to the north at the ebb phase. The tidal flow clearly travels around the Scroby Sand Banks close to the shore, due to the shallow water depths. There is little difference in free surface elevation seen here between the model results with and without a wind farm at this scale.

For a closer look at the impacts of the OWF, the water depth variation for a spring tide at the minimum water depth across the west side of the East Anglia mesh is compared in Figure 6.37 for the model runs without a wind farm (Figure 6.37a) and with a wind farm represented in the mesh (Figure 6.37b). The water depth across the region is very variable, the lowest water depths are seen at the sandbank where the Scroby Sands OWF site is located, a deep channel is seen to the west and north of the OWF site. There is little difference on the large scale between the water depth with and without a wind farm present, the natural variations are much greater than any created by the structure. However, at the Scroby Sands site the shallowest water depth extends further across the site for the case with a wind farm present than without.

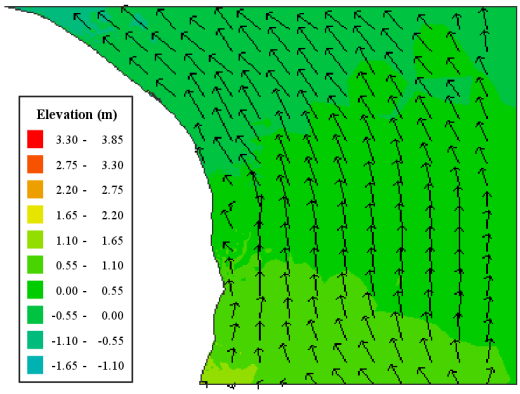

(a) Ebb phase, without OWF

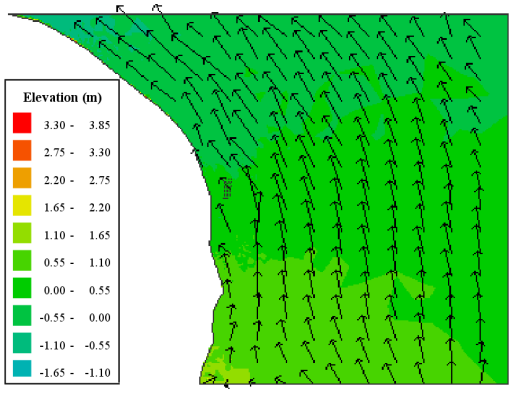

(b) Ebb phase, with OWF

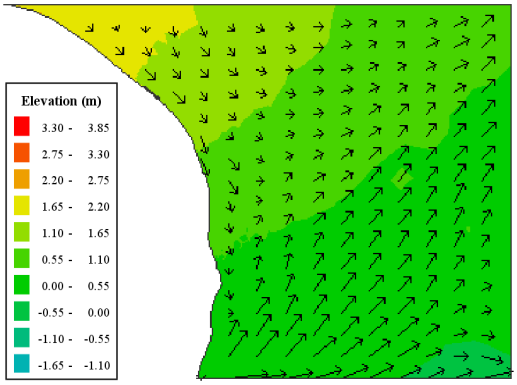

(c) Slackwater, without OWF

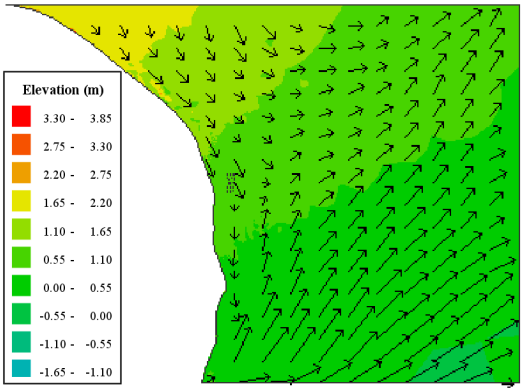

(d) Slackwater, with OWF

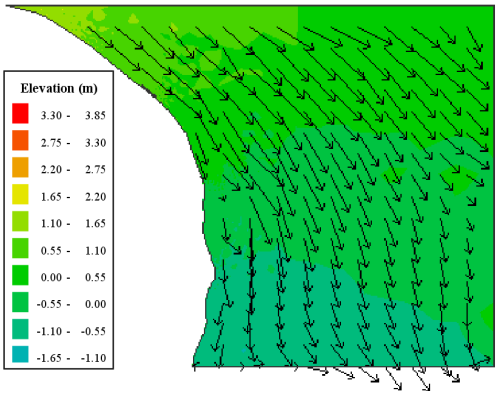

(e) Flood phase, without OWF

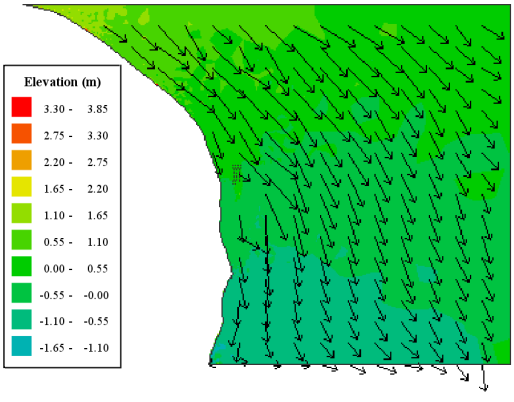

(f) Flood phase, with OWF

Figure 6.36: Free surface elevation and flow velocity for a spring tide coupled with wave 1 over the East Anglia mesh, compared at different phases of the tidal cycle with and without the wind farm

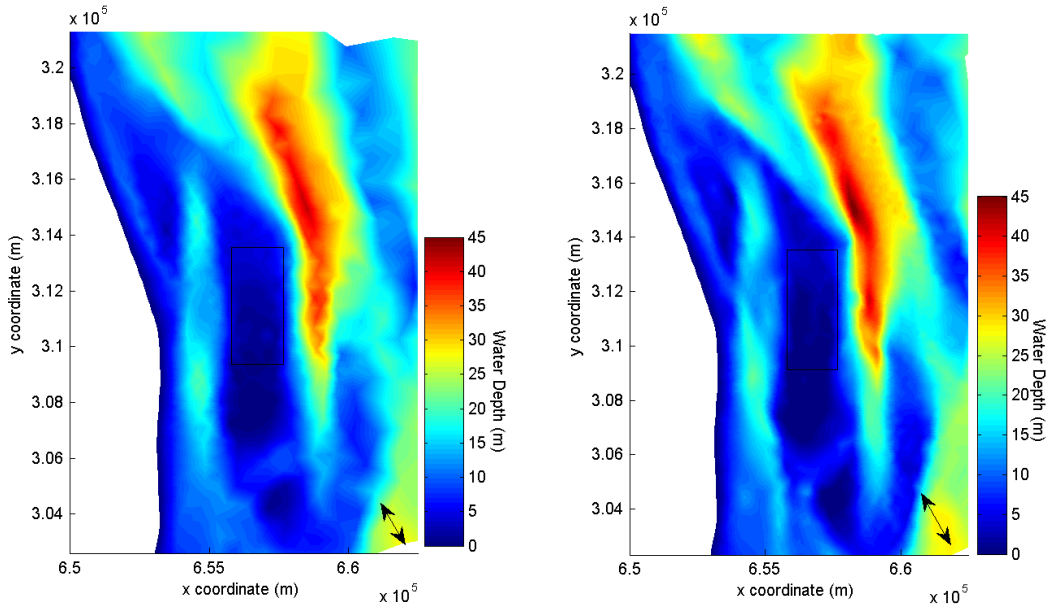

(a) (b)

Figure 6.37: Water depth variation across the East Anglia mesh at the minimum water depth for a spring tide only for a) mesh with no wind farm, b) mesh with wind farm

Flow velocity

Figure 6.38 presents the tidal velocity magnitude and direction across the East Anglia mesh for a spring tide coupled with wave 1. The velocity distribution is shown at a peak ebb and peak flood phase of the tidal cycle for the case with no wind farm (Figure 6.38a & 6.38c) and with the wind farm (Figure 6.38b & 6.38d). During the ebb phase of the tidal cycle the flow travels in a northerly direction. For both the no wind farm and wind farm case the lowest velocities are seen near the coast and at the Scroby sandbank. The greatest velocity are seen to the east and north-east of the sandbank, and are largely influenced by the water depth in the area (Figure 6.37). With the wind farm, there are areas of greater velocity close to the wind farm to the east and west, than seen with no wind farm. The higher velocities in the vicinity of the wind farm could be due to the flow being diverted due to the presence of the wind farm. At the wind farm site, during the ebb phase, the area of low velocity at the sandbank is extended further north, which could be due to the wind farm having a blocking effect on the flow. Similarly, during the flood phase the lowest velocities are seen

close to the coast and at the Scroby sandbank, with the greatest velocities to the north-east of the sandbank. With a wind farm present, greater velocities are seen very close to the wind farm to the north-east, than with no wind farm. The area of low velocity on the sand bank is extended slightly further north with a wind farm present.

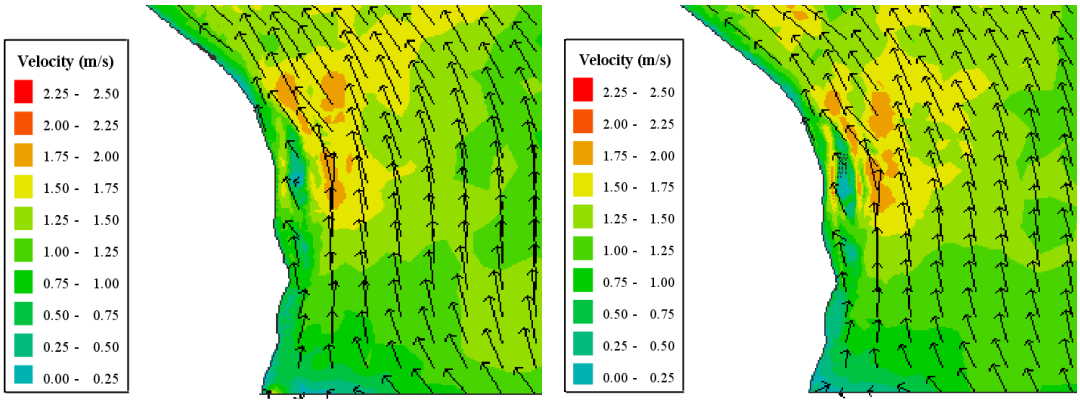

(a) Ebb phase, without OWF

(b) Ebb phase, with OWF

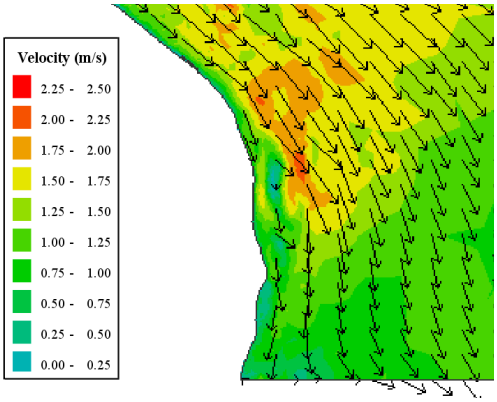

(c) Flood phase, without OWF

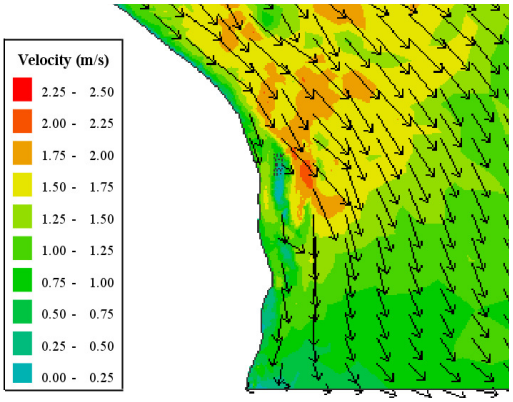

(d) Flood phase, with OWF

Figure 6.38: Flow velocity for a spring tide coupled with wave 1 over the East Anglia mesh, compared at different phases of the tidal cycle with and without the wind farm

Sediment transport and bed evolution

Figure 6.39 shows the computed transport flux across the East Anglia mesh with and without an OWF for a spring tide coupled with wave 1, at three phases of the tide. The sediment flux at this site shows a greater transport flux in the North of the region, close to the coast. The sediment transport flux is greater during the flood (Figure 6.39e) than the ebb (Figure 6.39a), with virtually no sediment flux

at slack water (Figure 6.39c). The greatest transport flux is seen to the east of the Scroby sand banks. The sediment flux at this location appears to be greater in the presence of a wind farm at both the ebb and flood phase, than with no wind farm present. This could be due to the flow being diverted in the presence of the wind farm as seen in Figure 6.38.

Figure 6.40 presents the residual sediment flux over a tidal cycle for the spring tide coupled with wave 1, with (Figure 6.40b) and without (Figure 6.40a) the Scroby Sands wind farm. Over much of the domain the residual sediment flux is very small or zero. The locations with the greatest residual sediment flux correspond with the areas of maximum velocity, as seen in Figure 6.38. For both cases the greatest residual flux is seen to the east of the Scroby sandbank. With the wind farm (Figure 6.40b), the residual sediment flux to the east of the sandbank has a greater magnitude, but a slightly smaller spread in the east direction, than for the case with no wind farm. With the wind farm there is also a high sediment flux to the west of the sandbank, which has a much smaller magnitude than for the no wind farm case. The diverted flow due to the the presence of the wind farm, as shown in Figure 6.38, has created this higher residual flux around the wind farm site.

The sediment flux into and out of the wind farm area is examined, by integrating the sediment flux over a tidal cycle along a box, of size $1730m$ x $3690m$, surrounding the site. The box surrounding the wind farm is presented in Figure 6.41, the top, bottom, left and right lines are used to integrate the sediment flux separately, allowing the sediment movement along the x and y directions to be examined. The sediment flux is calculated first for a spring tide only with no wind farm (Figure 6.42) and with a wind farm (Figure 6.43). The tidal cycle studied begins with the flood tide, followed by the ebb. With no wind farm present the sediment flux along the y direction (Figure 6.42a) begins with a net increase in sediment within the wind farm area as the tide moves across the wind farm site. In the flow reversal there is a greater sediment flux from the top of the wind farm site than the bottom, giving a net sediment decrease from the wind farm site.

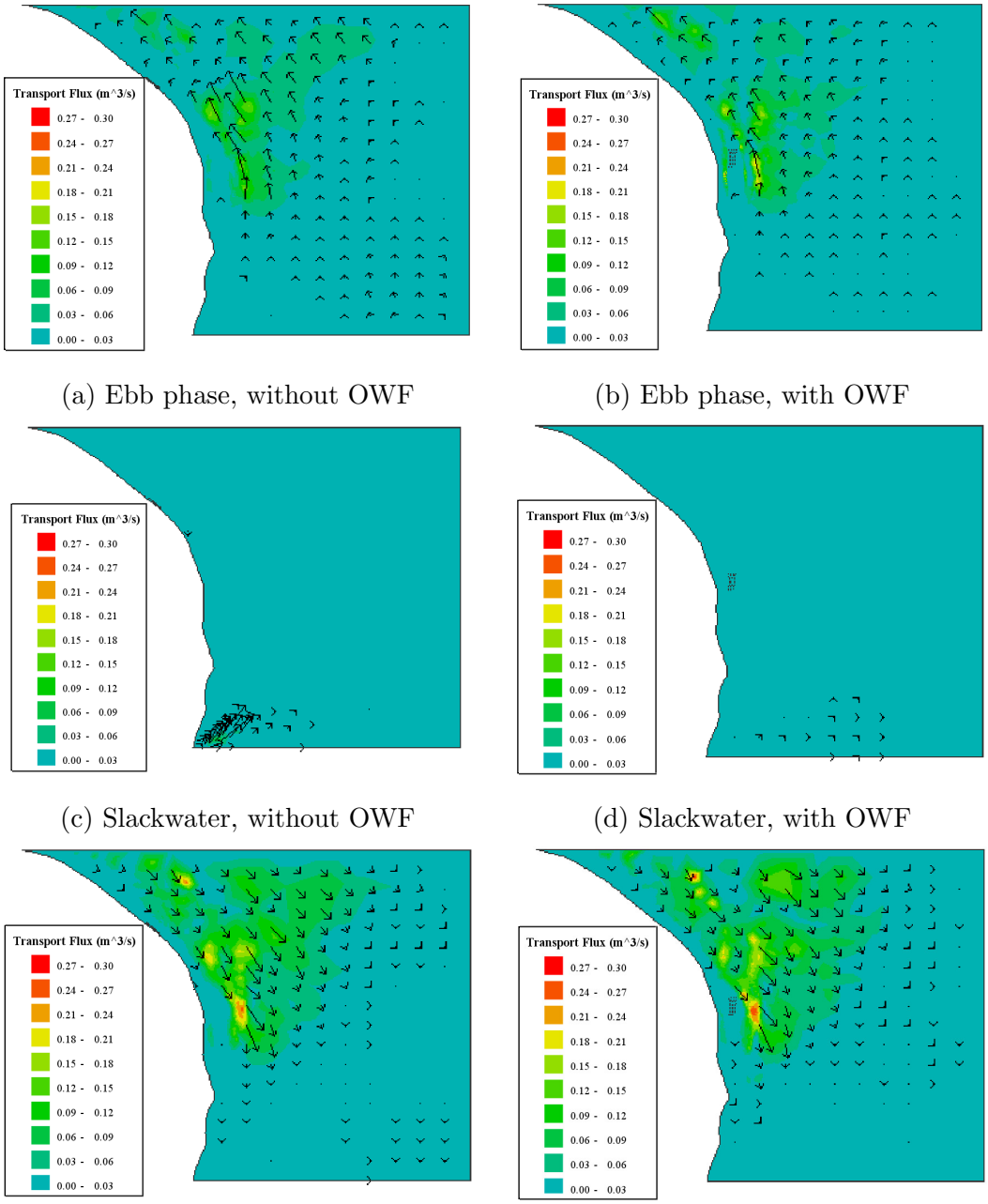

(a) Ebb phase, without OWF

(b) Ebb phase, with OWF

(c) Slackwater, without OWF

(d) Slackwater, with OWF

(e) Flood phase, without OWF

(f) Flood phase, with OWF

Figure 6.39: Sediment transport flux for a spring tide coupled with wave 1 over the East Anglia mesh, compared at different phases of the tidal cycle with and without the wind farm

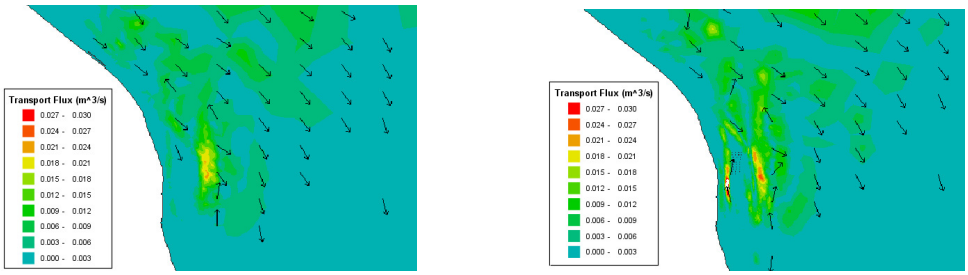

(a) No OWF (b) With OWF

Figure 6.40: Tidal residual sediment flux over the East Anglia mesh with and without a wind farm, for a tide only

Compared to the flux with no wind farm present (Figure 6.43a) the magnitudes of flux during the ebb flow are much smaller with a wind farm present, although the net flux follows the same direction. This is due to the wind farm slowing the flow over the top of the wind farm site as seen in Figure 6.38b, and therefore reducing the sediment flux.

The x direction flux for the case with no wind farm (Figure 6.42b) has a similar flux magnitude as the y direction. During the flood phase of the tide there is net sediment decrease as more sediment leaves the wind farm site than enters it. This is reversed in the ebb tide with a greater sediment flux into the wind farm area. When a wind farm is present (Figure 6.43b) the flux in the x direction is again of a lower magnitude than with no wind farm, due to the reduced velocities. The overall pattern of sediment flux is similar, as is the phase.

The sediment flux for a spring tide coupled with wave 1 shows a similar sediment flux pattern as the spring tide case when no wind farm is present (Figure 6.44). The flood part of the tidal cycle shows larger fluxes for the case with no wave in both the x and y direction, whilst the ebb phase shows similar values. With the wind farm present (Figure 6.45) there is little difference in the sediment flux in the y direction between the test run with a wave and without. However, in the x direction, the net sediment flux is reversed during the flood phase of the tidal cycle when the wave is included.

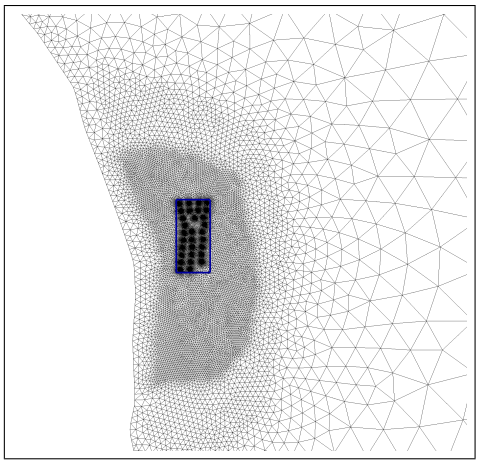

Figure 6.41: Map of East Anglia showing the location of integration box used to calculate the movement of sediment into and out of the Scroby Sands wind farm site

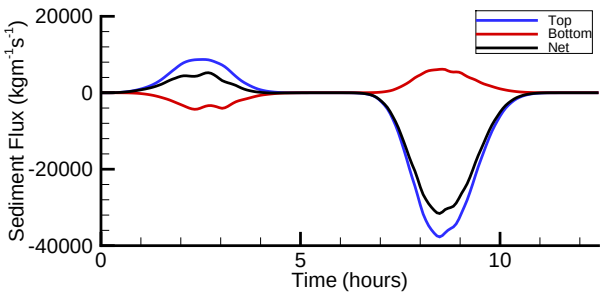

(a)

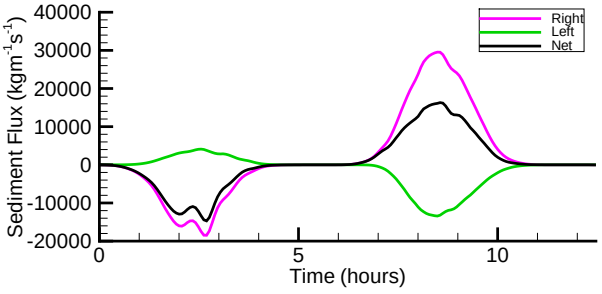

(b)

Figure 6.42: Sediment flux integrated along a box surrounding the wind farm area for a spring tide with no wind farm present. Showing the sediment flux through a) the top and bottom line, and b) the left and right lines

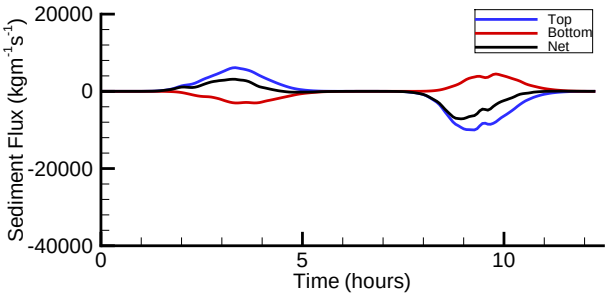

(a)

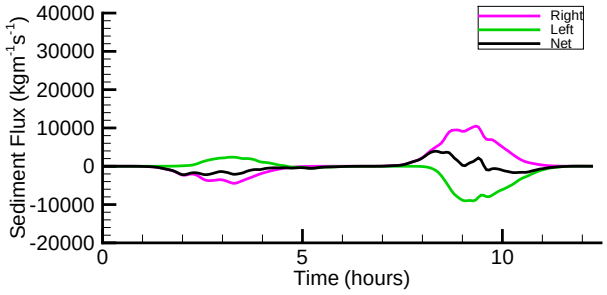

(b)

Figure 6.43: Sediment flux integrated along a box surrounding the wind farm area for a spring tide with the wind farm present. Showing the sediment flux through a) top and bottom line, and b) left and right line

The bed evolution over the wind farm site, covering an area of $6.4 \times 10^6 m^2$ is presented in Figure 6.46. The net sediment erosion/deposition varies between the different model conditions. It is clear that the erosion of sediment is linked to the wave conditions as the greatest wave height exhibits the largest erosion, with the lowest erosion for spring tides seen with no wave and wave 4. The neap tide case has very little influence on the bed evolution over a tidal cycle.

6.2.4 Near field impacts

Waves

The wave height across the top half of the Scroby Sands site is presented in Figure 6.47. The wave height is analysed here at the minimum water depth, for the case of the spring wave coupled with wave 1 (Figure 6.47a), and with wave 4 (Figure 6.47b). Over the wind farm site the wave height is very low, with amplitude increasing to the west of the site where there is fast flow velocities and deep water

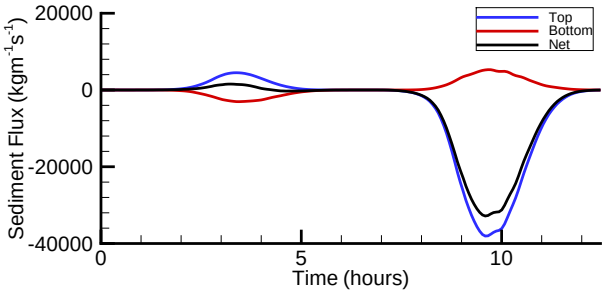

(a)

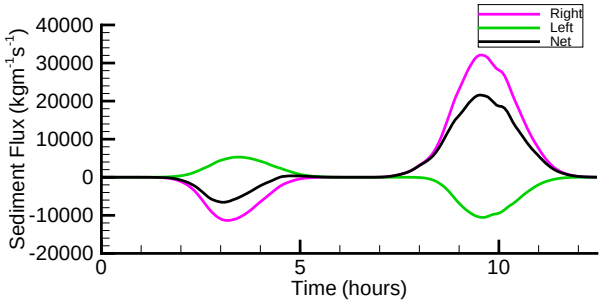

(b)

Figure 6.44: Sediment flux integrated along a box surrounding the wind farm area for a spring tide coupled with wave 1 with no wind farm. Showing the sediment flux through a) top and bottom line, and b) left and right line

depth. The wake patterns are stronger for the wave 1 case, which is expected as this has the greatest wave height, than the wave 4 case. In the shallow water the wakes follow the wave direction line, but this is modified in the deep water, with a direction shift off the sand bank. In both cases the wake effects are limited in extent and no interaction is seen between wakes at the individual structure.

The wave height modifications at the individual foundations are studied at a localised scale in Figure 6.48. The wave heights are presented around a monopile for the spring tide coupled with wave 1 (Figure 6.48a) and wave 4 (Figure 6.48b), as a mean over the tidal cycle. The wave height amplitude across the area is much lower than the boundary values for both waves, wave 1 has an input height at the boundary of $4.5m$, whilst wave 4 has a boundary value of $1.84m$. This decrease is due to the very low water depths at the Scroby Sands site. For the wave 1 case (Figure 6.48a), the wave height shows a sharp decrease in the wake of the pile, which quickly returns to near background values. For the wave 4 (Figure

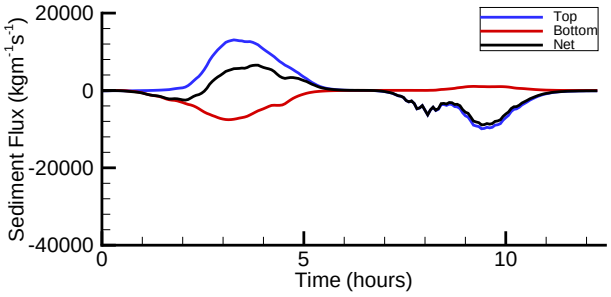

(a)

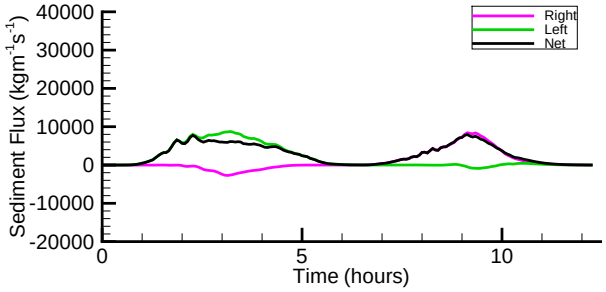

(b)

Figure 6.45: Sediment flux integrated along a box surrounding the wind farm area for a spring tide coupled with wave 1 with the wind farm present. Showing the sediment flux through a) top and bottom line, and b) left and right line

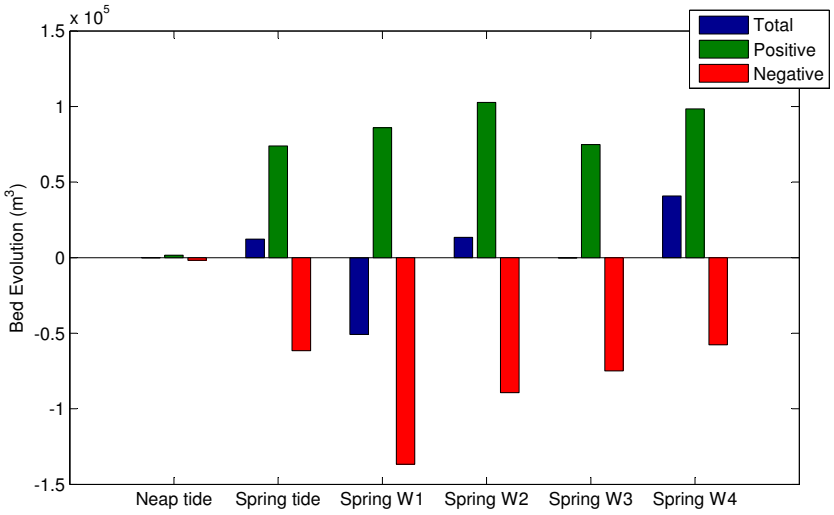

Figure 6.46: Bed evolution bar chart over the Scroby Sands wind farm site for the different tide test runs over a tidal period. The plot shows total evolution change, positive bed change and negative bed change

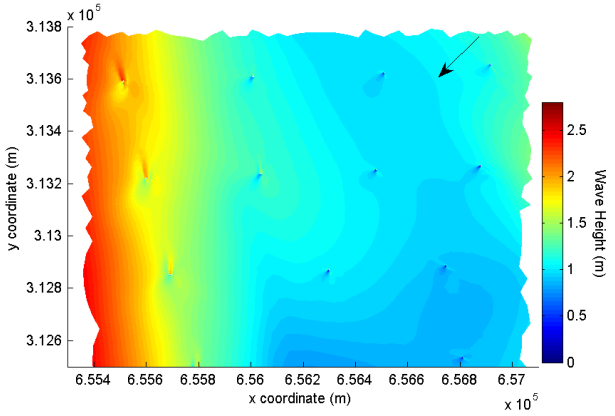

(a)

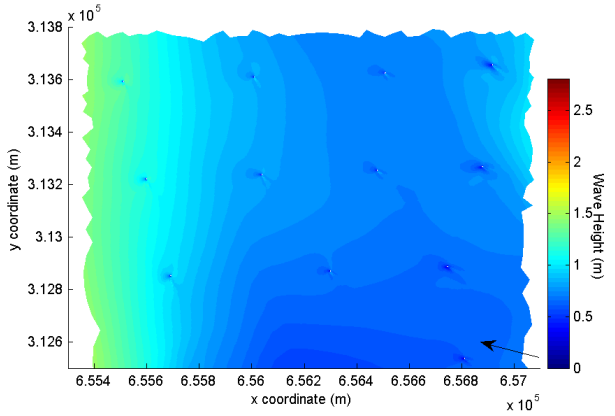

(b)

Figure 6.47: Wave height over the wind farm area at the minimum water depth for a) spring tide coupled with wave 1, and b) spring tide coupled with wave 4

6.48b) case the sharp decrease in wave height behind the pile is very short, but an area of slightly lower than background values does extend beyond the pile. An interesting feature at the wake 4 site is an increase in wave height at one side of the front of the pile, this is likely to be due to a strong wave-current interaction here.

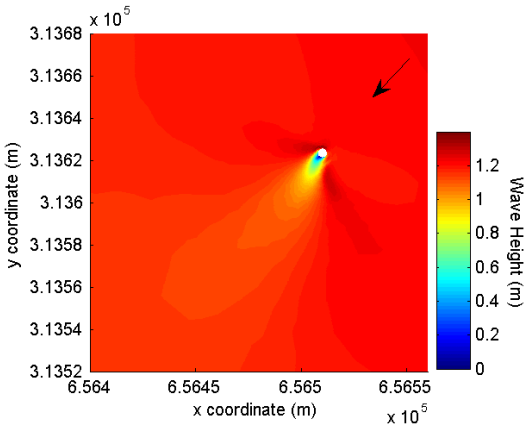

(a)

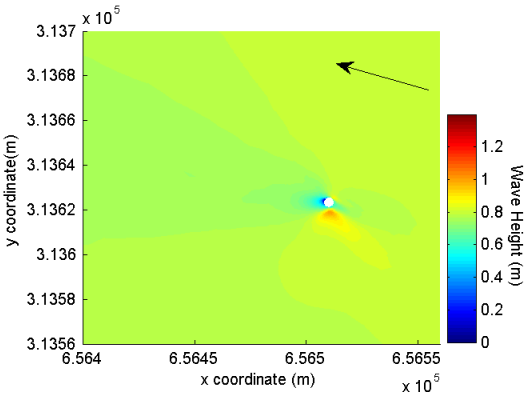

(b)

Figure 6.48: Mean wave height over one turbine monopile for a) spring tide coupled with wave 1, b) spring tide coupled with wave 4

The wave height cross section across a single turbine foundation, along the line of the model run wave direction, is shown in Figure 6.49. The wave heights are plotted as a tidal mean value to remove the influence of changes in water depth. For all model runs, the wave height at the pile location is significantly lower than the boundary value, due to the shallow site. The wave height increases towards the monopile, indicating reflection of the waves off the structure creating

wave-wave interactions, the reflection is greatest for the largest wave height. In the lee wake the wave height decreases to an almost zero value at the pile before increasing with distance away. There is a quick recovery of the wake to near background values, but for all the test cases the wave height is lowered by up to $0.1ms^{-1}$ at a distance of $38D$ behind the structure. This is similar result as seen for the Burbo Bank wind farm (Figure 6.21), where at $35D$ behind the pile wave height was reduced by up to $0.3ms^{-1}$.

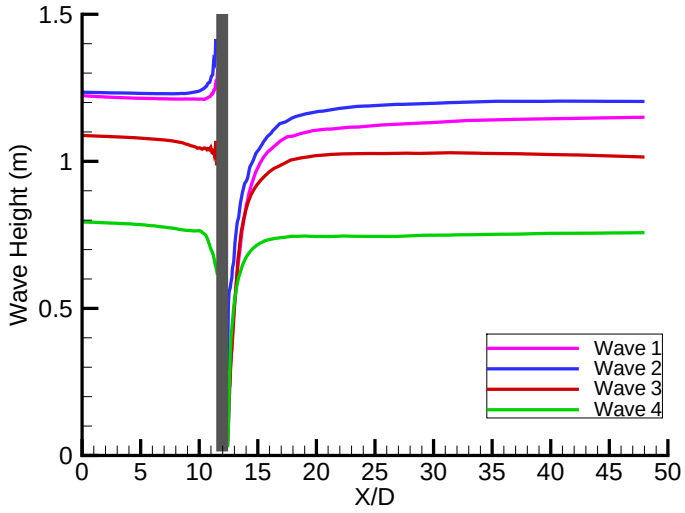

Figure 6.49: Mean wave height over one turbine monopile along the line of wave direction for all model runs

The wave direction modification caused by the structure interaction is not seen at the large scale of the wind farm site, however looking at the localised area around a turbine there is some modification. Figure 6.50 presents the wave direction change at a monopile foundation from the initial boundary wave direction. Results are shown at the peak water depth for the spring tide coupled with wave 1 (Figure 6.50a) and spring tide coupled with wave 4 (Figure 6.50a). For both cases there is a pattern of increasing and decreasing wave angle, as the waves are scattered and forced to travel around the structure, changing the wave direction. In the lee of the pile there is a large change in wave direction, due to the complicated structure interaction on the flow and waves. The wave direction modification pattern extends further from the pile for the wave 1 case than for

the wave 4 case, as the wave 1 case has a larger wave height.

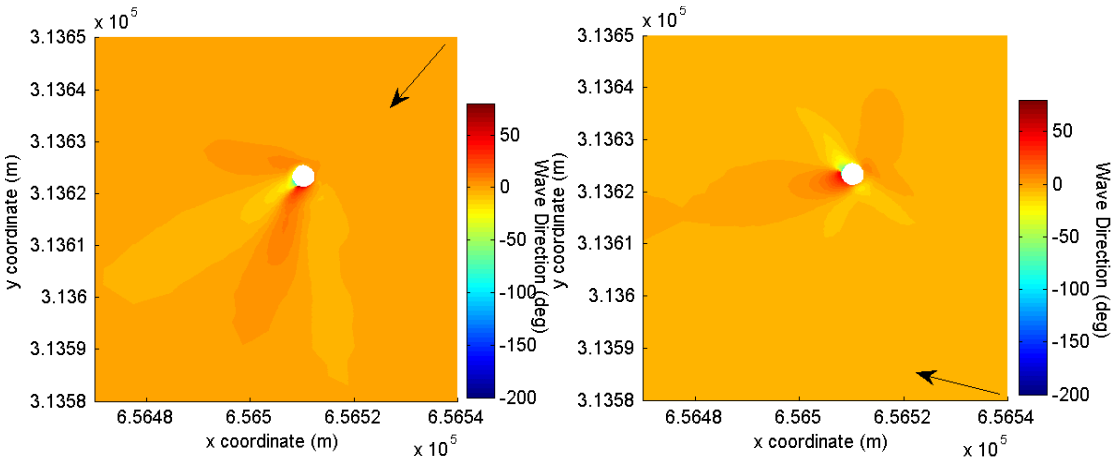

(a) (b)

Figure 6.50: Difference in wave direction at the peak water depth from the direction at the mesh boundary, over one monopile for a) spring tide coupled with wave 1, and b) spring tide coupled with wave 4

Water depth

Water depth variation across an individual monopile at the maximum water depth for a neap and spring tide is presented in Figure 6.51. The plots have different scales, to enable the impact at neap tide to be seen. For the spring tide (Figure 6.51b) there is a decrease in water depth preceding the pile, and in the wake high velocities are seen localised at the pile. For the neap tide case (Figure 6.51a) a different pattern of water depth variation is seen. The highest water depths are seen at the front of the pile slightly to the sides, here the high water depths spread away from the pile. In the lee wake of the pile there are two separate wakes, which extend $1D$ away from the pile, the wake here is of a much smaller extent than for the spring tide.

The water depth cross section along the mean tidal direction at the peak water depth, is plotted for all model runs in Figure 6.52. In all cases the variation in water depth over the pile recovers to background values within $10D$ behind the pile. The neap tide shows little variation across the structure, with a small

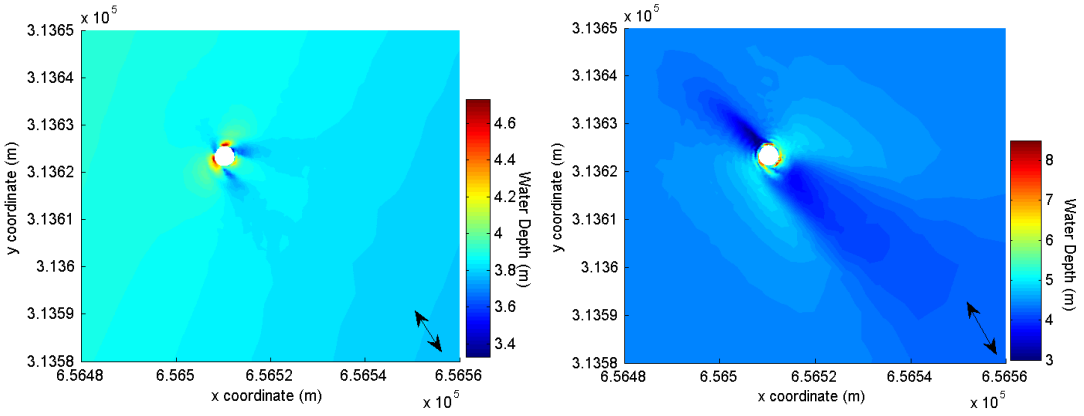

(a) (b)

Figure 6.51: Water depth variation for a single turbine foundation at the maximum water depth for a) neap tide only, and b) spring tide only

decrease in water depth in front and a high water depth behind the pile, which recovers very quickly back to ambient values. For all spring tide cases there are greater variations across the pile, with a sharper and longer decrease in water depth in front of the pile and a longer time to recover behind the pile. At the front of the pile there is a high water depth due to the tide reflecting off the structure. Very close to the pile in the wake, high water depths are seen which are not thought to be plausible in real life and are likely due to the simplification of the 3D flow in the model. The largest waves 1, 2, and 3 appear to suppress the water depth variation across the pile as the structure impact is less apparent in these cases, than from the spring tide only case. This is likely to be due to the angle of the wave shifting the wake in the water depth, so the interaction are seen to a lesser extent along the line of the mean tidal direction. The wave 4 direction is similar to the mean tidal direction, and shows greater decrease in water depth in front of the pile than the spring tide only case. Compared to the results from the Burbo Bank wind farm (Figure 6.25), the water depth at the Scroby Sands site recovers to background values further from the pile at $10D$ rather than $5D$ seen at the Burbo Bank site. At both sites the inclusion of waves with a similar direction to the mean tidal direction, sees larger variations in water depth, due to the wave influence.

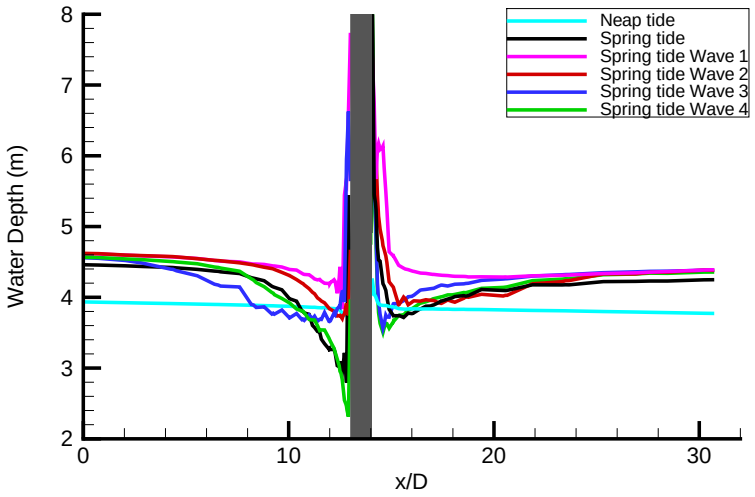

Figure 6.52: Water depth variation as a cross section along the line of mean tidal direction at the turbine, for all model runs

Flow velocity

The depth mean velocity variations across the top half of the Scroby Sands wind farm site are examined for a spring tide and a spring tide coupled with wave 1 in Figure 6.53. The depth mean velocity is examined at the peak ebb velocity. In both cases the velocities are fastest on the eastern side of the site, where there is deeper water. The lowest velocities are seen at the area with the shallowest water depth. This velocity pattern over the site means that the direction of the tidal flow also varies across the wind farm, as the flow curves around the sand bank. This is evidenced by the direction of the wakes seen in the lee of the monopiles, in the deeper areas the flow velocity is in a north-south direction. For both the spring tide (Figure 6.53a) and spring tide coupled with wave 1 (Figure 6.53b) cases the velocity wake effects are visible at the wind farm scale. For the spring tide only case, the wakes across the site are relatively similar in terms of length and do not appear to be very spread behind the pile. For the spring tide coupled with wave 1 case the wake effects are longer than for the spring tide only. The extent of the wake varies across the site and is much greater in the areas of strong velocity, suggesting a strong interaction between waves and currents in this region.

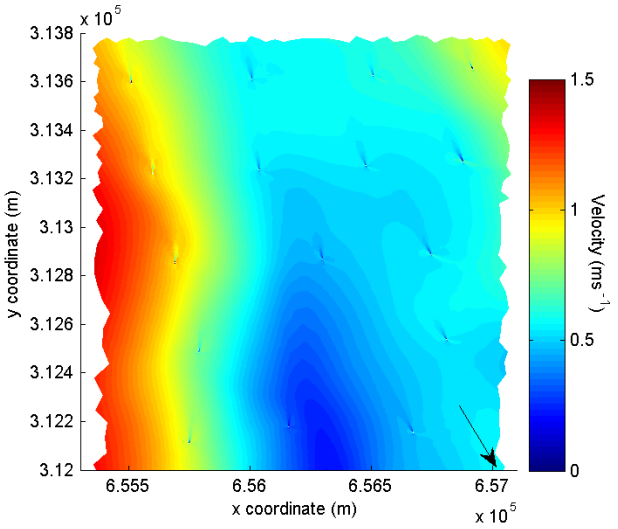

(a)

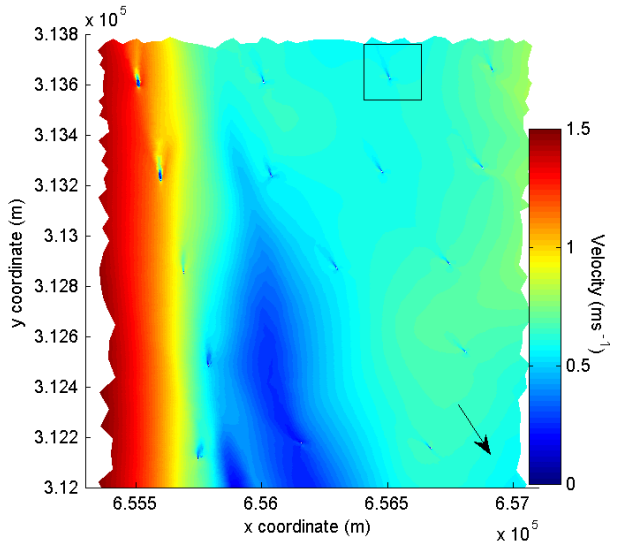

(b)

Figure 6.53: Velocity variation across the top half of the Scroby Sands wind farm site at peak ebb velocity for a) spring tide only, and b) spring tide coupled with wave 1

The depth mean velocity is also analysed at an individual foundation as highlighted in Figure 6.53, this monopile was chosen as it represents average conditions seen at the site. The depth mean velocity magnitude is shown in Figure 6.54 for a neap tide and a spring tide at the peak flood velocity. The neap tide case (Figure 6.54a) sees a decrease in velocity in front of the pile with a wake behind. In the neap tide case there are highest velocities at the side of the pile which spread to a distance of $3-4D$ away from the pile. This is not seen to such an extent in the spring tide case with just a small increase in velocity at the side. The wake extent is similar for both but the neap tide wake appears to be spread wider in the area behind the pile.

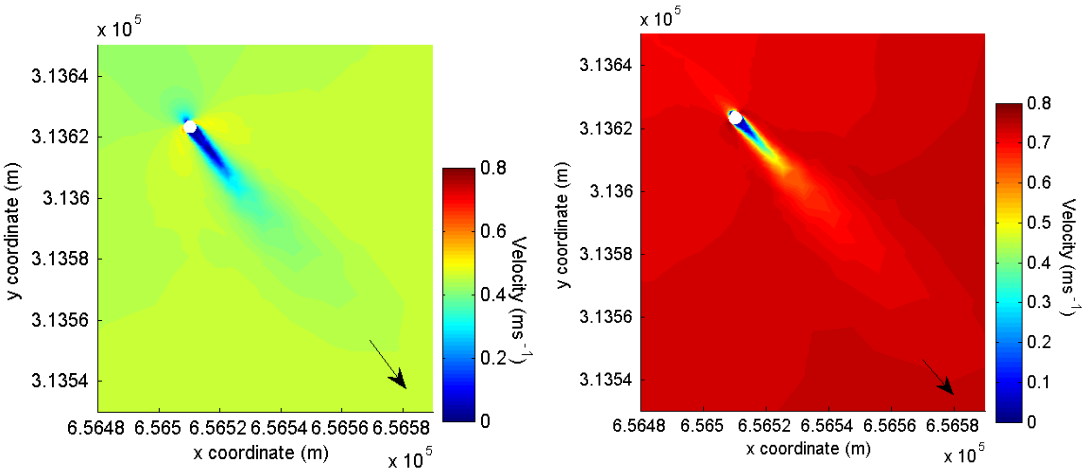

(a) (b)

Figure 6.54: Velocity variation across one turbine at peak flood velocity for a) neap tide only, and b) spring tide only

The vertical cross section taken at the peak flood velocity along the line of tidal direction is shown in Figure 6.55 for a neap tide only, spring tide only, and spring tide coupled with wave 1. The water depth in this location is only $3.5m$ so there is a rapid change in velocity between the surface and seabed. For the neap tide case there is little variation in front of the pile and a small decrease in velocity behind the pile which is greatest in the mid water column, this recovers quickly to the value before the pile. The spring tide case (Figure 6.55b) sees a logarithmic profile in front of the pile, and the velocity decreasing as the flow reaches the pile. There is an area of low velocity behind the pile, which recovers

to background values within $17D$. For the spring tide coupled with wave 1 case (Figure 6.55c) there is evidence of very high velocity at the pile, this is possibly due to the shift in direction of the wake as seen in Figure 6.53b caused by the wave impact on the velocity. For the wave 1 case, the recovery of the wake is much quicker than for the spring tide only case.

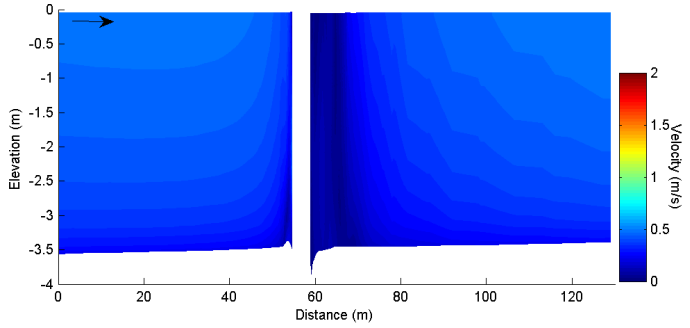

(a)

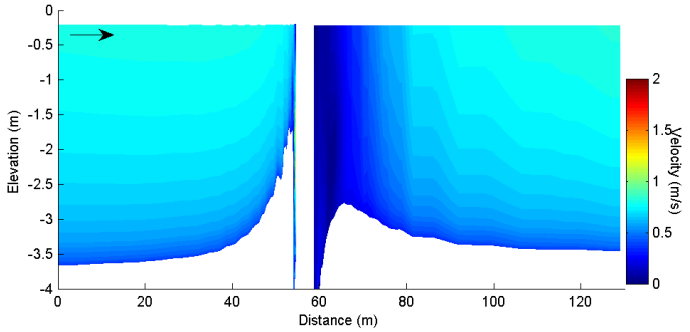

(b)

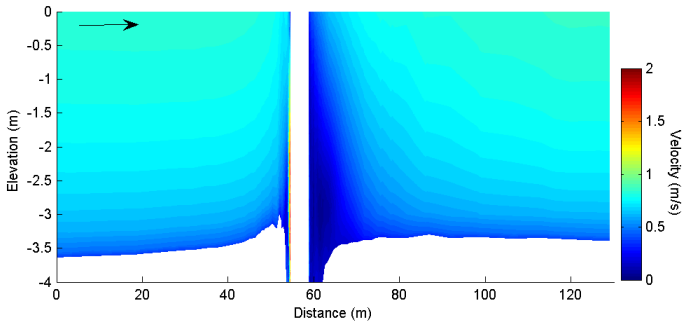

(c)

Figure 6.55: Velocity vertical cross section at peak flood velocity across one turbine for a) neap tide only, b) spring tide only, and c) spring tide coupled with wave 1

Figure 6.56 presents the vertical velocity profiles at various distances in front (Figures 6.56a, 6.56b & 6.56c) and in the wake (Figures 6.56d, 6.56e, 6.56f &

6.56g) of the monopile along the line of the mean tidal direction. As noted for Figure 6.55, a logarithmic profile is seen in front of the pile (Figures 6.56a & 6.56b) where the velocity varies with depth sharply near the bed, increasing only slightly with height further from the bed. The neap tide has an overall lower velocity across the water column, whilst the spring and spring tide coupled with wave 1, have a similar higher velocity. The vertical velocity profile is maintained in all cases, at a distance $5.5D$ in front of the pile. In the vicinity of the pile, $0.5D$ in front of the pile, the velocity profiles begin to be affected by the structure. The neap tide shows a greater velocity overall, and the spring tide coupled with wave 1 shows a greater velocity than the spring tide only, due to the wave impact on the velocity. At this location the bottom evolution also effects the velocity profiles.

In the wake of the pile, at a distance of $-05D$ from the pile (Figure 6.56d), the velocities are reduced across the water column. Turbulence occurs at this location, for the neap and spring tide cases the velocity is reversed in direction. This flow reversal is not seen for the spring tide coupled with wave 1 case, due to the wave interaction on the flow velocity. Further from the pile at a distance of $-4.5D$ in the wake of the pile (Figure 6.56e), the velocity profiles have begun to recover to ambient values. At this location the neap and spring tide cases are closest to the pre-structure values, whilst the spring tide coupled with wave 1 case has lower overall velocities. In all cases the slope of the line, showing the variation of the velocity with water depth, is steeper at this location than in the ambient velocity profiles. At a distance of $16.5D$ behind the pile, the vertical velocity distribution have recovered to background values.

6.2.5 Sediment transport and bed evolution

The tidal mean sediment transport at an individual pile is examined for the spring tide only, and the spring tide coupled with wave 1 case in Figure 6.57. For the spring tide case (Figure 6.57a), the sediment flux shows a clear pattern with the lowest fluxes occurring along the line of the mean tidal direction. This is greatest for the wake during the flood phase of the tidal cycle, as this wake has a greater

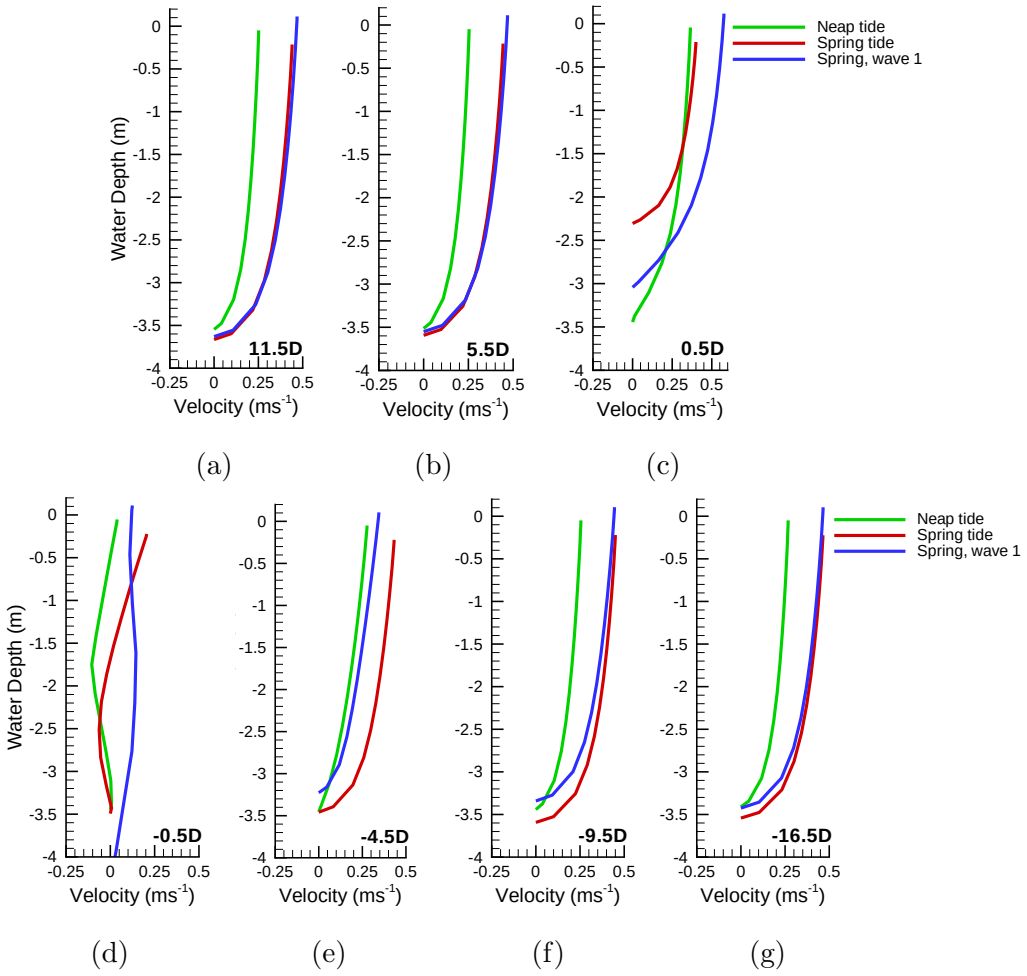

Figure 6.56: Vertical velocity profiles across a wind farm monopile at various distances from the monopile for a) neap tide only, b) spring tide only, and c) spring tide coupled with wave 1

extent than for the ebb phase of the tidal cycle. For the sediment flux for the spring tide coupled with wave 1 (Figure 6.57b), the lower sediment flux wake is shifted in direction due to the presence of the wave.

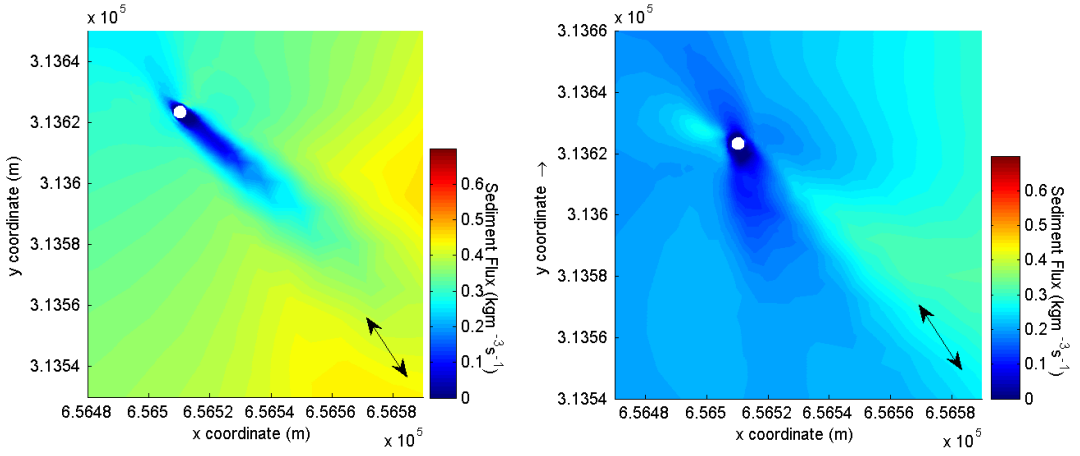

(a) (b)

Figure 6.57: Mean sediment transport over a tidal cycle at one turbine for a) spring tide only and b) spring tide with wave 1

The bed evolution over a tidal cycle at an individual monopile foundation is assessed for the four different wave conditions coupled with a spring tide (Figure 6.58). For all cases there is very little scour apparent, which is unexpected for this site. There is a strong pattern of deposition at the turbine following the line of the mean tidal direction, either side of this deposition are areas of erosion. There is also a small area of erosion very close to the pile, which shows very deep scour. The line of sediment deposition is shifted to the east for the cases with a wave direction which runs perpendicular to the mean tidal direction.

The total bed evolution over a tidal cycle in the area surrounding one foundation for all the test cases is presented in Figure 6.59. The bed change is calculated over an area of $5938m^2$. The bar chart presents the total bed evolution over the site, as well as the volume of negative bed change, i.e. erosion, and positive bed change, i.e. deposition. There is a general net erosion at the individual pile sites for the model runs. The deposition appears to be largely influenced by the wave direction, whereas the erosion shows little pattern.

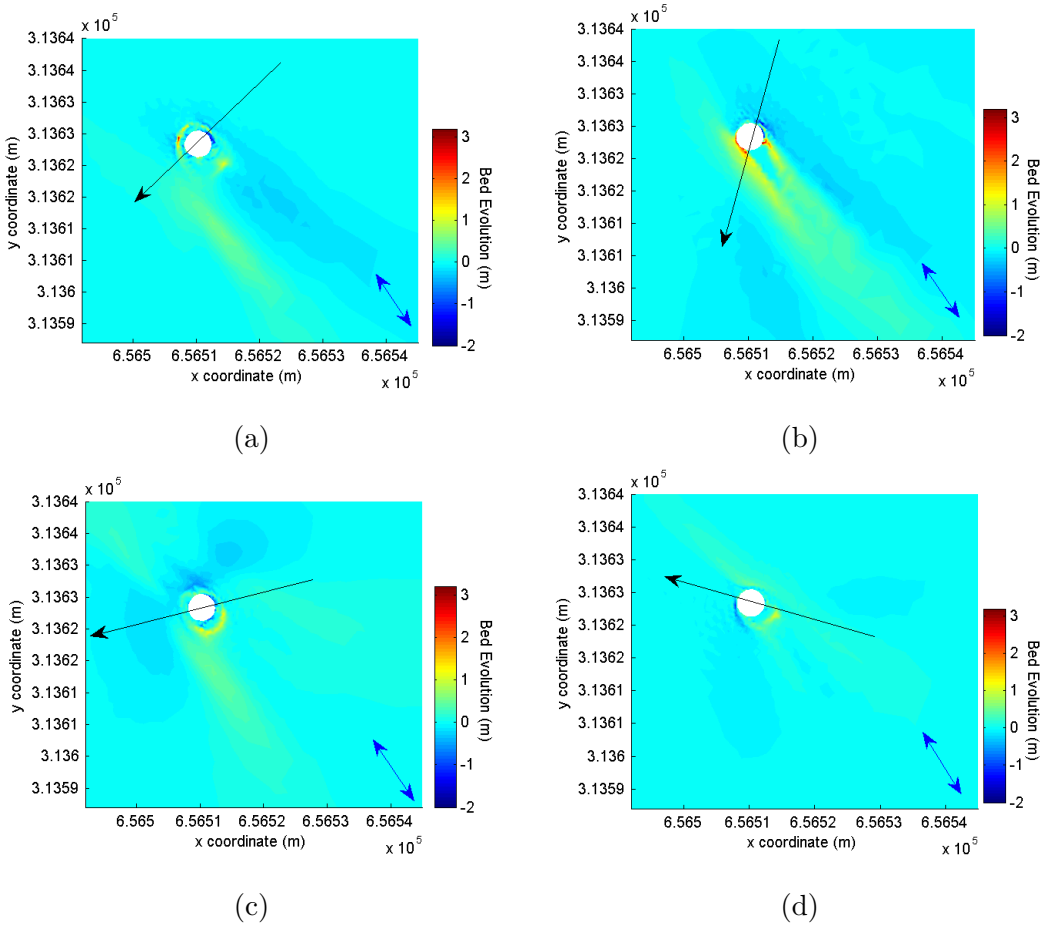

Figure 6.58: Bed evolution over a tidal cycle at one turbine for a) spring tide coupled with wave 1, b) spring tide coupled with wave 2, c) spring tide coupled with wave 3, and d) spring tide coupled with wave 4

Comparing the bed evolution over the wind farm site (Figure 6.46) to the bed evolution at one pile (Figure 6.59), shows a very different pattern for the test model runs. Therefore, the bed evolution at just one structure cannot be used to estimate the whole wind farm impact on bed evolution, especially in such a dynamic site as Scroby Sands.

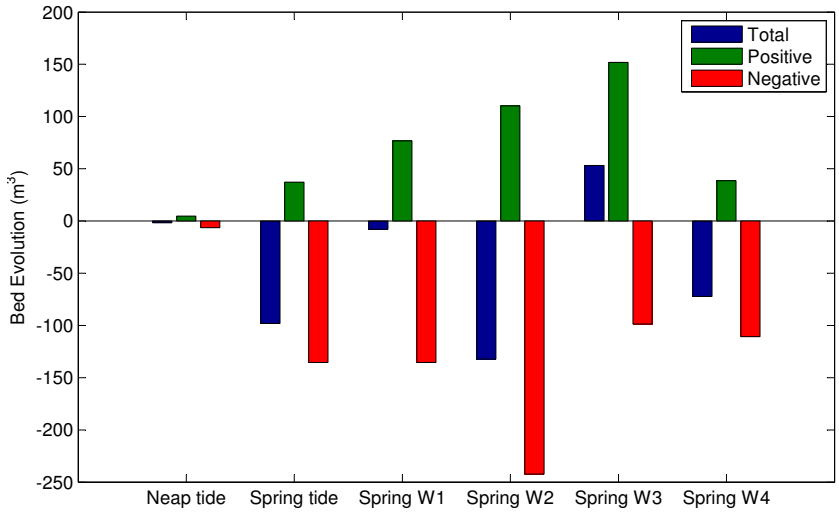

Figure 6.59: Bed evolution bar chart over one turbine at Scroby Sands for the different model runs. The plot shows total evolution change, positive bed change and negative bed change

Chapter 7

Morphological Model

The impacts on hydrodynamics, waves and sediment transport and morphology of the offshore wind farms at both sites have been highlighted for short time periods in the previous chapter. However, as the life cycle of a typical offshore wind farm is in the order of 20 years, it is important to study longer term implications of the structures.

In this chapter the influence on the Burbo Bank wind farm on large scale coastal morphology is assessed over a year period. The morphological prediction compares two methods for generating a set of representative waves, based on frequency of occurrence and the wave energy. The morphological predictions show that the wind farm in Liverpool Bay influences the sediment transport across the Great Burbo Flats and the dredged channel. The scour development at the individual turbines is also assessed and related to empirical scour depth formula and sediment scour patterns measured at the wind farm site.

7.1 Methodology

As discussed previously in Chapter 2, it is not feasible for all hydrodynamic forcing within a coastal domain over a period of years to be included in a computational model, due to computational expense. In order to model the wind farm impacts over a longer time period of a year, the model input is schematised and a morphological factor is used to lengthen the morphological development period.

The climatic wind conditions and any river inflow are reduced to yearly averages as discussed in Chapter 5. The tide is schematised to produce a morphological tide which accounts for patterns in sediment morphology change over a spring-neap cycle. The wave conditions are schematised using two different methods to produce representative wave conditions over a year. Finally a morphological factor is calculated, which is applied to the sediment transport model to account for long term predictions. In the following sections the model input reduction is calculated for Liverpool Bay.

7.1.1 Tidal schematisation

The tidal input has been reduced to a single morphological tide, which takes account of the the sediment transport residual and direction over a spring-neap cycle (Latteux, 1995). The method set out by Roelvink et al. (2012) is used to calculate the morphological tide, as follows;

- To reduce the computational time for calculating the morphological tide a coarser mesh is created. This coarser mesh is still capable of highlighting the variations in bathymetry within the region, but does not include the wind farm. The numerical mesh for Liverpool Bay is reduced to a mesh of approximately 2600 elements, which considerably reduces computation time.

- The model inputs are initially reduced, so that only those inputs with a significant impact on the sediment transport regime are included. The wind and riverine inputs are taken as constants as calculated in the Chapter 5.

- The model is run for a tide only, where TELEMAC is coupled with SISYPHE over an average spring-neap cycle.

- The sediment transport over the the spring-neap cycle is divided into contributions from the separate tidal cycles, and the bed evolution determined for each tidal cycle. The separate tidal cycles making up the spring-neap cycle are presented in Figure 7.1.

- The tidal cycles are weighted according to their occurrence over the spring-neap cycle and their contribution to bathymetry change. The weighting for each tidal cycle is calculated as;

$$Weighting = \frac{Evolution * Occurence}{\Sigma\left(Evolution * Occurence\right)} \tag{7.1}$$

- The morphological tide, tidal range can then be calculated using the equation;

$$Morpholgical\ tidal\ range = \Sigma\left(Tidal\ range * Weighting\right) \tag{7.2}$$

- The calculated morphological tidal range is then recreated by varying the tidal data input to produce the morphological tide.

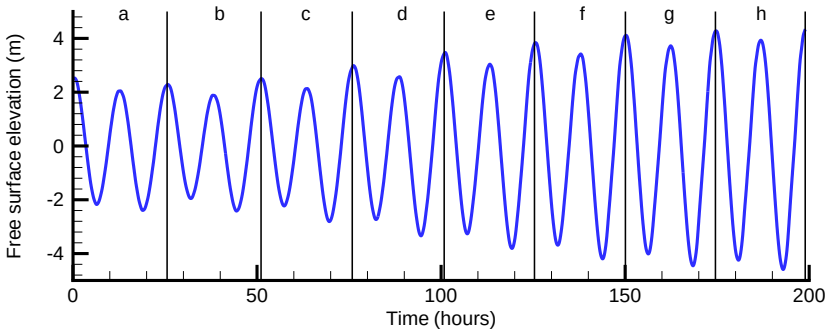

Figure 7.1: Free surface elevation over a spring-neap cycle for Liverpool Bay, the individual tidal cycles are highlighted

Table 7.1 presents the tidal ranges from an average spring neap cycle in Liverpool Bay with the computed bed level changes for the respective tides. The weighting factor, calculated by Equation 7.1, indicates that the smallest tides contribute very little to the overall bathymetry change within the region. The tidal range for the morphological tide is calculated, from Equation 7.2, as $8.27m$. Typically morphological tides have a tidal range that is $7-20\%$ higher than the mean tide (De Vriend et al., 1993), this holds true for the calculation for Liverpool Bay as the morphological tide has an amplitude that is 18% higher than the mean tide of $7.0m$.

Tide	Tidal Height Class (m)	Bed level change (m)	Occurrence	Weighting %
a	4.68	-0.352	1/14	0.50
b	4.92	-0.458	1/7	1.29
c	5.79	-1.07	1/7	3.01
d	6.81	-2.34	1/7	6.60
e	7.65	-4.61	1/7	12.99
f	8.30	-7.08	1/7	19.95
g	8.73	-11.81	1/7	33.29
h	8.94	-15.88	1/14	22.37

Table 7.1: Computed Bed level changes for Liverpool Bay for an average spring-neap cycle with the respective weighting factors

7.1.2 Wave schematisation

The wave input is also reduced to a set of wave conditions which replicate the average wave conditions over a year period, the method of many single representative waves is used. Two methods are studied here to schematise the year long wave conditions to generate a set of representative wave conditions. Method 1 divides the wave conditions into four bins based on the frequency of occurrence of the waves (Chesher and Miles, 1992), whilst Method 2 divides the wave conditions into four bins which have equal wave energy (Daly et al., 2013).

For both methods of wave input schematisation, a year long period of wave data is taken from the Liverpool Bay WaveNet Buoy over the period 01/01/2007 - 31/12/2007. The wave conditions over the period are initially grouped into wave direction ranges of 30°. The wave conditions for 2007 are presented in Figure 6.1. The four dominant wave directions are $285°, 315°, 255°$ and 345°, only the waves within the dominant wave direction range of $240° - 360°$ are further examined.

Method 1

Method 1 divides the wave conditions into representative waves based on the frequency of occurrence. For each of the dominant wave direction classes $285°, 315°, 255°$

Number	Wave Direction (°)	Wave Height (m)	Wave Period (s)
1a	255	1.09	4.89
1b	285	1.33	6.01
1c	315	1.12	5.63
1d	345	0.93	4.58

Table 7.2: Representative wave conditions chosen for the morphological model runs for Liverpool Bay. The wave conditions are selected using Method 1, based on the frequency of occurrence of the waves

and 345°, a representative wave height is calculated based on it's occurrence at the given direction, through the following equation;

$$H_0 = \left[\frac{\Sigma\left(f_w H_s\right)}{\Sigma f_w}\right] \tag{7.3}$$

where H_0 is the representative significant wave height, H_s is the significant wave height, and f_w is the frequency of any given wave height.

The representative waves are then assigned the mean period of the directional group. The four chosen representative wave conditions are presented in Table 7.2.

Figure 7.2 presents the significant wave height and wave direction distribution form the Liverpool Bay WaveNet Buoy, during 2007. The four representative wave conditions determined by Method 1 are shown on the plot, highlighting that this method selects the representative wave conditions based mainly on average conditions, rather than extreme conditions.

Method 2

Method 2 divides the wave conditions into bins of equal wave energy, from which representative wave conditions are selected. For each wave during the year 2007, the energy flux F_e is calculated as;

$$F_e = Ec_g \tag{7.4}$$

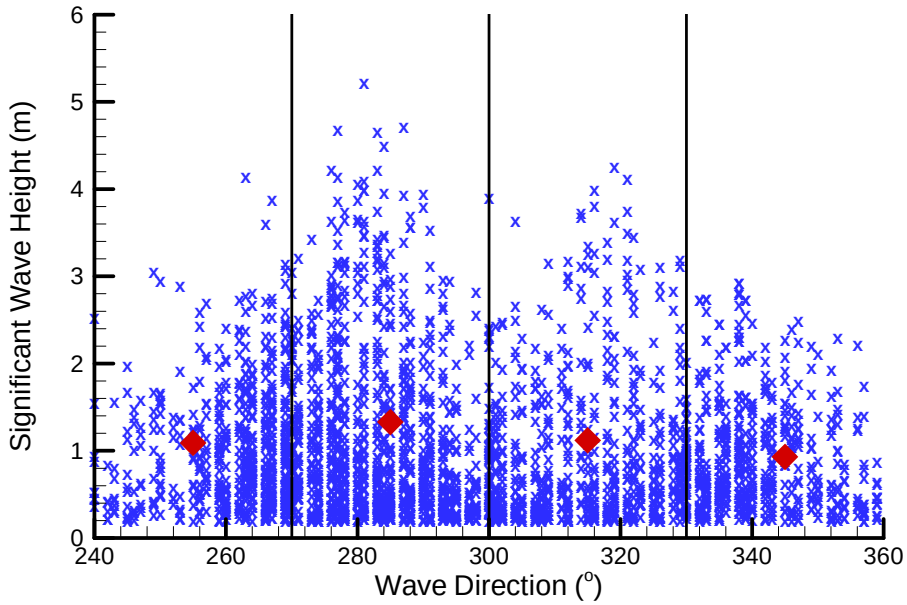

Figure 7.2: Wave condition distribution from the Liverpool Bay WaveNet Buoy during 2007. The representative wave conditions (red diamonds) are determined by Method 1, based on the frequency of occurrence of the waves

where E is the wave energy, and c_g is the wave group velocity.
The wave energy, E, is defined as;

$$E = \frac{1}{2}\rho g H_s^2 \tag{7.5}$$

where H_s is the significant wave height. The wave group velocity, c_g, is defined in deep water as;

$$c_g = g\frac{T_p}{4\pi} \tag{7.6}$$

where T_p is the peak period.
The equation for the energy flux, F_e, can therefore be written in the form;

$$F_e = \frac{1}{32\pi}\rho g^2 {H_s}^2 T_p \tag{7.7}$$

The cumulative sum of the energy flux, based on the waves ranked by direction, is used to generate four bins of equal wave energy flux. From these bins the significant wave height and wave direction are determined based on the mean energy flux within the bin. The wave period is calculated as an average from the respective bin. The representative wave conditions determined by Method 2 are

Number	Wave Direction (°)	Wave Height (m)	Wave Period (s)
2a	267.21	2.16	5.09
2b	280.24	3.28	5.78
2c	296.55	2.41	5.42
2d	333.25	2.28	4.83

Table 7.3: Representative wave conditions chosen for the morphological model runs for Liverpool Bay. The wave conditions are selected using Method 2, based on the wave energy flux

presented in Table 7.3.

The representative wave conditions determined by Method 2, are presented in Figure 7.3, with the significant wave height and wave direction distribution over the year 2007. It is clear that Method 2 takes into account the extreme conditions seen in the wave distribution.

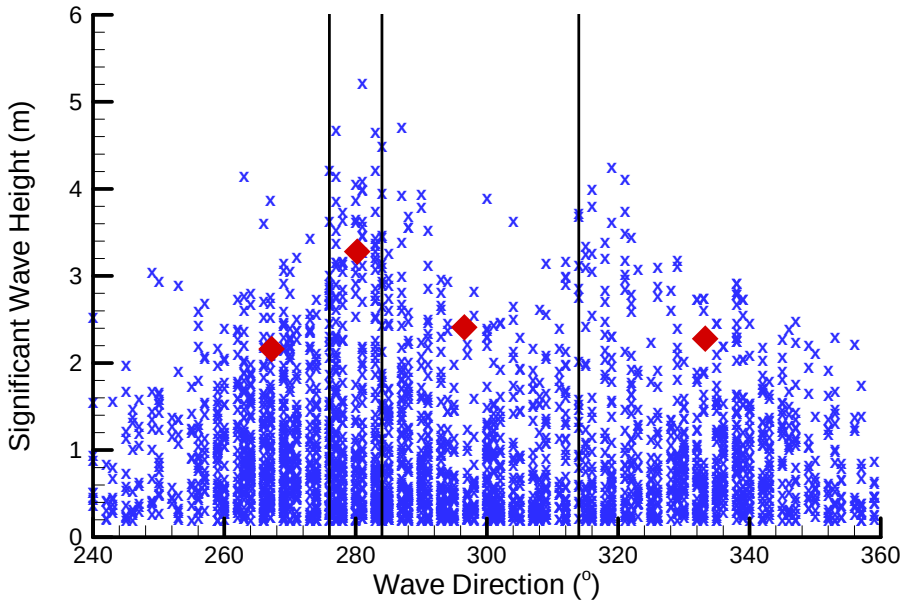

Figure 7.3: Wave condition distribution from the Liverpool Bay WaveNet Buoy during 2007. The representative wave conditions (red diamonds) are determined by Method 2, based on the wave energy distribution

The representative wave conditions have greater wave heights as calculated by Method 2, than Method 1. Therefore, it is likely that the wave conditions from Method 2 will generate a greater sediment flux. Method 2 also produces greater variability in wave height and wave direction bin range than seen for the representative wave conditions from Method 1.

7.1.3 Morphological Factor

The long term morphological evolution calculation is made using a Morphological acceleration factor (MOFAC) included in the sediment transport module SISYPHE. The bed level changes at each time step are multiplied by a morphological factor. The Morphological factor is calculated using the method of Dissanayake (2011), for both sets of wave conditions based on the occurrence and the contribution to bed level change.

The morphological tide coupled with the representative waves from both methods are run separately, and their contribution to bed evolution over one tidal cycle is calculated. The wave conditions are then weighted based on their contribution to bed evolution and occurrence of the wave direction. The morphological acceleration factor is calculated for a predicted morphological change over a period of a year. The morphological acceleration factor is calculated as;

$$MOFAC_i = \frac{T_{Morpho}}{T_{Hydro}} \times w_f \tag{7.8}$$

where $i = 1, 2, 3, 4$ index of the wave condition; T_{Morpho} is the morphological period; T_{Hydro} is the hydrodynamic period the model will be run for, w_f is the weighting factor for the wave conditions.

For the year long morphological period, the hydrodynamic period is chosen as 5 tides. A very large MOFAC value slows the computational time due to instability issues, a hydrodynamic period of 5 tides provides a good balance between stability and computational time. Using this method the morphology change for a year can be predicted by running the model for 5 tides. The final calculated MOFAC values for the Method 1 wave conditions are presented in Table 7.4, and

Wave	Bed Change (m)	Direction occurrence %	Weighting %	MORFAC
1A	-5.57	21.4	20.18	28.46
1B	-6.84	35.2	40.75	57.49
1C	-5.36	25.3	22.95	32.38
1D	-5.29	18.0	16.12	22.74

Table 7.4: Computed bed level changes within Liverpool Bay for the four representative wave conditions calculated by Method 1, with their respective weighting factors and calculated morphological acceleration factor

Wave	Bed Change (m)	Weighting %	MORFAC
2A	-0.468	28.49	40.19
2B	-0.483	11.84	16.71
2C	-0.475	28.97	40.87
2D	-0.481	30.69	43.29

Table 7.5: Computed bed level changes within Liverpool Bay for the four representative wave conditions calculated by Method 2, with their respective weighting factors and calculated morphological acceleration factor

for the Method 2 wave conditions in Table 7.5

7.2 Results

The representative wave conditions coupled with the morphological tide were run consecutively over 5 tidal cycles, for both methods, using the morphological factor to predict the morphological changes over the period of a year.

7.2.1 Sediment flux

The residual sediment transport fluxes over the whole of Liverpool Bay mesh are presented with no wind farm, for both Method 1 and Method 2 in Figures 7.4 & 7.5. The majority of Liverpool Bay has little or no residual sediment flux. The residual sediment flux is limited to the South-Eastern corner of the Bay, to in-

clude the Dee estuary, Mersey estuary, and the dredged channel. Within the Dee Estuary residual transport occurs, for both methods, around Hilbre Island and at the tidal flats. The Mersey estuary has the strongest residual sediment flux seen within Liverpool Bay. In the Mersey Estuary there is an area of divergence in the Narrows, to the south of the Narrows the dominant residual flux is to the south, moving sediment into the estuary, which, fits with the Mersey acting as a sediment sink, as discussed in Chapter 5. To the North of the Narrows, the residual transport flux is to the North-West into Liverpool Bay. From the mouth of the Mersey, the residual flux pathway is mainly along the dredged channel, with a smaller flux across the Burbo Flats.

The residual sediment flux calculated by Method 1 (Figure 7.4) and Method 2 (Figure 7.5) are largely similar across Liverpool Bay. For the Method 2 case, there is a greater sediment flux in the Mersey Narrows than for Method 1. There is also a larger area with high residual sediment flux at the mouth of the Mersey, into the dredged channel. The greater sediment fluxes calculated by Method 2 are due to the greater wave heights used to assess the morphological evolution.

Figures 7.6 & 7.7 present the residual sediment flux calculated by Methods 1 and 2, with the Burbo Bank wind farm represented in the mesh. Both methods show large differences in residual sediment flux with a wind farm compared with no wind farm. The results for Method 1, shows the flux in the Mersey estuary is greater and occurs over a larger area, than with no wind farm. With the wind farm a lower residual sediment flux magnitude occurs at the mouth of the estuary and into the dredged channel, however, the lower flux is spread over a larger lateral area. The residual flux from the Mersey Estuary across the Burbo Flats has a greater magnitude and is spread over a larger area with the wind farm present. This flux creates a residual sediment transport pathway to the south-east corner of the Burbo Bank wind farm. There is also a greater flux and wider spread, along the dredged channel to the north of the wind farm site.

The residual sediment flux modelling completed with Method 2 (Figure 7.7),

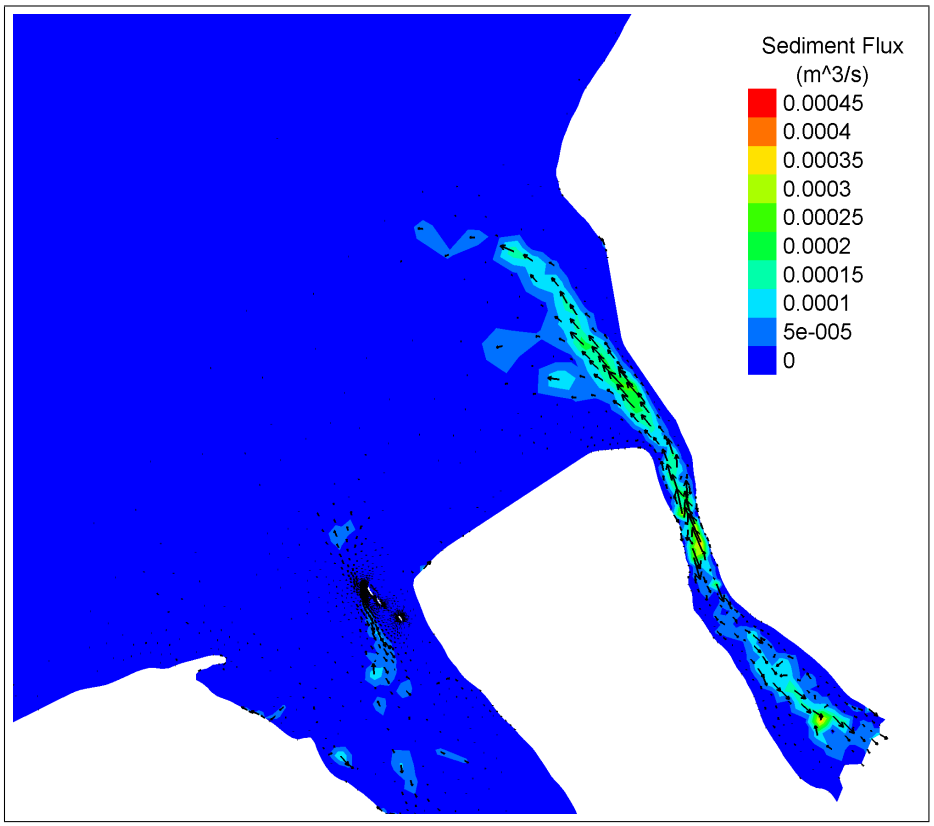

Figure 7.4: Residual sediment transport flux in Liverpool Bay over a year period without a wind farm, where the wave schematisation is determined by Method 1

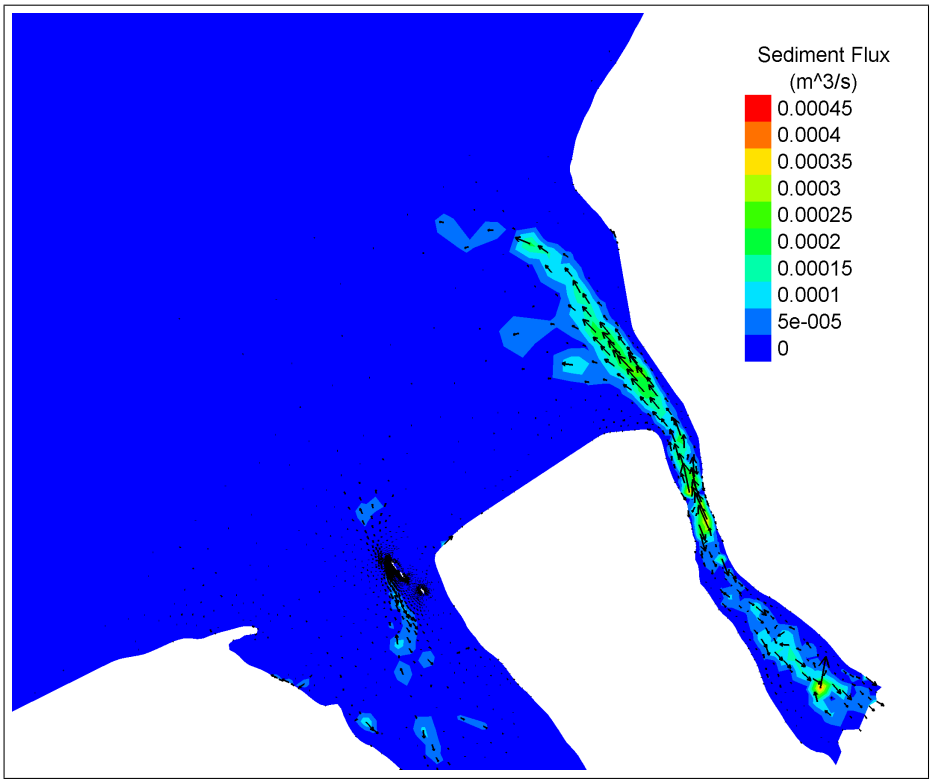

Figure 7.5: Residual sediment transport flux in Liverpool Bay over a year period without a wind farm, where the wave schematisation is determined by Method 2

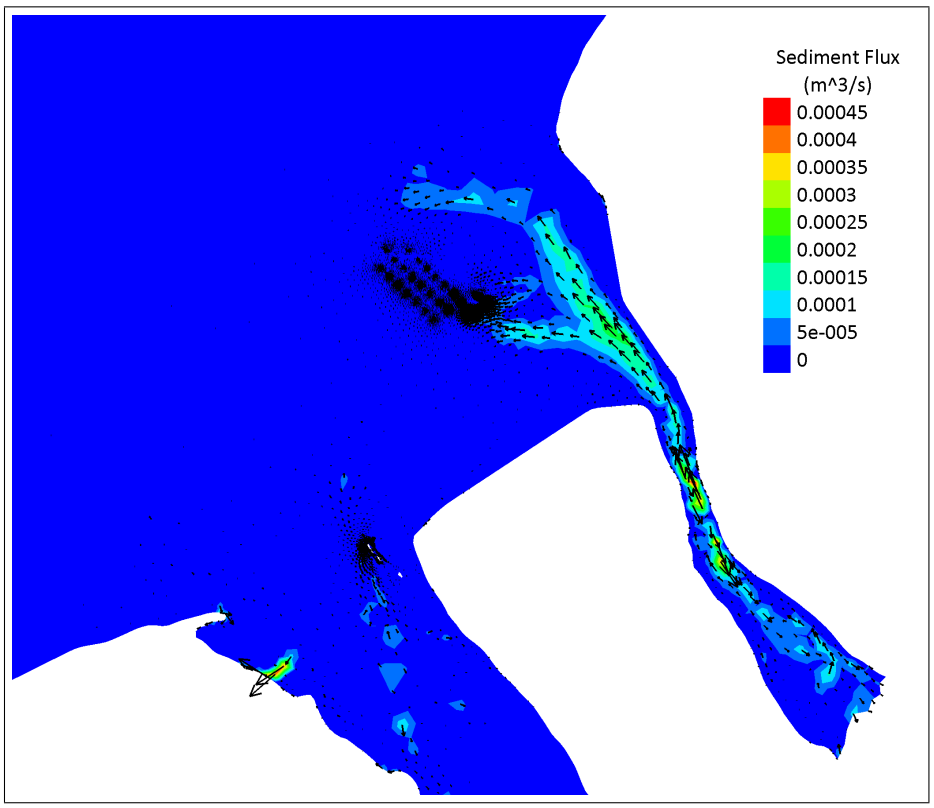

Figure 7.6: Residual sediment transport flux in Liverpool Bay over a year period with a wind farm, where the wave schematisation is determined by Method 1

shows a similar pattern with the wind farm as Method 1. With the wind farm present in the mesh, there is a lower sediment flux in the dredged channel compared with the no wind farm case, but this is spread over a larger area. There is also a greater sediment flux across the Burbo Flats and a larger residual sediment flux to the north of the wind farm site, than for the case with no wind farm. Additionally, the divergence point is less clear with the wind farm present, the residual flux appears to travel in a southerly direction in the middle of the channel, and northerly at the edge of the channel.

The Method 2 sediment flux modelling has a lower peak flux in the dredged channel and a lower flux in the Mersey Estuary, than for the Method 1 case. However, the Method 2 sediment flux is spread over a larger area.

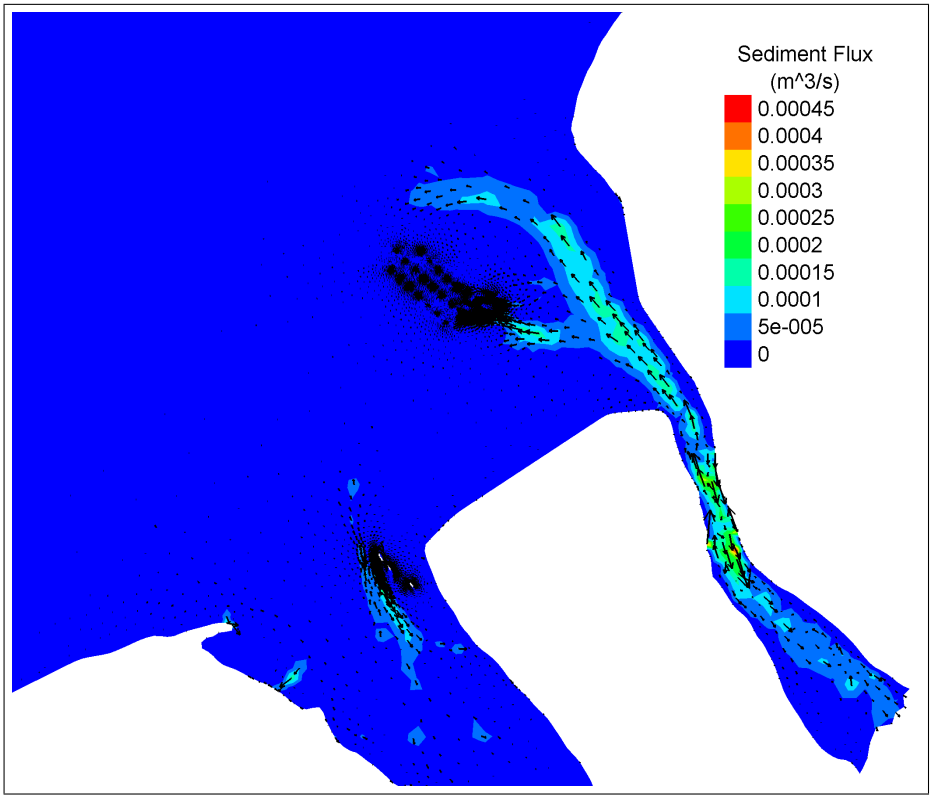

Figure 7.7: Residual sediment transport flux in Liverpool Bay over a year period with a wind farm, where the wave schematisation is determined by Method 2

The residual sediment flux pathways at the Burbo Bank wind farm array are presented in Figure 7.8 & 7.9, as determined by Method 1 and 2. Residual sediment fluxes are shown surrounding all the wind turbine foundation structures

within the array, for both methods. The greatest sediment fluxes are seen in the south-eastern corner of the wind farm array. For the Method 1 case, the two most south-easterly turbine foundations are impacted by the sediment flux pathway, with large residual fluxes at these turbines.

The residual sediment flux in the south-eastern corner of the wind farm are greater for Method 2 (Figure 7.9), than seen previously for Method 1, due to the higher wave heights modelled here. For Method 2, there are a larger number of turbine foundations influenced by the sediment flux pathway than for Method 1. The five most south-easterly foundations are impacted here, by the large residual flux into the wind farm array.

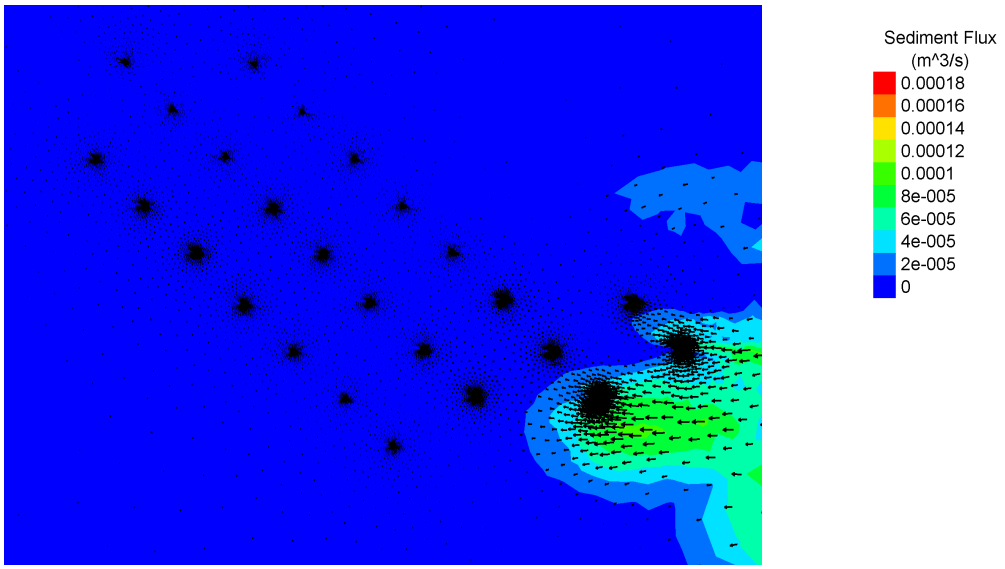

Figure 7.8: Residual sediment transport flux at the Burbo Bank wind farm over a year, with the wave schematisation determined by Method 1

The residual sediment flux at one structure is compared for Method 1 & 2, in Figures 7.10 & 7.11. The structure chosen for the comparison is the most northerly foundation, however, at most of the individual monopiles the residual sediment transport shows a similar pattern. In both cases the residual sediment flux is largely in a north-westerly direction, with the direction varying at the structure. There is little or no residual sediment flux in the wake of the structure for both structures, which spreads further from the pile for the Method 1 case.

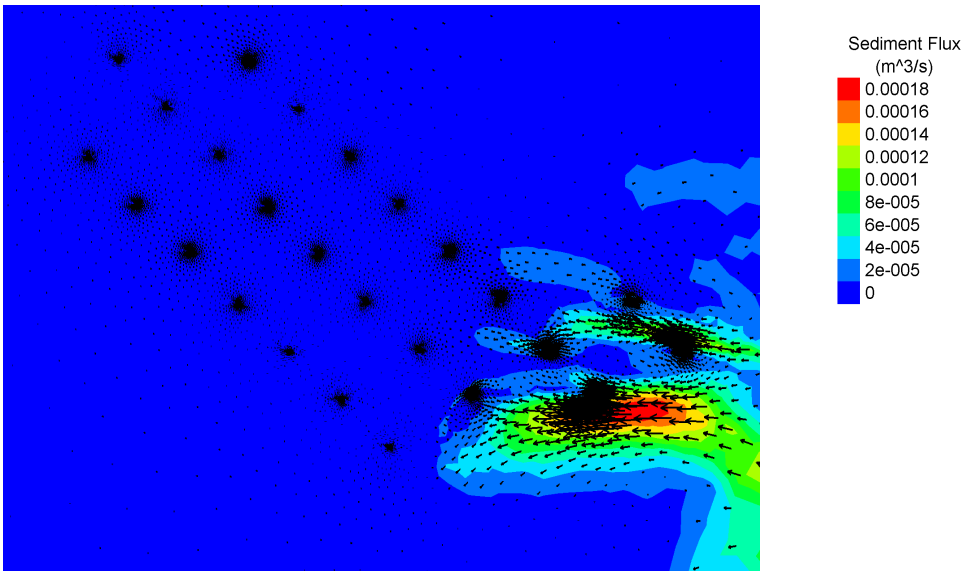

Figure 7.9: Residual sediment transport flux at the Burbo Bank wind farm over a year, with the wave schematisation determined by Method 2

The Method 2 case, shows a greater flux in front of the pile, than for Method 1.

7.2.2 Bed evolution validation

There are very limited morphological change measurements and studies from Liverpool Bay, which could be used to validate the morphological evolution predicted by this study. The validation of the morphological evolution is assessed here with the work of Blott et al. (2006), where bathymetric charts of Liverpool Bay are compared for the years 1912, 1949, 1988 and 2002. Blott et al. (2006) compares cross sections from the historical bathymetric charts at 5 locations in the south-eastern corner of Liverpool Bay (Figure 7.12) at the coordinates;

- Profile A: Y = 408000
- Profile B: Y = 404000
- Profile C: Y = 400000
- Profile D: Y = 398000
- Profile E: Y = 396000

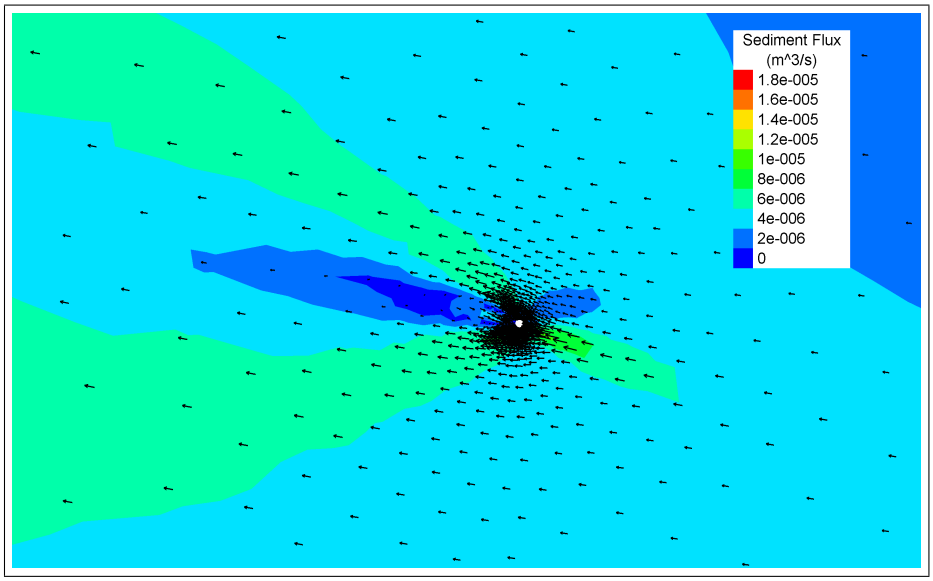

Figure 7.10: Residual sediment transport flux at one monopile foundation in the Burbo Bank wind farm over a year period, with the wave schematisation determined by Method 1

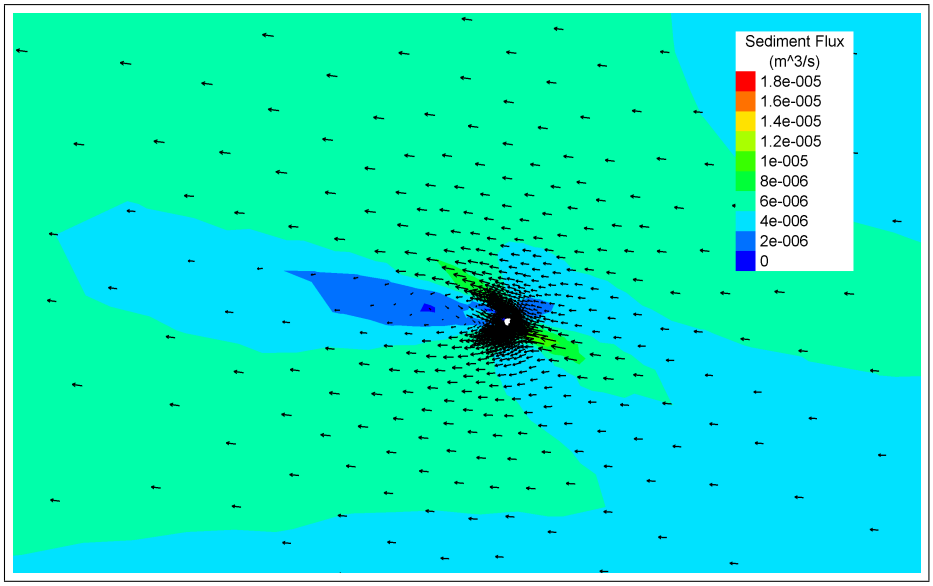

Figure 7.11: Residual sediment transport flux at one monopile foundation in the Burbo Bank wind farm over a year period, with the wave schematisation determined by Method 2

Figure 7.13 presents the comparison by Blott et al. (2006) of the morphological change from the historic bathymetric charts at the 5 cross sections. Profile A (Figure 7.13) shows accretion on Jordan's spit between 1912 an 1949, which migrates eastward until 2002. Profile B shows erosion and a western migration of Taylor's spit, with accretion at Askew spit and erosion of the Queen's Channel. Profiles C, D, and E present the cross section change over the Great Burbo Bank, where there is an eastward migration, whilst the Crosby Channel is at a constant depth (Blott et al., 2006).

The morphological change over the same cross sections are presented in Figure 7.14 for the original bathymetry used in the present study and the morphological change as predicted by Method 1 and 2. The cross section comparison by Blott et al. (2006) occurs over a period of decades, whilst the present study has determined morphological change over a year. As such the morphological change is on a much smaller change for this study than for Blott et al. (2006), however, it can still be used to get an estimate for the pattern of morphological change as well as an estimate on magnitude.

Profile A (Figure 7.14a) shows little morphological change for both methods over the year period. Profile B (Figure 7.14b) shows an initial bathymetry with a much shallower Queen's Channel than seen in Figure 7.13, there is a small accretion at Taylor's and Askew Spit and an accretion in the Queen's channel for both methods. Profiles C and D (Figures 7.14c & Figures 7.14d) shows an erosion over the year in the Crosby Channel, as well as some accretion over the Great Burbo Bank. This erosion and accretion pattern are similar to Figure 7.13, but are of a smaller magnitude as expected. Profile E (Figure 7.14e) sees little evolution over the Burbo Flats but some erosion in the Crosby Channel which is greater than seen in Figure 7.13. Similar patterns are seen as with the longer term evolution, as such the two morphological methods are thought to show sensible values within the right order of magnitude.

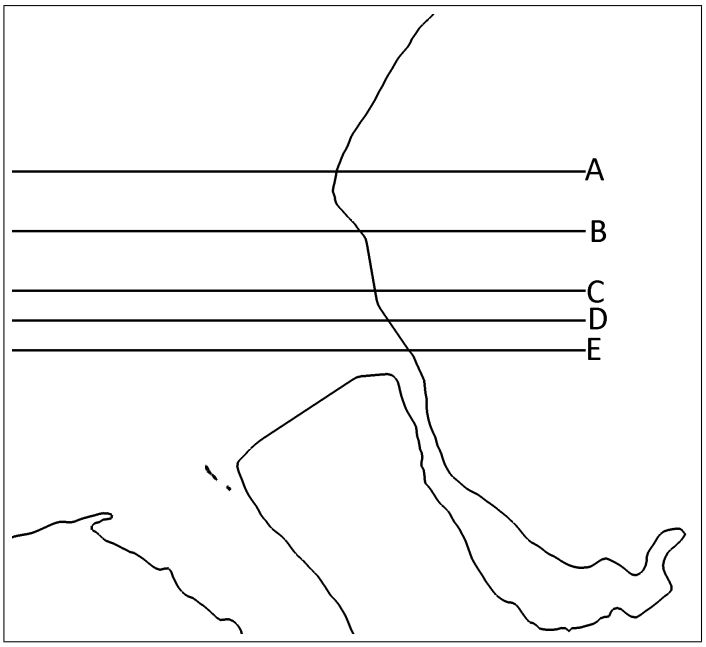

Figure 7.12: Cross section locations across the south-eastern corner of Liverpool Bay for assessing morphological change. From Blott et al. (2006)

7.2.3 Bed evolution

The bed evolution over the wind farm array is presented in Figures 7.15 & 7.16, for the bed morphology modelling by Method 1 and 2, respectively. Over the majority of Liverpool Bay there is no evolution, or a small accretion, which also occurs at the wind farm area. Within the wind farm site, there is a band of erosion running south-west to north-east across the middle of the wind farm, however, at the structures within this bank no evolution or a small accretion occurs. For both calculations the most southerly wind turbine foundations are surrounded by areas if accretion. For Method 2 (Figure 7.16), the accretion is greater in magnitude than for Method 1, and is spread over a larger area, influencing 5 turbines instead of the 3 for Method 1. This area of accretion corresponds to the residual sediment flux pathway which has moved more sediment across the Burbo Flats when a wind farm is present.

The bed evolution at one turbine foundation, chosen as the turbine in the centre if the array, is presented in Figures 7.17 & 7.18 for the model runs using Method 1 and 2, respectively. In both cases there are larger areas of deposition

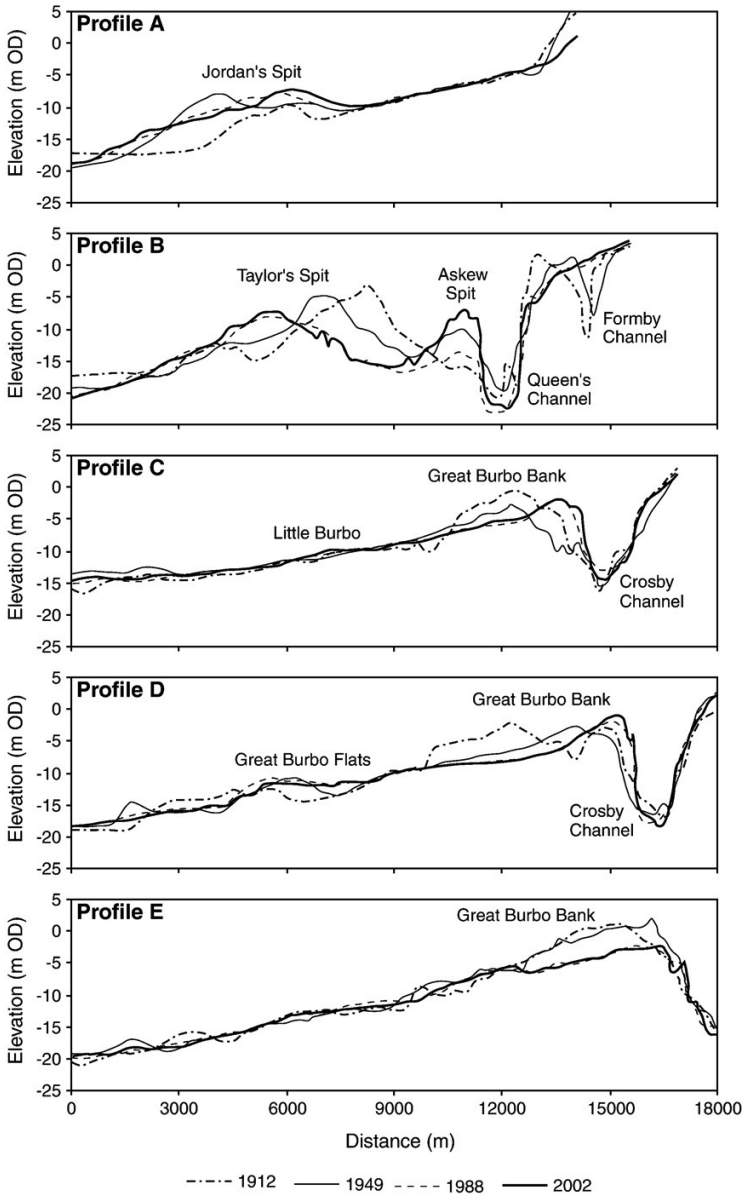

Figure 7.13: Blott et al. (2006) cross sections across the south-eastern corner of Liverpool Bay, based on bathymetric chart data

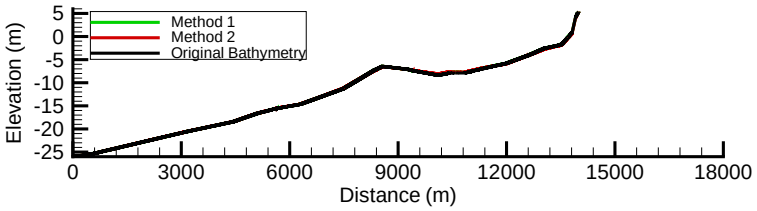

(a) Profile A

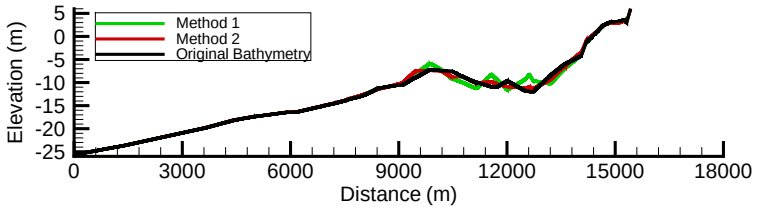

(b) Profile B

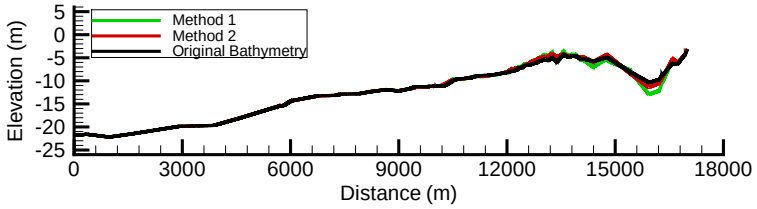

(c) Profile C

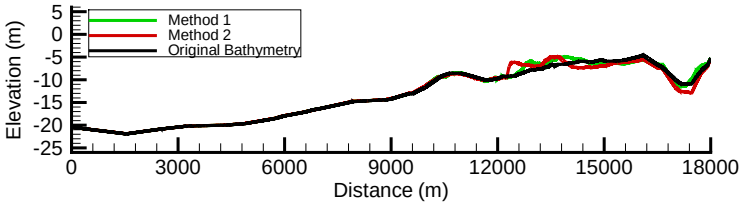

(d) Profile D

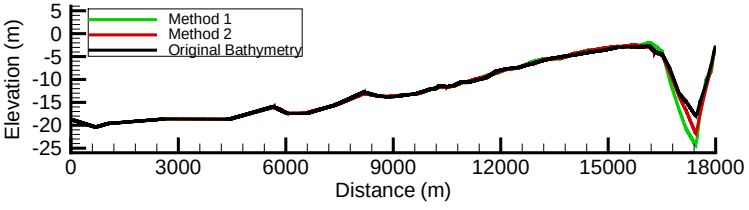

(e) Profile E

Figure 7.14: Cross sections across the south-eastern corner of Liverpool Bay for the original bathymetry and morphological change as calculated by Method 1 and 2

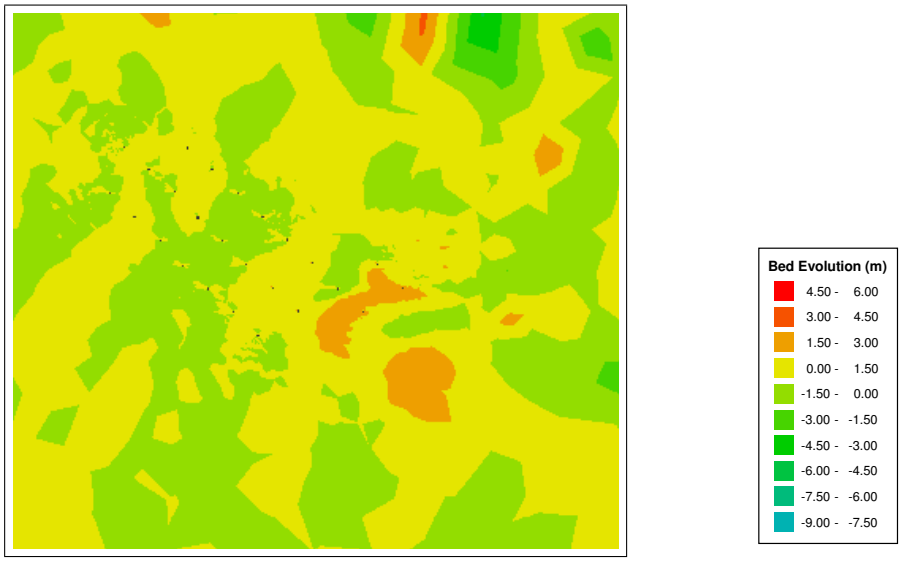

Figure 7.15: Bottom evolution distribution at the Burbo Bank wind farm site over a year period, with the wave schematisation determined by Method 1

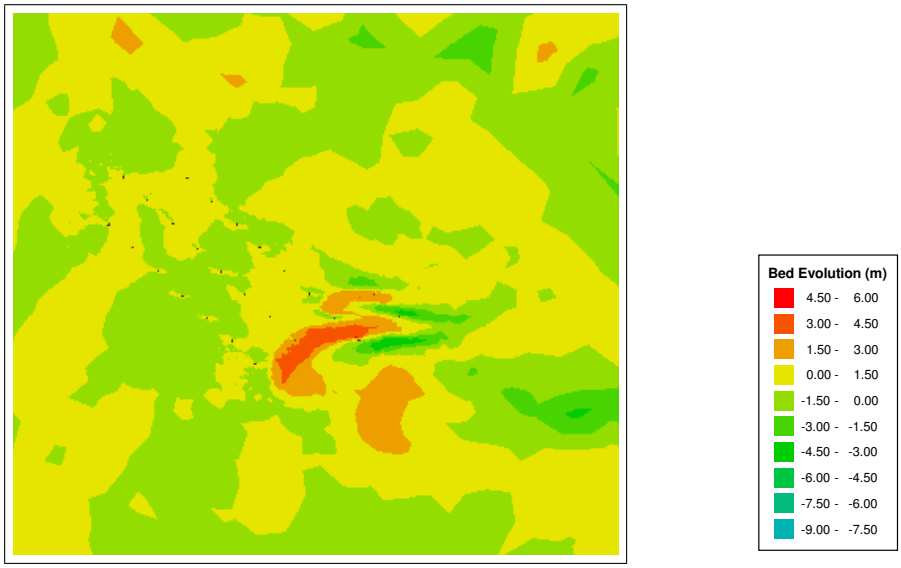

Figure 7.16: Bottom evolution distribution at the Burbo Bank wind farm site over a year period, with the wave schematisation determined by Method 2

surrounding the structure than erosion, this is not what is typically expected, although there are areas of scour surrounding the structures. The bed evolution at one pile for the Method 1 model runs, shows an area of accretion in line with the mean tidal direction at this location. The scour hole formation occurs at the sides of the pile, where the scour holes extent are within $1D$ of the monopile foundation. For the Method 2 model runs (Figure 7.18), a very different bed evolution pattern is seen at the structure, which, is likely due to the strong wave influence for Method 2. There are areas of accretion at the side of the pile, which reaches to heights of $1D$. The scour hole at the structure are very small in extent, stretching up to $0.25D$ away from the monopile. The scour holes are in line with the mean tidal flow at this location. Method 2 produces deeper scour holes than Method 1, but with a much smaller extent.

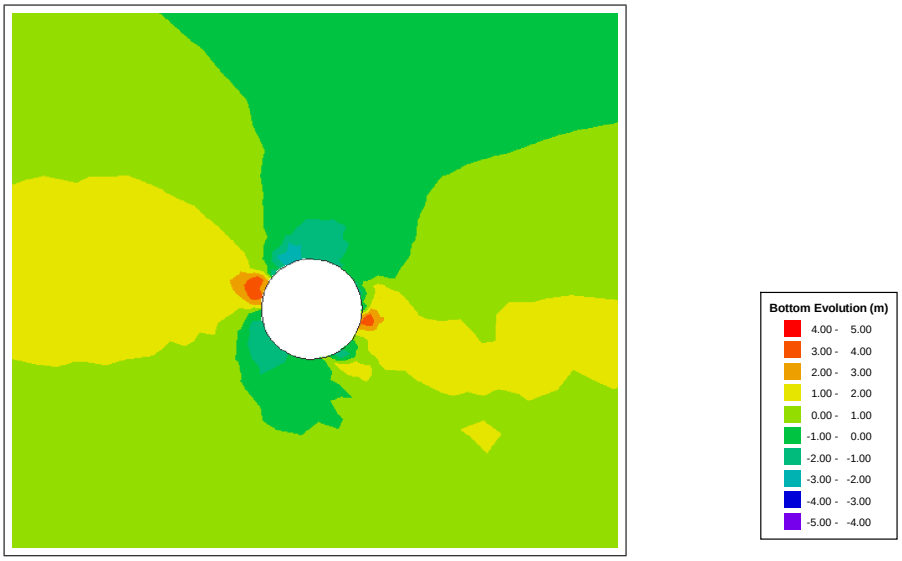

Figure 7.17: Bottom evolution distribution at at one monopile foundation in the Burbo Bank wind farm over a year period, with the wave schematisation determined by Method 1

Over the wind farm the deepest scour holes generated by Method 1, are found at the northern most structures within the array. Whilst for Method 2, the deepest scour holes are found at the most westerly structures, and at the two most easterly structures. The greatest scour hole extent for Method 1 is $-2.68m$ or $-0.536D$, with an average scour hole depth of $-0.34D$. For Method 2 the greatest

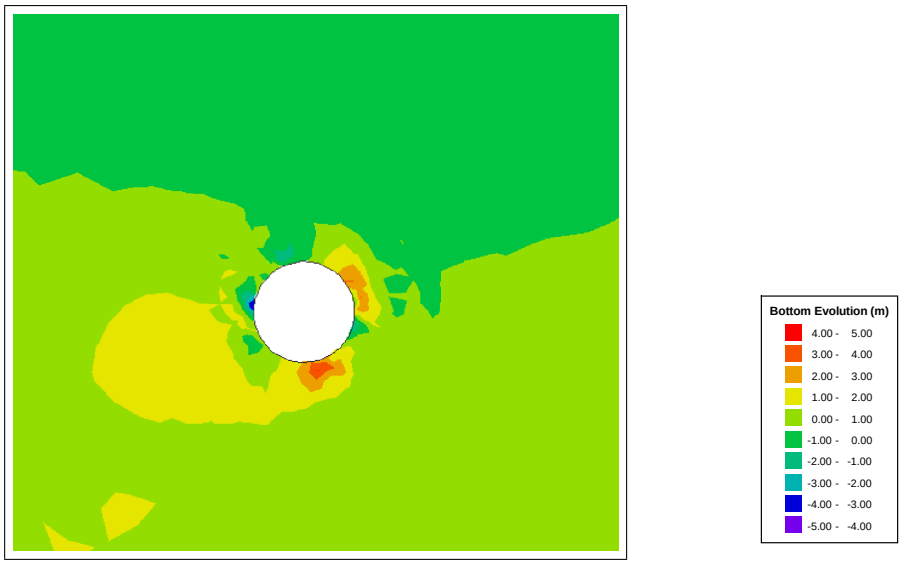

Figure 7.18: Bottom evolution distribution at at one monopile foundation in the Burbo Bank wind farm over a year period, with the wave schematisation determined by Method 2

scour hole is $-4.21m$ or $-0.84D$, with an average scour hole of $-0.46D$. Method 2 gives greater scour hole depth, as larger waves are included here, but the scour holes are smaller in extent than for Method 1 (Figures 7.17 & 7.18). The average accretion at the foundations is similar for both Methods with heights of $0.79D$ and $0.806D$ for Method 1 and 2, respectively.

The worst case scenario scour hole prediction formulae gives maximum scour depth of $1.3D$ (Det Norske Veritas, 2004) and $1.75D$ (Den Boon et al., 2004), which is much deeper than predicted here. As part of the Environmental Impact Assessment (EIA) for Burbo Bank, ABPmer (2002) estimated the scour hole potential using the formula of Sumer and Fredsøe (2001). The scour hole prediction for a 1 in 50 year return wave (wave height: $3.85m$, wave period: $7.19s$, wavelength: $69m$), gives an equilibrium scour depth estimated of $2.8m$ or $0.56D$, which is similar to the results from Methods 1 and 2.

Scour development monitoring at the Burbo Bank wind farm has been undertaken as part of post construction surveys. A few months after the installation of the wind turbines an armour layer was placed at the structures to prevent scour.

As this armour layer was not included in this study, and the no surveys were undertaken before the armouring was installed, the results from this study cannot be directly compared with measurements. The scour development at Burbo Bank, with the armouring, was assessed over the period November 2006 to April 2009 (Carroll et al., 2010) at six foundations. At the structures, four of the six showed erosion to the east and west of the pile, with accretion following the line of the tidal flow. Although the present study does not include the armouring at the wind farm foundations, the deposition and erosion pattern from measurements at the wind farm is the same as predicted by Method 1.

7.3 Conclusion

The wind farm site has been shown to have an influence on the large scale, long term, sediment transport. The sediment flux and bed morphological changes follow a similar pattern for both methods tested, but a different magnitude. The wind farm has been shown to cause a greater sediment flux across the Great Burbo Flats and an accretion at the south-east corner of the wind farm. As there is limited data available of shorter term morphological change within Liverpool Bay, it is difficult to assess the magnitude of the bed evolution predicted. However, the morphological change patterns within the south east corner of Liverpool Bay follow the longer time scale changes seen in bathymetric charts. The scour at a monopile is comparable to scour prediction formula, but significantly less than worst case scour predictions for both methods. Although not directly comparable to the results seen here as armouring was included at the site, the pattern of scour produced by Method 1 is similar to the scour pattern seen from monitoring at the Burbo Bank site.

Chapter 8

Conclusions and Future work

8.1 Representing the structure in the mesh

The complex flow structure due to the wave and current interaction with a wind turbine monopile, is not possible to fully resolve in a large scale coastal model. A CFD style model which is capable of modelling the flow structure cannot be used in this scale, due to the considerable computational time and expense. Coastal models are largely based on the shallow water assumptions, and are not suitable for determining turbulence at the small scale. Typically environmental impact assessments for offshore wind farm developments, use a friction term in the mesh to represent the wind turbine structure. This is a simplified approach, which is easy to apply to a model, and still allows fast computation time as the mesh doesn't need to be too fine. However, the flow structure is simplified, changes in the velocity and water depth are replicated but vortex shedding is not represented.

For this research the unstructured mesh within TELEMAC allows representation of the monopile foundation as an island in the mesh. The foundations were specified as 40 sided polygons, allowing an almost circular structure to be represented. However, unlike the resistance term method, the structure represented in the mesh needs a very fine resolution surrounding it, which does effect computing time considerably.

This method was validated against laboratory data for tidal conditions and

sediment transport, and compared with a Boussinesq model for waves. It was found that the flow structure around a monopile was replicated very well, given the simplifications the model is based on. However, the sediment transport validation had some difficulties. Scour was predicted well in front of the pile, but behind the pile accretion was predicted, rather than the scour seen in the experiment. This shows the limitations of the model, as it does not fully resolve the vertical flow. This is likely to have less influence in the tidal flows as the direction reverses, however, accretion was seen in the sediment transport predictions behind the monopile for both the Burbo Bank and Scroby Sands site.

It is therefore suggested that the solution may lie in a combination of the two techniques. The structure represented in the mesh with an bed shear stress term to allow better representation of the scour pattern. This would need validation against suitable laboratory data.

8.2 Impact of an OWF at a coastal scale

The impact of the wind farms at a coastal scale can modify large scale sediment pathways. At both the Burbo Bank and Scroby Sands site the wind farm impact on wave height at the coastal scale was not seen, but there was a small shift in wave direction. Modifications to the free surface elevation due to the presence of the wind farm, were also not clear at the coastal scale, although a small decrease in water depth was seen at parts of both wind farm sites. The flow velocity at both sites showed a small increase in velocities in the areas surrounding the wind farm, with the wind farm present. This increase in velocity indicates that the wind farm has a blocking effect on the flow, causing the flow to divert around the arrays. These modifications to the hydrodynamics have made an impact on sediment dynamics and pathways at both the wind farm sites.

In Liverpool Bay, the Burbo Bank wind farm caused changes in the main sediment pathway from the Mersey estuary, creating a greater sediment flux to the bottom of the wind farm site. The sediment flux across Burbo Bank suggested

that the wind farm acts to disperse the sediment flux, the structures enabled stirring allowing sediment transport to occur earlier in the tidal cycle. At Scroby Sands the wind farm acts to reduce the sediment flux due to the reduction in flow at the site.

8.3 Morphological impacts of an OWF over long time scales

The life span of an offshore wind farm is approximately 20 years, therefore it is important to study the impacts of an OWF on morphology over longer time periods. The method of long term prediction used in this study, for Liverpool Bay, involved a reduction of input terms to create a morphological tide, representative waves, and a morphological factor. The representative waves were selected by two different methods, the first selects the waves based on their frequency of occurrence, whilst the second selects representative waves based on the wave energy flux. The wave conditions were run sequentially, but no consideration was made to the wave chronology. Both methods were compared to a bathymetric chart study of Liverpool Bay, validating the pattern of morphological change.

The residual sediment flux pathways for both methods follow a similar pattern, which follows the results of the short term model runs. With the wind farm, the residual flux at the mouth of the Mersey is lower but covers a larger area. In addition there is a greater sediment flux across the Burbo Flats to the south-east corner of the wind farm, which causes accretion at this location. The sediment flux, and accretion is greater for the Method 2 model runs, due to the larger wave heights. At the wind farm site there is generally little morphological change or a small accretion, apart from across the middle of the site where there is a band of erosion. For both methods scour was seen at the foundation structures, but also areas of accretion. Sour holes were found to be deeper for Method 2 (max $0.84D$) than Method 1 (max $0.53D$), with both methods showing accretion heights of $0.8D$. Comparing to measurements at the site was hindered, as no survey exist before an armour layer was placed post-construction. However, the measurements

with the armour layer show a similar pattern of erosion and deposition, as was predicted by Method 1.

8.4 Future Work

- To further assess the validity of applying TELEMAC to the near field complex hydrodynamic pattern at a monopile structure. The validation was somewhat hampered in this study by a lack of available detailed laboratory data for model comparison. Use of a detailed CFD model to compare results may aid in determining key features that need to be included in the large scale model, such as the under-prediction of vertical velocities, and the non-linear pressure distribution near the structure.

- To attempt to remedy the sediment transport differences in the validation by applying a friction term at the seabed with the pile represented in the mesh.

- To include a wind reduction at the wind turbine in the model, to give a more realistic wave behaviour in the wake of the pile.

- To include scour prevention techniques, such as armouring, in the model

- To look at the influence of wave chronology when applying the Morphological Acceleration Factor, to assess wether seasonal changes in wave will impact the long term sediment pathway predictions.

- To study wind farm influences over longer time scales, including the influence of sea level rise and extreme weather conditions on coastal morphology.

Bibliography

ABPmer (2002), Burbo Offshore Wind Farm coastal process study, Technical report, Report for SeaScape Energy Ltd.

ABPmer (2011), The Galloper wind farm coastal processes assessment report, Technical report.

ABPmer (2012), Rampion wind farm: Coastal process assessment, Technical report, Report for E.ON Climate and Renewables UK Ltd.

ABPmer, CEFAS and HR Wallingford (2008), 'Review of round 1 sediment processes monitoring data lessons learnt'.

Alari, V. and Raudsepp, U. (2012), 'Simulation of wave damping near coast due to offshore wind farms', *Journal of Coastal Research* **28**(1), 143–148.

Amoudry, L., Bell, P. S., Black, K. S., Gatliff, R. W., Helsby, R., Souza, A. J., Thorne, P. D., Wolf, J. and House, M. (2009), 'A scoping study on: Research into changes in sediment dynamics linked to marine renewable energy installations', *NERC Marine Renewable Energy Theme Action Plan Report* .

Amoudry, L. O. and Souza, A. J. (2011), 'Deterministic coastal morphological and sediment transport modeling: A review and discussion', *Reviews of Geophysics* **49**(2).

Arshad, M. and O'Kelly, B. C. (2013), 'Offshore wind-turbine structures: A review', *Proceedings of the Institution of Civil Engineers, Energy* **166**(4), 139–152.

Bagnold, R. A. (1956), 'The flow of cohesionless grains in fluids', *Philosophical Transactions of the Royal Society of London. Series A, Mathematical and Physical Sciences* pp. 235–297.

Benoit, M., Marcos, F. and Becq, F. (1996), 'Development of a third generation shallow-water wave model with unstructured spatial meshing', *Coastal Engineering Proceedings* **1**(25).

Blott, S. J., Pye, K., Van der Wal, D. and Neal, A. (2006), 'Long-term morphological change and its causes in the Mersey Estuary, NW England', *Geomorphology* **81**(1), 185–206.

Bolaños, R., Thorne, P. D. and Wolf, J. (2012), 'Comparison of measurements and models of bed stress, bedforms and suspended sediments under combined currents and waves', *Coastal Engineering* **62**, 19–30.

Breusers, H., Nicollet, G. and Shen, H. (1977), 'Local scour around cylindrical piers', *Journal of Hydraulic Research* **15**(3), 211–252.

Brière, C., Abadie, S., Bretel, P. and Lang, P. (2007), 'Assessment of TELEMAC system performances, a hydrodynamic case study of Anglet, France', *Coastal engineering* **54**(4), 345–356.

Brown, J. (2008), Coastal area modelling: Sand transport and morphological change, PhD thesis, University of Wales, Bangor.

Brown, J. M. and Davies, A. G. (2009), 'Methods for medium-term prediction of the net sediment transport by waves and currents in complex coastal regions', *Continental Shelf Research* **29**(11), 1502–1514.

Brown, J. M. and Wolf, J. (2009), 'Coupled wave and surge modelling for the eastern Irish Sea and implications for model wind-stress', *Continental Shelf Research* **29**(10), 1329–1342.

Carreiras, J., Larroudé, P., Seabra-Santos, F. and Mory, M. (2000), 'Wave scour around piles', *Proceedings of 27th Conference on Coastal Engineering* .

Carroll, B. (2012), Morphodynamic impacts of a tidal barrage in the Mersey Estuary, PhD thesis, University of Liverpool.

Carroll, B., Cooper, B., Dewey, N., Whitehead, P., Dolphin, T., Rees, J., Judd, A., Whitehouse, R. and Harris, J. (2010), 'A further review of sediment monitoring data', *Cowrie ScourSed-09 eBook, UK* .

Chesher, T. and Miles, G. (1992), The concept of a single representative wave for use in numerical models of long term sediment transport predictions, *in* 'eds. RA Falconer, SN Chandler-Wilde and SQ Liu, Proc. 2nd Int. Conf. on Hydraulic and Environmental Modelling of Coastal, Estuarine, and River Waters', pp. 371–380.

Christiansen, M. B. and Hasager, C. B. (2005), 'Wake effects of large offshore wind farms identified from satellite SAR', *Remote Sensing of Environment* **98**(2), 251–268.

Cooper, B. and Beiboer, F. (2002), 'Potential effects of offshore wind developments on coastal processes', *ABP Marine Environmental Research LTD* .

Cowell, P. J., Stive, M. J., Niedoroda, A. W., Swift, D. J., de Vriend, H. J., Buijsman, M. C., Nicholls, R. J., Roy, P. S., Kaminsky, G. M., Cleveringa, J. et al. (2003), 'The coastal-tract (part 2): Applications of aggregated modeling of lower-order coastal change', *Journal of Coastal Research* pp. 828–848.

Daly, C. J., Bryan, K. R., Gonzalez, M. E., Klein, A. H. and Winter, C. (2013), Wave climate control of embayed beach equilibrium bathymetry, *in* 'Proceedings of Coastal Dynamics 2013'.

Davies, A. and Villaret, C. (2003), Sediment transport modelling for coastal morphodynamics, *in* 'Proceedings of coastal sediments', Vol. 3, Citeseer, pp. 18–23.

De Vriend, H., Capobianco, M., Chesher, T., De Swart, H. d., Latteux, B. and Stive, M. (1993), 'Approaches to long-term modelling of coastal morphology: A review', *Coastal Engineering* **21**(1), 225–269.

de Vries, W., Vemula, N. K., Passon, P., Fischer, T., Kaufer, D., Matha, D., Schmidt, B. and Vorpahl, F. (2011), 'Final report wp4. 2: Support structure concepts for deep water sites'.

Dean, R. G. and Dalrymple, R. A. (1991), *Water wave mechanics for engineers and scientists.*, World Scientific.

Den Boon, J., Sutherland, J., Whitehouse, R., Soulsby, R., Stam, C., Verhoeven, K., Høgedal, M. and Hald, T. (2004), Scour behaviour and scour protection for monopile foundations of offshore wind turbines, *in* 'Proceedings of the European Wind Energy Conference', Vol. 14.

Department of Energy and Climate Change (2012), UK Renewable energy roadmap: Update 2012, Technical report.

Det Norske Veritas (2004), Design of offshore wind turbine structures, Technical report, Offshore Standard DNV-OS-J101.

Dissanayake, P. K. (2011), Modelling Morphological Response of Large Tidal Inlet Systems to Sea Level Rise, PhD thesis, UNESCO-IHE, TU DELFT.

Dong, P. and Chen, H. (2001), 'Wave chronology effects on long-term shoreline erosion predictions', *Journal of waterway, port, coastal, and ocean engineering* **127**(3), 186–189.

Egbert, G. D. and Erofeeva, S. Y. (2002), 'Efficient inverse modeling of barotropic ocean tides', *Journal of Atmospheric and Oceanic Technology* **19**(2), 183–204.

Elgar, S., Guza, R. T. and Freilich, M. H. (1988), 'Eulerian measurements of horizontal accelerations in shoaling gravity-waves', *Journal of Geophysical Research-oceans* **93**(C8), 9261–9269.

Gandara, R. R. and Harris, J. (2012), 'Nearshore wave damping due to the effect on winds in response to offshore wind farms', *Coastal Engineering Proceedings* **1**(33), waves–55.

Harris, J., Whitehouse, R. and Benson, T. (2010), 'The time evolution of scour around offshore structures', *ICE-Maritime Engineering* **163**(1), 3–17.

Heaps, N. (1972), 'Estimation of density currents in the Liverpool Bay area of the Irish Sea', *Geophysical Journal of the Royal Astronomical Society* **30**(4), 415–432.

Heaps, N. (1983), 'Storm surges, 1967–1982', *Geophysical Journal International* **74**(1), 331–376.

Hervouet, J.-M. (2007), *Hydrodynamics of Free Surface Flows: Modelling with the finite element method*, Wiley.

Hjorth, P. (1975), *Studies on the nature of local scour*, Inst. för Teknisk Vattenresurslära, Lunds Tekniska Högskola, Lunds Univ.

Holt, J. and James, I. (2001), 'An s coordinate density evolving model on the north west european continental shelf 1. model description and density structure.', *Journal of Geophysical Research* **106**, 14015–14034.

Horrillo-Caraballo, J. M. and Reeve, D. E. (2008), 'Morphodynamic behaviour of a nearshore sandbank system: The Great Yarmouth Sandbanks, UK', *Marine Geology* **254**(1), 91–106.

Howarth, M. J., Player, R. J., Wolf, J. and Siddons, L. A. (2007), HF radar measurements in Liverpool Bay, Irish Sea, *in* 'OCEANS 2007-Europe', IEEE, pp. 1–6.

Howlett, E. R., Rippeth, T. P. and Howarth, J. (2011), 'Processes contributing to the evolution and destruction of stratification in the Liverpool Bay ROFI', *Ocean Dynamics* **61**(9), 1403–1419.

HR Wallingford (1991*a*), Mersey barrage feasibility study: Stage ii, Hydraulic and sedimentation study, Technical report.

HR Wallingford (1991*b*), Mersey Barrage Feasibility Study: Stage II, hydraulic and sedimentation study, Technical report.

HR Wallingford (1992), Mersey Barrage Feasibility Study: Stage IIIa, 3D mathematical modelling of tidal flows and sedimentation, Technical report, HR Wallingford.

HR Wallingford, CEFAS, U., Posford Haskoning and DOlier, B. (2002), 'Southern North Sea sediment transport study, Phase 2', *HR Wallingford Report* **4526**.

Kirkil, G., Constantinescu, S. and Ettema, R. (2008), 'Coherent structures in the flow field around a circular cylinder with scour hole', *Journal of Hydraulic Engineering* **134**(5), 572–587.

Lambkin, D., Harris, J., Cooper, W. and Coates, T. (2009), 'Coastal process modelling for offshore wind farm environmental impact assessment: Best practice guide', *COWRIE Limited, London* .

Latteux, B. (1995), 'Techniques for long-term morphological simulation under tidal action', *Marine Geology* **126**(1), 129–141.

Lesser, G. R. (2009), 'An approach to medium-term coastal morphological modelling'.

Lesser, G., Roelvink, J., Van Kester, J. and Stelling, G. (2004), 'Development and validation of a three-dimensional morphological model', *Coastal engineering* **51**(8), 883–915.

Liu, X. (2008), *Numerical models for scour and liquefaction around object under currents and waves*, ProQuest.

Meyer-Peter, E. and Müller, R. (1948), Formulas for bed-load transport, *in* 'Proceedings of the 2nd Meeting of the International Association for Hydraulic Structures Research', Stockholm, pp. 39–64.

Morison, J., Johnson, J. and Schaaf, S. (1950), 'The force exerted by surface waves on piles', *Journal of Petroleum Technology* **2**(5), 149–154.

Moulinec, C., Denis, C., Pham, C.-T., Rougé, D., Hervouet, J.-M., Razafindrakoto, E., Barber, R., Emerson, D. and Gu, X.-J. (2011), 'TELEMAC: An efficient hydrodynamics suite for massively parallel architectures', *Computers & Fluids* **51**(1), 30–34.

Navitus Bay Development Limited (2014), Navitus bay wind park environmental statement, Technical report.

Neill, S. P., Litt, E. J., Couch, S. J. and Davies, A. G. (2009), 'The impact of tidal stream turbines on large-scale sediment dynamics', *Renewable Energy* **34**(12), 2803–2812.

Nezu, I. and Nakagawa, H. (1993), 'Turbulence in open channels', *AA Balkema, Rotterdam, The Netherlands* .

Nielsen, P. (1992), *Coastal bottom boundary layers and sediment transport*, Vol. 4, World scientific.

Park, H. and Vincent, C. (2007), 'Evolution of Scroby Sands in the East Anglian coast, UK', *Journal of Coastal Research SI* **50**, 868–873.

Pingree, R. and Griffiths, D. (1979), 'Sand transport paths around the British Isles resulting from M2 and M4 tidal interactions', *J. Mar. Biol. Assoc. UK* **59**, 497–513.

Polton, J. A., Palmer, M. R. and Howarth, M. J. (2011), 'Physical and dynamical oceanography of Liverpool Bay', *Ocean Dynamics* **61**(9), 1421–1439.

Polton, J. A., Palmer, M. R. and Howarth, M. J. (2013), 'The vertical structure of time-mean estuarine circulation in a shallow, rotating, semi-enclosed coastal bay: a liverpool bay case study with application for monitoring', *Continental Shelf Research* **59**, 115–126.

Ponce de León, S., Bettencourt, J. and Kjerstad, N. (2011), 'Simulation of irregular waves in an offshore wind farm with a spectral wave model', *Continental Shelf Research* **31**(15), 1541–1557.

Rees, J., Larcombe, P., Vivian, C. and Judd, A. (2006), 'Scroby Sands offshore wind farm: Coastal processes monitoring', *Final Rep. for the UK Department of Trade and Industry* p. 51.

Reeve, D., Li, B. and Thurston, N. (2001), 'Eigenfunction analysis of decadal fluctuations in sandbank morphology at Great Yarmouth', *Journal of Coastal Research* pp. 371–382.

Renewable UK (2012), Wind energy in the UK: State of the industry report, Technical report.

Renewable UK and The Crown Estate (2013), Building an industry: Updated scenarios for industrial development, Technical report.

Ribberink, J. S. (1998), 'Bed-load transport for steady flows and unsteady oscillatory flows', *Coastal Engineering* **34**(1), 59–82.

Robins, P. E. and Davies, A. G. (2010), 'Morphological controls in sandy estuaries: The influence of tidal flats and bathymetry on sediment transport', *Ocean Dynamics* **60**(3), 503–517.

Rodi, W. (1997), 'Comparison of LES and RANS calculations of the flow around bluff bodies', *Journal of Wind Engineering and Industrial Aerodynamics* **69**, 55–75.

Roelvink, D., Reniers, A. et al. (2012), *A guide to modeling coastal morphology*, Vol. 12, World Scientific.

Roulund, A., Sumer, B. M., Fredsøe, J. and Michelsen, J. (2005), 'Numerical and experimental investigation of flow and scour around a circular pile', *Journal of Fluid Mechanics* **534**, 351–401.

Royal Haskoning (2010), Kentish flats offshore wind farm extension environmental scoping study, Technical report, Report for Vattenfall UK Limited.

Sarpkaya, T. (1987), 'Oscillating flow about smooth and rough cylinders', *Journal of Offshore Mechanics and Arctic Engineering* **109**, 307.

Simoons, E. (2012), Edge scour around an offshore wind turbine, Master's thesis, Delft University of Technology.

Simpson, J. H., Burchard, H., Fisher, N. R. and Rippeth, T. P. (2002), 'The semi-diurnal cycle of dissipation in a ROFI: Model-measurement comparisons', *Continental Shelf Research* **22**(11), 1615–1628.

Soulsby, R. (1997), *Dynamics of marine sands: A manual for practical applications*, Thomas Telford.

Steijn, R. (1992), Input filtering techniques for complex morphological models, Technical report, Delft Hydraulic Report.

Sumer, B. M. (2014), *Liquefaction Around Marine Structures*, World Scientific.

Sumer, B. M., Bundgaard, K. M. and Fredsøe, J. M. (2005), 'Global and local scour at pile groups', *International Journal of Offshore and Polar Engineering* **15**(3).

Sumer, B. M., Christiansen, N. and Fredsøe, J. (1997), 'The horseshoe vortex and vortex shedding around a vertical wall-mounted cylinder exposed to waves', *Journal of Fluid Mechanics* **332**, 41–70.

Sumer, B. M. and Fredsøe, J. (2001), 'Wave scour around a large vertical circular cylinder', *Journal of waterway, port, coastal, and ocean engineering* **127**(3), 125–134.

Sumer, B. M. and Fredsøe, J. (2002), *The mechanics of scour in the marine environment*, World Scientific.

Sumer, B. M., Fredsøe, J. and Christiansen, N. (1992), 'Scour around vertical pile in waves', *Journal of Waterway, Port, Coastal, and Ocean Engineering* **118**(1), 15–31.

Sumer, B. M., Hatipoglu, F. and Fredsøe, J. (2007), 'Wave scour around a pile in sand, medium dense, and dense silt', *Journal of Waterway, Port, Coastal, and Ocean Engineering* **133**(1), 14–27.

Sutherland, J., Walstra, D., Chesher, T., Van Rijn, L. and Southgate, H. (2004), 'Evaluation of coastal area modelling systems at an estuary mouth', *Coastal Engineering* **51**(2), 119–142.

Thomas, C., Spearman, J. and Turnbull, M. (2002), 'Historical morphological change in the Mersey Estuary', *Continental Shelf Research* **22**(11), 1775–1794.

Thornton, E. B. and Guza, R. (1983), 'Transformation of wave height distribution', *Journal of Geophysical Research: Oceans (1978–2012)* **88**(C10), 5925–5938.

Thurston, K. (2011), Morphological evolution of nearshore sand banks: The Great Yarmouth banks, UK, PhD thesis, University of East Anglia.

Tseng, M.-H., Yen, C.-L. and Song, C. (2000), 'Computation of three-dimensional flow around square and circular piers', *International Journal for Numerical Methods in Fluids* **34**(3), 207–227.

Van Rijn, L. C., van Rijn, L. C. and van Rijn, L. C. (1993), *Principles of sediment transport in rivers, estuaries and coastal seas*, Vol. 1006, Aqua publications, Amsterdam.

Weilbeer, H. and Jankowski, J. (2000), A three-dimensional non-hydrostatic model for free surface flows–development, verification and limitations, *in* 'Proc. Of 6th International Conference Estuarine and Coastal Modeling', pp. 162–177.

Whitehouse, R. (1998), *Scour at marine structures: A manual for practical applications*, Thomas Telford.

Whitehouse, R. J., Harris, J. M., Sutherland, J. and Rees, J. (2011), 'The nature of scour development and scour protection at offshore windfarm foundations', *Marine Pollution Bulletin* **62**(1), 73–88.

Wolf, J; Flather, R. (2005), 'Modelling waves and surges during the 1953 storm', *Philosophical Transactions of the Royal Society A: Mathematical, Physical and Engineering Sciences* **363**(1831), 1359–1375.

Wolf, J., Souza, A. J., Bell, P. S., Thorne, P. D., Cooke, R. D. and Pan, S. (2008), 'Wave, currents and sediment transport observed during the LEACOAST2 experiment'.

Appendices

.1 Publications

This appendix contains paper for the International Conference on Coastal Engineering (ICCE) 2012:

Christie, E., Li, M., & Moulinec, C. (2012). Comparison of 2D and 3D large scale morphological modelling of Offshore Wind Farms using HPC. Coastal Engineering Proceedings, 1(33).

COMPARISON OF 2D AND 3D LARGE SCALE MORPHOLOGICAL MODELING OF OFFSHORE WIND FARMS USING HPC

Elizabeth Christie[1], Ming Li[2] and Charles Moulinec[3]

The rapidly developing offshore wind farm sector has increased the need to understand if wind farm placement and design has any impact on large scale coastal processes. This paper looks at high resolution hydrodynamic and morphological modeling of offshore wind farms in both 2D and 3D to determine whether either model is capable of representing complex flow patterns around monopile structures and subsequent sediment transport.

Keywords: offshore wind farm; TELEMAC; coastal modeling

INTRODUCTION

With recent increased development of Offshore Wind Farms (OWF), it is important to determine any impact they have on large scale coastal hydrodynamics and morphodynamics for coastal management.

It is well established, Whitehouse (1998), Sumer & Fredsøe (2002) that wind turbine monopiles modify the localized hydrodynamics to create a complex 3D flow structure of vortices, which results in scour hole formation. Currently modeling the coastal scale impact of the OWF often involves parameterization of these localized effects, typically by including a resistance term at point locations to represent the structure (Lambkin et al. 2009). This process often means that structures are not identified in the computational mesh. The flow is oversimplified as 3D vortices are not explicitly included in the model results, with the consequence that sediment transport is not accurately represented.

The present research intends to determine whether high resolution large scale modeling of OWF's with the structure represented is capable of adequately describing the complex near field flow and its effect on sediment dynamics by comparing 2D and 3D large scale morphological models.

METHODS

Liverpool Bay (Figure 1) located in the Eastern Irish Sea, has been selected as a test bed. Within Liverpool Bay are three OWF's; Burbo Bank, North Hoyle and Rhyl Flats, consisting of 25, 30 and 25 monopile turbines respectively, with a diameter of 4-5m. Liverpool Bay is tidal dominated with a peak tidal range of 10m with strong currents and waves (Polton et al. 2011). The sediment dynamics are strongly affected by the hydrodynamics, with the Mersey estuary acting as a sediment sink.

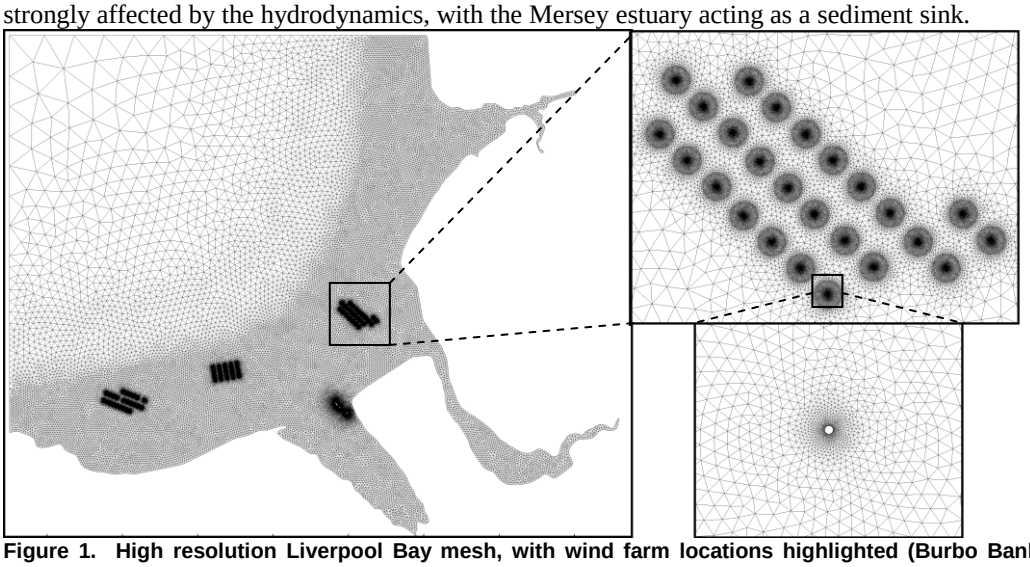

Figure 1. High resolution Liverpool Bay mesh, with wind farm locations highlighted (Burbo Bank, North Hoyle, Rhyl Flats). The mesh is comprised of 325,000 elements in 2D.

[1] Department of Engineering, University of Liverpool, Brownlow Hill, Liverpool, L69 3GH, UK
[2] Department of Engineering, University of Liverpool, Brownlow Hill, Liverpool, L69 3GH, UK
[3] Science and Technology Facilities Council, Daresbury Laboratory, Daresbury Science and Innovation Campus, Warrington, Cheshire, WA4 4AD, UK

The TELEMAC modeling system, which consists of a hydrodynamic module TELEMAC 2D/3D, together with sediment transport module SISYPHE, was used to model Liverpool Bay. The finite element method was used to solve the equation system. The mesh (Figure 1) used consists of approximately 325,000 elements for the 2D case in order to represent the structure detail. The monopole turbines are represented as an island in the grid with concentric rings of increasing mesh size for detailed resolution. For the 3D case the water column is divided into 10 equal height depth layers, creating a mesh of approximately 3.25 million elements for the required vertical resolution.

Boundary conditions used include offshore open boundary with the tidal water level or riverine discharge specified and solid wall shoreline boundaries. The model is driven by scaled representative tides calculated by the Tidal Model Driver (Egbert & Erofeeva, 2002) for 7 tidal constituents (M2, S2, N2, K2, P1, O1, K2). Riverine discharge is also included as a model input with annual mean flow rate specified at the boundaries of the Dee, Mersey, Douglas and Ribble estuaries as 33.70m^3/s, 37.22 m^3/s, 4.16 m^3/s, 33.04 m^3/s respectively. The Smagorinsky turbulence model is used for horizontal turbulent modeling with the mixing length model used for vertical turbulence in the 3D case. Bottom friction is calculated by the Chézy formula with a Chézy coefficient of 24. Sediment transport is modeled with the Meyer-Peter bed load transport formula with a single sediment size class of diameter 0.23mm, and the morphology is updated with the Exner equation.

The model is run for both 2D and 3D cases over a full spring-neap cycle. To cope with the large computational mesh sizes, the TELEMAC system is run in parallel using the facility at Liverpool University and HECToR. Previous tests on similar size mesh have shown good performance in scaling, Moulinec et al. (2011).

Model results were calibrated against available coastal tide gauge data (Figure 2) at 4 locations in Liverpool Bay; Llandudno, Gladstone dock, Hilbre Island and Alfred Dock. The model free surface elevation shows good agreement with the tide gauge data over the tidal cycle in all 4 locations. Some phase shifting is seen at the Alfred Dock site, which is likely due to the fact that it is located at a shallow depth and the uncertainties in local bathymetry plays significant role.

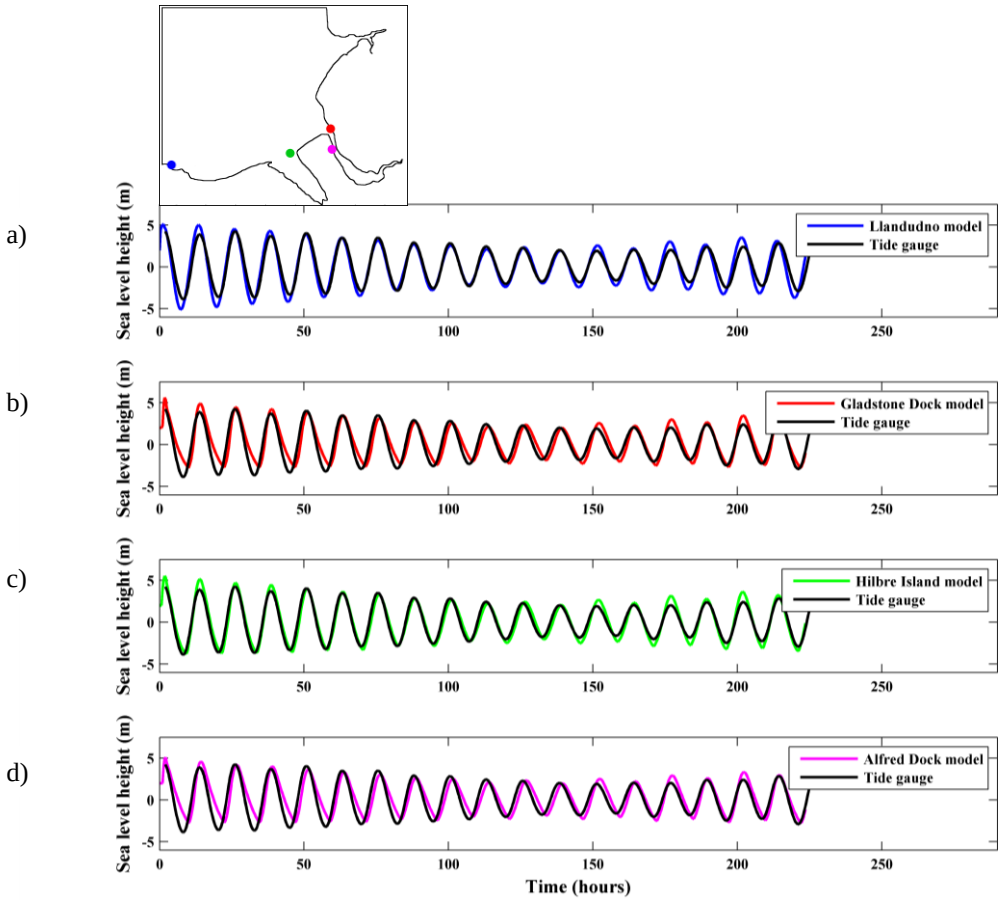

Figure 2. Tidal gauge sea level height comparison with modeled data at 4 locations in Liverpool Bay over a spring-neap cycle, a) Llandudno, b) Gladstone Dock, c) Hilbre Island, d) Alfred Dock.

The sea surface currents for the 3D mesh are calibrated against high frequency radar data covering Liverpool Bay (Howarth et al. 2007). Two sites were selected for calibration (Figure 3), located between the three wind farm sites. Generally the model results show good agreement with the radar data in the velocity magnitude at both sites. However, a phase shift is seen during neap tides between modeled and radar data at both locations, but at spring tides the model and data are in phase. This is considered due to the fact that the model doesn't take into account wind effect which is significant to the surface flow in this region.

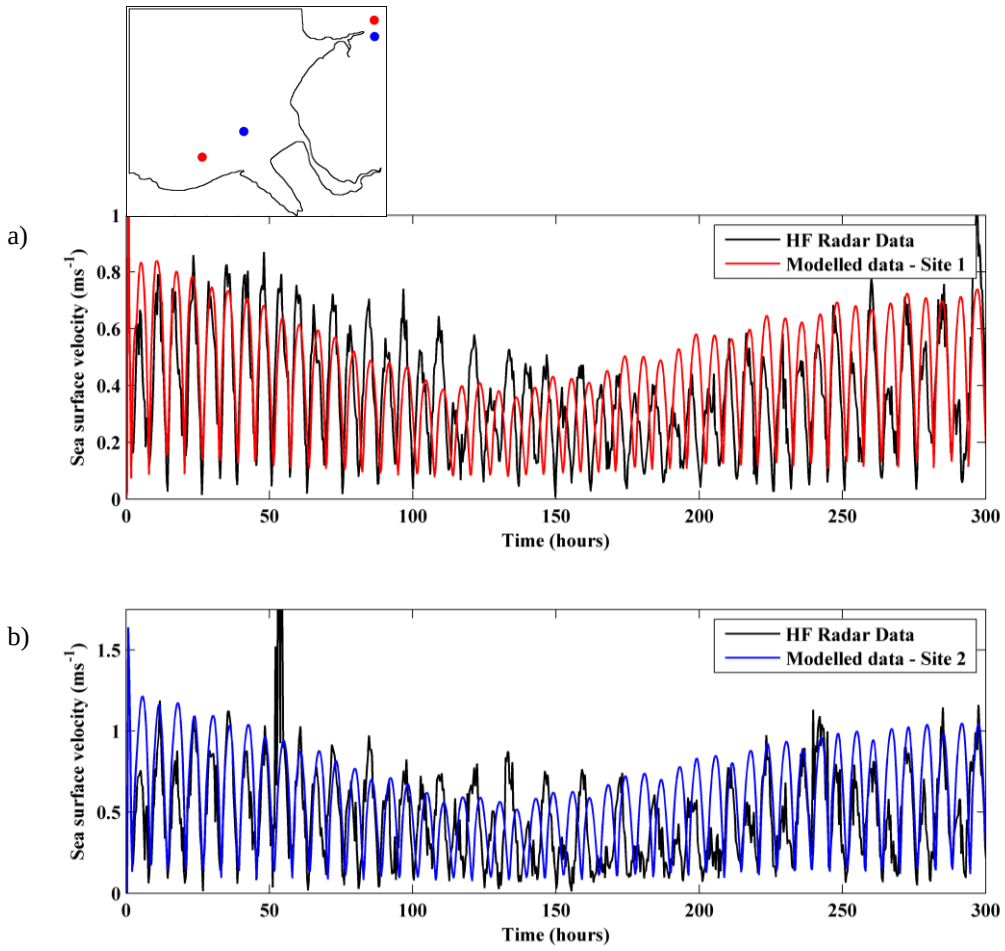

Figure 3. High frequency radar sea surface velocity measurements compared with model data at two locations in Liverpool Bay, a) site 1, b) site 2

RESULTS

The data generated from the models are cross-compared for the 2D and 3D scenarios and used to identify the impacts from the structure on both hydrodynamics and sediment transport.

Figure 4 shows the noticeable decrease in the depth averaged velocity occurs in the wake of each monopile foundation at the Burbo Bank site. This lee wake is greatest at the peak flood, where the wake tail can be seen stretched over 200-300 meters behind certain structures. However the effect of the wind farm array as a whole is fairly limited and no interaction can be seen between adjacent piles wakes.

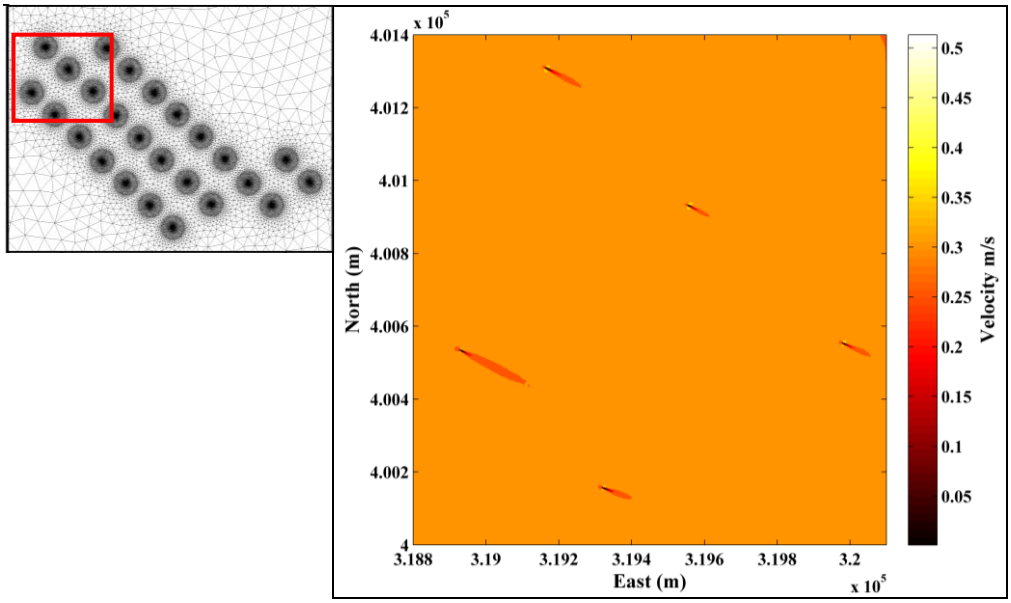

Figure 4. Depth averaged velocity over part of the Burbo Bank wind farm (highlighted|) for the 2D model run.

Figure 5 shows details of the flow structure behind an individual monopile during a peak flood spring tide computed by 2D and 3D runs. The 2D model run (Figure 5a) suggests a larger wake than the 3D model run (Figure 5b), although the deceleration pattern is similar in both cases. High velocities are seen at the side edges if the pile consistent with streamlines contracting. The 3D model run has larger acceleration than the 2D results, likely to influence scour hole formation.

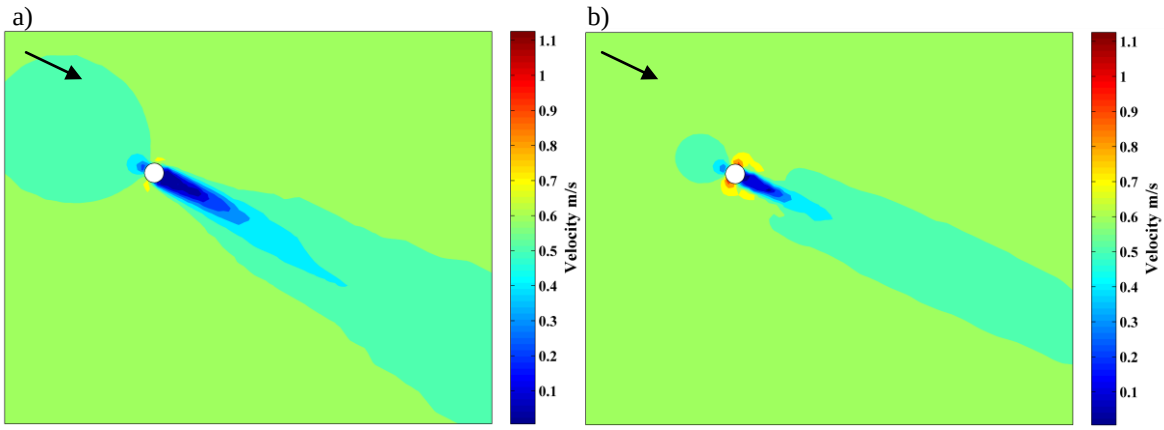

Figure 5. Peak flood vertically depth averaged velocity distribution around one monopile turbine at the North Hoyle wind farm for a) 2D model and b) 3D model. The arrow indicates the main current direction.

A similar pattern is seen at the peak ebb phase of the tide in Figure 6. The 2D (Figure 6a) case has greater shadowing effect of the monopile than the 3D (Figure 6b) case, although the difference in wake size is less pronounced than at peak flood (Figure 5). For both runs the lee wake is smaller in the ebb phase than flood phase, this is likely due to the water depth being lower in the ebb phase of the flow. Again the 3D model shows greater velocities at the sides of the pile than the 2D model run.

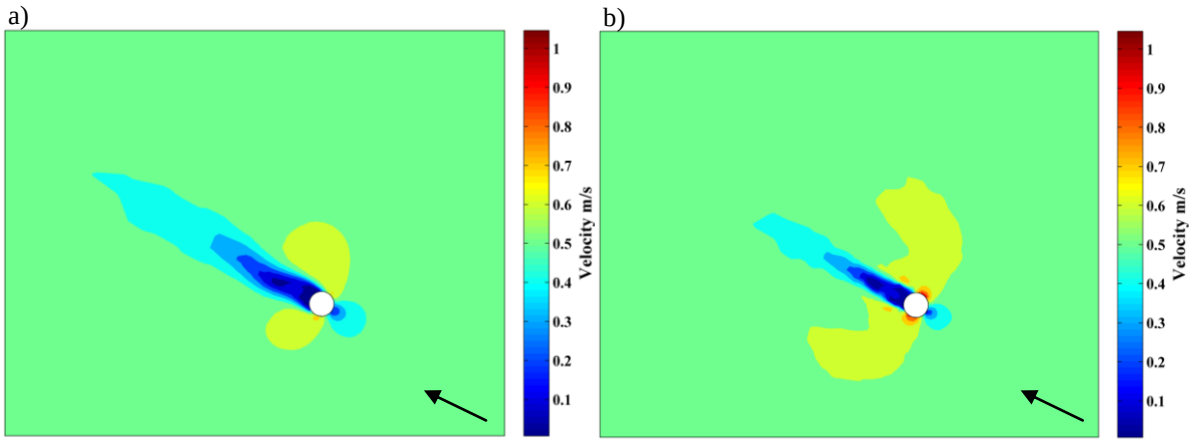

Figure 6. Peak ebb vertically depth averaged velocity distribution around one monopile turbine at the North Hoyle wind farm for a) 2D model and b) 3D model. The arrow indicates the main current direction.

As a 2D model is only able to provide depth averaged flow velocities, the complex flow structure known to occur around monopiles under tidal forcing cannot be identified. Results from the 3D model run however, shows marked differences between the bed and surface velocity distribution in Figure 7. At the surface (Figure 7a) the flow pattern structure is similar to that of the depth –averaged velocity, with a decrease in velocity in the wake of the pile and increased acceleration at the side of the pile. Near the bed (Figure 7b) the wake is much shorter, approximately the length of the pile diameter. The high velocities at the side of the pile become the prominent feature at the bed, which will significantly impact the scour pattern.

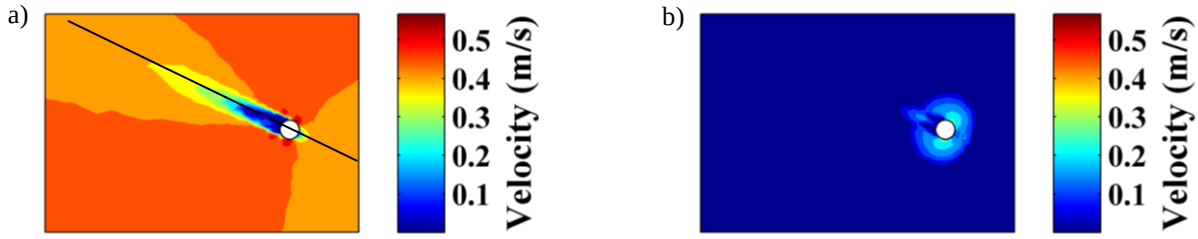

Figure 7. Velocity distribution at one monopile turbine at the North Hoyle wind farm for the 3D model run at a) the surface and b) the bottom. Black line indicates the cross-section for Figure 8.

A vertical cross-section is taken across the monopile for the 3D model run as indicated in Figure 7, in order to create a vertical velocity profile of the influence of the monopile on the hydrodynamics (Figure 8). A logarithmic vertical profile is seen in front of the pile, followed by a reduced steep horizontal velocity profile to zero at the monopile wall. Behind the monopile there is a strong wake with low velocities behind the pile which gradual recovers to form a logarithmic profile around 30-40m away from the monopile.

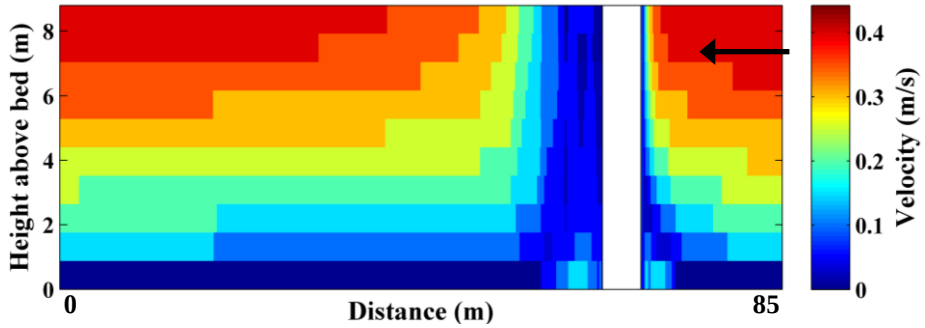

Figure 8. Vertical cross section velocity profile at one monopile turbine at the North Hoyle wind farm for the 3D model run. The arrow indicates the main current direction.

Figure 9 shows the bed evolution over a 1.5 spring tides for both the 2D (Figure 9a) and 3D runs (Figure 9b). In both cases a scour pattern is seen around the monopile foundation, this is due to the acceleration of the flow leading to an increase in bed shear stress and subsequent increase in sediment transport. In both model runs an area of deposition is also apparent between the scour holes where sediment has been deposited from the eroded area. The 2D model run (Figure 9a) suggests an asymmetry in scour depth, which is due to the asymmetry in the size of the wake in the ebb and flood flow for the 2D run. The reason is considered as the 2D case relies on a logarithmic profile to determine the bed shear stress in the calculation of sediment transport, consequently, during the ebb the 2D result will have smaller bed shear stress force given a similar mean velocity profile as in the 3D case, which leads to less sediment transport.

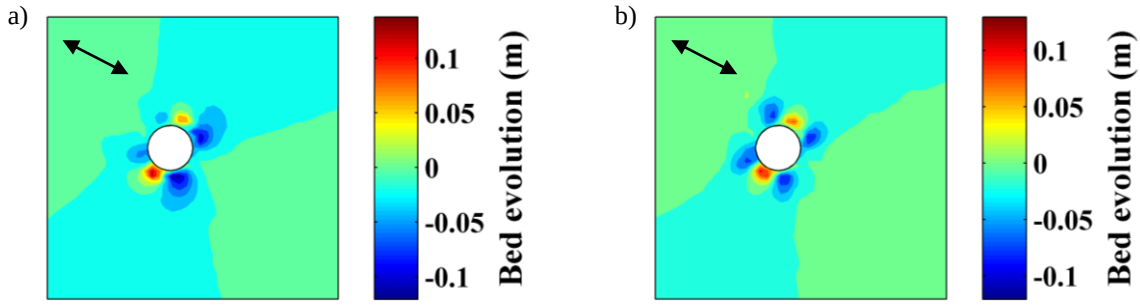

Figure 9. Bed evolution over 1.5 spring tides at one monopile turbine at the Burbo Bank wind farm for a) the 2D model and b) the 3D model run. Arrows indicate dominant tidal direction.

Figure 10 presents the bed evolution over 18 tides using the 3D model. The scour pattern becomes more apparent, with significant scour hole formation of up to 0.7m depth. The area the scour hole covers has increased in comparison with the short model runs shown previously. The areas of deposition also have increased, but to a smaller magnitude than the scour depth increase, suggesting that the deposition area will be less significant over longer runs.

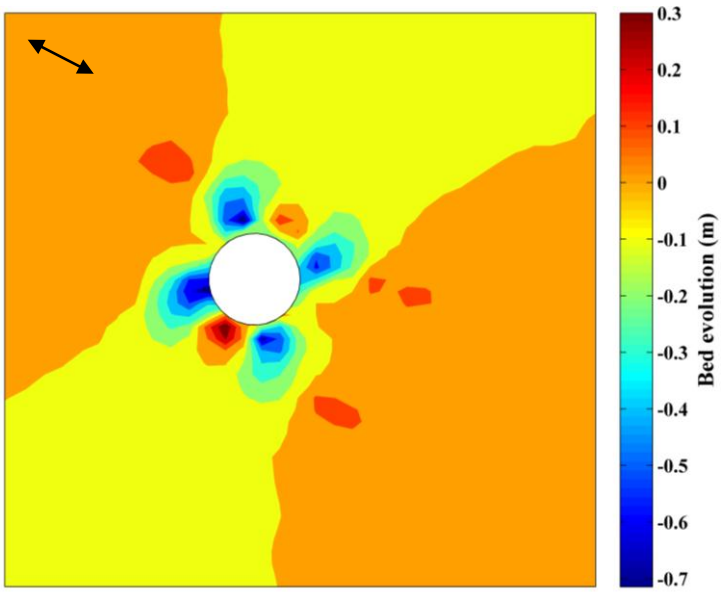

Figure 10. Bed evolution over 18 tides at one at one monopile turbine in the Burbo Bank wind farm for the 3D model run. Arrow indicates dominant tidal direction.

CONCLUSION

The 2D and 3D models are largely similar in the large scale with differences most prominent in the localized area around a monopile. At near scale around the monopile the 2D and 3D runs both give similar patterns of change in velocity, although it is more pronounced in the 2D case. The 3D model is

shown to be capable of representing the complex vertical velocity patterns around the monopile. Scour patterns are similar to patterns seen in tank tests although areas of deposition are formed in both model runs.

ACKNOWLEDGMENTS

This project is partially supported by EPSRC UK through DTA and Hector Class 1b Access Funding, it is also acknowledged that data from the National Oceanography Centre, UK is used for model operation and calibration

REFERENCES

Egbert, G.D., and S.Y. Erofeeva. 2002. Efficient inverse modeling of barotropic ocean tides. *Journal of Atmospheric and Oceanic Technology*, 19, 183-204.

Howarth, M.J., Player, R.J., Wolf, J., and L.A. Siddons. 2007. HF radar measurements in Liverpool Bay, Irish Sea. *Oceans 2007 – Europe*. 1-6.

Lambkin, D.O., Harris, J.M., Cooper, W.S., and T. Coates. 2009. Coastal process modeling for Offshore Wind Farm environmental impact assessment: Best practice Guide. *COWRIE Report*

Moulinec, C., Denis, C., Pham, C-T., Rougé, D., Hervouet, J-M., Razafindrakoto, E., Barber, R.W., Emerson, D.R., and X-J. Gu. 2011. TELEMAC: An efficient hydrodynamic suite for massively parallel architectures. *Computers & Fluids*, 51, 30-34.

Polton, J.A., Palmer, M.R., and M.J. Howarth. 2011. Physical and dynamical oceanography of Liverpool Bay, *Ocean Dynamics*, 61, 1421-1439.

Sumer, B.M., and J. Fredsøe. 2002.*The mechanics of scour in the marine environment.* Advanced series on Ocean Engineering. World Scientific.

Whitehouse, R. 1998. *Scour at Marine Structures*. Thomas Telford.